

Washington University in St. Louis
Washington University Open Scholarship

All Theses and Dissertations (ETDs)

5-24-2009

A New Quantitative Method for the Taxonomic Identification of Tetrapods

Stephanie Kuster

Washington University in St. Louis

Follow this and additional works at: <https://openscholarship.wustl.edu/etd>

Recommended Citation

Kuster, Stephanie, "A New Quantitative Method for the Taxonomic Identification of Tetrapods" (2009). *All Theses and Dissertations (ETDs)*. 891.

<https://openscholarship.wustl.edu/etd/891>

This Dissertation is brought to you for free and open access by Washington University Open Scholarship. It has been accepted for inclusion in All Theses and Dissertations (ETDs) by an authorized administrator of Washington University Open Scholarship. For more information, please contact digital@wumail.wustl.edu.

WASHINGTON UNIVERSITY IN ST. LOUIS

Graduate School of Arts and Sciences

Department of Earth and Planetary Sciences

Thesis Examination Committee:

Jill D. Pasteris, Chair

Jeffrey G. Catalano

Robert F. Dymek

Frank A. Podosek

Herman Pontzer

D. Tab Rasmussen

A NEW QUANTITATIVE METHOD FOR THE TAXONOMIC
IDENTIFICATION OF TETRAPODS

by

Stephanie Novak Kuster

A dissertation presented to the Graduate School of Arts and Sciences
of Washington University in partial fulfillment of the
requirements for the degree of

DOCTOR OF PHILOSOPHY

August 2009
Saint Louis, Missouri

copyright by
Stephanie Novak Kuster
2009

ABSTRACT OF THE DISSERTATION

A New Quantitative Method for the Taxonomic Identification of Tetrapods

by

Stephanie Novak Kuster

Doctor of Philosophy in Earth and Planetary Sciences

Washington University in St. Louis, 2009

Research Advisor: Professor Jill D. Pasteris

The rarity of good fossil samples throughout geologic time frequently makes fossil identification difficult. This dissertation presents a new, multivariate, statistically validated method to identify tetrapods based on quantification of the shapes of microstructural features in cortical bone of the postcranial skeleton. The ultimate goal is to reduce the reliance on rare, near-complete fossil skeletons. The method is validated on a set of 15,745 mammalian microstructural features from eleven diverse species. An additional set of 21,122 microstructural features from one species serve to examine microstructural variation within a single skeleton. Microstructural measurements were made on thin-sections using optical microscopy.

Initial tests of the method were applied to extant mammals whose taxonomic affinities were known. Three case studies comparing (1) the left tibiae from 11 mammals, (2) the mid-body of each left rib in *Odocoileus virginianus*, and (3) five cross-sections from left rib seven of *O. virginianus* represented tests of inter-taxonomic, intra-skeletal, and intra-bone microstructural variation, respectively.

Principal Component Analysis of measurements on the tibiae of 11 mammals was successful in discerning a taxonomic signal in the shape and size characteristics of primary vasculature, secondary osteons, Haversian canals, primary lacunae, and secondary lacunae. No single microstructure or measurement is sufficient to account for taxonomic variation. Rather, size, shape, and orientation of various microstructural features, in combination, define and distinguish the taxa. Soft Independent Modeling of Class Analogy properly reassigned test samples from several taxa. In contrast with the results from the multi-species set, analysis of the intra-skeletal and intra-bone case studies revealed no pattern of microstructural variation. The data suggest that the microstructural variation within a skeleton is small compared to variation between taxa and that intra-skeleton variation will not affect the overall taxonomic designation. All principal component analyses were tested and found to be significant at the 95% confidence level using Multiple Discriminant Analysis.

This work establishes a methodology for using bone microstructural features as a means for reconstructing taxonomic identity and supports continued research on this methodology, with the goal of applying it to rare fossil specimens in order to enable a next-generation approach to paleoecological analysis.

Acknowledgments

“There are many things in life that will catch your eye, but only a few will capture your heart...pursue those.”

The pursuit of a doctoral degree can be an astoundingly individual adventure. However, in the pursuit of enlightenment and knowledge, I was lucky enough to be supported tirelessly by mentors, advisors, and friends. Thank you, Jill, for indulging and respecting my independence and reminding me that rising to the occasion is necessary and worth the toil even when the wind in my sails was waning. I will be forever grateful. To the MacGyver of the thin-section laboratory—Bob Poly—I couldn’t have done it without you. If anyone ever needs to build a cut-off saw from a piece of gum and some duct tape, Bob is your man.

Deep bows of gratitude go to Eric Welsh—as if creating an algorithm to measure the microstructures automatically was not enough, your constant excitement about my project was inspiring. I truly enjoyed conversations with Eric and Anders Berglund about the utility of principal components analysis. Thank you for enduring my frustrations as I slowly walked the path of statistical enlightenment.

Washington University has been a most valuable resource and support, especially Tyson Research Center. I have never seen such enthusiasm to be a part of the rendering of a deer skeleton. Thank you also to the Missouri Department of Transportation for providing me with the white-tailed deer used in my analyses.

Thank you to my friends at colleagues at the St. Louis Science Center, especially Carl Campbell and Ron Giesler. It has been truly wonderful working with you and inspiring so many people with the wonders of scientific inquiry.

I appreciate the advice and guidance of my dissertation committee members, Jeffrey Catalano, Bob Dymek, Jill Pasteris, Frank Podosek, Herman Pontzer, and Tab Rasmussen, who graciously agreed to forge the path of a truly interdisciplinary dissertation.

I have been fortunate to receive grants from the Paleontological Society and the Association of Applied Paleontological Sciences to support my doctoral work. I am very thankful for their financial support. I am also very grateful for the monetary support from the Department of Earth and Planetary Sciences and Graduate School of Arts and Sciences through teaching fellowships. Thank you to the North Carolina Museum of Natural Science and the Museum of Comparative Zoology at Harvard for graciously providing mammalian tibiae for this study.

A large and glorious thank you to my friends, especially H. McKeag, K. Shaw, E. Harlan, R. Garrison, T. Arbor, H. Ramsey, J. Griffes, J. Miller, C. Campisano, G. Connellee, P. Vincenti, B. Blom, N. Nimmo. M. Pyle, K. Lichtenberg, R. Ziegler, K. Chaturvedi, and E. Emry. Your endurance and selfless love throughout these years has been truly inspiring. To my mom, your strength, perseverance, and love is palpable. I am sure that my dad would have been so proud of his little girl. Although he is no longer in bodily form, his soul and love lives on through me (as well as his nose and chin). That is a legacy that no one can deny. My mom and dad always made it very clear that I should make my own path in life. Thank you from the bottom of my heart for supporting me and enduring the extra production of gray hair as I adventured around the world. To my brothers Mark and Chris, I have always looked up to you. Thank you for being so great at what you do. It gave me so much to work for! To my husband Dan, you can make the sun shine on even the cloudiest of days. You inspire me, support me, and each day I pinch myself to make sure that I am not dreaming. I love you!

Stephanie Novak Kuster

Washington University in Saint Louis
August 2009

In joyous memory of my father, Edward Charles Novak.

Contents

Abstract	ii
Acknowledgments	iv
List of Figures	x
1 Introduction	1
1.1 Hypothesis	2
1.2 Literature Review of Osteohistology	8
1.2.1 History of bone microstructural analysis	8
1.2.2 Microstructural Differences in Taxa	12
1.3 Bone	15
1.3.1 Bone Function	15
1.3.2 Types of Bone	16
1.3.3 Molecular and Cellular Biology of Bone	17
1.3.4 Bone Micromorphology	21
1.4 Taxonomy Versus Phylogeny	31
2 The Location of Variation Amongst Dinosaurian Species	34
2.1 Introduction	34
2.2 Methods	35
2.3 Considerations and Assumptions	37
2.4 Results	39
2.5 Discussion	40
2.5.1 Skull and Dentition	41
2.5.2 Postcranial Remains and the Next Frontier of Distinguishing Dinosaurian Species	42
2.6 Conclusion	45
3 Methods	47
3.1 Introduction	47
3.2 Preparation of Bone for Histological Analysis	47
3.2.1 Petrographic Thin-Section Procedure	49
3.2.2 Microscopy and Micrographs	52
3.3 Quantitative Metrics for Analysis	53
3.3.1 Measurable Microstructural Units	54

3.3.2	Elliptical Microstructural Features	54
3.3.3	Microstructural Shape Considerations	55
3.3.4	Metric Geometry	57
3.4	Analysis of Microstructure	67
3.4.1	The Welsh Algorithm	68
3.4.2	Statistical Analysis	71
4	Extant Mammals as Taxonomic Test Subjects	72
4.1	Introduction	72
4.2	Mammalian Skeletal Gross Morphology	73
4.3	Mammalian Osteohistology	75
4.4	Mammalian Specimens: Primary Dataset	78
4.4.1	The Tibia	80
4.4.2	Order Carnivora	82
4.4.3	Order Rodentia	92
4.4.4	Order Didelphimorphia	96
4.4.5	Order Lagomorpha	98
4.4.6	Order Primates	102
4.5	Intra-skeletal and Intra-bone Variation	109
4.5.1	<i>Odocoileus virginianus</i>	109
4.5.2	Variation Datasets	110
5	Principal Components Analysis of the Primary Dataset and Dataset Modeling	124
5.1	Introduction	124
5.2	Collection of Microstructural Data	125
5.2.1	Dataset Hierarchy	126
5.3	Statistical Methods: Selection and Application	141
5.3.1	Principal Components Analysis	141
5.3.2	PCA of the Primary Dataset	144
5.3.3	Input	145
5.3.4	Retention and Discarding of Principal Components	154
5.3.5	Output	155
5.4	Results of Principal Components Analyses	159
5.4.1	Run 1	159
5.4.2	Run 2	169
5.4.3	Run 3	180
5.5	Soft Independent Modeling of Class Analogy	192
5.5.1	Data organization	195
5.5.2	Results: PCA by class	195
5.5.3	Results: SIMCA	201
5.6	Conclusions	208

6	Multiple Discriminant Analysis and Significance Tests of the Primary Dataset	210
6.1	Introduction	210
6.2	Multiple Discriminant Analysis: Run 1	213
6.2.1	Run 1A: Secondary Osteons	213
6.2.2	Run 1B: Haversian Canals	214
6.2.3	Run 1C: Primary Lacunae	219
6.2.4	Run 1D: Secondary Lacunae	219
6.2.5	Run 1E: Primary Vasculature	222
6.2.6	Run 1: Conclusions	225
6.3	Multiple Discriminant Analysis: Run2	225
6.3.1	Run 2: Results	228
6.3.2	MDA Run 2: Conclusions	228
7	Microstructural Variation in <i>Odocoileus virginianus</i>: The Ribs as a Case Study	233
7.1	Introduction	233
7.2	Intra-skeletal variation	235
7.2.1	Analysis	235
7.2.2	PCA Results	236
7.3	Intra-bone Variation	238
7.3.1	Analysis	240
7.3.2	PCA Results	241
7.3.3	Multiple Discriminant Analysis of the Intra-bone Dataset	245
7.4	Conclusion	248
8	Conclusions and Perspectives	252
8.1	Purpose	252
8.2	Conclusions	253
8.3	Future Work	255
8.4	Perspectives	257
Appendix A	Terms and Definitions	259
Appendix B	Diagnostic Characters in Dinosaurian Species	262
Appendix C	Determination of Longitudinal Orientation	280
	Curriculum Vitae	308

List of Figures

1.1	The visual comparison of bone microstructure suggests discrete morphologies, combinations, and arrangements of features unique to each taxon. A portion of the mid-diaphysis of the left tibia is shown for: (A) a bobcat; (B) rhesus monkey; (C) snowshoe hare; (D) capuchin monkey; (E) ruffed lemur; (F) raccoon; (G) black bear; and (H) opossum. Scale = 0.5mm	6
1.2	An overview of bone ranging from macroscopic (A) to nanoscopic (H) structural levels. Whereas the level of this dissertation is mostly concerned with parts B and C of this figure, the influences of the other structural and organizational levels of bone formation and remodeling had to be taken into account in order to develop the methodology presented in this study. Figure adapted from Pasteris et al., 2008. . .	19
1.3	The magenta box (A) encloses several primary vascular canals. The outlines of the canals are also marked in magenta. Primary laminae and lacunae sweep around the primary vascular canals, rather than enclosing the canals in concentric circles. In further distinction to the secondary osteons (B), the primary osteons are not enclosed by a cement or “reversal line.” The red dotted line (B) traces the reversal line of that secondary osteon. The approximately central Haversian canal is marked in blue. <i>Felis rufus</i> tibia. Scale = 0.5mm	23
2.1	The literature revealed 227 morphological differences that distinguished species within 39 dinosaurian genera. Genera are arranged by dinosaurian “group” and are listed within each “group” by alphabetical order. The vertical blue line separates cranial (to the left) from postcranial characteristics (to the right). The total number of recorded differences is highlighted in yellow.	38
2.2	The number of dinosaurian genera for which cranial remains are preserved for all of their species (black bar) compared to that subset of genera for which cranial diagnostic characters distinguish its species (gray bar). If cranial skeletal remains exist for all species within a genus, at least one cranial diagnostic character likely will have been reported. No cranial remains are known for some of the species of <i>Diplodocus</i> (Sauropodomorpha), yet there are cranial diagnostic characters that distinguish the species with in that genus.	43

2.3	The number of dinosaurian genera for which postcranial remains are preserved for all of their species (black bar) compared to that subset of genera for which postcranial diagnostic characters distinguish its species (gray bar). Presence of postcranial material for all species within a genus does not ensure that even one postcranial character has been designated as diagnostic.	44
3.1	Permanent equipment and consumables used in the thin-sectioning procedure.	48
3.2	Each long bone and rib from <i>O. virginianus</i> was measured and cut into five equal sections (1-5). All other mammal specimens were cut only at the mid-point of the diaphysis. The mid-point of the diaphysis (3) was determined as equidistant from the proximal suture (PS) line and distal suture (DS) line of the articular ends. Left humerus of <i>O. virginianus</i>	50
3.3	Secondary lacunae (cyan) are those lacunae which are found inside the reversal line (red) of secondary osteons. Primary lacunae (green) are found in the primary bone. Scale =0.5mm.	56
3.4	A schematic representation of a long-bone shaft and corresponding osteonal shaded cylinder (A) in the cortical bone that is oriented at some angle to the longitudinal axis of the diaphysis. This angle can be calculated at the intersection of the red and blue planes. The red plane represents the orientation of the thin-sections cut for this study (perpendicular to the long axis of the diaphysis). The blue plane is perpendicular to the long axis of the osteonal cylinder.	58
3.5	A two-dimensional Cartesian coordinate system was used to define the minor and major axes of elliptical cross-sections of microstructures. A schematic of a Haversian canal (A) is represented with line segment AB as the minor axis and line segment CD as the major axis. A secondary osteon (B) is represented with line segment EF as the minor axis and line segment GH as the major axis. The major and minor axes are always perpendicular to each other. However, in nested microstructures, such as the secondary osteon and Haversian canal shown here, the major axes of the larger and smaller ellipses may not be parallel (C). To account for this possibility, each microstructure is measured individually.	60
3.6	Highly magnified, the periosteal surface of a long bone or rib appears uncurved (A, red arrow). The transverse orientation angle, Θ_P , of the secondary osteon shown here as an example is determined as the angle between a line tangent to the periosteal surface and the extension of the major axis (GH) of the microstructure (B). Lemur tibia. Scale = 0.2mm	62

3.7	The major axis of a secondary osteon, line segment GH, represented in a two dimensional Cartesian coordinate system (A) can be translated/projected into a three-dimensional coordinate system by adding the Z-axis (B). The relative length of the major axis of the secondary osteon ellipse is indicative of the angle Θ_L between the Z-axis (i.e. longitudinal axis of the diaphysis) and the longitudinal axis of the osteon. Line segment G'H' represents the translation/projection of line segment GH in three-dimensional space.	64
3.8	Angle Θ_L represents the orientation of the vacuature or secondary osteon (SO) in relation to the longitudinal axis of the diaphysis (A). The red bar represents the plane of the thin-section cuts made in this study and the blue bar represents the plane that is perpendicular to the long axis of the secondary osteon cylindrical (SO). A cross-section parallel to the blue plane (B) shows the secondary osteon to have a hypothetically circular shape with radius r . A cross-section parallel to the red plane (i.e. actual orientation of the thin-section) shows an elliptical shape of the same osteon, with minor axis radius, r (C). The radius of the minor axis remains constant in all cross-sections (of varying Θ_L) under consideration. The deviation of the half-length of the major axis from r is indicative of the angle of the secondary osteon with respect to the diaphysis.	65
3.9	The marking and calculation of metrics from the digital micrographs begin with (A), digitally marking by hand the microstructures in colors corresponding to the feature type. Application of the Welsh algorithm overprints the features (B), allowing for individual checking of the micrographs to ensure that the correct measurements are being made. The yellow, dotted rectangle in (B) defines an area magnified in (C). The endpoints of the axes of the elliptical shapes are represented by the minute yellow crosses, and the centroids are represented by the cyan dots. Portion of a <i>Felis rufus</i> left tibia. Scale bar for (A) and (B) equals 2.5mm.	70
4.1	A schematic of cortical bone histology, with the four major types of bone separated by lines of arrested growth. Note that the separation of bone types and the variety of bone types in one sample are typically not seen all together in one cortical cross-section. The figure is for illustrative purposes only. Modified from Boef and Larsson, 2007, p.64	76
4.2	Summary showing all taxa included in the Primary Dataset and corresponding tibial measurements. All measurements are in millimeters.	79
4.3	The skeletal anatomy of <i>Odocoileus virginianus</i> (white-tailed deer). .	81

4.4	<i>Canis latrans</i> (Coyote) tibia (A) with a corresponding micrograph showing representative microstructural arrangement (B) and schematic (C). A continuous layer of secondary bone is bounded on both sides by primary bone along the periosteal and endosteal surfaces. Scale for (A) = 2cm. Scale for (B,C) = 0.5mm.	84
4.5	<i>Felis rufus</i> (Bobcat) tibia (A) with a corresponding micrograph showing representative microstructural arrangement (B) and schematic (C). Secondary bone of varying width occurs in the endosteal region of the cortex, bounded by a wide layer of primary bone on the periosteal surface and a thin layer along the endosteal surface. Scale for (A) = 2cm. Scale for (B,C) = 0.5mm.	87
4.6	<i>Procyon lotor</i> (Raccoon) tibia (A) with a corresponding micrograph showing representative microstructural arrangement (B) and schematic (C). Areas of secondary and primary bone alternate across the width of the cortex, beginning and ending with primary bone of the periosteal and endosteal surfaces, respectively. Scale for (A) = 2cm. Scale for (B,C) = 0.5mm.	89
4.7	<i>Ursus americanus</i> (Black bear) tibia (A) with a corresponding micrograph showing representative microstructural arrangement (B) and schematic (C). Areas of secondary and primary bone intermingle along the width of the cortex, with secondary bone present to the edge of the endosteal surface. Scale for (A) = 2cm. Scale for (B,C) = 0.5mm.	91
4.8	<i>Marmota monax</i> (Groundhog) tibia (A) with a corresponding micrograph showing representative microstructural arrangement (B) and schematic (C). There is an optically distinct interface between the bone of the periosteal surface, primary bone, secondary bone, and endosteal bone. Scale for (A) = 2cm. Scale for (B,C) = 0.5mm.	94
4.9	<i>Castor canadensis</i> (Beaver) tibia (A) with a corresponding micrograph showing representative microstructural arrangement (B) and schematic (C). There is an optically distinct interface between the bone of the periosteal surface, primary bone, and secondary bone; no endosteal bone is present. Scale for (A) = 2cm. Scale for (B,C) = 0.5mm.	97
4.10	<i>Didelphis virginianus</i> (Opossum) tibia (A) with a corresponding micrograph showing representative microstructural arrangement (B) and schematic (C). Primary bone with radial primary vasculature dominates the width of the cortex. Scale for (A) = 2cm. Scale for (B,C) = 0.5mm.	99
4.11	<i>Lepus americanus</i> (Snowshoe hare) tibia (A) with a corresponding micrograph showing representative microstructural arrangement (B) and schematic (C). Secondary bone is continuous along the endosteal surface, but is not constant in width; it intermingles with primary bone of the outer cortex. Scale for (A) = 2cm. Scale for (B,C) = 0.5mm.	101

4.12	<i>Varecia variegata variegata</i> (Lemur) tibia (A) with a corresponding micrograph showing representative microstructural arrangement (B) and schematic (C). Showing almost a quintessential “textbook” bone microstructural arrangement, a thin layer of periosteal bone flanks the outer edge of the diaphysis followed inwardly by regular widths of primary, secondary, and endosteal bone. Scale for (A) = 2cm. Scale for (B,C) = 0.5mm.	103
4.13	<i>Macaca mulatto</i> (Rhesus monkey) tibia (A) with a corresponding micrograph showing representative microstructural arrangement (B) and schematic (C). A single layer each of primary and secondary bone dominate the thin-section. A thin layer of endosteal bone flanks the inner edge of the diaphysis, but there is not a distinct layer of periosteal bone on the outer edge of the cortex. Scale for (A) = 2cm. Scale for (B,C) = 0.5mm.	106
4.14	<i>Cebus sp.</i> (Capuchin monkey) tibia (A) with a corresponding micrograph showing representative microstructural arrangement (B) and schematic (C). There is a “textbook” example of mammalian microstructural arrangement. A distinct layer of periosteal bone caps the outer edge of the cortex, followed inwardly by equal widths of primary and secondary bone, without an optically distinct interface between. A thin layer of endosteal bone flanks the inner edge of the diaphysis. Scale for (A) = 2cm. Scale for (B,C) = 0.5mm.	108
4.15	The long bones of the left portion of the appendicular skeleton of the specimen of <i>Odocoileus virginianus</i> used in this study. The forelimb includes the humerus (A), radius and ulna (B), and metacarpal (C). The hindlimb includes the metatarsal (D) and femur (E). The left tibia was shattered in the deer-vehicular accident. Scale = 5cm.	111
4.16	Left ribs of the <i>Odocoileus virginianus</i> specimen used in the current study. Rib 1 is the anterior-most rib in the series. Scale = 5cm. . . .	112
4.17	Right mandible of the <i>Odocoileus virginianus</i> specimen used in this study. The tooth patterning indicates that the specimen was approximately 2 years old at the time of death, as evidenced by fully erupted molars I-III with sharp cusps, the loss of the “milk” premolars, and the not yet fully erupted permanent premolar III.	113
4.18	Rib body and diaphyseal measurements of the appendicular skeleton of the <i>Odocoileus virginianus</i> specimen used in the current project. The diaphyses of long bones were measured between the proximal and distal epiphyseal sutures along the anterior portion of the bone shaft.	114

4.19	<i>Odocoileus virginianus</i> left rib 7. The total length of the rib body (red, dotted line) was measured before determination of cut placement (A). Cut three is the mid-point of the rib body, equidistant from the proximal and distal ends (B). The other four cuts divide the rib equally and are made perpendicular to the rib body. Scale = 5cm.	116
4.20	<i>Odocoileus virginianus</i> left rib 7 (A) with a corresponding micrograph showing representative microstructural arrangement of Cut 3 (B) and a schematic (C). Sub-equal widths of primary and secondary bone occupy the cortex. The cortex is generally very vascularized. Scale for (A) = 5cm. Scale for (B,C) = 0.2mm.	118
4.21	<i>Odocoileus virginianus</i> left rib 7, (A) with a corresponding micrograph showing representative microstructural arrangement of Cut 1(B) and a schematic (C). Sub-equal widths of primary and secondary bone occupy the cortex. There is no distinct periosteal bone. Scale for (A) = 5cm. Scale for (B,C) = 0.2 mm.	119
4.22	<i>Odocoileus virginianus</i> left Rib 7 (A) with a corresponding micrograph showing representative microstructural arrangement of Cut 2 (B) and a schematic (C). Secondary bone makes up double the width of the primary bone. Scale for (A) = 5cm. Scale for (B,C) = 0.2mm.	121
4.23	<i>Odocoileus virginianus</i> left Rib 7 (A) with a corresponding micrograph showing representative microstructural arrangement of Cut 4 (B) and a schematic (C). Sub-equal widths of primary and secondary bone make up the cortex. There is no distinct periosteal bone. Scale for (A) = 5cm. Scale for (B,C) = 0.2mm.	122
4.24	<i>Odocoileus virginianus</i> left Rib 7 (A) with a corresponding micrograph showing representative microstructural arrangement of Cut 5 (B) and a schematic (C). Sub-equal widths of primary and secondary bone make up the cortex. The primary bone shows a low density of vascularization. Scale for (A) = 5cm. Scale for (B,C) = 0.2mm.	123
5.1	The five hierarchical levels of data specificity are illustrated here using the Groundhog tibia as an example. Tiers I and II correspond to the entire tibia and the single cross-section taken from the mid-diaphysis for microstructural analysis. Tier III is represented by each micrograph in the cross section. Tier IV refers to each of the five microstructural types (secondary osteon, Haversian canal, secondary lacunae, primary lacunae, primary vasculature). Tier V is represented by the series of specific metrics used to characterize each of the types of microstructures in the cross-section. The number of measurements made depends on the type of microstructure.	127

5.2	Tabulation of the number of microstructural units of each of the five types measured within all 161 micrographs. The total number of microstructural units is dominated by the number of measured primary vascular canals, the majority of which were measured from the Hare. The number of micrographs per cross-section ranged from 5 to 32, from which 15,745 microstructural units were measured in total.	129
5.3	The number of microstructural units measured per micrograph ranged from 46 to 448 and was dominated by secondary osteons and Haversian canals. The bear had the highest number of microstructural units measured in one cross-section, 5151.	131
5.4	The number of microstructural units measured per micrograph ranged from 30 to 101 and was dominated by primary vascular canals. This microstructural dominance is evident in the totals per microstructural type, showing the primary vasculature with a total of 709 measured units in the Beaver cross-section compared to only 75 units each for secondary osteons and Haversian canals.	132
5.5	The bobcat cross-section is dominated by secondary osteons (687) and Haversian canals (701) compared to the primary vasculature (231). The total number of microstructural units measured per micrograph ranged from 69 to 178.	133
5.6	Summary table of the microstructural units measured in the Capuchin monkey cross-section. Despite large differences in the number of microstructural units measured per micrograph, i.e., 10 to 90, the total number of measured secondary osteons, Haversian canals, and primary vascular canals is close to equal.	133
5.7	The coyote cross-section is dominated by secondary structures. Many of the micrographs do not show any primary vascular canals. The accompanying absence of primary lacunae indicates that the lack of primary vascular canals was due to bone remodeling rather than simple lack of vascularization in the primary bone. Total microstructural units measured per micrograph ranged from 16 to 82.	134
5.8	The total number of microstructural units measured per micrograph ranges from 19 to 65. The partitioning of the microstructures into types reveals that there were many more primary vascular canals in the cross section (81) than secondary osteons and Haversian canals (31 each).	134
5.9	In contrast to the Bear (Figure 5.3), the cross-section of the Hare is dominated by primary vascular canals (1126) and has a dearth of secondary osteons (54) and Haversian canals (54). Given the size of the cross-section, there was a relatively large number of microstructural units measured per micrograph, ranging from 95 to 263.	135

5.10	The lemur cross-section is dominated by primary vascular canals (492) rather than secondary osteons (103) and Haversian canals (102). The number of microstructural units measured per micrograph ranged from 71 to 162.	135
5.11	The opossum has the lowest number of micrographs per tibial cross-section. The cross-section shows many more primary vascular canals (233) than secondary osteons (32) and Haversian canals (33). The number of microstructural units measured per micrograph range from 32 to 130.	136
5.12	The raccoon cross-section shows many more primary vascular canals (539) than secondary osteons (184) and Haversian canals (181). The number of microstructural units measured per micrograph ranged from 68 to 139.	136
5.13	The cross-section of the rhesus monkey showed more secondary osteons (309) and Haversian canals (309) than primary vasculature(84). Given the abundance of primary lacunae (about the same for the secondary lacunae), it appears that although primary bone was present, it was not highly vascularized. The number of microstructural units measured per micrograph ranged from 33 to 108.	137
5.14	In the simplest case, the number of secondary osteons equals that of Haversian canals. Some deviation from this equality is due to the occurrence of two or more Haversian canals within a single osteon (A, red arrows). Only those secondary osteons showing the entire circumference of the reversal line (B, red outline) were marked for measurement. The secondary osteon outlined in green has been partly overprinted and is not considered in the analysis. Examples sourced from <i>O.virginianus</i> rib (A) and <i>F. rufus</i> tibia. Scale for A = 0.2mm. Scale for B = 0.5mm.	138
5.15	Each metric used in Runs 1, 2, and 3 is represented by an abbreviation that refers to the type of microstructure and the specific measurement being applied to it.	140
5.16	When microstructural measurements are averaged for a cross-section, additional arithmetic functions can be applied to the direct measurements in order to derive additional relationships among microstructures of different types.	142
5.17	An example of the raw output from the Welsh computer program using a portion of the data obtained from the periosteal portion of sample 10 (micrograph) of the bobcat thin-section. The three dots in each of the sections of the last row and column signify the continuation of data. Please refer to the text for further details	147
5.18	A summary table of PCA Runs 1, 2, and 3 of the Primary Dataset. .	148

5.19	A portion of the data input for Run 1 of the Primary Dataset showing individual data points used to illustrate the spreadsheet structure. Cells containing three dots symbolize the continuation of data. Only columns for the 10 metrics of the secondary osteons are shown. All metrics shown in Figure 5.20 appear here as columns.	149
5.20	The metrics that can be applied to individual measurements with no averaging are denoted with check-marks. Only these measurements are used in Run 1 of the Primary Dataset.	150
5.21	A portion of the data input for Run 2 of the Primary Dataset using micrographs as “samples.” Cells containing three dots symbolize the continuation of data.	151
5.22	A portion of the data input for Run 3 of the Primary Dataset using the entire cross-section of each taxon as a “sample.” The values listed are averaged over an entire thin-section. Cells containing three dots symbolize the continuation of data.	153
5.23	The primary vascular canal outlined in red in this figure deviates from the expected “elliptical” shape, making measurement by best-fit ellipse (blue shading) subject to greater error in representation. Measurement of the actual shape outline will give a better representation of the “real” circumference.	157
5.24	The eigenvalues and r^2 values for each of the five principal components analyses of the Primary Dataset included in Run 1. Using the Kaiser-Guttman rule (eigenvalue must be ≥ 1.0), PCA of the secondary osteons, primary lacunae, and secondary lacunae results in two informative principal components, whereas analyses of the Haversian canals and primary vasculature result in three principal components to explain the variance in the dataset.	160
5.25	The scores (A) and loadings (B) plots for PCA of the Primary Dataset using only microstructural metrics of secondary osteons. Principal component 1 is graphed on the x-axis and principal component 2 on the y-axis.	162
5.26	The loadings plots for PCA of the Primary Dataset using only microstructural metrics of the Haversian canals. Before removal of 6 outliers (A) and after the removal of 6 outliers (B).	163
5.27	The scores plots for PCA of the Primary Dataset using only microstructural metrics of the Haversian canals (A) Before removal of 6 outliers and (B) after the removal of 6 outliers.	165
5.28	The scores (A) and loadings (B) plots for PCA of the Primary Dataset using only microstructural metrics of primary lacunae. Principal component 1 is graphed on the x-axis and principal component 2 on the y-axis	167

5.29	The scores (A) and loadings (B) plots for PCA of the Primary Dataset using only microstructural metrics of secondary lacunae. Principal component 1 is graphed on the x-axis and principal component 2 on the y-axis	168
5.30	The scores (A) and loadings (B) plots for PCA of the Primary Dataset using only microstructural metrics of primary vascular canals. Principal component 1 is graphed on the x-axis and principal component 2 on the y-axis	170
5.31	A table (A) and plot (B) of the eigenvalues for Run 2 of the Primary Dataset. The red star represents the cut-off for the valid eigenvalues as determined by the Kaiser-Guttman criterion. The red arrow is the eigenvalue cut-off using the Cattell Scree Test.	172
5.32	The loadings plot for Run 2 of the Primary Dataset, showing an enlarged view of the variables that explain the least amount of variance in the PC1-PC2 plane.	173
5.33	The loadings plot for Run 2 of the Primary Dataset, showing an enlarged view of the variables that explain a large amount of variance along positive principal component 1. There is a small amount of covariance with positive PC2.	174
5.34	The loadings plot for Run 2 of the Primary Dataset, showing an enlarged view of the variables that explain a large amount of variance along positive principal component 1. There is a small amount of covariance with negative PC2.	175
5.35	The loadings plot for Run 2 of the Primary Dataset, showing an enlarged view of the variables that explain a large amount of variance along negative principal component 1.	176
5.36	The loadings plot for Run 2 of the Primary Dataset, showing an enlarged view of the variable that explains a large amount of variance along positive principal component 2.	177
5.37	The loadings plot for Run 2 of the Primary Dataset, showing an enlarged view of the variable that explains a large amount of variance along negative principal component 2.	178
5.38	The scores plot for Run2 of the Primary Dataset showing clustering and separation of data points (each representing one micrograph) according to taxon.	179
5.39	Orthogonal views of the Primary Dataset in Run 2 looking at the X-Y plane down the positive Z-axis (A), the X-Z plane down the positive Y-axis (B), and the Y-Z plane down the positive X-axis (C).	181
5.40	Orthogonal views of the Primary Dataset in Run 2 looking at the X-Y plane down the negative Z-axis (A), the Y-Z plane down the negative Y-axis (B), and the X-Z plane down the negative X-axis (C).	182

5.41	A table (A) and plot (B) of the eigenvalues for Run 3 of the Primary Dataset. The red star represents the cut-off for the valid eigenvalues as determined by the Kaiser-Guttman criterion. The red arrow is the eigenvalue cut-off using the Cattell Scree Test.	183
5.42	The loadings plot for Run 3 of the Primary Dataset, showing an enlarged view of the variables that explain the greatest amount of variance along positive principal component 1.	184
5.43	The loadings plot for Run 3 of the Primary Dataset, showing an enlarged view of the variables that explain the greatest amount of variance along negative principal component 1.	185
5.44	The loadings plot for Run 3 of the Primary Dataset, showing an enlarged view of the variable that explains the greatest amount of variance along positive principal component 2.	186
5.45	The loadings plot for Run 3 of the Primary Dataset, showing an enlarged view of the variable that explains the greatest amount of variance along negative principal component 2.	187
5.46	The loadings plot for Run 3 of the Primary Dataset highlighting the variables that explain the greatest amount of the variance along positive principal component 1. There is a small amount of covariance with negative PC2.	188
5.47	The scores plot for Run 3, where each sample is one taxon, of the Primary Dataset showing the separation of the taxa in 3D space.	189
5.48	Orthogonal views of the Primary Dataset in Run 3 looking at the X-Y plane down the negative Z-axis (A), the X-Z plane down the negative Y-axis (B), and the Y-Z plane down the negative X-axis (C). The red dotted-line represents the diagonal distribution of the Primates in PC space, and the blue-dotted line likewise connects the Carnivora bear, coyote, and raccoon along a differently oriented diagonal line.	191
5.49	The open red circle represents a test sample. The Euclidean distances from the test sample to the two models PC1 (1) and PC1 (2) are $e_i(1)$ and $e_i(2)$, respectively. The Mahalanobis distance from the test sample to PC1 (1) is $h_i(1)$	193
5.50	Eigenvalues and the variance (r^2) explained by each local taxon model in SIMCA analysis.	197
5.51	The loadings plot for the Bear local model in SIMCA analysis.	198
5.52	The loadings plot for the Bobcat local model in SIMCA analysis.	199
5.53	The loadings plot for the Beaver local model in SIMCA analysis.	200
5.54	The loadings plot for the Coyote local model in SIMCA analysis.	202

5.55	A series of Coomans' plots showing pairwise comparisons between taxa and the critical values associated with the local model of each taxon (red lines). The colors of the points refer to the SIMCA-predicted taxon and the labels refer to the actual taxonomic origin of the datapoint. Additional pairwise plots are found in Figure 5.56.	203
5.56	A series of Coomans' plots showing pairwise comparisons between taxa and the critical values associated with the local model of each taxon (red lines). The colors of the points refer to the SIMCA-predicted taxon and the labels refer to the actual taxonomic origin of the datapoint. Additional pairwise plots are found in Figure 5.55.	204
5.57	The membership plots for each taxon in the SIMCA analysis show the Mahalanobis distances to each local model (labeled on x-axis) represented. For a test sample to be assigned to a taxon, it must have the shortest Mahalanobis distance to that taxon.	206
5.58	A Coomans' plot showing the twelve test samples that were assigned correctly to the bobcat local model whose training set had been depleted to only nine samples.	209
6.1	A series of tables and the canonical discriminant functions chart from the multiple discriminant analysis of the PCA scores of Run 1A (secondary osteons) of the Primary Dataset. The scores values for each principal component are significant to 95% confidence level.	215
6.2	The classification results from the multiple discriminant analysis of the PCA scores values of Run 1A (secondary osteons) of the Primary Dataset.	216
6.3	A series of tables and the canonical discriminant functions chart from the multiple discriminant analysis of the PCA scores of Run 1B (Haversian canals) of the Primary Dataset. The scores values for each principal component are significant to 95% confidence level.	217
6.4	The classification results from the multiple discriminant analysis of the PCA scores values of Run 1B (Haversian canals) of the Primary Dataset.	218
6.5	A series of tables and the canonical discriminant functions chart from the multiple discriminant analysis of the PCA scores of Run 1C (primary lacunae) of the Primary Dataset. The scores values for each principal component are significant to 95% confidence level.	220
6.6	The classification results from the multiple discriminant analysis of the PCA scores values of Run 1C (primary lacunae) of the Primary Dataset.	221
6.7	A series of tables and the canonical discriminant functions chart from the multiple discriminant analysis of the PCA scores of Run 1D (secondary lacunae) of the Primary Dataset. The scores values for each principal component are significant to 95% confidence level.	223

6.8	The classification results from the multiple discriminant analysis of the PCA scores values of Run 1D (secondary lacunae) of the Primary Dataset.	224
6.9	A series of tables and the canonical discriminant functions chart from the multiple discriminant analysis of the PCA scores of Run 1E (primary vasculature) of the Primary Dataset. The scores values for each principal component are significant to 95% confidence level.	226
6.10	The classification results from the multiple discriminant analysis of the PCA scores values of Run 1E (primary vasculature) of the Primary Dataset.	227
6.11	A series of tables from the multiple discriminant analysis of the PCA scores of Run 2 micrographs of the Primary Dataset. The scores values for each principal component are significant to 95% confidence level. .	230
6.12	The canonical discriminant functions plot from the multiple discriminant analysis of the PCA scores of Run 2 of the Primary Dataset. . .	231
6.13	The classification results from the multiple discriminant analysis of the PCA scores of Run 2 of the Primary Dataset.	232
7.1	A summary table showing the number of each type of microstructure measured per rib. The total number of microstructural units measured for this case study was 13,572.	235
7.2	A table (A) and scree plot (B) of the eigenvalues associated with the PCA exploring the variance in mid-body cross-sections of Ribs 2 through 12. The red star represents the eigenvalue cut-off per the Kaiser-Guttman rule. The red arrow on the scree plot points to the “elbow” that indicates the number of principal components that should be retained per the Cattell scree test.	237
7.3	The scores of the inter-rib case study are plotted in three dimensions, corresponding to the first, second, and third principal components. . .	239
7.4	A summary table showing the number of each type of microstructure measured per cross-section of Rib 7. The total number of microstructural units measured for this case study was 7,550.	240
7.5	A table of the eigenvalues (A) associated with the PCA exploring the variance in microstructural morphology within Rib 7. The scree plot of the eigenvalues (B) does not show a distinct “elbow”. The red star indicates the cut-off for retained eigenvalues under the Kaiser-Guttman rule.	242
7.6	The scores of the intra-rib case study are plotted in three dimensions that correspond to the first, second, and third principal components. .	243
7.7	Orthogonal views of the intra-rib dataset looking onto the X-Y plane down the positive Z-axis (A), the X-Z plane viewed down the positive Y-axis (B), and the Y-Z plane viewed down the positive X-axis (C). .	244

7.8	The loadings plot for the intra-bone dataset, highlighting the variables that explain the greatest amount of the variance along principal component 1 (blue boxes) and principal component 2 (green boxes). The yellow box highlights the variables in the dataset that explain very little of the variance.	246
7.9	A series of tables from the multiple discriminant analysis of the PCA scores of the intra-bone dataset. The scores values for each principal component are significant to 95% confidence level.	249
7.10	The classification results from the multiple discriminant analysis of the PCA scores values of the intra-bone dataset.	250
C.1	A series of schematics representing cylindrical microstructural bodies (secondary osteons, Haversian canals, primary vasculature). The angle Θ is the angle that the cylindrical microstructural body deviates from parallel with the longitudinal axis of the diaphysis. The variable r is equal to the radius of the minor axis of the microstructure and R is equal to the radius of the major axis of the microstructure.	281
C.2	Θ is determined using a derivation of the Pythagorean Theorem	282

Chapter 1

Introduction

The ability to identify and classify the fossilized remains of extinct organisms underlies all types of higher-order systematic and paleoecological hypotheses. In vertebrate paleontology, fossilized bones are central to what is known about extinct specimens. Unique amongst biological materials, bone is more likely to weather the passage of geologic time than is its soft-tissue counterparts, providing a window into the faunal component of the geologic past. What are the trends and details of vertebrate evolution? How has the faunal component of a paleoenvironment changed over time? These questions drive the hypotheses in vertebrate paleontology. Fossil bone provides the mechanism by which these hypotheses can be tested.

Fossil specimens are translated into “data points” as a result of a four-step process; (1) discovery, (2) collection, (3) preparation, and (4) identification. Skeletal discovery can be rapid. The most productive rock formations, such as the Cretaceous Dinosaur Park Formation in Alberta, Canada, can produce approximately one partial skeleton every two weeks during a typical summer field season a few months in length (D. A. Russell, pers. comm., 2004). Once discovered, however, the rate-limiting steps in the process become the collection, preparation, and identification of the specimen. The time it takes to collect and prepare a fossil specimen depends on the size and fragility of the bones, the completeness of the skeleton, and the resistance of the rock matrix in which it was entombed. Careful preparation of a fossil specimen is key-not only does this part of the process remove rock matrix from the bones, it also exposes the delicate morphology needed to identify the skeleton. The final three steps typically take a few years per specimen. With so much time invested in the gathering of a

single datapoint, it is clear how this slow trickle of data would inhibit the testing of paleobiological hypotheses.

Analysis and comparison of bone are traditionally achieved by an individual's examination of the gross morphology. Closer scrutiny of this process reveals that not only is the procedure subjective, but also that there are limitations to the information provided by the gross morphology of skeletal hard parts. The problems with the established procedure of fossil vertebrate identification are two-fold: (1) a near-complete fossil skeleton is currently a *de facto* requirement for identification; (2) vertebrate paleontology is restricted by a rarity of good samples and the low quality of bone preservation throughout geologic time. How can these energy barriers to specimen identification be lowered so as to produce taxonomically valid specimens in a reduced amount of time?

1.1 Hypothesis

The hypothesis tested in this dissertation is that taxonomic identification of extant and extinct tetrapods can be achieved through the rigorous, quantitative analysis of the microstructures in cortical bone.

Fossilized bones preserve a wealth of information, from gross morphology to microstructure. Current taxonomic techniques identify skeletal remains by the presence, absence, and morphological form of a group of homologous features present within a fossil skeleton. Often, the particular skeletal elements that are preserved do not embody the skeletal characteristics indicative of a particular vertebrate's "morphological space", thus rendering it very difficult or impossible to identify the animal to a very specific level. Not all bones have equal diagnostic potential using the current method of identification. Depending on the animal, the bone element, and the features that are preserved, it may be possible to identify the bone to the "familial" level, or in fortuitous circumstances, the generic level. The ability to classify an isolated element to the species level is rare, but this tends not to be a crippling issue, as the genus is the typical operational taxonomic unit in vertebrate paleontology (Holtz, 1998). Regardless of the high level of difficulty and uncertainty in fossil taxonomy, identifications of fossil vertebrate animals have been, and continue to be, decided on the

basis of fragmentary or isolated elements (Hunt et al., 1998; Le Loeuff and Buffetaut, 1991; Leidy, 1856). As with any subjective practice, differences of opinion about what constitutes a diagnostic feature or the presence or absence of the form thereof becomes a major consideration in the identification process—after all, there exists no objective ground truth upon which to build a hierarchy. This qualitative process of description and identification dominates taxonomic identifications and has muddled ongoing analyses of the fossil record through time.

The potential for errors in taxonomic identification increases as the number of bones from a skeleton recovered is reduced. Although there is much bone material preserved in the fossil record, it cannot always be identified. The recovery of diagnostic (i.e., taxonomically identifiable) skeletal elements is rare and recoveries of complete or nearly complete skeletons remain the anomalous and prized occurrences. Disarticulated skeletons and isolated and fragmentary bone discoveries are far more common than those of associated skeletons (Holtz et al., 2004). Despite the questionable fossil record quality, what is known about extinct vertebrates continues to grow. Scientific literature suggests that specimens are now classified on the basis of more complete skeletons than in the past (Benton, 2008). Regardless, geologic time is vast, and collective knowledge of the fossil record from any geological time period remains incomplete.

A large proportion of tetrapod fossils collected and housed at museums and universities have been deemed “useless” because the bones are incomplete, fragmentary, and/or cannot be identified using traditional, qualitative methods. Thus, bone fragments serve only as simple clues that the stratigraphic horizon contains bone material and maybe a more complete specimen may be found nearby. The fragments are rarely collected or examined unless they are in association with a more complete specimen. Isolated complete bones, however, are usually collected and, depending on the part of the skeleton represented, can yield varying amounts of taxonomic information (different bones carry different diagnostic potential). But what if all bones could have potential to lead to specimen identification? Useful taxonomic information could then be extracted from fragments and isolated bones, increasing the quality of the fossil record and allowing those faunal datapoints to be integrated into the context of paleoecological systems as well as from more complete specimens.

Gross morphological data encode low-frequency information. The differences in gross morphology between a massive *Tyrannosaurus* (Brochu, 2003) femur and a gracile *Struthiomimus* femur are obvious to a human observer because they span easily observable macroscopic length scales. However, morphological information is not always as straight forward as a size difference, especially when dealing with closely related specimens at the genus or species level. It is the idea of the “morphological species” that has allowed the subjective analysis of bone features to persist. Bone shapes are complex and are often not conducive to “tape measure” measurements that would provide quantitative data about bone shape. Bone microstructure, however, encodes information at a much higher spatial frequency; the information is well-preserved by the same mineral replacement processes that fossilize gross features. However, observing the spatial data present in bone microstructure usually requires a microscope—it exists on a different length scale than gross morphology. For the same reason that gross morphology is easily observed, whereas microstructures are not—size—a small bone feature or microstructure is more likely to avoid the destructive processes of geologic time, versus a large whole bone. The morphology and arrangements of microstructural features within the cortex of bone come up against the same arguments as the gross morphological features in their description. Quantitative description is difficult because the arrangements can be complex and difficult to describe using a “tape measure” method. Even if such measurements are made, the unexplored variation in the arrangements across and within specimens confounds any partitioning of the measurements into taxonomic meaning. However, the microstructures themselves are easily measured quantitatively, once the basis of bone formation and remodeling has been taken into account. This suggests that bone microstructural features may be an untapped source of data in fossilized bone and would support a quantitative method for taxonomic identification.

Efforts to extract useful taxonomic information from bone microstructure have been ongoing since the mid-1800’s, but thus far, none has been able to achieve a higher level of diagnostic power or to demonstrate robust quantitative objectivity. The discrete morphologies, combinations, and arrangements of bone microstructural components have long been suspected to be specific to particular vertebrate groups (Agassiz, 1843; Amprino, 1947; Enlow and Brown, 1956, 1957, 1958; Foote, 1911, 1913; Harsanyi, 1990; Hogler et al., 2003; Jowsey, 1966, 1968; Locke, 2004; Parfitt, 1983; Queckett, 1855; Ricqlès, 1986, 1990; Skedros et al., 1997). Figure 1.1 clearly illustrates visual

patterns in bone microstructures from various species. The hypothesis that is explored and tested in this dissertation has its foundation deep within the historical literature, but it is to be the first quantitative study of this hypothesis, the first that seeks to develop a simple, reproducible means by which isolated and fragmentary skeletal elements can be identified, the first to collect statistically significant numbers of samples from diverse species, and the first to apply modern statistical analysis to identify the sources of variation in microstructures.

The ability to identify a taxon based on the morphology of microstructures found in cortical bone would be a powerful identification tool. To be a useful diagnostic tool, bone microstructure must be shown to: (1) be measurable in a minimally destructive way; (2) correlate with the taxonomic hierarchy, (3) be relatively insensitive to uncorrelated features. Differences in cortical microstructural morphology may be the result of taxon-specific, phenotypic expression of genotypic differences, as well as of outside influences (e.g., biomechanical stresses) imposed on the skeleton throughout life. Inter-taxonomic differences in enzyme and protein expression during formation of secondary osteons, in tandem with the aforementioned biomechanical stresses, may allow for enough phenotypic osteological change in the secondary osteon, for example, that the differences can be detected and used to discriminate among forms. Regardless of the size of the bone fragment to be thin-sectioned and analyzed, bone microstructures will be present, because the largest microstructure, the secondary osteon, is generally less than 300 micrometers in diameter. Bone microstructures also tend to be abundant, as some increase in number with age (Amprino, 1963; Ascenzi et al., 1965, 2004; Baltadchiev, 1994; Bumrerraj and Katz, 2001; Chinsamy, 1995b; Currey, 1964; Enlow, 1977; Frost, 1963; Jowsey, 1966; Mulhern and Ubelaker, 2003; Mundy et al., 2003; Robling and Stout, 2000). Identifying bones based on microstructural morphology may increase, quite significantly, the amount of fossil vertebrate data recoverable in a given assemblage. This approach could augment the way extinct vertebrates are classified by reducing the reliance on gross morphological characteristics in taxonomy.

The purpose here is not to evaluate the cellular and molecular differences in bone microstructural formation or the nature of the biomechanical stresses in bone. Rather, the goal is to use the phenotypic expression of those differences to create a database of the quantifiable microstructural features of known taxa against which isolated

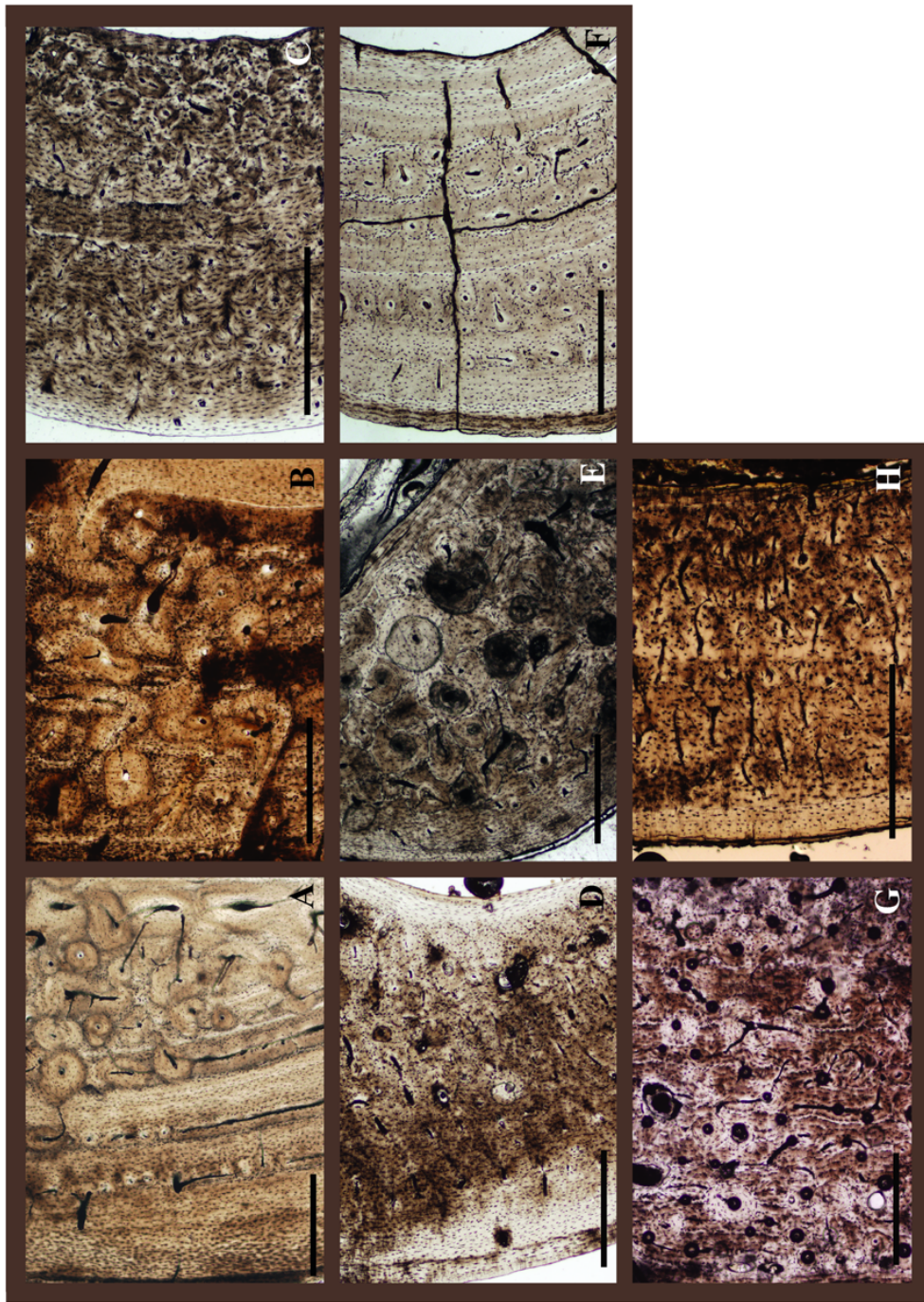


Figure 1.1: The visual comparison of bone microstructure suggests discrete morphologies, combinations, and arrangements of features unique to each taxon. A portion of the mid-diaphysis of the left tibia is shown for: (A) a bobcat; (B) rhesus monkey; (C) snowshoe hare; (D) capuchin monkey; (E) ruffed lemur; (F) raccoon; (G) black bear; and (H) opossum. Scale = 0.5mm

skeletal elements and fragments with no other means of identification may be compared. Essentially, each taxon will have a microstructural “fingerprint.” Because of the variability inherent within bone microstructure, a quantitative means of describing microstructure morphology is favored over more qualitative presence/absence or descriptive methodologies. Quantitative analysis of microstructural features ensures repeatability of the procedure and minimizes subjectivity. The analysis of microstructures for taxonomic identification will remove much of the dependence on gross skeletal features so that even those bones of the skeleton that are now of little taxonomic value even when they are well preserved (e.g., ribs), might be useful for specimen identification. This dissertation aims to “make something useful out of the useless” by focusing on the development of a rigorous, quantitative means by which isolated and fragmentary bones of fossil tetrapods may be taxonomically identified, to create the first microstructural database of extant mammal specimens, and to explore to what extent microstructural morphology represents a “taxonomic fingerprint.”

This dissertation is a series of eight chapters. The remainder of the current chapter is devoted to the history of bone histology and background information, to provide a context for the micromorphological features whose measurements are addressed in later chapters. Chapter 2 is a retrospective analysis, with the Dinosauria as a case study, used for the evaluation of past taxonomic practices. Chapters 3-7 investigate a forward-looking plan, describing the methodology used in this dissertation and exploring three datasets of microstructure features. All of the datasets are exploratory and are statistically analyzed to show (1) the microstructural metrics explaining the greatest amount of variance in each dataset, and (2) how much variation is present within and between taxonomic samples. Chapter 8 summarizes this work. The goal of the dissertation is to establish a suite of characteristic microstructural features that are generally applicable to tetrapods, which can be quantitatively and reproducibly measured and that, through statistical analysis, can be used to infer taxon.

1.2 Literature Review of Osteohistology

1.2.1 History of bone microstructural analysis

Observation of the microscopic structure of bone began in the early 17th century shortly after the invention of the compound microscope (Martin and Burr, 1989). Skeptical of the images that they were seeing, many early scientists were not convinced that the details shown were actually part of the bone (Bostock, 1825). Instead, many thought that the structures were an artifact of the new form of microscopy and assumed that the structures did not exist in nature. The effect of this skepticism coupled with the poor resolution of the early microscope caused many bone microstructures, including osteons, to go undescribed in detail for many years. The microscopic structure of compact bone, specifically the extensive canal system, was first formally described by van Leeuwenhoek in 1678 (Enlow, 1962). Clopton Havers added a more extensive description of bone structure in 1691 in a treatise entitled *Osteologia Nova* (Havers, 1691). Initial descriptions focused on the porous nature of bone, canal systems within the bone, and the “laminar” structure. In his treatise, Havers described in detail the remodeling structure that, many years later, would bear his name. The overall canal system, however, was first formally recognized by van Leeuwenhoek in 1678 (Martin and Burr, 1989). Because of the confusion as to which man should get the credit for its discovery, the often-referenced “Haversian system” is referred to exclusively as the “secondary osteon” by many bone histologists.

During the 150 years after 1693, there was little advancement in the study of the microstructure of bone. Previously published information was simply recapitulated by others. Revolutionary experiments, such as that of Du Hamel, who in 1739 revealed greater structural detail by staining bone thin sections using madder roots (the first use of staining techniques while viewing microstructure of bone), were rejected by the most prominent anatomists and physiologists of that time. It was not until the beginning of the 19th century that new information on the microstructure of bone was published and finally accepted in the scientific community. It is not an accident that this flurry of new information coincided with the advance of the microscope. Secondary osteons were described in greater detail in the middle of the 19th century (Bruns, 1841; Cruveilhier, 1844). These later observations of secondary osteons were

based heavily on comparisons with van Leeuwenhoek's original description. With the improvement of microscopic and histological techniques, however, the microstructures were able to be viewed at higher magnifications. These structures now were considered authentic rather than artifacts produced by poor microscopy. The repeated and thorough descriptions of the bone microstructures allowed investigators to reach beyond morphology and to begin to address the variation in the structures of the Vertebrata across a large number of taxa (Todd and Bowman, 1845). Specialization within the discipline ensued.

Although histological study has been performed on bones from both extant and extinct vertebrates, the study of the bone histology in fossil animals is deeply rooted in the history of comparative histology. Because most fossil material is of hard skeletal tissues, histology offers an additional line of inquiry into an otherwise very limited source of information. Comparative vertebrate paleohistology was established in the renowned work of Agassiz (1843), *Recherches sur les poisons fossils*, published in Neuchatel (1833-1844) (Ricqlès, 1990). Although Agassiz's publication was limited in the diversity of vertebrates addressed, soon to follow was work by Queckett, who published two of the first papers focusing on comparative vertebrate histology and paleohistology, mostly of tetrapods (Queckett, 1849a,b). He went on to publish a large, strikingly beautiful, illustrated catalogue of the collection of histological thin sections housed at the Museum of the Royal College of Surgeons of England (Queckett, 1855). The figures, produced using the camera lucida technique invented by William Hyde Wollaston in 1807, illustrate the bone sections in intricate detail at several magnifications. Most of the illustrations were drawn using two magnifications, 95- and 440-fold, to ensure a great amount of detail. The illustrations are still considered highly accurate and are comparable with the detail revealed in present microscope photography. In the second book of this two-volume set, Queckett described 945 histological preparations of vertebrate animals including 385 fishes, 103 reptiles, 60 birds, and 397 mammals. In addition, there were 18 plates containing 432 representations of what Queckett deemed as "the most striking specimens." This work was the first to illustrate the osteohistology of the dinosaur *Iguanodon anglicus* Holl, 1829. Other fossil specimens figured in the catalog are *Labyrinthodon*, *Pterodactylus*, *Ichthyosaurus*, *Colossochelys atlas*, *Glyptodon clavipes*, *Mastodon*, and *Megaceros hibernicus*, among others.

Illustration of histological images was most impressive during this time. Without the availability of good photographic techniques, each plate had to be drawn by hand. The work of Queckett set the bar for the detailed and careful presentation of bone microstructures, as well as their description. More descriptions and illustrations followed, encompassing many more extinct vertebrates including ichthyosaur and pleisiosaur bone tissues (Kiprijanoff, 1881). The figures and methodology in Kiprijanoff's publication also have had great influence on depictive styles and methodological approaches to paleohistology. One of the first researchers to use polarized light illustrated and described the bone histology of a Cretaceous crocodile and several Tertiary mammals (Schaffer, 1889), rounding out the great paleo-osteohistological works and advances of the 19th century. The production of these large osteohistological publications did not slow with the transition into the 20th century. Seitz described over 30 fossil reptilian and amphibian specimens in one of his works (Seitz, 1907). Foote published three large monographs in 1911, 1913, and 1916 pertaining to the comparative histology of the femur (Foote, 1911, 1913, 1916). His analyses began with the description and depiction of the femora of 46 different animals, including amphibians, reptiles, birds, and mammals (Foote, 1911). This was the first publication to have a large comparative database for the histology of a single element of the vertebrate skeleton. Foote expanded his dataset to include more orders, genera, and species of what he considered "lower animals" as well as three races of man. He published the largest of the three manuscripts in 1916 (Foote, 1916). Included are 440 detailed descriptions and 467 drawings of femora made directly from the thin-sections with the help of an Edinger Drawing Apparatus. The bones depicted are in various stages of development and show clearly the different bone types, particularly the distribution of secondary osteons. When possible, femora from the same species were described at different stages of development. Foote's monograph is perhaps the first attempt to characterize the ontogenetic histologic sequence of a particular taxon. Not only did Foote give detailed descriptions and illustration of the specimens, but he also gave a comprehensive overview of bone microstructure and the factors that influence the type of structures. Adding to the aforementioned publications at the beginning of the 20th century, were descriptions of primitive tetrapod bone (Gross, 1934).

By the middle of the 20th century there was evidence of the changing perspective on paleohistological research. Previously, the effort had been directed towards large

numbers of descriptions that addressed a large range of taxa. Instead of focusing on just qualitative description of the bone structure, osteohistological study was shifting to encompass broader evolutionary, physiological, and ecological implications of specific bone shapes and configurations. Instead of viewing histologic descriptions as stand-alone information, the microstructures were placed into the context of their origin and function. During the middle of the 20th century, a series of publications presented qualitative descriptions of 528 long bones of humans and other mammals (Forster and Goldbach, 1954; Goldbach and Hinuber, 1955; Hinuber, 1951). Enlow and Brown (1956; 1957; 1958) followed that attempt with a three-part series that provided an extensive overview of histodiversity in the major tetrapod groups, both extant and extinct. Although the publication was extensive and contained relatively detailed, modern descriptions, Enlow and Brown did not indicate the place on the particular bone from which the sample was extracted. Moreover, most descriptions were based on only one specimen for each taxon. Thus, the scope of intertaxonomic variation and the comparisons of bone microstructures between taxa were limited. Regardless, they are highly informative and well-cited works, and the literature on histodiversity continued to build (Enlow, 1963).

As a departure from completely qualitative analyses of bone microstructure, Singh et al. (1974) produced a semi-quantitative comparative study of 44 bone specimens of extant animals, most of which had died at the Bronx Zoo. Based on qualitative classifications of bone microstructure, Enlow and Brown (1956; 1957; 1958) characterized the osteohistology of six orders of mammals. Each thin section was evaluated under the microscope. The number and size of primary longitudinal canals were measured, and the number of lacunae was counted per field of view. It is difficult to discern whether their “primary longitudinal canals” are primary osteons or some other primary vascular feature. No oblique canals of any kind were counted in their analysis. Whereas secondary osteons were taken into account in their final description of the taxa, they only recorded the population density of such structures, not the shape and size. Because the number of secondary osteons present within the bone increases with the age of an animal, records of their population density are uninformative unless the ages of the zoo animals were known. Unfortunately, the ages of most of the animals were not indicated. The Singh et al.(1974) study is also problematic because the thin-sections they studied had been decalcified prior to viewing. The lack of mineral eliminated some of the morphology indicative of certain microstructures.

A very well-constrained early study of histodiversity, particularly for the goal of distinguishing human from non-human bone in archaeological sites, was done by Jowsey (1966). She addressed femora and ribs from a number of animals (mostly domestic) of a large age range. All animals were active at the time of death, showed no sign of metabolic bone disease, and died of sudden trauma or cardiac infarction. The thin-sections from the femora were taken perpendicular to the longitudinal axis of the diaphysis and at the mid-diaphysis. Rib sections were taken eight to 20 centimeters from the spine (Jowsey, 1966). Her consideration of location of the thin-sections, especially in the femur, allows for a direct comparison among the specimens with valid results.

More specialized analyses of the histological structures present in extinct taxa, especially dinosaurs, comprise the majority of such publications during the latter decades of the 20th century. Histological characteristics of extinct organisms have been studied from a variety of perspectives and for various purposes, including, physiology, phylogeny, and age calculations (Botha and Chinsamy, 2000; Chinsamy, 1990, 1992, 1995a,b, 1997; Chinsamy and Barrett, 1997; Chinsamy and Rubidge, 1993; Chinsamy et al., 1994, 1998a,b; Horner et al., 1999, 2000, 2001; Padian et al., 1995, 2001, 2004; Ricqles, 1968, 1972, 1974, 1980, 1986, 1990; Ricqles et al., 1997, 2001, 2003, 1991). Ushering in the increasingly quantitative treatment of bone microstructures was the introduction of a procedure by which to classify the different categories of bone within the cortex of a specimen (Boef and Larsson, 2007).

1.2.2 Microstructural Differences in Taxa

The early histological work of vertebrate paleontologists in the late nineteenth century was initiated in order to answer taxonomic questions rather than functional ones (Ricqles, 1990). As early as 1849, publications suggested that paleohistology might be a means by which to identify taxa (Queckett, 1849a,b). A solid basis for the idea that histology could reveal taxonomy was being developed through the ongoing examination and illustration of the microstructure of bone (Foote, 1911, 1913, 1916; Queckett, 1855). However, testing this hypothesis was an arduous process as a result of still-developing microscopic techniques and the overwhelming number of measurements that had to be made directly in the field of view of the microscope or

on hand-drawn illustrations. It had long been recognized that the cortex of bone, regardless of taxon, was composed of a series of standard microstructures. Instead of directing their attention to one or very few structures, early investigators tried to consider all of the microstructures as a collective whole. Overwhelmed with information and perhaps also due to the lack of convenient statistical analysis, scientists largely abandoned the use of bone microstructure to address taxonomic questions. Histological examination of bone evolved toward gaining insight into the physiological, biomechanical, phylogenetic, and ontogenetic growth characteristics of both extant and extinct taxa (Botha and Chinsamy, 2000; Buffetaut, 1982; Chinsamy, 1990, 1992, 1995a,b, 1997; Chinsamy and Barrett, 1997; Chinsamy and Rubidge, 1993; Chinsamy et al., 1994, 1998a,b; Currey, 1962; Curry, 1999; Horner, 1992; Horner et al., 1999, 2000, 2001; Padian et al., 1995, 2001, 2004; Pawlicki, 1985; Ray et al., 2004; Ricqles, 1968, 1972, 1974, 1986, 1990; Ricqles et al., 1997, 2001, 2003, 1991; Singh et al., 1974; Skedros et al., 2004; Steyer et al., 2004).

The discussion of histodiversity as a means by which to taxonomically identify a specimen received relatively little attention during the last century. Ricqles (1990) reviewed the history of the use of histological characteristics for taxonomic differentiation and the problems associated with this approach. He reinforced the need to consider the typological-structural diversity at the level of the individual, and he maintained that the microstructure of bone is at least in part controlled by the local conditions of skeletal formation and remodeling. Significant variation is observed in bone even in a comparison of different fields of view of a single thin section or between thin sections from different parts of a single bone (Ricqles, 1990).

Many publications mention the use of bone microstructure as a means to identify taxa, but typically only in passing (Amprino, 1947). Amprino (1947) was the first to use microradiographs to catalog the variation in appearance of cortical bone intertaxally. As optical microscopic, measurement, and statistical techniques improved in the middle of the last century, there was a small revival of the effort to showcase taxonomic diversity in bone microstructure. Unfortunately, descriptions of the variation were qualitative to semi-quantitative at best. Efforts were concentrated on amassing datasets for a wide variety of taxa and, in most cases, describing the microstructure based on one thin-section (Enlow and Brown, 1956, 1957, 1958; Forster and Goldbach, 1954; Goldbach and Hinuber, 1955; Harsanyi, 1990; Hinuber, 1951;

Jowsey, 1966, 1968; Singh et al., 1974). Enlow and Brown (1956) provided the beginnings of a standardized qualitative classification system for the types of cortical bone present in different taxa. Their three-volume set describes the bone microstructure in a diverse array of taxa, highlighting qualitative differences between taxa and setting the standard for discussion of histodiversity in the 20th century (Enlow and Brown, 1956, 1957, 1958).

More recent osteohistological research on the remains present in archaeological sites addressed the use of bone microstructure specifically to determine if human bone could be distinguished from non-human bone based on the secondary osteonal structure (Forster and Goldbach, 1954; Goldbach and Hinuber, 1955; Harsanyi, 1990; Hinuber, 1951; Jowsey, 1966, 1968; Kenyeres and Hegyi, 1903; Singh et al., 1974). Researchers were interested in the dichotomous designation of bones within the assemblage as “human” or “not human,” but not the specific identification of the taxa by means of osteohistology. Although the methodologies were mostly semi-quantitative, there were some positive results suggesting that *Homo sapiens* could be discerned from other mammals by their bone microstructure. Species-specific differences in bones of mammals were mentioned briefly in a qualitative context by Jowsey (1966) and Harsányi Harsanyi (1990).

More recently, examination of smaller scale bone microstructures found within cortical bone, called canaliculi, suggested that they might be indicative of taxonomic differences (Rensberger and Watabe, 2000). Canaliculi are canals with diameters in the micrometer range, that connect lacunae and serve as communication conduits within the ossified bone. According to the qualitative observations of Rensberger and Watabe (2000), there are morphological differences in canaliculi among dinosaurs, birds, and mammals. Additionally, they found that canalicular morphology and arrangement within the bone were also distinctive in various groups of dinosaurs, a conclusion that is of great importance to the present project as an example of the application of histology to taxonomy. (Rensberger and Watabe, 2000) also observed that the organization of collagen fiber bundles seemed to vary from one dinosaur group to another.

Attempts to distinguish taxa using bone microstructure were abandoned as continuing study of the microstructure yielded a myriad of complications from physiological,

lifestyle, and environmental influences that would affect the bone structure (Ricqles, 1990). Taxonomic osteohistological research has been hampered not only by inherent typological structural diversity at the intraspecific and individual level but also by small sample size (Singh et al., 1974). Despite their preliminary results showing apparent quantifiable differences in the bone microstructure of vertebrates, Singh et al. (1974) were of the opinion that any attempt to qualitatively distinguish between the taxa in their study would not be viable simply due to the small number of samples that were evaluated. Insufficient sample size is also a limitation in several other analyses of this type (e.g. (Harsanyi, 1990; Jowsey, 1966)).

An intriguing conference abstract reported the quantifiable and morphological differentiation of two species of *Equus* based on the structure of the osteons (presumably secondary osteons) (Davenport and Ruddell, 1995). Unfortunately, the abstract lacks methodological detail, the authors cannot be located, and the analysis was never followed up by a more complete documentation of the research. This fairly recent abstract was the catalyst for the present project. The morphology of secondary osteons and other measurable microstructures contained in the cortical bone are the focus of quantitative methodology presented in this dissertation, created to differentiate taxonomically between specimens.

1.3 Bone

1.3.1 Bone Function

Bone tissues provide mechanical support, protection of vital organs, hematopoiesis, and mineral homeostasis (Martin and Burr, 1989; Steele and Bramblett, 1988). Mechanical support ranges from the general strength and stiffness of bone necessary for proper organism function to the morphology of bone microstructures that are pivotal in order to avoid fracture and to repair fractures that do occur. Bone is lightweight, but strong per unit volume. Tests show it to be stronger than lead and to have more flexibility relative to its size than a spider web. Mechanical support of the skeleton is provided by the bones of the appendicular skeleton. Bones of the axial skeleton protect the organs, although some elements of the axial skeleton also assist with overall

support. The gross morphology of bone and the morphology of the microstructures within the ossified tissue often reflect the mechanical needs and locomotive habits of a particular organism. The skeleton has adapted through time to increase efficiency and to provide reinforced structural support for areas of the bone that are subject to the greatest stress. The hematopoietic function of bone is concentrated in areas with large amounts of trabecular bone, such as the proximal femur, the iliac crest, and the vertebral centrum. Hematopoietic function has been shown to be coupled closely with the maintenance of calcium balance (Broadus, 2003). The mineral component of bone not only contributes to the structural bone lattice, but also serves as chemical storage that may be accessed for use in a variety of bodily functions when dietary intake of calcium, phosphorous, or both is insufficient. Cortical bone stores the bulk of bone mineral components, accounting for its dense character; however, it has been shown that extraction of calcium and phosphorus occurs almost exclusively within the trabecular bone. The morphology of trabecular bone increases the exposed surface area of the bone, making the extraction of elements easier than from the dense and less accessible cortex. Once bone material has been removed, it typically is replaced promptly by secondary bone. The shared responsibility of mineral homeostasis between the cortical and trabecular bone allows the body to respond efficiently to rapidly shifting needs for calcium.

1.3.2 Types of Bone

There are three main types of bone, two of which will be the focus of this project. Subchondral bone, which is the ultra-smooth bone located on the articular ends of long bones or anywhere there is a joint with a covering of cartilage, will not be dealt with further. Of interest to this project are cortical and trabecular bone. Although the microstructural measurements for this project will be taken from the cortex, the close relationship of the cortex and trabeculae make it necessary to describe both types of bone. A transverse section through the diaphysis of a long bone reveals a dense, outer rim of cortical bone and, internally to that, spongy trabecular bone. Trabecular bone, also referred to as cancellous or “spongy” bone, is present in the core of all parts of long bones, but is dominant within the articular ends (Figure 1.2 (A, B)). Trabecular bone almost completely fills the articular ends, covered only by a

thin layer of cortical bone on the articular surface. Trabecular bone is also the main type found in the iliac crests and vertebral centra. As the colloquial name “spongy bone” implies, trabecular bone is an interconnected lattice of anastomosing struts, called trabeculae (Steele and Bramblett, 1988), giving it a “spongy” appearance. The struts of bone are of various thicknesses and comprise a combination of collagen and mineral just as in cortical bone. Between the struts lie soft tissue and vascularization responsible, in part, for hematopoiesis. Trabecular bone, as the most easily resorbed bone, is more susceptible than cortical bone to the effects of many metabolic bone diseases such as osteoporosis. If the bone of the trabeculae is resorbed at a greater rate than it is replaced, the struts become weakened and disconnected from each other. Once disconnected, the struts cannot be reattached, and the bone in that area becomes weakened and more susceptible to fracture. Hip fractures and the separation of the femoral head in the elderly are an unfortunate example of this effect.

Varying widths of cortical bone surround the trabecular bone. The dense, smooth, cortical bone provides the skeleton with a balance of strength and flexibility (Currey, 2002). The durability of cortical bone is a result of a balance between the amount of collagen and mineral that make up the cortex. Whereas there is some inherent variation in the amounts of each component within an individual skeleton and between different species, too much or too little collagen or mineral could predispose the bones to damage. Cortical bone is thickest close to the mid-point of the diaphysis of long bones. It is often highly remodeled as a result of mechanical stresses on and damage to the bone throughout the life of the animal.

1.3.3 Molecular and Cellular Biology of Bone

Bone is composed of noncollagenous proteins, collagenous proteins, and inorganic mineral (Baron et al., 1993; Martin and Burr, 1989; Steele and Bramblett, 1988), as shown in Figure 1.2(D) and Figure 1.2(E). The ground substance of the bone, the osteoid, is primarily composed of glycoproteins and proteoglycans (Baron, 2003). The proteins of the osteoid are thought to contribute to the calcification process and the fixation of the hydroxylapatite crystallites to the collagen fibers. However, the role of noncollagenous proteins in bone is not well understood at present. Approximately 90% of the collagenous proteins are Type I collagen and, generally, the collagen fibers

are preferentially oriented within the bone (Ascenzi et al., 2004; Baron, 2003). The orientation of the fibers changes from layer to layer within bone, giving the appearance of lamellae and allowing the highest density of collagen per unit volume. The orientation of fibers in the laminae that make up the trabecular and periosteal bone may differ from that in the concentric lamellae found around a vascular canal. The specific patterns of fiber orientation have been the focus of research to determine the effect on the mechanical properties (Currey, 2002). Research suggests that the arrangement of collagen fibers is spatially specific, in order to provide increased durability to the bone wherever the compressional and tensional stresses are focused. During increased rates of bone formation associated with the healing of fractures, in tumors, and as a result of some metabolic bone diseases, collagen fibers are deposited in a disorganized fashion. The quick, disorganized deposition of collagen and mineral in so-called woven bone stabilizes the injured area. It is followed by a period of bone remodeling that allows more optimized organization of the fibers to better support the bone in the long term.

The mineral component of bone consists of crystals of carbonated hydroxylapatite, $\text{Ca}_{10}(\text{PO}_4)_6(\text{OH})_2$ (Figure 1.2 G,H). Bone apatite crystallites are tens of nanometers in their longest dimension, and they account for about 70wt% (or 50% vol) of typical cortical bone. The crystals form an intimate nanocomposite with the collagen fibers, occurring on collagen microfibrils and within the collagen fibers. The close coupling of collagen and mineral gives to bone its properties of both flexibility and strength (Currey, 2002).

Osteoblasts

Osteoblasts are bone-forming cells. Osteoblasts begin as undifferentiated mesenchymal stem cells during the early stages of development. Undifferentiated mesenchymal stem cells are capable of forming a variety of lineages apart from the osteoblastic lineage, including chondrocytes, adipocytes, myoblasts, stomal cells, and fibroblasts. Formation of the mature osteoblast is a step-wise process and differentiation occurs under the influence of fibroblast growth factors (FGFs), bone morphogenetic proteins (BMPs), and Wnt proteins. The necessary transcription factors for this process are Runx2 and Osterix. As proliferation of the mesenchymal stem cells occurs, some of

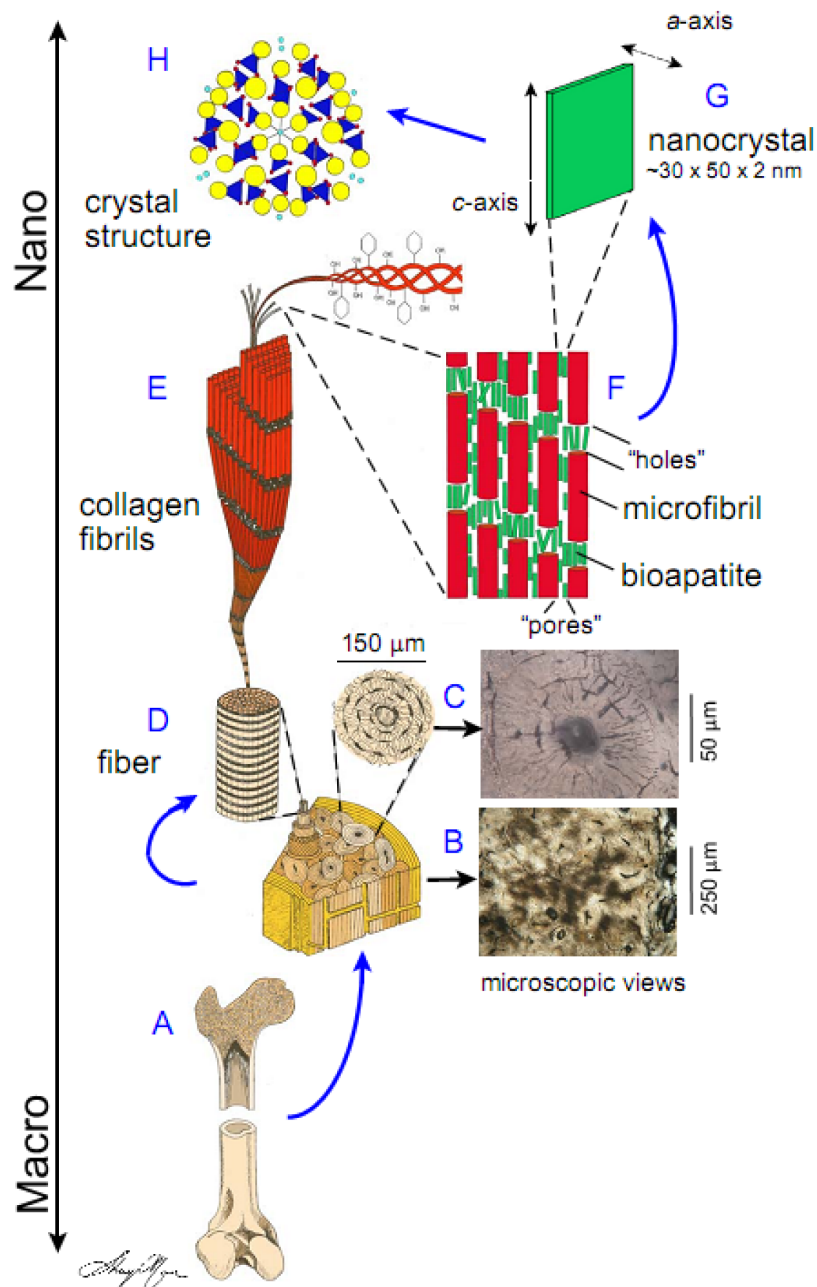


Figure 1.2: An overview of bone ranging from macroscopic (A) to nanoscopic (H) structural levels. Whereas the level of this dissertation is mostly concerned with parts B and C of this figure, the influences of the other structural and organizational levels of bone formation and remodeling had to be taken into account in order to develop the methodology presented in this study. Figure adapted from Pasteris et al., 2008.

them differentiate into preosteoblasts. Prior to the formation of the preosteoblasts, the proliferating cells may differentiate and change into different cellular lineages including those not involved in the bone-forming process. However, once the cell is a preosteoblast, there is no reversal process; it is committed to becoming an osteoblast. As the preosteoblast changes to form an osteoblast, it is considered mature. Mature osteoblasts are found in clusters of cuboidal cells along the surface of the bone, and they line the bone matrix before it is calcified (i.e. develops apatite crystallites). Osteoblasts are not mobile. At the conclusion of primary bone deposition around a particular group of osteoblasts, the latter become enveloped within the calcified matrix (Aubin et al., 1993; Baron, 2003; Lian et al., 2003).

Osteocytes

Once the osteoblasts become deeply embedded within the bone matrix and are no longer capable of producing bone, they are known as osteocytes (Baron, 2003). Osteocytes are housed within lacunae or flat, lining cells. Once embedded within the newly formed bone, the osteocytes decrease in volume and protein formation ceases. The morphology of the osteocyte changes with age and functional activity. Although most of the bone production capability has been inactivated in osteocytes, they have been shown to deposit small amounts of bone around the periphery of the lacunae in which they are housed. It has also been suggested that they play a role in cellular communication between structures within the bone. Osteocytes remain in communication with each other and with the active bone surface via gap junctions and filamentous processes. The filamentous processes are in place prior to ossification and form a network of canaliculi. This communication system is extensive and physiologically important. The total surface area of the cellular components in the combined network of canaliculi and lacunae is estimated to range between 1000 and 5000 m² for Homo sapiens. Likewise, 1 to 1.5L of extracellular fluid fills a periosteocytic space around the canaliculi and lacunae. The osteocyte will eventually be resorbed as a result of osteoclastic activity (Baron, 2003).

Osteoclasts

Osteoclasts are bone-resorbing cells. They are multinucleated cells containing anywhere from 4 to 20 nuclei, usually found at the interface between the calcified bone matrix and the bone marrow (Baron et al., 1993). Unlike osteoblasts, the osteoclasts are rarely found in large groups. There are usually only one or two osteoclasts per resorptive site. The osteoclast's attachment is characterized by a deeply folded border on a plasma membrane, allowing a greater surface area for resorption of the bone matrix. The ruffled border is sealed to the bone by a dense margin of actin (Baron et al., 1993; Baron, 2003; Mundy et al., 2003; Tolar et al., 2004). Sealing of the outer margin creates an isolated compartment for the osteoclast and facilitates the chemical reactions that occur within the compartment during resorptive activity (Baron, 2003; Baron et al., 1993; Boskey, 2003; Broadus, 2003).

Formation of the osteoclast follows a series of steps similar to formation of the osteoblast. The development of the osteoclast begins in the mononuclear/phagocytic lineage, and the cell differentiates at the early stages using the transcription factors PU-1 and MiTf. These transcription factors are responsible for the cell's commitment to the myeloid lineage. Proliferation of the monocyte lineage and expression of the RANK receptor requires the macrophage-colony stimulating factor (M-CSF) receptor. Commitment to the osteoclast lineage requires the presence of RANKL, produced by the stromal cells, as well as a number of other enzymes which all have downstream effects on RANK signaling. Unlike the osteoblast, which becomes embedded in the calcified bone matrix and changes morphology to become an osteocyte for the duration of its existence, the osteoclast is suspected to disappear as a result of apoptosis once resorptive activity is no longer needed. The apoptosis of osteoclast cells is thought to be triggered by estrogen (Baron et al., 1993).

1.3.4 Bone Micromorphology

The general microstructure of bone is evolutionarily conservative. Even in the earliest true vertebrates, all of the major microstructures, including lacunae, canaliculi, lamellae, and vascular canals, were present and highly developed (Ricqles, 1990). No

additional or unique microstructural components have appeared, and only a few vertebrate groups did not develop the normal suite of microstructures (e.g., in some reptiles, bone is avascular, lacking the primary osteons that are in most other vertebrate taxa). The absence of these structures is most likely due to the overall physiology and rate of growth of the animal and not to their incapability in producing such structures (Enlow and Brown, 1958; Ricqles, 1990). Only the organization and arrangement of the microstructural components change within different taxa, thought to be a result of physiological and mechanical optimization of the organism.

Primary Bone

Prior to a discussion of the general nature of bone microstructure, it is important to note that many microstructures have more than one term associated with them, such as primary laminae. Primary laminae are often referred to as primary or circumferential lamellae (Enlow and Brown, 1956, 1957, 1958). Because the terminology can be confusing, please refer to Appendix A for the definitions of the terms that will be used in the remaining chapters of the dissertation. The terminology used here will follow that of Locke (2004) unless otherwise noted.

The bones of most taxa consist of an outer cortical layer of primary bone made of vascular or non-vascular lamellae, depending on the physiological and mechanical needs of the vertebrate. Lamellae within the cortex are typically three to seven micrometers thick and are organized into three different arrangements (Enlow and Brown, 1958). (1) Lamellae are generally organized circumferentially around the cortex in groups separated by vascularization; such groups are called primary laminae (Locke, 2004). (2) Within the primary laminae are primary osteons surrounded by concentric lamellae (Figure 1.3(A)). (3) Lamellae also surround the Haversian canal, contributing to the form of the secondary osteon (Figure 1.3(B)). Primary osteons are centered on vascular canals, which provide nutrients and communication within the bone. These concentric structures are not to be confused with secondary osteons, which are similar in appearance. In addition to possessing a central vascular canal and surrounding concentric lamellae, secondary osteons are defined at their extremities by a cement line (reversal line), as highlighted in color in Figure 1.3(B).

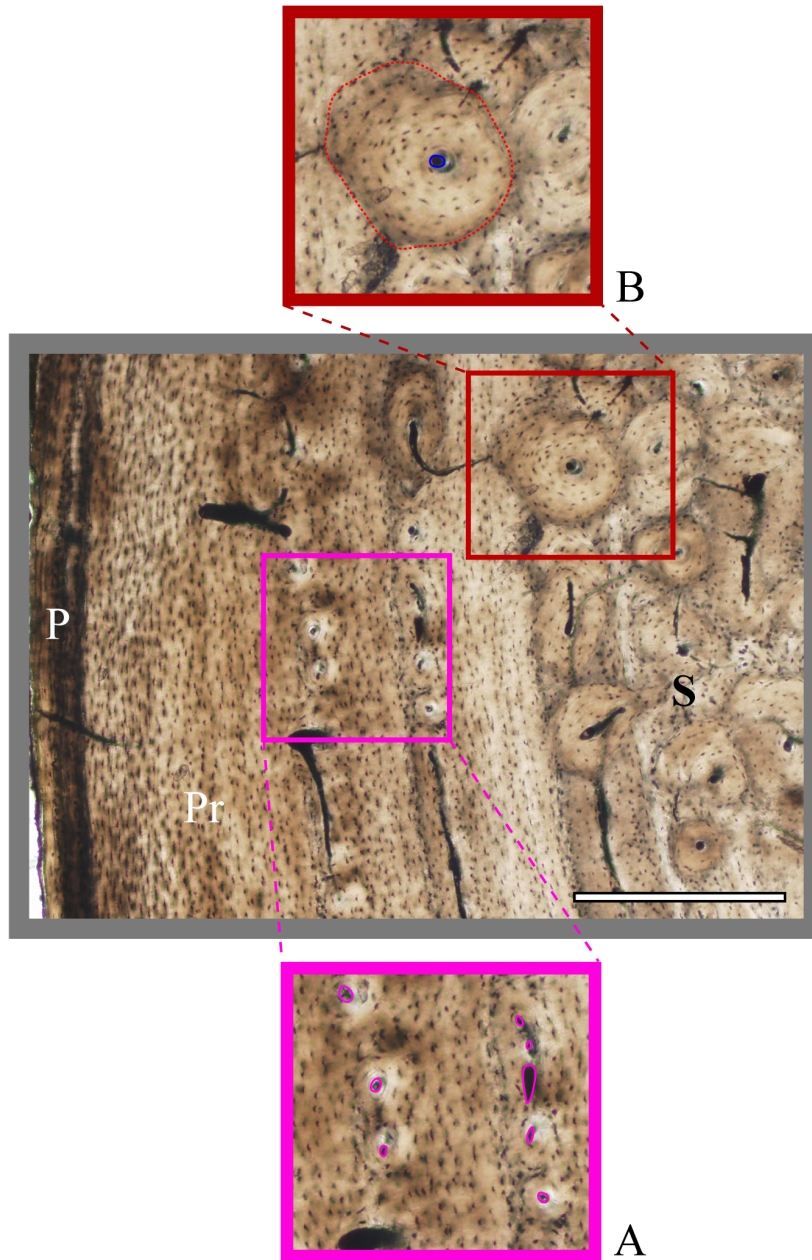


Figure 1.3: The magenta box (A) encloses several primary vascular canals. The outlines of the canals are also marked in magenta. Primary laminae and lacunae sweep around the primary vascular canals, rather than enclosing the canals in concentric circles. In further distinction to the secondary osteons (B), the primary osteons are not enclosed by a cement or “reversal line.” The red dotted line (B) traces the reversal line of that secondary osteon. The approximately central Haversian canal is marked in blue. *Felis rufus* tibia. Scale = 0.5mm

Despite the typological appearance of cortical bone, there can be variation within its microstructural arrangements both inter- and intrabone. Whereas some vertebrates (including amphibians, “reptiles,0” birds, and mammals) have no variation in cortical microstructure within the skeleton, there are many taxa that exhibit extreme variation (Enlow and Brown, 1958). The rib of *Bos taurus* (ox), for example, is composed of secondary bone tissue, but the femur of the ox (with the exception of the muscle insertions in which secondary osteons dominate) is made up largely of primary lamellar tissue (Currey, 1962). When describing the histological characters of bone in a particular taxon, skeletal variation must be taken into consideration. For comparison across taxa, the variation must be controlled by point-specific discussions of a particular bone or part of a bone.

Secondary Bone and Cortical Bone Remodeling

The periodic resorption of bone by osteoclasts and new deposition of bone by osteoblasts is a natural cycle in the bones of most vertebrates. Bone remodeling occurs to varying degrees depending on the overall physiology of the animal. In some vertebrates, such as many of the Mammalia, bone is continually remodeled. This process produces secondary osteons that can be viewed in thin-section.

The actions of osteoclasts and osteoblasts are coordinated during remodeling in both trabecular and cortical bone. Remodeling occurs on autonomous, focused packets of bone that are independent of other packets also undergoing remodeling throughout the skeleton (Mundy et al., 2003). As a result, remodeling is locally controlled by mechanisms of the particular bone’s microenvironment, such as the effects of mechanical stresses and the need for calcium mobilization. Remodeling always follows the same procedure, commencing with osteoclastic resorption and finishing with bone replacement by osteoblasts (Frost, 1964).

It has been suggested that remodeling in cortical bone is controlled, at least in part, by parathyroid hormone (PTH) and 1,25 dihydroxyvitamin D3 [1,25(OH)2D3] (Martin and Burr, 1989; Mundy et al., 2003). As the mechanical and physiologic needs of the skeleton change throughout the life of a vertebrate, the bone must compensate for resorptive activity by deposition of new bone. Failure of the skeletal system to

repair itself or to replace resorbed material will result in the weakening of the bones and will make them more susceptible to future structural problems. Cortical bone is removed from the skeleton primarily at the endosteal surface, and within other focused volumes in the mid-cortex that may need repair (Mundy et al., 2003). New bone is deposited within newly forming secondary osteons as well as at the periosteal surface. Periosteal accretion of bone occurs throughout life and gradually adds to bone diameter. Of particular interest to the current investigation is bone remodeling, which involves the development of secondary osteons.

Secondary Osteon Morphology

Secondary osteons (referred to as Haversian systems in some literature) are the replacement structures that “fill the columnar gaps” when bone material has been resorbed by the body (Figure 1.2 (B)). In transverse cross section, a secondary osteon consists of a sub-central vascular canal surrounded by concentric lamellae that contain lacunae, which house osteocytes, and canaliculae, which interconnect the lacunae (Figure 1.2 (C)). The border of the secondary osteon is defined by a visually distinct cement or “reversal” line as shown in Figure 1.3 (C). This border is the result of the cessation of bone resorption and the commencement of bone deposition during the remodeling process. The vascular canal, also known as the Haversian canal, ranges in diameter from ≈ 50 to 90 micrometers (Frost, 1961). Concentric lamellae that surround the Haversian canal, often referred to as osteonal lamellae, in combination with the visually distinct “reversal line,” give secondary osteons their characteristic and easily recognizable appearance. The presence of many lamellae gives secondary osteons an average diameter of 200 to 300 micrometers in human bone (Martin and Burr, 1989). Secondary osteons are easily distinguished from primary osteons by the arrangement of the lamellae, and by the presence of a cement/reversal line that marks the outer border of the secondary osteon (Hert et al., 1994; Martin and Burr, 1989).

The orientations of osteons vary throughout an individual bone (Cooper et al., 2003; Hert et al., 1994; Stout et al., 1999). Osteonal systems, i.e. arrays of osteons, have been described as having a longitudinal, spiraling morphology in long bone (Cohen and Harris, 1958; Tappen, 1977). Differences in osteon orientation have been observed in different taxa (Martin and Burr, 1989). In a few such studies, the average angle

of orientation was found to be 12 relative to the longitudinal direction of the bone (Cohen and Harris, 1958; Lanyon and Bourn, 1979). This angle coincides with the principal strain direction in the tibiae of sheep (Lanyon and Bourn, 1979) and in the femora of canines (Cohen and Harris, 1958). Based on radial and tangential sections of a canine femur, the spiral arrangement of the osteonal systems was found to begin at the periosteal surface of the bone and to proceed distally towards the endosteum. Enlow and Brown (1958) noted that, in the long bones of Carnivora, the secondary osteons were not arranged in uniform, longitudinal systems, but followed an irregular, apparently inconsistent, tortuous course as seen in the cortices of many mammalian groups. Recent examination suggests that, in the distal ends of long bone in man, the orientation of osteons is parallel to the longitudinal axis of the diaphysis (Hert et al, 1994). Three-dimensional studies (Hert et al., 1994) show that Haversian canals follow particular patterns through the bone that seem to reflect the dominant directions of mechanical stresses. In summary, the secondary osteon is generally not parallel to the longitudinal axis of the diaphysis, but, instead, is at some angle to that axis. Throughout the diaphysis, studies so far have found that the inclination of the osteons ranges from 0° to 15° with respect to the bone's longitudinal axis, with higher-angle inclination typically at the proximal end. Several studies have also noted that corresponding sections of contralateral bones had nearly the same number and distribution of osteons (Amprino and Marotti, 1964; Currey, 1964). This observation suggests that bones are affected symmetrically by mechanical forces in the process of bone remodeling.

Secondary bone is rarely represented by a discrete, isolated structure within the cortex. Rather, secondary bone entails anastomosing or branching patterns of multiple secondary osteons that create a complex remodeling structure (Cooper et al., 2003; Martin and Burr, 1989). In order to get the "overall trend" of the branching osteonal complex, the orientation of a large number of secondary osteons must be measured with respect to the longitudinal axis of the diaphysis. Osteonal distortion, i.e., deviation from circular cross-section, in transverse sections taken from the diaphysis is noted by many researchers (Amprino, 1963; Enlow, 1962; Harsanyi, 1990; Jowsey, 1966; Stout et al., 1999), but none has analyzed and interpreted these observations. In previous studies, secondary osteons were excluded from the dataset if they deviated too far from a circular profile in a transverse cross section (Jowsey, 1966). If the distortion was minimal, the lesser of the two diameters was recorded in the data

sets (Harsanyi, 1990; Jowsey, 1966). Many early studies used only the diameter of the Haversian canal to classify the histological structure. This practice failed to take into consideration that the diameter of the Haversian canal is dependent on a “snapshot” of bone remodeling—bone remodeling ceases with death, which may result in many Haversian canals that are larger than what were to be their final diameters. In *Homo sapiens*, Haversian canal diameter has been found to increase slightly during ontogeny, whereas the diameter of the entire secondary osteon (defined by the cement line) does not. There has been no evaluation of size change of the Haversian canal over the course of any non-human tetrapod’s life.

In *Homo sapiens*, bone research efforts have been and continue to be channeled toward the detailed study of cortical structure and habit in order to better understand bone diseases and to provide adequate treatments for those diseases (Hogler et al., 2003). In non-human tetrapods, emphasis has not been placed on characterizing the cortical bone system. Both normal and pathological development of cortical bone has been well-documented for all stages of human ontogeny. The intensive study of human bone microstructure is germane to the understanding of the development and remodeling of cortical bone in all vertebrates and serves as a basis for the method of the present study. No bones from *Homo sapiens* will be used in the current dataset because of the large range of biomechanical lifestyles within the human population. Wide-ranging locomotive lifestyles and activity levels affect bone microstructure (Robling and Stout, 2000). For instance, it is very likely that the rate and pattern of bone remodeling of an Olympic athlete would vastly differ from that of a graduate student who sits for long periods of time while doing research and writing her dissertation. The same arguments are also raised against the use of domestic animals in the present study. Animals that reside in an enclosed pasture and have their food regularly provided by the farmer, tend to make minimal movements even during normal day-to-day grazing. Such restrictions on motion and unnatural control of the movements that do occur, make it undesirable to compare domesticated with wild animals. The difference between wildtype bone microstructure and that of captively bred animals was documented in *Alligator mississippiensis* by (Padian et al., 2004). It is promising for the current study, however, that the osteon structure and alignment in human vs. non-human tetrapods is sufficiently different to appear distinctive to the naked eye (Harsanyi, 1990; Jowsey, 1966).

Secondary Osteon Formation

Secondary osteons are bone replacement structures that are very common within Mammalia, Aves, and Dinosauria (Botha and Chinsamy, 2000; Buffetaut, 1982; Buffrenil et al., 1990; Bumrerraj and Katz, 2001; Chinsamy, 1990, 1995a; Chinsamy et al., 1998a,b; Currey, 1962; Curry, 1999; Diaz and Rajtova, 1975; Havill, 2004) and are present in some “reptiles” and fossil forms, such as dicynodonts (Chinsamy and Rubidge, 1993; Enlow and Brown, 1957; Padian et al., 1995, 2004; Ray et al., 2004). In mammals that undergo secondary bone replacement, the secondary structural imprinting occurs over a primary cortical pattern that is qualitatively distinctive to each particular group (Enlow and Brown, 1957). Whereas variation among secondary osteons in humans is gradually becoming well-understood (Ardizzoni, 2001; Ascenzi et al., 2004; Cooper et al., 1966; Harsanyi, 1990; Hert et al., 1994; Jowsey, 1966, 1968; Stout et al., 1999), variation among the osteons of other vertebrates has been addressed by only a few authors (Harsanyi, 1990; Jowsey, 1966; Singh et al., 1974). What is known is that the formation of secondary osteons is evolutionarily conservative (Ricqles, 1990), which is of great importance to the method proposed in this dissertation. Because the formation of secondary osteons follows the same series of predictable steps for each type of vertebrate, at least some quantitatively measurable differences in the microstructural bone systems are likely to be unique to that organism. Therefore, it is necessary to have a basic understanding of the mechanisms behind the formation of secondary osteons.

Secondary osteons form by the erosion of (primary) laminae and the deposition of circumferential lamellae (Locke, 2004). The cells responsible for the initiation of bone remodeling may originate on any bone surface not covered by cartilage or otherwise inhibited from the remodeling process (Martin and Burr, 1989; Mundy, 2003). Resorption is most likely to begin at periosteal and endosteal surfaces, although bone resorption has been found to occur in already existing secondary bone (Locke, 2004; Parfitt, 1983). The mechanism that triggers the remodeling process has not been resolved (Martin and Burr, 1989; Mundy et al., 2003). Several investigations suggest that activation is signaled by repeated mechanical loading or fatigue damage (Enlow, 1977; Frost, 1963, 1964, 1966; Martin and Burr, 1982). Hormonal activation of remodeling has also been suggested, with the activation driven by parathyroid hormone

(PTH) and 1- α , 25-(OH) $_2$ vitamin D $_3$, both regulatory hormones involved in bone remodeling (Rodan and Martin, 1981).

The process of secondary osteon formation was first described in 1853 (Tomes and De Morgan, 1853). More detailed investigations and descriptions of the process were published in the 1960s (Frost, 1963, 1964; Johnson, 1964, 1966) and set the standard for continuing research in this area. The structure resulting from the coordinated effort of osteoclasts and osteoblasts is referred to as a Basic Multicellular Unit (BMU) (Frost, 1963). As a functional unit, the secondary osteon is a BMU, referring to the bone contained within the cement (reversal) line plus the Haversian canal (Martin and Burr, 1989). During formation of the BMU, there are three phases of bone remodeling. Referred to as the ARF process, the first phase is activation (A), which is followed by resorption (R) and then by bone formation (F). In humans, the ARF process is completed in approximately 200 days (Baron, 2003). Activation begins with formation of osteoclasts from stem cell populations. The osteoclasts created at this stage survive the entire resorptive process before being subject to apoptosis when they are no longer needed. The differentiation of osteoclasts takes approximately three days, after which the section of bone to be resorbed is targeted and opened by the acidic secretions of the osteoclasts. Once resorption begins, movement of the osteoclasts follows a longitudinal direction (relative to the longitudinal axis of the bone) and progress of the osteoclasts is approximately 40-50 μ m per day (Martin and Burr, 1989). During this stage of remodeling, the cells are arranged in the characteristic “cutting-cone” (Baron, 2003; Mundy et al., 2003) typical to the formation of all secondary osteons. In tangential and radial cross section, cutting cones are observed passing one another in opposite directions (Martin and Burr, 1989), showing that the resorptive activity does not have a preferential direction. It is also possible that the resorption tunnel may be “double-ended”, activating at a single location and resorbing in opposite directions (Tappen, 1977).

Once the resorption period has ceased, there is a time lag before redeposition. The reversal from osteoclastic to osteoblastic activity occurs over a few days. Deposition of bone begins around the periphery of the tunnel created by the cutting-cone, averaging a rate of radial closure of 1-2 μ m per day. The (earliest secondary) bone deposited around the periphery of the cutting-cone is what is recognized as the cement/reversal line of the completed secondary osteon. The material initially deposited

by the osteoblasts is osteoid, an unmineralized matrix of bone. After a lag time of approximately 10 days, the mineral component of bone is deposited. Approximately 60% of the calcification of unmineralized bone matrix occurs within the first 24 hours (Parfitt, 1983), taking place within and between collagen fibers. The cylindrical cutting-cone does not completely refill with bone matrix. Instead, a central, cylindrical region of the secondary osteon is left empty for vascularization of the structure. This vascular space is the Haversian canal, the diameter of which is somewhat species specific (Martin and Burr, 1989).

Secondary osteons are generally less than 250 micrometers in diameter regardless of the body size of the vertebrate (Jowsey, 1966). There seems to be a general increase in size of secondary osteons as the size of the vertebrate increases, but it is rare that the osteons within an individual are consistently over 250 μ m in diameter. The size of secondary osteons does not change significantly with ontogeny. However, the size of the Haversian canal increases over time in human long bones. Possible variation in Haversian canal diameter with ontogeny has not been investigated for non-human vertebrates. Secondary osteons are complex structures (Cohen and Harris, 1958; Hert et al., 1994; Stout et al., 1999). Due to the concentration of remodeling structures around muscle attachment sites, biomechanical stress has been thought to be the major component responsible for remodeling dynamics. Muscle attachment sites are generally under a greater amount of mechanical stress than the rest of the bone (Lanyon and Bourn, 1979). Whereas the mechanisms by which cells are signaled to differentiate into secondary bone are still under study (Mundy et al., 2003), a prominent hypothesis is that the BMUs respond to mechanical loads, fatigue damage, or both (Martin and Burr, 1982) to begin the remodeling process.

Secondary Osteon Biomechanics

Secondary bone shows reduction in compressive and shear strengths, flexural fatigue strength, and resistance to tension compared to primary cortical bone (Carter and Spengler, 1978). A study of secondary osteons indicated that the maximum values for resistance to tensile, compressive, and shear forces before failure varied among individual osteons (Ascenzi and Bonucci, 1964, 1967, 1968, 1972). The differences in values were thought to be attributable, at least in part, to the mechanical stresses

locally extant in the part of the bone from which the osteon was extracted. Variation in stress resistance was also thought to result from variation in collagen fiber orientation in each lamella (which is also suspected to be the result of mechanical influence). The osteonal lamellae, although their microstructural arrangements seem the same at the micrometer scale, differ quite significantly in structural properties and resistance. In the human femur, the orientation of the collagen fibers differs depending on whether the part of the bone in which they are located is subject to tensile or compressive forces (Currey, 2002; Portigliatti-Barbos et al., 1983, 1984). Regions subjected to tensile stresses have a greater proportion of longitudinally oriented collagen fibers than regions of compressive stress. Bone volumes subject to compressive stress contain more transversely oriented collagen fibers. Electrical properties of cortical bone also may be responsible for the alignment of osteons (Martin and Burr, 1989). Osteoblastic and osteoclastic differentiation and activity may be controlled by strain-induced electric potentials that encourage osteons to align with the principal compressive strain direction. The population density of osteons also may be due, in part, to the electrical potentials caused by mechanical strain. Subperiosteal osteons are associated with a strongly positive surface charge related to a greater amount of tensile stress. Negative surface charges on bone are usually associated with compressive mechanical stresses and appear in areas dominated by circumferential lamellae (McElhaney, 1967). Such osteon distribution factors may prove useful in the analysis and interpretation of the locomotive habits of both extant and extinct vertebrates. Such factors may also contribute to taxonomic differentiation.

1.4 Taxonomy Versus Phylogeny

The intended goal of the present study is to develop a methodology that will allow researchers to distinguish and identify taxa within a stratigraphic horizon or assemblage. It is important to note that the goal of the present investigation is not to infer any phylogenetic relationships among the taxa included in the datasets. The method presented in this dissertation is intended to detect the taxonomic “fingerprint” of a specimen rather than to infer specimen relationships. Admittedly, some phylogenetic characters may be discovered from microstructural analysis. The distinction in goals is important to clarify because, particularly in the paleosteohistological literature,

the terms phylogeny and taxonomy are closely associated and often used in a complementary manner during discussion. Unfortunately, the terms are also often used synonymously (Ricqles, 1990). This practice is clearly inappropriate. Whereas phylogeny refers to the evolution or evolutionary history of a genetically related group of organisms, taxonomy is the study of the general principles of scientific classification of organisms.

There is a general understanding within vertebrate paleontology that a taxonomic classification cannot be developed by way of phylogenetic study. For example, if there is a “knob” on the femur, it is presumed to mean something in a phylogenetic sense. If it is absent, it also presumably means something. The knob is coded in a phylogenetic character matrix as a one (present) or a zero (absent). However, the discrete morphology of the knob itself is rarely addressed at a detailed level during phylogenetic analysis. Detailed description of a specimen, in contrast, is usually reserved for and limited to the identification of the specimen taxonomically. Therefore, the disconnect with phylogenetic analysis arises as the detailed morphology of gross characters is not included in the evaluation. Interestingly, phylogenetic analysis that incorporates paleohistology has been criticized on the basis that there is too much variability within bone microstructure to make it a useful phylogenetic character. A look at a histological section will reveal a myriad of structures that are seemingly alike and also seemingly randomly arranged. There are no “knobs” to be declared present or absent on a secondary osteon, like those paleontologists are used to on a gross morphological scale. While reference to gross morphology in phylogenetics has become a comfortable and cosmopolitan practice among vertebrate paleontologists, investigation into the microstructure of bone is relatively rare and is only employed by “specialists” within the field.

The absence of a large, active community of bone microscopists and interpreters results in much speculation about bone micromorphology, as well as common misunderstanding and confusion of terms. Another intellectual barrier to the regularized interpretation of bone micromorphology (compared to gross morphology) is the need to deal with specific challenges in evaluating variations at a fine spatial scale. The skills to analyze the microstructure of a bone must be honed more carefully than those to describe gross morphology. Evaluation of bone micromorphology demands

a system that does not rely simply on the presence or absence of a particular feature to enable taxonomic identification and, perhaps, to reveal phylogenetic relationship.

The remaining chapters of this dissertation deal with specific aspects of taxonomy and the proposal and testing of a quantitative means of representing micromorphologic features of bone and their taxon-specificity.

Chapter 2

The Location of Variation Amongst Dinosaurian Species

2.1 Introduction

There is no quantitative principle governing the designation of a new dinosaurian species. Paleontologists operate under a loosely defined “morphological species concept” that allows specimens of the same genus to be designated as different species only if, in addition to the morphological characters that unite them within that genus, there are also gross morphological distinctions (Benton and Pearson, 2001; Carrasco, 1998; Hey, 2001; Lewin, 1986; McAlester, 1962; Miller, 2001; Simpson, 1951; Sokal, 1973; Weller, 1961). The challenge in the taxonomy of extinct organisms, particularly vertebrates, is that time typically has reduced the evidence of shared genetic material to only the preserved bone. Moreover, the rarity of bone preservation has left the fossil record inherently incomplete, but abounding in fragmentary specimens (Holtz et al., 2004). Being able to identify these incomplete and fragmentary specimens would bring vast amounts of new data to paleontological inquiry. The methodology and test datasets in the chapters that follow focus on using characteristics of bone microstructure from the postcranial vertebrate skeleton to taxonomically distinguish tetrapods. In order to substantiate the purpose and importance of focusing on the postcranial skeleton in the new method of using bone microstructure, this chapter presents a literature-based evaluation of the anatomical location of published skeletal variations among dinosaurian species.

The Dinosauria was one of the most successful vertebrate groups, dominating nearly all terrestrial niches for over 160 million years. Despite the relatively large amount of dinosaurian skeletal material available, there is still a struggle to resolve taxonomic and phylogenetic issues, the foundation of paleontology. Whereas the genus is the typical, operational taxonomic unit in dinosaurian paleontology, species-level taxonomy remains the goal (Holtz, 1998). In most cases, remarkably, a dinosaurian genus has only one species assigned to it (Weishampel et al., 2004). This Chapter, however, focuses exclusively on those dinosaurian genera that have more than one species assigned to them. This is an historical overview of congeneric dinosaurian species, cataloging the number of morphological differences present between species and identifying the skeletal sections containing those differences. The goal is not to define the concept of dinosaurian species, but rather to highlight those areas of the skeleton that have been and continue to be the focus of the classification process.

Abbreviations- **D**, morphological differences in dentition; **D#**, differences in number of teeth; **F**, forelimb; **H**, hindlimb; **PC**, pectoral girdle; **PL**, pelvic girdle; **R**, ribs; **RO**, overall more robust/gracile; **RP**, part of body more robust/gracile; **S**, skull; **SC**, scutes; **SG**, number of species within the genus; **SZO**, overall size; **T**, total number of differences; **V**, morphological differences in vertebrae; **V#**, differences in the number of vertebrae.

2.2 Methods

A complete survey of morphological variations within a dinosaurian skeleton requires that each ossification be considered individually. In order to do this, the number of ossifications in a “generalized” dinosaurian skeleton must be determined. The overall morphology of the dinosaurian skeleton is extremely variable. Consideration of the morphological differences between such dinosaurian groups as the Theropoda and the Sauropoda clearly illustrates this skeletal variation. Despite the phenotypic differences among dinosaurs, their skeletons, like those of most tetrapods, are composed of generally the same suite of elements. For the present historical survey, the number of total ossifications is based on the skeleton of *Herrerasaurus* (Reig, 1963), a late Triassic theropod considered to be a basal member of the Dinosauria (Galton, 1985;

Reig, 1963), and the survey is enhanced by an overview of more derived dinosaurian osteology. A total of 332 distinct, named ossifications are recognized, not including dentition.

Each bone was weighted equally in the analysis. To avoid giving too much weight to serially repeated bones in the axial column and to compensate for the highly variable number of vertebrae within the dinosaurian skeleton, the vertebral column was represented by one of each type of vertebra. Each specimen was considered to have an atlas, an axis, one cervical vertebra, one dorsal vertebra, one sacral vertebra, one anterior caudal vertebra, and one distal caudal vertebra. Just as the number of serially repeated bones was reduced for consideration, bilaterally duplicated bones were reduced by one half. Ribs are both serially repeated and bilaterally duplicated. One of each type of rib, including cervical, dorsal, and sacral ribs, as well as a chevron, was included in the analysis. If a skeletal distinction for taxonomic purposes was present in a bilaterally or serially duplicated bone, the assumption was that the same distinction also is present in the match of the pair or in all bones of the series, respectively. Sensory elements, such as sclerotic plates, stapes, and hyoids, were not diagnostic for any of the taxa in this investigation and thus, were not included in the total bone count. Using the guidelines set above, the total number of bones was reduced from 332 ossifications to 89, including one of each type of dentition (a premaxillary, maxillary, and dentary tooth). Without bone repetition, the remaining 89 bones used in this study will herein be referred to as the “reduced dinosaurian skeleton.”

For purposes of analysis and comparison, the dinosaurian skeleton was partitioned into morphological categories including discrete body sections as follows: Skull, Dentition, Vertebral Column, Pectoral Girdle, Forelimb, Ribs, Pelvic Girdle, Hindlimb, and Scutes. Morphological categories also included any characters relating to overall size and robustness, as well as differences in the size and robustness of individual bones. For all species, each diagnostic character was assigned to its respective body section or size/robustness column in a spreadsheet format.

The skeletal differences of 104 dinosaurian species belonging to 39 genera were considered (see Figure 2.1 and Appendix B in this investigation (Averianov, 2002; Barrett et al., 1998; Blows, 1996; Boulenger, 1881; Brown, 1912, 1913, 1916; Brown and

Schlaikjer, 1942; Buffetaut and Le Loeuff, 1991; Bunzel, 1871; Carpenter and Wilson, 2008; Chao, 1962; Cheng, 1983; Cope, 1876; Currie and Zhao, 1993; Currie et al., 1990; Galton, 1975, 1983; Galton and Powell, 1980; Galton and Taquet, 1982; Garcia and Pereda Suberbiola, 2003; Gauffre, 1993; Gilmore, 1924, 1930, 1933; Godefroit et al., 1999, 2008; Hatcher, 1901, 1903; Haughten, 1924; He et al., 1984; Holl, 1829; Holland, 1924; Holmes et al., 2001; Hooley, 1925; Horner, 1992; Hu, 1973; Hulke, 1881; Jensen, 1988; Kurzanov and Tumanova, 1978; Lambe, 1902, 1913, 1914, 1915; Lambert et al., 2001; Lehman, 1989; Lydekker, 1877, 1879, 1888, 1889; Mantell, 1825; Marsh, 1878, 1884, 1889, 1890a,b, 1894; Matheron, 1869; McIntosh and Williams, 1988; Meyer, 1861; Nopsca, 1900, 1915; Osborn, 1923, 1924a,b; Ostrom, 1961; Parks, 1920, 1922, 1923, 1933; Raath, 1969; Rowe, 1989; Russell, 1996; Ryan and Russell, 2005; Sankey, 2001; Sereno and Chao, 1988; Sternberg, 1928, 1933, 1935, 1940; Stromer, 1915; Sues, 1997; Upchurch et al., 2004; Virchow, 1919; Weishampel and Bjork, 1989; Weishampel et al., 2003; Williamson and Carr, 2002; Wiman, 1931; Xu, 1997; Xu et al., 2000, 2003; Yates, 2003; Young, 1930, 1939, 1958; Zhou and Wang, 2000). The reported differences between dinosaurian species were cataloged based on a combination of primary publications on the species and subsequent information that has been published since the original species diagnosis. In the comparison of two or more species within the same genus, the most recently attributed species was used as the reference taxon. In cases of only two species within a genus, calculating the number of differences was straightforward. The number of differences was determined by comparing the most recently classified species to the type species of the genus. If there were more than two species attributed to a genus, the only differences counted were those diagnostic characters of the most recently classified species that were distinct from all other species in the genus. Each specimen was assumed to be osteologically complete.

2.3 Considerations and Assumptions

Fossil skeletons are likely to be incomplete. Moreover, there is a high probability that those skeletal elements that are preserved do not embody all of the characteristics indicative of a particular dinosaur's "morphological space." Although this work attempts to include only those species that are accepted currently as legitimate, this is

		Morphological Category																	
		GENUS	SG	T	S	D	D#	V	V#	PC	R	F	PV	H	SC	SZO	RO	RP	
Theropoda		<i>Caudipteryx</i>	2	4						1		1	2						
		<i>Chirostenotes</i>	2	4	3												1		
		<i>Microraptor</i>	2	4								2	1	1					
		<i>Ornithomimus</i>	2	4											2		1	1	
		<i>Richardoestesia</i>	2	7		7													
		<i>Sauornithoides</i>	2	2			1										1		
		<i>Spinosaurus</i>	2	1				1											
		<i>Synraptor</i>	2	4	4														
		<i>Syntarsus</i>	2	2	1										1				
		<i>Velociraptor</i>	2	7	7														
Sauropodomorpha		<i>Apatosaurus</i>	4	5				1		1		3							
		<i>Camarasaurus</i>	4	8				7					1						
		<i>Diplodocus</i>	4	2	2														
		<i>Haplocanthosaurus</i>	2	8				2					3			1		2	
		<i>Melanorosaurus</i>	2	3										3					
		<i>Plateosaurus</i>	2	2				1					1						
		<i>Titanosaurus</i>	2	3				3											
Thyreophora		<i>Amtosaurus</i>	2	3	3														
		<i>Edmontonia</i>	2	2	2														
		<i>Pinacosaurus</i>	2	4	4														
		<i>Polacanthus</i>	2	10				4		1	1			1	2	1			
		<i>Struthiosaurus</i>	3	3				1						1			1		
Ornithomoda		<i>Camptosaurus</i>	3	21	2			11		1		1	6						
		<i>Dryosaurus</i>	2	21	12		2	1				5		1					
		<i>Rhabdodon</i>	2	3	3														
		<i>Gryposaurus</i>	3	3	1	2													
		<i>Iguanodon</i>	6	10	6	3	1												
		<i>Lambaeosaurus</i>	2	11	9								1					1	
		<i>Parasaurolophus</i>	3	2	2														
		<i>Prosaurolophus</i>	2	2	2														
		<i>Saurolophus</i>	2	19	10				1	1		1	3	3					
		<i>Valdosaurus</i>	2	2										2					
		<i>Zalmoxes</i>	2	5	1					3			1						
Pachycephalosauria		<i>Sphaerotherolus</i>	2	2	2														
Ceratopsia		<i>Centrosaurus</i>	2	5	5														
		<i>Chasmosaurus</i>	5	13	13														
		<i>Leptoceratops</i>	2	5	5														
		<i>Protoceratops</i>	2	4	4														
		<i>Psittacosaurus</i>	11	7	6				1										
TOTALS			104	227	109	12	4	32	2	8	1	13	20	14	2	6	1	3	

Figure 2.1: The literature revealed 227 morphological differences that distinguished species within 39 dinosaurian genera. Genera are arranged by dinosaurian “group” and are listed within each “group” by alphabetical order. The vertical blue line separates cranial (to the left) from postcranial characteristics (to the right). The total number of recorded differences is highlighted in yellow.

a subjective part of science, and there may be some healthy difference of opinion. Dinosaurian taxonomy is always in a state of revision; species of dinosaur are continually defined, synonymized, and dissolved (Benton, 2008). There are several dinosaurian genera that were excluded from this study because one or more of the species has been dissolved or is problematic. Within the Saurischia, the two species of the theropod genus *Erectopus* have recently been reduced to a single species (Allain, 2005). Also excluded were the sauropodans *Omeisaurus*, *Rayososaurus*, *Mamenchisaurus*, *Dicraeosaurus*, *Brachiosaurus*, and *Saltasaurus*. There is some concern over whether *Omeisaurus tianfuensis* (He and others, 1984) is a new species because, although it is a more complete skeleton, it exhibits no new diagnostic characters in the skeletal material that overlaps with that of *Omeisaurus junghsiensis* (Young, 1939, Zhang and Chen, 1996). *Rayososaurus* was not included because the validity of the genus is still under debate (Bonaparte, 1996; Calvo and Salgado, 1995). *Mamenchisaurus* is considered here as a “wastebasket taxon” whose morphology is in need of major revision (He et al., 1996; Hou et al., 1976; Pi et al., 1996; Young, 1954; Young and Chao, 1972; Zhang et al., 1998) as are the morphologies of *Dicraeosaurus*, *Brachiosaurus*, and *Saltasaurus*. Within the Ornithischia, morphologic details of *Stegosaurus*, *Probrachiosaurus*, and *Edmontosaurus* are in need of organization and revision. The genus *Hypacrosaurus* is not included because the species *H. stebingeri* (Horner and Currey, 1994) is based on embryonic and neonatal material and no diagnostic characters are stated with the description of this material. Both *Stegoceras* and *Prenocephale* are problematic taxa (Sullivan, 2003). A special note is made here about the ornithischian *Pinacosaurus*. This genus is included in the study, but with some caveats. The diagnostic characters of *P. mephistocephalus* (Godefroit et al., 1999) that were reported as tentative due to the ontogenetic age of the specimen and not considered here.

2.4 Results

Based on the reduced dinosaurian skeleton (89 ossifications), the literature on the 39 dinosaurian genera revealed 227 morphological differences that distinguished species (Figure 2.1). Within the Dinosauria, those morphological features that distinguish cogenetic species are confined to only about 6.5% of the individual ossifications in

the reduced dinosaurian skeleton. An average of 5.8 diagnostic characters distinguishes species assigned to the same genus. The distribution of the differences for each genus is summarized in Figure 2.1. The total number of differences between congeneric species ranged from a minimum of one skeletal difference between species of *Spinosaurus* Stromer 1915, to a maximum of 21 skeletal distinctions among the species of the genera *Dryosaurus* Marsh 1894 and *Camptosaurus*. Most importantly for the broader study, a total of about 55% of the diagnostic differences in cogenic species of dinosaur occurred in the skull and dentition, whereas 41% occurred in the postcranial skeleton. The remaining 4.4% were distinctions related to the size and robustness of skeletal elements. Organized in descending order of number of diagnostic characters within each body section, morphological differences in the cranial bones (not including the dentition) accounted for about 48% of the total number of differences, the vertebral column for 14.5%, the pelvic girdle for 8.8%, the hindlimb for 6.2%, the forelimb for 5.7%, morphological changes in the dentition for 5.3%, pectoral girdle for 3.5%, overall specimen size difference for 2.6%, changes in the number of teeth for 1.8%, robusticity changes in a skeletal element for 1.3%, scutes for 0.9%, differences in the number of vertebrae for 0.9%, ribs for 0.4%, and overall changes in robustness for 0.4%. Thus, cranial characteristics alone accounted for a greater number of differences than all the post-cranial characteristics combined.

2.5 Discussion

One of the assumptions of this exercise was that all of the dinosaurian species were known from osteologically complete material. Fossil quality of newly designated dinosaurian species has been shown to have risen in the past 30 years (Benton, 2008). However, there is still a large number of species that are known only from fragmentary skeletons, including several valid species that date to the late 1800s and are included in this survey. To augment the interpretation of the data presented above, it is worth reviewing and considering what material is preserved in each species before deciding whether we are taking full advantage of the skeleton for taxonomic differentiation.

2.5.1 Skull and Dentition

Dinosaurian skull material has been prized for its perceived uniqueness and rarity in the fossil record. Even when only small portions of skull material are present, analysis of that material often reveals a morphological difference that is interpreted as a diagnostic characteristic for species differentiation. All of the species in 26 of the 39 genera in this study are represented by skeletal material that included at least part of the skull and/or dental material. The genera with preserved skull and/or dental material are *Syntarsus* Raath 1969, *Richardoestesia* Currie et al. 1990, *Chiostenotes* Gilmore 1924, *Sinraptor* Currie and Zhao 1993, *Sauornithoides* Osborn 1924a *Microraptor* Xu et al. 2000, *Velociraptor* Osborn 1924a, *Pinacosaurus* Gilmore 1933, *Edmontonia* Sternberg 1928, *Amtosaurus* Kurzanov and Tumanova 1978, *Rhabdodon* Mathéron 1869, *Zalmoxes* Weishampel et al. 2003, *Dryosaurus*, *Camptosaurus*, *Iguanodon* Mantell 1825, *Gryposaurus* Lambe 1914, *Prosaurolophus* Brown 1916, *Saurolophus* Brown 1912, *Lambaeosaurus* Parks 1923, *Parasaurolophus* Parks 1922, *Sphaerotherolus* Williamson and Carr 2002, *Psittacosaurus* Osborn 1923, *Protoceratops* Granger and Gregory 1923, *Leptoceratops* Brown 1914, *Centrosaurus* and *Chasmosaurus* Lambe 1915. For all of those 26 genera, portions of the skull or dentition were used to differentiate congeneric species with the exception of *Microraptor*. Interestingly, although not all of the species of *Diplodocus* Marsh, 1884 have preserved skull material available, the skull was still used for species diagnosis in addition to postcranial distinctions (Hatcher, 1901; Holland, 1906, 1924; Marsh, 1878, 1884).

Of the 104 species cataloged, 14 species are known only from skull and dental remains: *Richardoestesia gilmorei* Currie et al., 1990, *Richardoestesia isosceles* Sankey, 2001, *Velociraptor osmolskae* Godefroit and others, 2008, *Amtosaurus magus* Kurzanov et Tumanova, 1978, *Amtosaurus archibaldi* Averianov, 2002, *Diplodocus lacutris* Marsh, 1884, *Rhabdodon septimanicus* Buffetaut and Le Loeuff, 1991, *Zalmoxes shqiperorum* Weishampel et al., 2003, *Iguanodon fittoni* Lydekker, 1889, *Sphaerotherolus buchholzae* Williamson and Carr, 2002, *Sphaerotherolus goodwini* Williamson and Carr, 2002, *Psittacosaurus ordosensis* Russell and Zhao, 1996, *Protoceratops hellenikorhinus* Lambert et al., 2001, and *Chasmosaurus russelli* Sternberg, 1940.

Moving up one hierarchical level, 17 genera that include two or more species are distinguished from each other using only skull and dental remains. Three of the 17

genera, *Richardoestesia*, *Amtosaurus*, and *Sphaerotholus*, are known solely by skull and dental material. In six of those 17 genera, however, *Sinraptor*, *Pinacosaurus*, *Edmontonia*, *Gryposaurus*, *Prosaurolophus*, and *Parasaurolophus* all included species that have complete postcranial skeletons as well as skull and dental remains.

The number of cranial features in which cogenetic species differ often tracks with the amount of skull and dental preservation (Figure 2.2). When there is a greater amount of cranial material preserved, there tends to be a larger number of defined cranial diagnostic characters. The total number of cranial ossifications and dentition accounts for 39.3% of the 89 bones in the reduced dinosaurian skeleton used in this study. With a total of 55.1% of dinosaurian diagnostic characters found in the cranium, it appears that there is a prioritization of cranial material with regard to species diagnosis. It must also be considered that specimens very often do not preserve a complete skull. Cranial material is rare when compared with postcranial remains, is often incomplete, and is often distorted. However, attraction to cranial material is justified given that the skull alone is comprised of 64 separate and highly varied ossifications. The variation present within the ossifications of the skull cannot be matched by the postcranial ossifications, many of which are serially repeated.

2.5.2 Postcranial Remains and the Next Frontier of Distinguishing Dinosaurian Species

Unlike for cranial characters, the distribution of designated postcranial diagnostic characters in dinosaurian groups does not track with the amount of material preserved (Figure 2.3). In this study, 31 of the 39 genera contain species whose specimens preserved at least part of the postcranial skeleton, but for only 20 of those 31 genera have species been distinguished based on postcranial characters. Fourteen of the 39 genera in this study distinguish cogenetic species using only post-cranial remains (Figure 2.1), the majority of which species did not have skull material available. When there is no cranial material, postcranial remains are highly scrutinized for morphological differences. The results of the present study suggest that the postcranium has been a low-priority focus historically, but that it is very useful in species diagnosis. In this sense, it may hold untapped potential for the diagnosis of taxa.

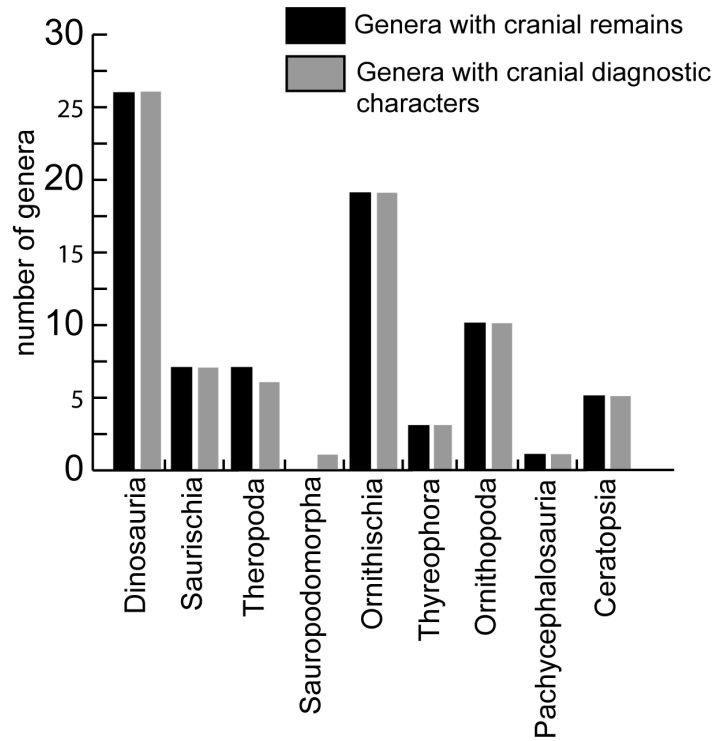


Figure 2.2: The number of dinosaurian genera for which cranial remains are preserved for all of their species (black bar) compared to that subset of genera for which cranial diagnostic characters distinguish its species (gray bar). If cranial skeletal remains exist for all species within a genus, at least one cranial diagnostic character likely will have been reported. No cranial remains are known for some of the species of *Diplodocus* (Sauropodomorpha), yet there are cranial diagnostic characters that distinguish the species within that genus.

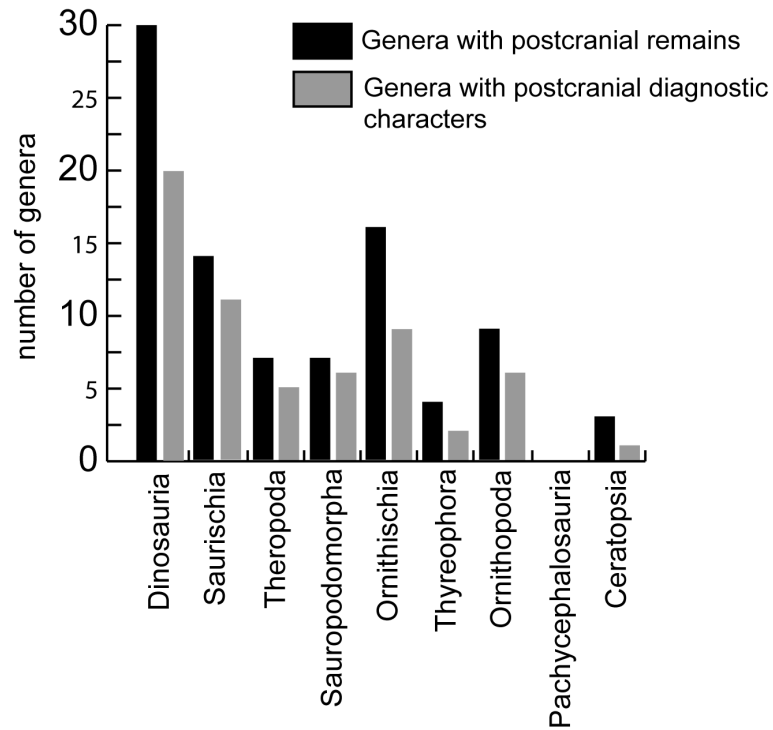


Figure 2.3: The number of dinosaurian genera for which postcranial remains are preserved for all of their species (black bar) compared to that subset of genera for which postcranial diagnostic characters distinguish its species (gray bar). Presence of postcranial material for all species within a genus does not ensure that even one postcranial character has been designated as diagnostic.

In many of the genera, complete postcranial remains are present in addition to substantial cranial material, yet few or no diagnostic characters are reported for the postcranium. This observation may reflect an actual absence of postcranial skeletal differences, but this outcome seems unlikely. Despite the heavy, preferential focus on only the cranial material in the literature, there are still numerous examples of the successful species diagnosis in the absence of any skull material. **The fact is that the majority of bones found in the dinosaurian fossil record belong to the postcranium.** Paleontologic descriptions and analyses of specimens need to reflect this abundance in order to create a more complete view of morphological changes through time. Galton (1975, 1983), in his works on the hypsilophodontid, *Dryosaurus*, extensively compares both the cranial and postcranial material from two species, the result of which is 21 diagnostic characters. This thorough effort is among the minority in dinosaurian description. Yet, the implications of such careful study go beyond species diagnosis to address evolutionary and paleogeographical questions.

2.6 Conclusion

This study serves as a benchmark in historical validation of the recognized, congeneric dinosaurian species. The results are also a reminder that species designation is subject not only to skeletal preservation, but also to historically developed methodologies and to the biases of anatomical focus, which may be due to the desire to highlight one's own work and one's institution. The process of species recognition is, therefore, not even-handedly applied across all fossil material.

The pattern of diagnostic character distribution, however, is largely grounded in the skeletal material present for each species. The very extensive use of any cranial material present for evaluating congeneric species, with the exception of *Microraptor*, contrasts with the limited use of postcranial material in the diagnosis of species. This outcome suggests a bias in the analysis of dinosaurian specimens, showing a preference toward cranial material when distinguishing new species. Cranial material will almost always yield diagnostic characters. A shift in skeletal scrutiny toward those parts of the body shown here to carry very little taxonomic focus, such as the

forelimbs, hindlimb, ribs, and pectoral girdle, therefore, could produce a more well-rounded perspective on the dinosaurian skeleton. A comparison of Figure 2.2, Figure 2.3, and the tabulated results in Figure 2.1 support the investigation of alternative methods for taxonomic identification using postcranial material of fossil tetrapods.

As vertebrate paleontology moves forward, there should be a time when the subjectivities of taxonomic classification will give way to standard, quantitative methods of specimen analysis. Although there are reports of short protein sequences preserved in dinosaurian collagen (Asara et al., 2007; Schweitzer et al., 2005a,b, 2007) and color preserved on feather impressions (Vinther et al., 2008), the majority of preserved material that will be available to paleontologists in the foreseeable future is replaced bone material. What are the options for more quantitative assessment of bone features that will give taxonomic information? The results of this study suggest that postcranial bones and their inherent features are the answer to the above question. The data assessment documents that postcranial bones in the Dinosauria (1) typically are poorly described compared to cranial bones (Figure 2.1) and (2) are less likely than cranial bones to be used to define a species, making postcranial bones an available, but largely untapped resource (Figure 2.3). The lack of detailed descriptions of postcranial material means that their diagnostic influence is uncertain, suggesting a solid cause for future study.

Of interest to the current thesis project is the potential for quantification of postcranial bone morphologic features in order to alleviate taxonomic problems in fossil specimens. Such an approach is well-suited for the analysis of the microstructural features of bone.

Chapter 3

Methods

3.1 Introduction

This study involves a microscopic and statistical analysis of the microstructural features of tetrapod bone. This chapter describes (1) the methods of sample preparation, (2) the features that were measured, (3) the geometry of the microstructural metrics used in analysis, (4) the tools used for micrographic and statistical analysis, and (5) the metrics used in the analysis.

3.2 Preparation of Bone for Histological Analysis

The described thin-sectioning technique has been applied successfully to the bone of modern mammals, dinosaur bone, and lithologic samples. Although there is no absolute “correct” way to make histological sections of hard tissues, published techniques generally use the same set of core processes (Buffrenil et al., 1990; Chinsamy, 1992; Enlow and Brown, 1956). While maintaining the core process, I also sought to minimize cost given the lapidary equipment that was available in the Department of Earth and Planetary Science at Washington University in Saint Louis and my choices in consumable products. For a list of the thin-section equipment and materials, refer to Figure 3.1.

EQUIPMENT

ITEM	MANUFACTURER	MODEL	NOTES
Tile Saw			
Thin-section cut-off saw	Ward's Natural Science	135	5" diamond blade
Vacuum oven	Napco	5851	
Ecomet Polisher/Grinder	Buehler		
Lapping and polishing machine	Logitech	PM2A	
Grinding wheels			10, 74 μm grit

CONSUMABLES

ITEM	MANUFACTURER	MODEL	NOTES
Petrographic Slides	Lakeside	27mm x 46mm	
Low viscosity epoxy resin	Buehler	Epo-thin	
Low viscosity epoxy hardener	Buehler	Epo-thin	
Specimen cups/ring molds	Leco	various	Reusable
Release agent	Leco	811-269	
Microid diamond compound extender	Leco	811-002	
Diamond polishing powder	Beta diamond products		1 μm
Diamond polishing pads	Leco	809-505	12"

Figure 3.1: Permanent equipment and consumables used in the thin-sectioning procedure.

3.2.1 Petrographic Thin-Section Procedure

The procedures used for preparing sections of bone can be divided into six phases: (1) Photography and measurement of specimen gross morphology, (2) sectioning of bone, (3) embedding of sectioned bone, (4) grinding and polishing the surface to be affixed to the slide, (5) mounting the stub, and (6) cutting, grinding, and polishing the upward-facing bone surface.

Photography and Measurement of Specimen Gross Morphology

The thin-section procedure is a destructive process, and some aspects of the gross morphology of a bone will be lost during the creation of a slide. To offset the destructive impact, all bone specimens were photographed in anterior, posterior, medial, lateral, proximal, and distal views before sawing began. I recorded the maximum length of each specimen and, if applicable, also the diaphyseal lengths along the anterior, medial, and interosseous margins, minimum diaphyseal width, and the mediolateral and anteroposterior widths of both the proximal and distal ends of the bone. Overall bone description was also recorded. The descriptions below refer to both the comparative studies among the different mammalian groups and the analysis of microstructural variation carried out on a single skeleton of a white-tailed deer.

Sectioning of Bone

I divided the diaphysis (i.e., shaft) or body (in the case of ribs) of each *O. virginianus* bone specimen into five equal transverse sections (Figure 3.2), with the exception of the phalanges. Because of their smaller size, the phalangeal diaphyses were divided into three sections each. The mid-diaphysis for each long bone was located at a measurement equidistant from each epiphyseal suture line along the anterior margin. The mid-point of the rib body was located at a measurement equidistant from the proximal and distal ends. Four additional markings (two additional markings on the phalanges), two proximal and two distal to the mid-diaphyseal point, completed the division of the shaft for initial cutting of the specimen. All other mammals were sectioned only at the mid-diaphysis using the same guidelines explained above.

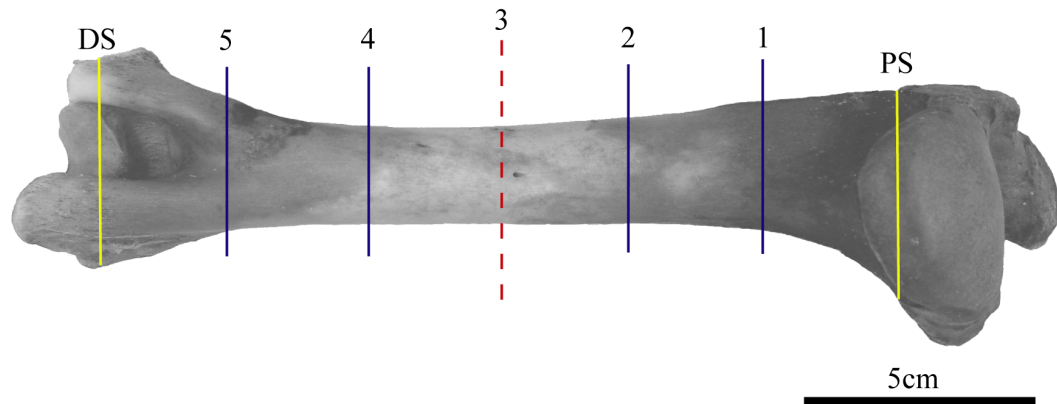


Figure 3.2: Each long bone and rib from *O. virginianus* was measured and cut into five equal sections (1-5). All other mammal specimens were cut only at the mid-point of the diaphysis. The mid-point of the diaphysis (3) was determined as equidistant from the proximal suture (PS) line and distal suture (DS) line of the articular ends. Left humerus of *O. virginianus*.

Rough cuts of the bone were made on a tile saw fitted with a diamond blade. To ensure that the bone diaphysis was perpendicular to the blade, the epiphyses were placed on small sand bags and leveled before cutting. After cutting, I marked each bone section with a waterproof pen to indicate the proximal direction and the section number. The most proximal section was always labeled as “section 1” (3.2).

Embedding of Sectioned Bone

Modern bones can become brittle over time and need to be embedded in a resin or other suitable mounting medium to ensure their structural integrity throughout the thin-sectioning process. I used a low viscosity epoxy, Epo-thin, that can either be cold-cured or forced with heat. In order to allow for easy specimen release after the epoxy has cured, the Leco reusable cup molds used to hold the specimens during the embedding process were coated with release agent (Figure 3.1). I placed a small amount of Epo-thin epoxy, prepared according to the directions, in each cup mold prior to the emplacement of each specimen to ensure full coverage by the epoxy of the specimen and reduction of air bubbles. This study required that all bone specimens

be placed in the cup molds with the distal end facing down. After placement of all specimens, I added enough Epo-thin to each mold to cover the specimen. All specimens were then placed in a vacuum oven set to 70C and evacuated for approximately 20 minutes to remove any air bubbles from the epoxy. After 20 minutes, the vacuum was released slowly and the specimens were left to cure in the oven for no less than 7 hours. Once cured, the specimens were allowed to come to room temperature before removal from the cup mold.

Grinding and Polishing of the Surface to be Affixed to the Slide

To prepare each specimen for adhesion to the petrographic slide, I ground and polished the distal side of each specimen using a series of abrasive-embedded metal plates or wheels on a water-lubricated Ecomet polisher/grinder by Buehler. Two wheels were used in succession with grit sizes of 75m and 10m, respectively. The manual grinding technique consisted of a series of no less than 160 figure-8's per specimen per grit size to achieve desired results. A 10m polish was sufficient to enable clear visualization during microscopy as well as to allow for good specimen adhesion to the slide.

Mounting the Stub

The dry, polished surface of the bone stub was then mounted onto a petrographic glass slide. A small amount of Epo-thin was used to affix the distal end of the bone specimen to the slide, making sure that no air bubbles were present. Each slide with its attached specimen then was weighted on top and placed on a hot plate set to 70C for no less than 7 hours to allow the epoxy to cure.

In the steps that follow the mounting of the bone sample onto the glass slide, the specimen is exposed to a large volume of water. To ensure proper identification of each slide, I etched the specimen number, bone type, and saw-cut number into the glass.

Cutting, Grinding, and Polishing the Upward-Facing Bone Surface

To reduce grinding and polishing of the proximal end of each specimen, excess sample was removed with a 5" diamond blade mounted on a water-cooled Ingram thin-section cut-off saw. Each bone sample was reduced in thickness to 2mm. I ground and polished the proximal end to remove saw blade marks following the same procedure as for the distal end prior to adhesion to the glass slide. However, an additional polishing step was added using 1m diamond polishing powder on a precision lapping and polishing machine by Logitech. Polishing proceeded for no less than 30 minutes or until the desired final thickness was achieved. I determined optimal thickness of each thin-section individually using a light microscope. The goal was to thin the sample sufficiently to allow crisp visualization and measurement under the microscope. All thin-section thicknesses were on the order of tens of micrometers. Adhesive labels were used for the final labeling of the slides.

3.2.2 Microscopy and Micrographs

All microscopy was done using an Olympus BH-2 (the "BobScope") polarized light microscope mounted with Olympus digital microscope camera DP70. I digitally micrographed each specimen in its entirety, creating a mosaic of images using either objective 5x or 10x, depending on the needs of the analyses to follow. Optimal visualization and light control were achieved using the MicrosuiteTM Five image analysis software by Olympus.

In all digital micrographs, the periosteal surface of the bone is parallel to the left side of the field of view. Each thin-section is photographed entirely beginning with the anterior-most point of the bone and then rotating incrementally in a counterclockwise direction. Repeat measurements of the same microstructures are avoided by marking a starting/ending point on the thin section to signal when the images are complete and also by comparing consecutive photos.

3.3 Quantitative Metrics for Analysis

Testing the hypothesis of tetrapod identification on the basis of bone microstructure demands the ability to make quantitative measurements on analogous microstructures in the cortical bone of different tetrapods. The goal of my measurements is the objective, reproducible quantification of physical structure. Among the challenges in developing an acceptable methodology was the need for quantitative metrics that would help reduce measurement error (see Bailey and Byrnes, 1990) while maximizing the ease of repeatability among researchers. The metrics presented here were selected on the basis of the known biology of primary bone formation and the remodeling of bone to produce secondary structures (Amprino, 1948, 1963; Amprino and Marotti, 1964; Ardizzoni, 2001; Ascenzi and Bonucci, 1961, 1964, 1967, 1968, 1972; Ascenzi et al., 1965, 2003, 2004; Aubin et al., 1993; Baltadchiev, 1994; Baron et al., 1993; Borah et al., 2001; Boskey, 2003; Broadus, 2003; Bromage et al., 2003; Bumrerraj and Katz, 2001; Burr et al., 1988; Carter and Spengler, 1978; Cohen and Harris, 1958; Cooper et al., 2003, 1966; Cuppone et al., 2004; Currey, 1960, 1964; Eckardt and Hein, 2001; Enlow, 1962, 1966, 1977; Frasca et al., 1976; Frost, 1961, 1963, 1964, 1966; Georgia and Albu, 1988; Haines, 1942; Hara et al., 2002; Hert et al., 1994; Jacobs and Echstein, 1997; Jaworski et al., 1981; Johnson, 1964, 1966; Kamioka et al., 2001; Kragstrup, 1985; Kragstrup and Melsen, 1983; Kuznetsov et al., 2004; Lanyon and Bourn, 1979; Lian et al., 2003; Locke, 2004; Marotti and Zallone, 1980; Martin and Burr, 1982; McElhaney, 1967; Metz et al., 2003; Mishof et al., 2003; Mishra and Knothe Tate, 2003; Mohsin et al., 2002; Mulhern and Ubelaker, 2001, 2003; Mundy et al., 2003; Nemeskeri and Harsanyi, 1968; Nyssen-Behets et al., 1997; Pfeiffer, 1998; Pidaparti and Burr, 1992; Portigliatti-Barbos et al., 1983, 1984; Qiu et al., 2003; Robling and Stout, 1999, 2000; Rodan and Martin, 1981; Rouiller et al., 1952; Ruangwit, 1967; Sedlin and Frost, 1963; Skedros et al., 1997, 2001, 2003a,b, 2004; Tappen, 1977; Teitelbaum, 2004; Thompson and Gunness-Hey, 1981; Tolar et al., 2004; Tomes and De Morgan, 1853; Wachter et al., 2002; Whitson, 1972; Williams et al., 2004; Yeager et al., 1975).

The measurements discussed herein were not optimized for and therefore may not be congruent with evolutionary processes; the aim is not to describe evolutionary pathways. Taxonomy and phylogeny, of course, are not synonymous (Cubo et al.,

2005). Although there may be phylogenetic implications to this work, they are beyond the scope of this research. The goal at this time is taxonomic identification.

3.3.1 Measurable Microstructural Units

Both primary and secondary microstructural features were considered for this investigation including (1) primary vasculature, (2) primary lacunae, (3) secondary osteons, (4) secondary vasculature or Haversian canals, and (5) secondary lacunae (please refer to the glossary in Appendix 1). Each complete measured microstructure was treated as one measurable unit (analogous to one tooth or one vertebra if this work were based on those elements). For example, one secondary osteon, defined as a unit of bone enclosed within a continuous cement (reversal) line is equal to one measurable unit. The sub-central vascular canal (Haversian canal) within the border of the secondary osteon is a separate measurable unit (1.3).

3.3.2 Elliptical Microstructural Features

In two-dimensional transverse cross-section, all the measured structures are nearly elliptical. The appearance typically deviates slightly from elliptical because of inherent natural variation as well as because the shapes of the vascular canals and secondary osteons are affected by branching or anastomosing that can occur along their lengths. For this investigation, however, all the microstructures are considered as true ellipses. Ellipses contain very few homologous points that can serve as morphometric landmarks. Similar challenges occur commonly in quantifying the shape of highly rounded features of certain invertebrates, such as those involving the shapes of ostracod tests (Elewa, 2003). Such shape measurement challenges in evolutionary studies have been overcome by applying a series of elliptical Fourier Transform techniques Haines and Crampton (2000) or by shape analysis using the Superformula (Gielis, 2003).

As discussed above, the current study is focused only on taxonomic identification rather than evolutionary pathways. This focus allows the usage of analogous reference points rather than evolutionarily homologous points, and thus justifies straightforward measurements. The metrics used herein are defined and discussed below. Given

that the microstructures addressed here are present in any cortical bone section, all measurements are applicable regardless of taxon.

3.3.3 Microstructural Shape Considerations

Primary and Secondary Lacunae

Lacunae (Figure 3.3) are the spaces that bone-cells occupy after the cells are finished depositing bone. After recent research established that cell size correlates with genome size in vertebrates (Gregory, 2001), Organ et al. (2007) used the information to establish the genome size of extinct vertebrates, mainly avian and non-avian dinosaurs. Their findings showed that in non-avian dinosaurs there was a bimodal distribution of lacunar size represented by the Ornithischia and the Theropoda. Only one sauropod specimen was included in the analysis, and its lacunar size was intermediate between those of the aforementioned dinosaurian groups. Although it is not stated specifically in the publication, by establishing the differences in genome size using the volume of the lacunae, Organ et al. (2007) also linked the cell-size with the type of tetrapod group.

Lacunae are measured in the present study in order to discriminate those located in primary bone from those in secondary bone and to investigate possible correlation of lacunar size with taxonomic identity when applied in a large population of samples.

Secondary Osteons

As discussed above, secondary osteons appear elliptical in transverse cross section. The circumference of the secondary osteon follows the cement (reversal) line, the outer border of the structure (Ascenzi et al., 2003, 2004; Cohen and Harris, 1958; Diaz and Rajtova, 1975; Enlow, 1977; Frost, 1963; Mundy et al., 2003). The cement line is a distinct physical boundary around the secondary osteon that is deposited at the cessation of bone resorption and the commencement of bone deposition. The recognition of the cement line makes measurement of the osteon unambiguous and repeatable.

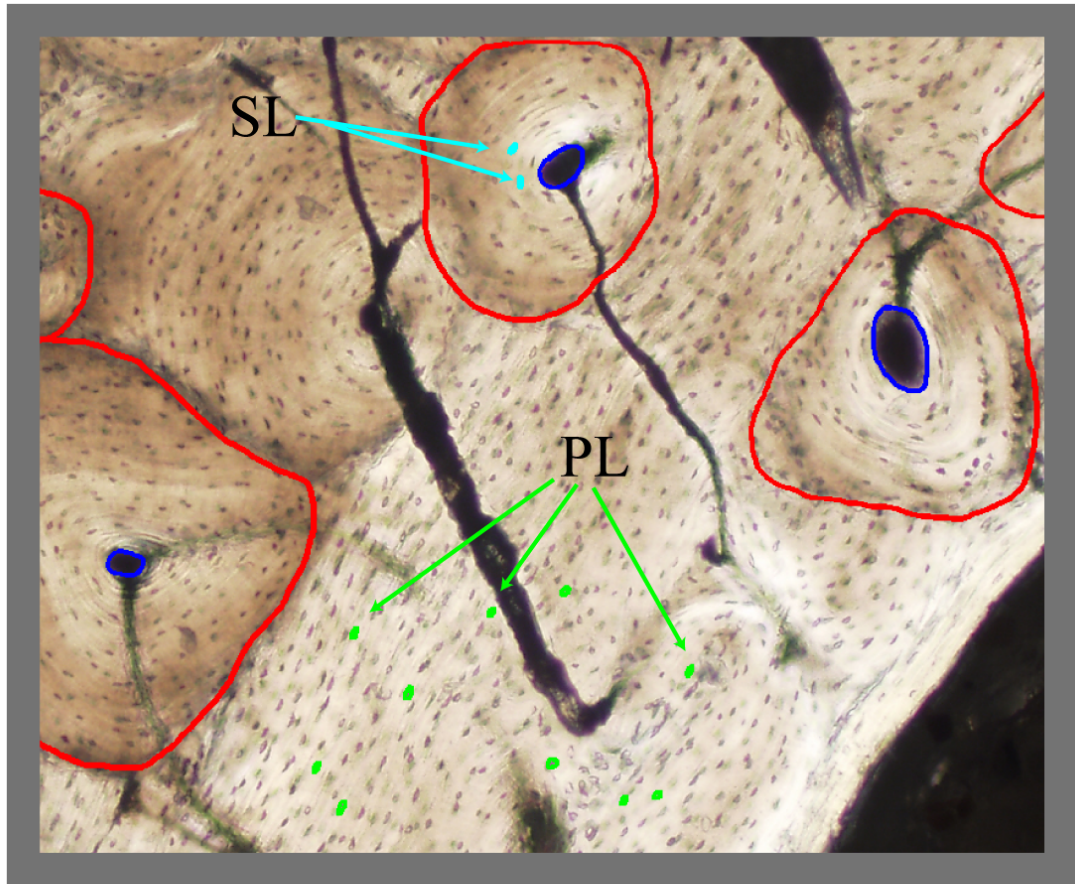


Figure 3.3: Secondary lacunae (cyan) are those lacunae which are found inside the reversal line (red) of secondary osteons. Primary lacunae (green) are found in the primary bone. Scale =0.5mm.

Serial sectioning of bone and, more recently, micro-tomographic imaging of bone have demonstrated that secondary osteons are actually cylinders of circular cross-section. In three dimensions, secondary osteons are a series of cylindrical tubes throughout the length of the diaphysis, oriented at some angle relative to the longitudinal axis of the bone (Cohen and Harris, 1958; Cooper et al., 2003; Hert et al., 1994; Stout et al., 1999; Tappen, 1977) (Figure 3.4). Thus, the elliptical appearance of these microstructures in a transverse cross section is a direct result of the orientation of the structures with respect to the longitudinal axis of the diaphysis. For example, if all osteons were parallel to the longitudinal axis of the diaphysis, the microstructures would show as circles in transverse cross-sections cut perpendicular to that axis (as done here). In most instances, however, this is not the case.

Primary and Secondary Vasculature

The shape of primary and secondary vasculature (Haversian canals) in two-dimensions and three-dimensions is similar to the shape of secondary osteons. Bone vasculature is also a series of cylindrical vessels that appear as ellipses in transverse cross-section and that are oriented at some angle relative to the longitudinal axis of the diaphysis.

3.3.4 Metric Geometry

The measurements described below are the principal variables that were used to evaluate (1) the morphology of primary and secondary bone microstructure in two dimensions, (2) the transverse orientation of the major axes of primary and secondary microstructures with respect to the periosteal surface, and (3) the longitudinal orientation of primary and secondary microstructures.

For each metric, analogous reference points are defined with respect to a Cartesian coordinate system. The specified measurements are explained, justified, and described to enable reproduction by others.

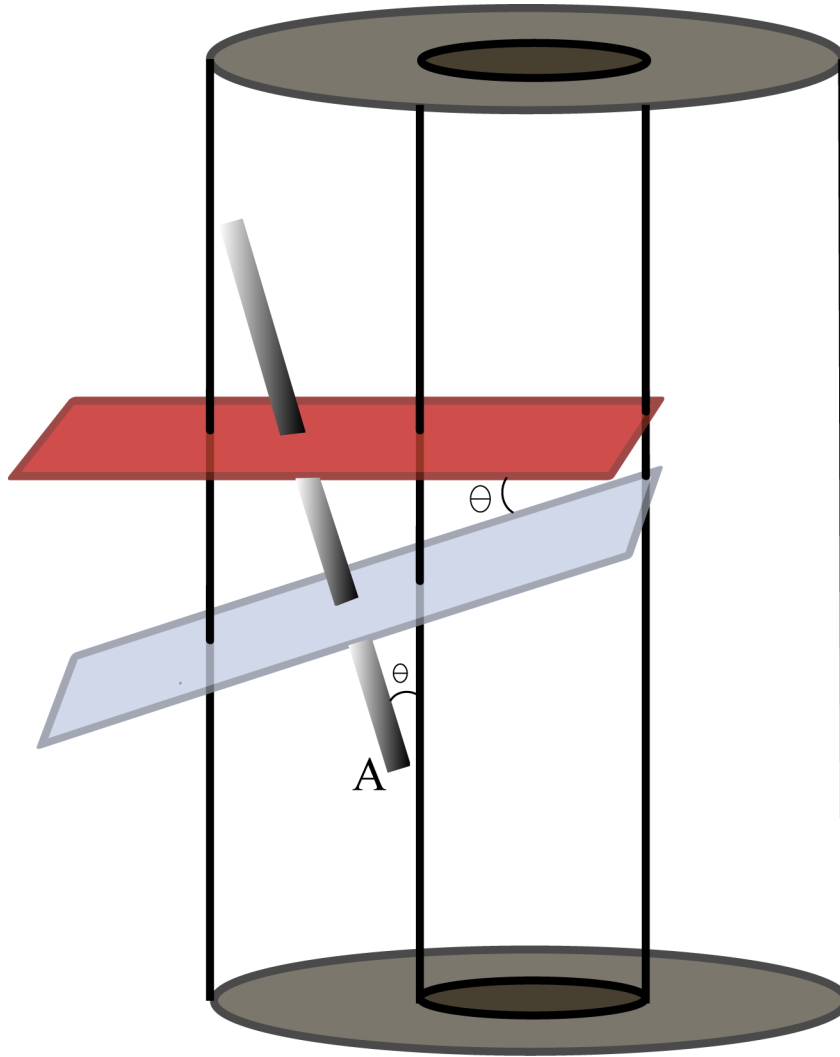


Figure 3.4: A schematic representation of a long-bone shaft and corresponding osteonal shaded cylinder (A) in the cortical bone that is oriented at some angle to the longitudinal axis of the diaphysis. This angle can be calculated at the intersection of the red and blue planes. The red plane represents the orientation of the thin-sections cut for this study (perpendicular to the long axis of the diaphysis). The blue plane is perpendicular to the long axis of the osteonal cylinder.

Major and Minor Axes

All bone microstructures measured in this study are nearly elliptical, and therefore all major and minor axes are determined in the same manner. To illustrate the concept, a secondary osteon (large ellipse) and its corresponding Haversian canal (small ellipse) are represented by nested ellipses (Figure 3.5).

The minor axis of the small ellipse is represented by **line segment AB** (Figure 3.5 A). In a two-dimensional Cartesian coordinate system, **Point A** can be defined as the origin and **Point B** is located at some distance from **A** along the positive X-axis. **Points A** and **B** are the terminal points of **line segment AB**, and correspond to the intersection of the line representing the minimum distance across the ellipse with the outer border of the small ellipse. The minimum diameter of the small ellipse, **line segment AB**, is always perpendicular to the Y-axis in the Cartesian plane. **Line segment AB** is the minor axis of the small ellipse.

The major axis of the small ellipse is represented by **line segment CD** (Figure 3.5 A), oriented perpendicular to **line segment AB**. **Points C** and **D** are the terminal points of **line segment CD**, and correspond to the intersection of the line representing the maximum distance across the small ellipse with the outer border of the small ellipse, perpendicular to **line segment AB**. Because the shape of the bone microstructures may deviate from a perfect ellipse, the major axis of the small ellipse may not intersect the midpoint of **line segment AB**. **Line segment CD** is the major axis of the small ellipse.

Analogous measurements are made for the minor (**line segment EF**) and major (**line segment GH**) axes of the large ellipse (Figure-MajMin B). The major and minor axes of nested microstructures may be oriented slightly differently (Figure 3.5 C). Therefore, the minor and the major axes of nested ellipses must be measured separately.

Microstructure Transverse Orientation

The transverse orientations of all units of primary vasculatures, secondary osteons, and Haversian canals are calculated using the relationship between the major axis and

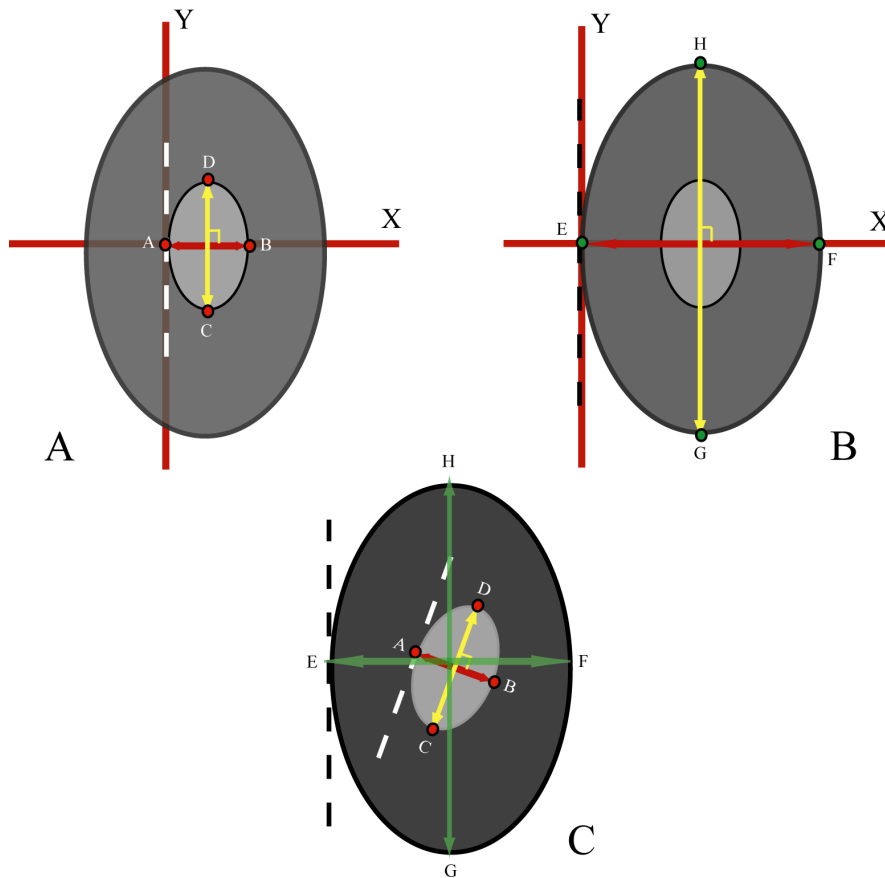


Figure 3.5: A two-dimensional Cartesian coordinate system was used to define the minor and major axes of elliptical cross-sections of microstructures. A schematic of a Haversian canal (A) is represented with line segment AB as the minor axis and line segment CD as the major axis. A secondary osteon (B) is represented with line segment EF as the minor axis and line segment GH as the major axis. The major and minor axes are always perpendicular to each other. However, in nested microstructures, such as the secondary osteon and Haversian canal shown here, the major axes of the larger and smaller ellipses may not be parallel (C). To account for this possibility, each microstructure is measured individually.

the periosteal surface (Figure 3.6). The periosteal surface is the outermost surface of bone and is the site of continuous bone deposition throughout life. When viewed in transverse cross-section, the periosteal surface curves radially around the diaphysis. Fortunately, at high magnification, the surface generally appears uncurved (Figure 3.6 A). Therefore, in this study, the periosteal surface was treated as a linear feature to simplify angular measurements.

The transverse orientation angle is the angle between a line tangent to the periosteal surface and the linear extrapolation of the major axis of the ellipse. On a Cartesian coordinate system, the periosteal surface is represented by the X-axis (Figure 3.6 B) and all microstructures are located in quadrants two and three. The measurements of angle θ_P lie between 0° and 179° . Angular measurements of 0° occur when the major axis of the ellipse is parallel to the tangent line. An angular measurement of 180° is not considered because it indicates the same orientation as 0° .

Microstructure Longitudinal Orientation

As discussed above, bone vasculature and secondary osteons are cylindrical tubes of circular cross-section oriented at some angle with the bone shaft. Because most of these microstructures appear in transverse cross-section as ellipses rather than circles, the tilt angle of the cylinder with respect to the longitudinal axis of the bone can be calculated using the major axis of the ellipse. In many of the previous studies that have measured the size of secondary osteons, those that are not circular (or close to it) were dismissed from the dataset as being non-informative as to the “true” nature of osteon morphology (Jowsey, 1966). However, non-circular microstructures are recognized as important in the present study, because they are indicative of their three-dimensional orientation within the bone shaft. Longitudinal orientation of the primary vasculatures, secondary osteons, and Haversian canals are calculated here as an acknowledgment that there may be a taxon-specific signal resulting from phylogeny, mechanical stresses on the skeleton, or both (Martin and Burr, 1989).

A three-dimensional Cartesian coordinate system 3.7 is used to illustrate the longitudinal relationship of the structures within the diaphysis. The placement of the ellipse with respect to the X- and Y-axes is the same as used for finding the major and minor

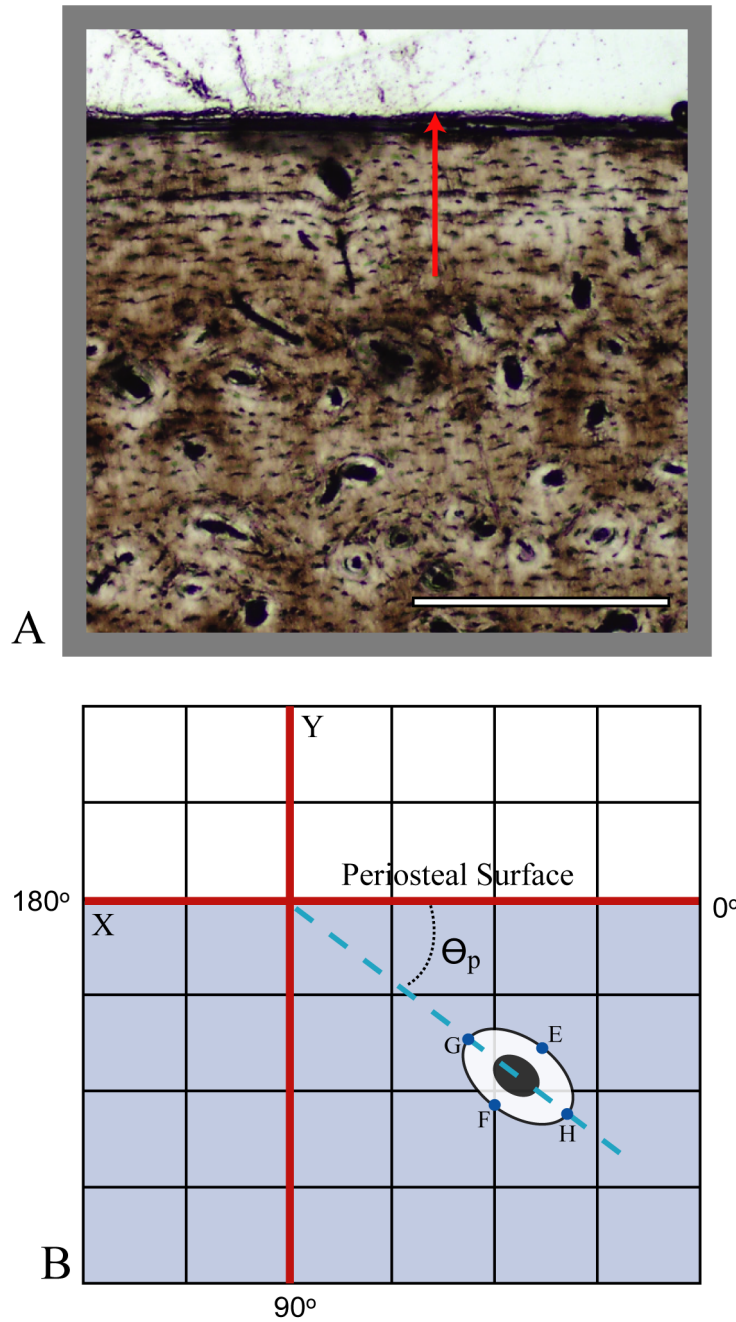


Figure 3.6: Highly magnified, the periosteal surface of a long bone or rib appears uncurved (A, red arrow). The transverse orientation angle, Θ_P , of the secondary osteon shown here as an example is determined as the angle between a line tangent to the periosteal surface and the extension of the major axis (GH) of the microstructure (B). Lemur tibia. Scale = 0.2mm

axes of the ellipses. On the two-dimensional Cartesian coordinate plane, the major axis (GH) of the secondary osteon, used here as an example 3.7(A), is oriented identically to the example in Figure-MajMin B. In Figure 3.7 (B), the longitudinal axis of the diaphysis is represented by the Z-axis. The longitudinal axis of the secondary osteon will be at some angle, θ_L , relative to the Z-axis. The angle is defined between the values of 0° (parallel to the Z-axis) and 90° (perpendicular to the Z-axis) 3.7(B).

As shown on Figure 3.8 A, the angle, θ_L , also can be measured between the perpendicular to the longitudinal axis of the diaphysis (red) and the perpendicular to the longitudinal axis of the primary vasculature, secondary osteon, or Haversian canal (blue). Likewise, that angle can be calculated based on the degree of ellipticity revealed by a cross-section oriented perpendicular to the longitudinal axis of the diaphysis, as in Equation 3.1. In practice, the angle is calculated using a derivation of the Pythagorean Theorem (Appendix C).

$$\Theta_L = \sin^{-1}\left(\sqrt{1 - \frac{r^2}{R^2}}\right) \quad (3.1)$$

where

$$\begin{aligned} r &= \frac{1}{2}\text{-length of the minor axis} \\ R &= \frac{1}{2}\text{-length of the major axis} \\ \Theta &= \text{calculated angle} \end{aligned}$$

Theoretically, the length of the minor axis is the “true” diameter of the cylindrical canal of the microstructural feature, illustrated in Figure 3.8, comparing B and C. Therefore, the higher the ratio of R: r, the greater the angular displacement of the longitudinal axis of the microstructure canal from the longitudinal axis of the diaphysis. It should be noted here that the angle θ_L does not indicate the directionality of angular tilt. For example, if a secondary osteon has a major axis that is oriented anteroposteriorly at an angle, θ_L , of 0° , it is not known whether the osteonal cylinder tilts toward the anterior or posterior of the bone. Currently, the determination of this additional directionality is beyond the scope of this dissertation.

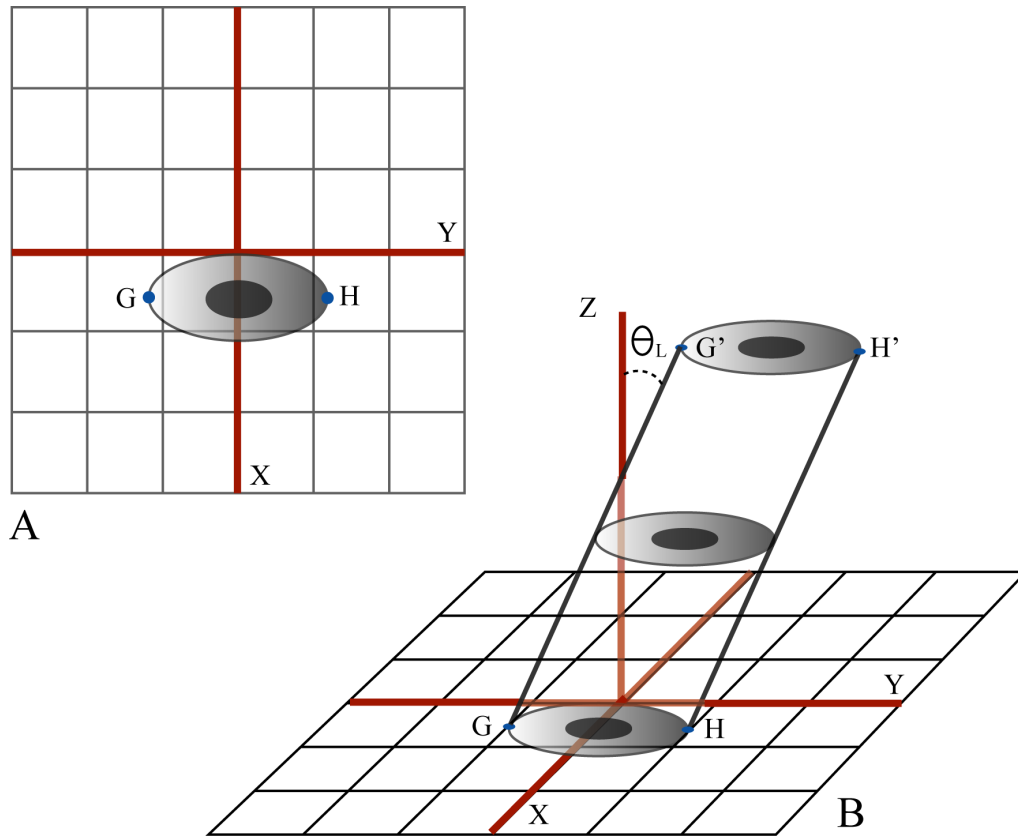


Figure 3.7: The major axis of a secondary osteon, line segment GH, represented in a two dimensional Cartesian coordinate system (A) can be translated/projected into a three-dimensional coordinate system by adding the Z-axis (B). The relative length of the major axis of the secondary osteon ellipse is indicative of the angle Θ_L between the Z-axis (i.e. longitudinal axis of the diaphysis) and the longitudinal axis of the osteon. Line segment G'H' represents the translation/projected of line segment GH in three-dimensional space.

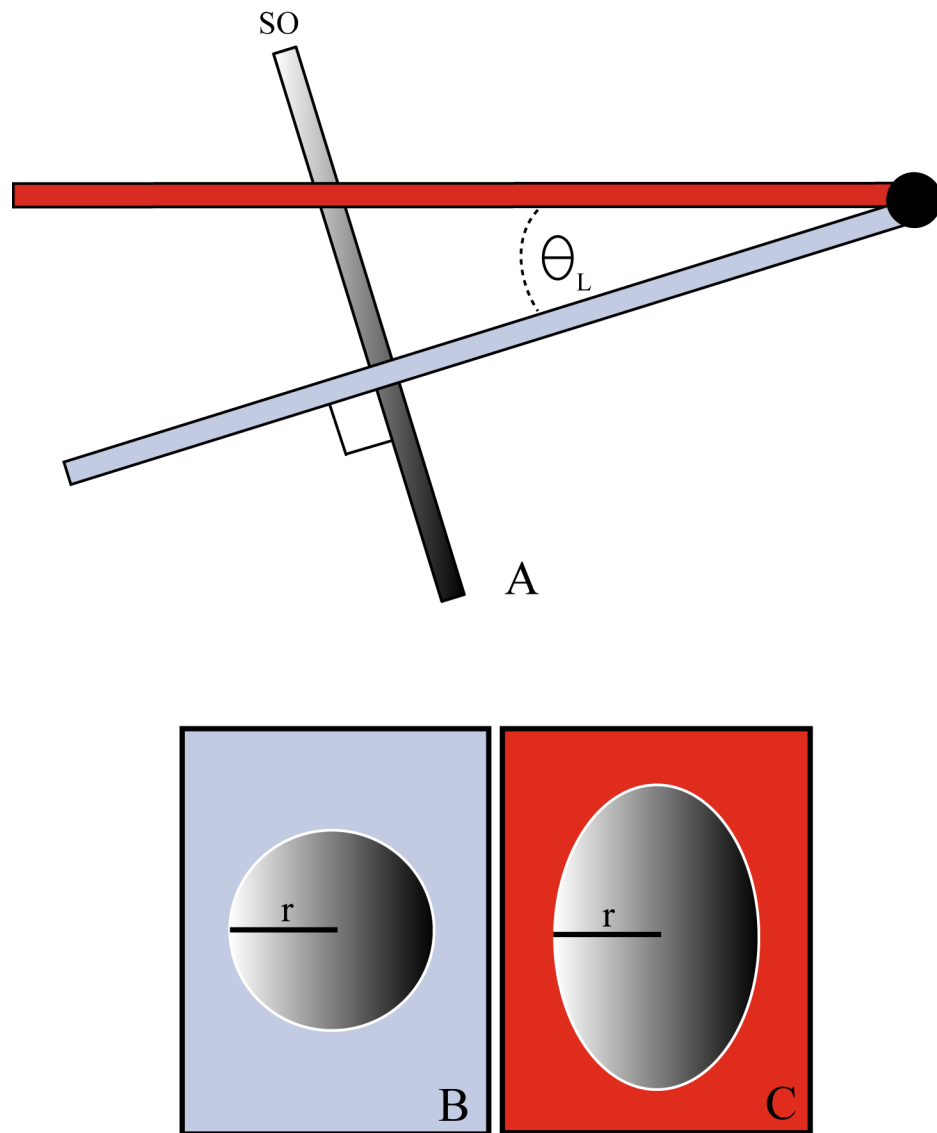


Figure 3.8: Angle Θ_L represents the orientation of the vacuature or secondary osteon (SO) in relation to the longitudinal axis of the diaphysis (A). The red bar represents the plane of the thin-section cuts made in this study and the blue bar represents the plane that is perpendicular to the long axis of the secondary osteon cylinder (SO). A cross-section parallel to the blue plane (B) shows the secondary osteon to have a hypothetically circular shape with radius r . A cross-section parallel to the red plane (i.e. actual orientation of the thin-section) shows an elliptical shape of the same osteon, with minor axis radius, r (C). The radius of the minor axis remains constant in all cross-sections (of varying Θ_L) under consideration. The deviation of the half-length of the major axis from r is indicative of the angle of the secondary osteon with respect to the diaphysis.

Lacunar Area

Lacunae are known to be close to three-dimensional ellipsoids in shape. In order to characterize the shape of these features, one measures the major and minor axes of ellipses defined in transverse cross-section. Two types of lacunae are distinguished in this dissertation, primary and secondary, which are categorized based on where they occur in the thin-section. Secondary lacunae are those that lie within the cement line of a measured secondary osteon. Primary lacunae are those found in any part of the primary bone of the cross-section (Figure 3.3).

The true maximum major and minor axes of the ellipsoidal lacunae are not always parallel to the transverse cut of the thin section. To increase the probability of measuring (almost) true major and minor axial lengths, the largest lacunae are measured for the dataset. Ten lacunae of each type (primary and secondary) are measured per micrograph. Unfortunately, the absence of measurements in the ellipsoid's third dimension prevents the estimation of lacunar volume. Instead, shape area is calculated using the formula for the area of an ellipse, as in Equation 3.2.

$$A_L = \pi \cdot r \cdot R \quad (3.2)$$

where

$r = \frac{1}{2}$ -length of the minor axis

$R = \frac{1}{2}$ -length of the major axis

$A_L =$ calculated area of ellipse

Metrics and Abbreviations

The following is a list of metrics considered in this dissertation, with appropriate abbreviations: (1) Minor Axis of the Primary Vasculature (MinPV), (2) Minor Axis of the Primary Lacuna (MinPL), (3) Minor Axis of the Secondary Lacuna (MinSL), (4) Minor Axis of the Haversian Canal (MinHC), (5) Minor Axis of the Secondary Osteon (MinSO), (6) Major Axis of the Primary Vasculature (MajPV), (7) Major Axis of the

Primary Lacuna (MajPL), (8) Major Axis of the Secondary Lacuna (MajSL), (9) Major Axis of the Haversian Canal (MajHC), (10) Major Axis of the Secondary Osteon (MajSO), (11) Angle of the Primary Vasculature Orientation relative to the Periosteal surface (PVPeri), (12) Angle of the Haversian Canal Orientation relative to the Periosteal surface (HCPeri), (13) Angle of the Secondary Osteon Orientation relative to the Periosteal surface (SOPeri), (14) Angle of Primary Vasculature Orientation with respect to the Longitudinal axis of the diaphysis (PVLong), (15) Angle of Haversian Canal Orientation with respect to the Longitudinal axis of the diaphysis (HCLong), (16) Angle of Secondary Osteon Orientation with respect to the Longitudinal axis of the diaphysis (SOLong), (17) Primary Vasculature cross-sectional Area (PVA), (18) Primary Lacuna cross-sectional Area (PLA), (19) Secondary Lacuna cross-sectional Area (SLA), (20) Haversian Canal cross-sectional Area (HCA), (21) Secondary Osteon cross-sectional Area (SOA), (22) Primary Vasculature Circumference (PVC), (23) Primary Lacuna Circumference (PLC), (24) Secondary Lacuna Circumference (SLC), (25) Haversian Canal Circumference (HCC), (26) Secondary Osteon Circumference (SOC), (27) Bounding Ellipse Area for Primary Vasculature (PVAEllipse), (28) Bounding Ellipse Area for Primary Lacuna (PLAEllipse), (29) Bounding Ellipse Area for Secondary Lacuna (SLAEllipse), (30) Bounding Ellipse Area for Haversian Canal (HCAEllipse), and (31) Bounding Ellipse Area for Secondary Osteon (SOAEllipse). The bounding ellipse refers to the best-fit ellipse calculated for that feature.

3.4 Analysis of Microstructure

Preliminary tests of this method were achieved by manually measuring a reduced number of metrics by hand on digital micrographs of cortical bone from a domestic dog, domestic horse, and domestic pig. The open-access software, ImageJ (Rasband, 1997-2008), provided a convenient format for loading digital images, adjusting for the scale of the micrograph, and exporting the measurements into a spreadsheet that would be used in later statistical analyses. Because this is such a time-consuming and arduous process, it quickly became clear that large datasets, such that those presented in this dissertation, would require a more efficient method of micrograph analysis. The application of a semi-automatic method of measurement not only increased the speed

of microstructure measurement, but also the accuracy of measurements compared to that of “by-hand” measurements. The details of the process are described below.

3.4.1 The Welsh Algorithm

The Welsh Algorithm was created in collaboration with Dr. Eric Welsh for specific application to this study. Its purpose is automatic counting of metrics from all digitally marked microstructures. The algorithm was created based on consideration of the shapes of interest in transverse sections of bone and the assumptions outlined above.

Microstructure Marking Procedure

Application of the Welsh computer program requires that each microstructural type of interest on the digital images be outlined with a different color. All shapes outlined in a specific color are measured and tabulated, and their group statistics calculated. The user specifies which colors to use for tracing shape boundaries. I chose colors using the RGB color model and designated colors as follows: (1) Primary vasculature, magenta, RGB #FF00FF, (2) Primary lacunae, green, RGB #00FF00, (3) Secondary osteon, red, RGB #0000FF, (4) Secondary vasculature, blue, RGB #0000FF, and (5) Secondary lacunae, cyan, RGB #00FFFF.

I digitally marked by hand each microstructure with the corresponding color using Adobe Photoshop CS3 (Figure 3.9(A)). The pen tool, in combination with a stylus pad input device, allowed for the most efficient manual marking and ensured a closed outline. All color strokes were 1 pixel wide.

Algorithm Mechanics

The algorithm assigns to each microstructural unit a best-fit ellipse from which the lengths of its minimum and maximum axes are determined. Best-fit ellipses are specified as those that yield the same first two principal moments of inertia as the

original microstructural shape. Ellipse circumference is calculated using the Reduced Ahmadi 2006 approximation (<http://dx.doi.org/10.3247/SL2Math07.001>), because it offers the optimal blend of accuracy and computational efficiency. Major and minor axes are derived directly from the best-fit ellipse. The borders of shape-bounding boxes are defined by the minimum bounding rectangle parallel to the principal axes of the shape.

Concentric shapes can be accommodated, provided that the concentric borders are spatially separated and distinguished by a different color (e.g., the Haversian canal is within the border of the secondary osteon). Areas of shapes are calculated as the sum of the pixels within and including the shape-border pixels. The circumference of the actual marked border is calculated by temporarily expanding the shape borders by one pixel both horizontally and vertically, then summing the number of horizontal and vertical moves required to traverse the expanded border. Diagonal moves are weighted by an additional factor of approximately 1.168 pixels, assuming an average diagonal move of 20° .

Output

In addition to the metrics listed above, the algorithm output also computes statistical moments of the counted features, including standard deviation, skewness, kurtosis, and coefficients of variation for each microstructure type. Metrics of individual microstructural units may be visually verified against the specific output image for accuracy (Figure 3.9). As illustrated in Figure 3.9(B), the digitally hand-marked micrograph is overprinted by the algorithm to show all microstructures shaded with their respective colors. For each shape, the defining endpoints used to calculate the lengths of major and minor axes are displayed, as is the centroid (Figure 3.9(C)). By comparing output from the Welsh program with the manually marked input, it was possible to verify that every feature was appropriately counted and tabulated.

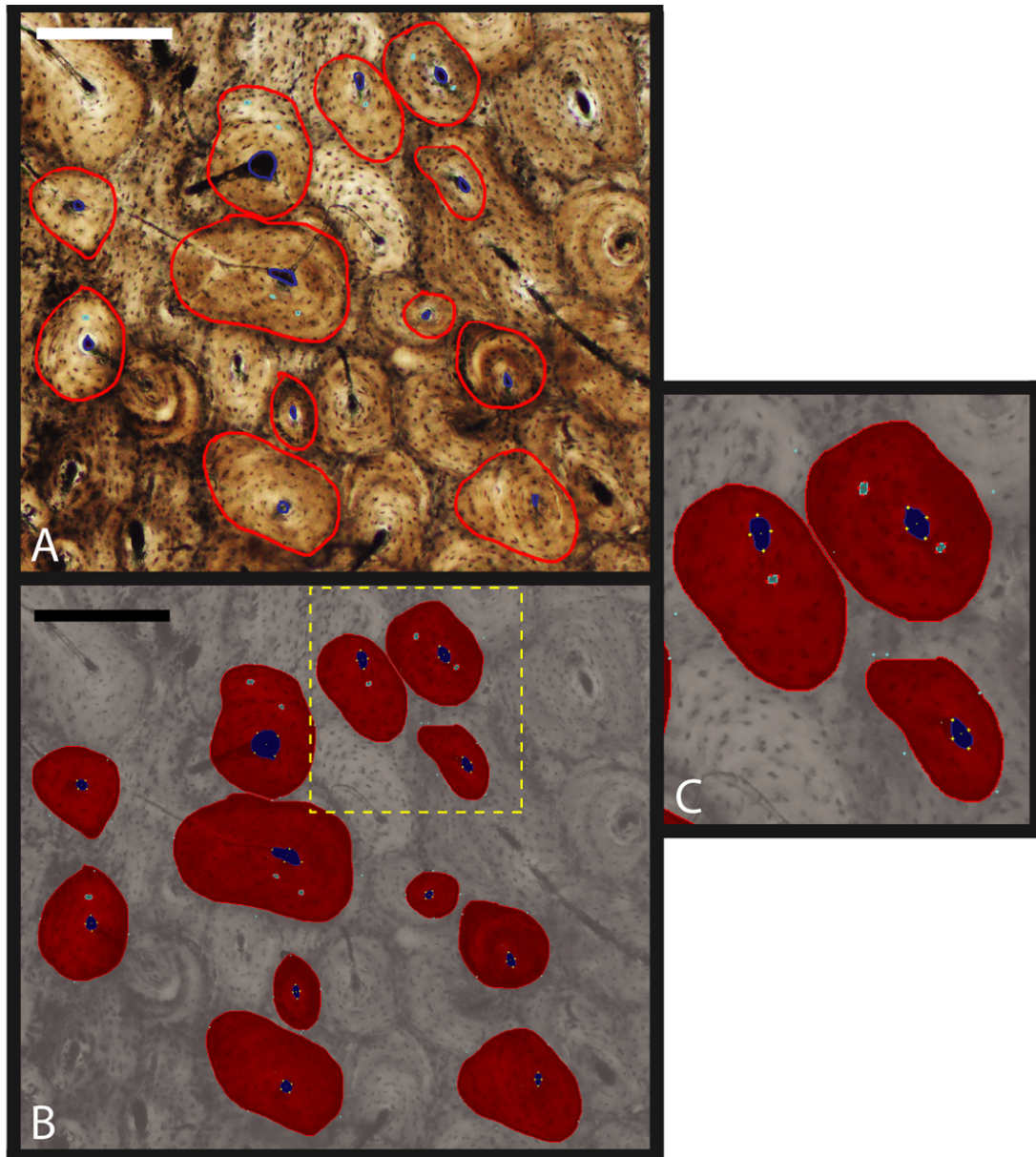


Figure 3.9: The marking and calculation of metrics from the digital micrographs begin with (A), digitally marking by hand the microstructures in colors corresponding to the feature type. Application of the Welsh algorithm overprints the features (B), allowing for individual checking of the micrographs to ensure that the correct measurements are being made. The yellow, dotted rectangle in (B) defines an area magnified in (C). The endpoints of the axes of the elliptical shapes are represented by the minute yellow crosses, and the centroids are represented by the cyan dots. Portion of a *Felis rufus* left tibia. Scale bar for (A) and (B) equals 2.5mm.

3.4.2 Statistical Analysis

Statistical analysis of the data was achieved using the statistical analysis package Evince (Umbio, 2009) and PASW Statistics by SPSS. The statistical technique of Principal Component Analysis (PCA) was used to explain, in a mathematically optimal way, variance amongst the samples. Details of the statistical treatment of each dataset are discussed in more detail in subsequent chapters.

Chapter 4

Extant Mammals as Taxonomic Test Subjects

4.1 Introduction

There are two goals of this dissertation: (1) to explore the variation in bone microstructure within and between species according to the methodology described in Chapter 3 and (2) to make the first test of the hypothesis that tetrapods can be taxonomically distinguished by their cortical bone microstructure. The longer-term goal is to apply this methodology to the bones of extinct tetrapods. The initial tests of the hypothesis and methodology presented in Chapter 3, however, were done on extant mammals, because (1) the rarity of fossil vertebrate specimens typically precludes any destructive extraction techniques, (2) extant mammals are not of questionable taxonomic validity, unlike fossil specimens, (3) mammals exhibit a diversity in locomotive mechanics, dietary habits, and niche partitioning whose effects must be explored, and (4) the bone microstructure of extant mammals is very similar to the types and arrangements of microstructural features in extinct mammals, Aves, dinosaurs, and mammal-like reptiles (Enlow and Brown, 1958; Ricqlès, 1980, 1990).

This chapter describes the mammals whose bone microstructures were measured and analyzed to test the hypothesis of their taxonomic relevance. Presented first is a review of mammalian osteology and bone histology to provide context for more detailed descriptions of the mammalian specimens analyzed in the test datasets. Because the preparation of the specimens for this study is a destructive process, detailed descriptions of each bone's gross morphology before thin-sectioning provide a record of the

material for future reference. The gross morphological descriptions are then paired with a representative histological image from each specimen to complete the mammalian overview in preparation for dataset analysis in the chapters that follow.

ABBREVIATIONS- calcaneus, **cl**; carpus, **ca**; caudal vertebrae, **cv**; cervical vertebrae, **cerv**; distal articular end, **D**; dorsal vertebrae, **dv**; endosteal bone, **Eb**; endosteal surface, **E**; femur, **fe**; humerus, **hu**; innominate, **in**; lumbar vertebrae, **lv**; metacarpal, **mc**; metatarsal, **mt**; optically discernable interface, **odi**; patella, **pa**; periosteal bone, **Pb**; periosteal surface, **P**; phalanges, **ph**; primary bone, **Pr**; proximal articular end, **Px**; ribs, **r**; sacrum, **sa**; scapula, **sc**; secondary bone, **S**; skull, **sk**; tibia, **ti**; inter-trabecular space, **Tr**; ulna, **ul**.

4.2 Mammalian Skeletal Gross Morphology

During development of the mammalian skeleton, bone is differentiated into two types, intramembranous and endochondral, based on the process by which each becomes an ossified material within the skeleton (Baron, 2003; Steele and Bramblett, 1988). Bones of both types of formation are analyzed in this dissertation. Both types of bone also undergo internal remodeling throughout life. Intramembranous bone includes skeletal structures that make up the pectoral girdle, ribs, and all of the bones in the skull. Colloquially known as “flat” bones, they are composed of two cortical plates separated by a thin trabecular layer. There is no medullary cavity. During development of flat bones, the material differentiates from the mesenchyme, forming a thick cellular substance that, unlike endochondral bone formation (see below), ossifies immediately with no intermediate cartilage form.

Endochondral bone also begins with differentiation of mesenchymal cells, but unlike intramembranous bone, it forms a cartilage precursor that will eventually ossify and form the diaphysis. The cartilage precursor, because it is the first area to develop, is referred to as the primary ossification center (Baron, 2003). Synchronous with the formation of this cartilage model is a ring of ossified woven bone in the midshaft area. When the ossification of the woven bone finishes, blood vessels, originating from the ossified ring, penetrate the cartilage. Mineral and collagen replacement of the remaining cartilage commences with this vascular invasion into the otherwise

avascular cartilage model. These first vessels that penetrate the cartilage are responsible for bringing the blood supply that will nourish hematopoietic bone marrow in the medullary cavity, located in the center of the diaphysis. Once the diaphysis is ossified, lateral bone growth continues throughout life along the diaphysis by very slow deposition of bone matrix on the periosteal surface. Resorption of bone material occurs at the border of the medullary cavity, the endosteal surface.

Of interest to this investigation are the endochondral bones of the appendicular skeleton. In mammals, as well as across the whole of the Vertebrata, the long bones that make up the fore- and hind-limbs are fairly conservative in morphological arrangement. The forelimb consists of the humerus, most proximal to the body, and the radius and ulna in the distal part of the limb. The hindlimb consists of the femur, most proximal to the body, and the tibia and fibula distally. Surveying the Mammalia, there are several instances of specialization within both the fore- and hind-limbs that result in reduction or loss of one of the distal elements of the limb, the most prevalent being the reduction or loss of the fibula. The proximal elements of the fore- and hind-limb, the humerus and femur, respectively, are always present.

In mammals, all long bones have a conservative general morphology. Long bones consist of three main parts: the diaphysis, the epiphysis, and a transitory section called the metaphysis (Haines, 1942). The diaphysis, or midshaft, is the primary center of ossification during development, is generally cylindrical, and makes up the majority of the bone material in the long bone. The diaphysis is often featureless with the exception of muscle scarring that may be present closer to the proximal and distal ends. The epiphyses, the secondary centers of ossification, cap the diaphysis at the proximal and distal ends. The epiphyses are the more flaring articular ends that allow for smooth and specialized connection with the bone or bones proximal and distal to them. The diaphysis and epiphysis are connected by a transitional, cartilagenous zone, the metaphysis. Epiphyseal cartilage, also referred to as growth plates, is located within the metaphysis and allows for longitudinal growth of the long bone. The metaphysis, along with the epiphyseal cartilage, eventually disappears as a result of ossification during ontogeny as longitudinal growth of the bone is completed (Baron, 2003).

4.3 Mammalian Osteohistology

This section provides a general introduction to and description of mammalian osteohistology; the specific microstructural arrangement for each taxon will be addressed later in this chapter. Most of the previous studies and characterizations of non-human, mammalian bone microstructure have been directed at domestic animals (Enlow and Brown, 1956, 1957, 1958; Georgia and Albu, 1988; Harsanyi, 1990; Jowsey, 1968; Mori et al., 1999, 2003). Although domestic mammals are not used in this study, they provide an excellent base knowledge of osteohistologic structures and a model against which comparisons can be made with microstructural arrangements found in the wild mammalian counterparts described later in this chapter. There is not a large body of literature on the comparative bone histology of extant mammals. What is generalized about the microstructure of the whole group is often inferred from domestic members of the Artiodactyla and Perisodactyla.

Laminar bone, in general, makes up the primary structure of all compact bone in the Mammalia (Locke, 2004). Resembling the rings of a tree (Figure 4.1), the laminae (often referred to erroneously as “lamellae”) are arranged circumferentially and separate endothelium-lined vascular compartments Locke (2004). Each lamina is a composite of several, smaller circumferential lamellae. This bone type is vascularized first by primary osteons and then remodeled continuously throughout life, forming a varying number of secondary osteons (Amprino, 1948, 1963; Amprino and Marotti, 1964; Ascenzi and Bonucci, 1964, 1967, 1968, 1972; Ascenzi et al., 2004; Carter and Spengler, 1978; Cooper et al., 2003, 1966; Currey, 1964; Enlow, 1962, 1966, 1977; Frost, 1963, 1964; Havill, 2004; Hert et al., 1994; Johnson, 1966; Locke, 2004; Mundy et al., 2003). Throughout the life of the animal, primary laminar bone is often increasingly obscured by secondary bone (Enlow and Brown, 1957; Locke, 2004). The laminar bone histology of cattle has been described as having a “general, characteristic” mammalian appearance (Currey, 1962).

The bone histology of the Artiodactyla and Perisodactyla is the most well known in the Mammalia because of the availability of domestic animals in these groups. Most histological analysis pertaining to the Artiodactyla has been accomplished using cattle. In many cases, the bone microstructure of extant artiodactyls is highly convergent

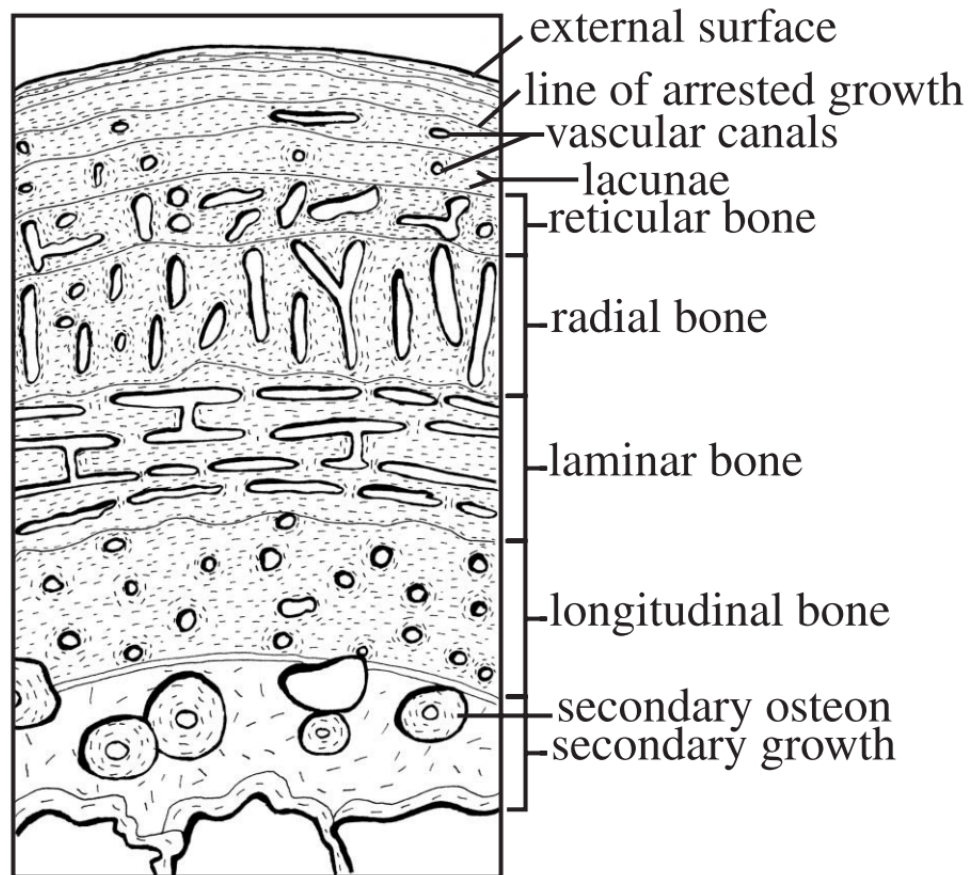


Figure 4.1: A schematic of cortical bone histology, with the four major types of bone separated by lines of arrested growth. Note that the separation of bone types and the variety of bone types in one sample are typically not seen all together in one cortical cross-section. The figure is for illustrative purposes only. Modified from Boef and Larsson, 2007, p.64

with that of dinosaurs, showing a plexiform arrangement (Currey, 1962). The histological structure of the long bones of artiodactyls follows a generalized pattern (Enlow and Brown, 1958) of a well-organized laminar tissue (Locke, 2004) (Figure 4.1). Laminar bone is typified by the orderly appearance of vascular canals (Enlow and Brown, 1956). The predictable vascular canal arrangement in cortical bone differentiates artiodactyls from other mammalian Orders. The epiphysis of the long bones usually appears less organized than the cortex of the diaphysis. The cortex in the epiphysis is classified as reticular with extensive secondary osteonal remodeling (Enlow and Brown, 1958). Remodeling usually begins in the endosteal region. Complete primary bone replacement by secondary osteons has been observed even in young bone (Enlow and Brown, 1958).

The domestic *Equus* typically represents the Perissodactyla in the literature. Qualitatively, the cortical bone in perissodactylan specimens does not show the regularity in the vascularization throughout the skeleton that is evident in the cortical bone of Artiodactyla. In *Equus* vascular arrangement differs depending on the skeletal element and the location within a particular bone, such as the microstructural arrangement in the diaphysis compared with that of the epiphysis of a long bone. Generally, the epiphyses of *Equus* long bones show an irregular reticular organization of the primary bone, characterized by randomly branching vasculature. The diaphyseal vasculature is more organized, referred to qualitatively as plexiform bone. Remodeling of the primary bone is most prevalent in the endosteal region, and complete primary bone replacement by secondary osteons has been observed even in the cortical bone of very young *Equus* specimens (Enlow and Brown, 1958).

In addition to articles on the Artiodactyla and Perissodactyla, there is also a small amount literature pertaining to the cortical structure of the Carnivora (Diaz and Rajtova, 1975). Enlow and Brown (1958) provided an informative overview of carnivorian bone microstructure, addressing the characteristics of at least one specimen of each major extant carnivore as well as of several extinct taxa. Carnivora included in the survey were the Paleocene *Dissacus* and *Didymictis*, Eocene *Oxyaena*, Oligocene *Dinictis* and *Mustelavus*, modern *Ursus*, *Felis*, *Mehitis*, *Procyon*, *Mustela*, *Canis*, and *Taxidea*, among others. The primary structure of the cortex of bones of the Carnivora is generally reticular lamellar (described as laminar by Locke, 2004) (Enlow and Brown, 1958). Exceptions to this are the bones of *Ursus* and *Canis*, showing a

“plexiform” outer cortex similar to the primary microstructural arrangement in the Artiodactyla. As age of the carnivore increases, there is extensive secondary remodeling in the mid-cortex of the diaphyses. Unlike the secondary bone of the Artiodactyla and Perissodactyla, the remodeled carnivorian cortex is confined to a zone sandwiched between periosteal and endosteal regions of primary laminar organization. The endosteal laminar region is usually thicker than the periosteal region. Secondary bone is less prevalent in the epiphyseal regions of long bones of carnivores compared to those of ungulates and, throughout the life of the carnivore, it is likely that the primary bone structure will remain clearly visible (Enlow and Brown, 1958).

4.4 Mammalian Specimens: Primary Dataset

The Primary Dataset referred to herein is the dataset consisting of 11 representative specimens from five mammalian orders, Carnivora, Rodentia, Didelphimorphia, Lagomorpha, and Primates, which were used for this first test of the hypothesis (Figure 4.2). Results of the test are presented in Chapter 5 of this dissertation. Obtaining specimens to include in the Primary Dataset was very challenging. Even though the taxa desired are all extant, the tibiae were difficult to obtain from museum collections: not only were they going to be subjected to destructive analytical techniques, but the purpose for destruction was to explore an untested methodology. The tibiae analyzed were graciously provided on loan from either the North Carolina Museum of Natural Science (NCSM) or the Museum of Comparative Zoology, Harvard (MCZ). The result of those granted requests, however, was a compilation of mammals that satisfied the goal of breadth in dataset construction, but that was optimized for little else (i.e. geography, more specific phylogenetic comparisons, etc). All mammals in the Primary Dataset are terrestrial and exert regular, load-bearing pressure on their skeleton. Flying or primarily aqueous mammals (Orders Cetacea, Chiroptera, Sirenia, and Dermoptera) were not included in the Primary Dataset, because bone stress is quite different in those media. There are also no domestic animals in the Primary Dataset (Padian et al., 2004).

Order	Family	Genus	Species	Common name	Specimen number	Total length (mm)	Diaphysal length	Anteroposterior width of proximal epiphysis	Mediolateral width of proximal epiphysis	Anteroposterior width of distal epiphysis	Mediolateral width of distal epiphysis
Primates	Strepsirrhini	<i>Varecia</i>	<i>variegata</i>	ruffed lemur	MCZ 59274	137.32	116.55	16.26	19.24	11.02	13.48
	Cercopithecoidea	<i>Macaca</i>	<i>mulatta</i>	rhesus monkey	MCZ 64360	134.77	107.67	15.58	21.39	11.06	13.21
	Cebidae	<i>Cebus</i>	sp.	capuchin monkey	MCZ BOM 438	103.86	84.58	13.42	17.51	8.87	11.3
Lagomorpha	Leporidae	<i>Lepus</i>	<i>americanus</i>	snowshoe hare	MCZ 60888	114	102.04	13.66	14.31	8.38	12.14
Rodentia	Sciuridae	<i>Marmota</i>	<i>monax</i>	groundhog	Not cataloged	76.92	61.95	12.91	16.17	9.16	9.8
	Castoridae	<i>Castor</i>	<i>canadensis</i>	American beaver	Not cataloged	N/A	107.23	N/A	N/A	N/A	N/A
Didelphimorphia	Didelphidae	<i>Didelphis</i>	<i>virginianus</i>	opossum	NCSM 8368	88.56	74.35	11.57	13.69	8.5	6.94
Carnivora	Canidae	<i>Canis</i>	<i>latrans</i>	coyote	Not cataloged/EC	159.56	136.37	28.78	28.48	15.63	18.95
	Felidae	<i>Felis</i>	<i>rufus</i>	bobcat	Not cataloged/EC	155	133.67	25.79	31.32	17.08	20.59
	Procyonidae	<i>Procyon</i>	<i>lotor</i>	raccoon	NCSM 2674	115.97	100.22	19.13	21.65	10.44	13.54
	Ursidae	<i>Ursus</i>	<i>americanus</i>	black bear	NCSM 5363	N/A	172.62	N/A	N/A	27.37	34.13

Figure 4.2: Summary showing all taxa included in the Primary Dataset and corresponding tibial measurements. All measurements are in millimeters.

4.4.1 The Tibia

All bone samples were extracted from the mid-diaphysis of the left tibia in a transverse plane perpendicular to the long-axis of the diaphysis. Through two parallel saw cuts, a one-centimeter-bone plug was removed from each specimen prior to beginning the thin-section procedure. The same specific bone from each skeleton was analyzed in order to evaluate and refine the methodology. Clearly, if the hypothesis failed at this level of sample comparison, then it could not succeed in the presence of complications from intra-element and intra-skeletal variation.

The tibia is the large, medial bone of the distal hindlimb in tetrapods, which transmits weight between the femur (proximally) and the bones that make up the pes (for plantigrade locomotors) or what ancestrally used to be the pes (for digitigrade locomotors). The metatarsals in artiodactyls and perissodactyls, for example, have been elongated and raised to create a functional, third hinge in the hindlimbs, which, to a “normal” observer, now seems like part of the leg rather than the pes (Figure 4.3). The fibula, if present, articulates laterally with the tibia. Relative to other long bones, the articular ends of the tibia are slightly expanded compared with the diaphysis. There are two condyles on the proximal articular surface that, in life, contact the complementary structures on the distal end of the femur. The morphology and size of the medial and lateral tibial condyles vary within the Mammalia (see descriptions below). The shape of the distal articular end varies greatly due to evolutionary changes in the structure of the mammalian angle. In most cases, however, the medial malleolus remains as a prominent feature.

The patellar tendon inserts just below the articular surface on the tibial tuberosity, a protrusion of bone on the proximal end of the anterior tibial margin. The other two margins of the tibia, the medial and interosseus, combine to create a tibial shaft with an overall triangular cross-section. Longitudinally, the shaft ranges from straight to s-shaped. If the fibula is present, corresponding articular facets are located on the proximal and distal ends of the interosseus margin.

The tibia was selected here because of its availability for destructive research. Only the left tibia was used for the Primary Dataset because corresponding sections of

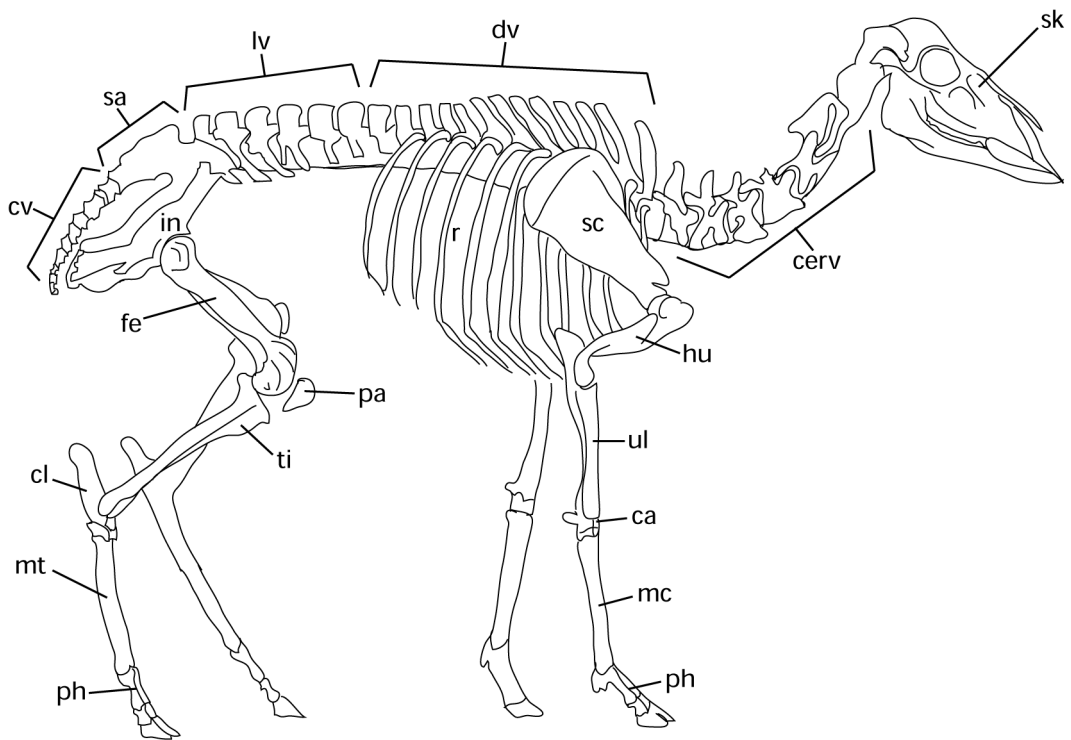


Figure 4.3: The skeletal anatomy of *Odocoileus virginianus* (white-tailed deer).

contralateral bones have been shown to have nearly the same microstructural arrangement (Amprino and Marotti, 1964; Currey, 1964). This observation suggests that bone remodeling processes act symmetrically and that the morphology of the secondary osteons and other microstructures will also be complementary.

4.4.2 Order Carnivora

Canis latrans

Family: Canidae

Common name: Coyote

Accession number: NCSM not cataloged/EC

Description of the left tibia (Figure 4.4 A): The specimen is slightly more gracile (i.e. less robust) relative to the other specimens in the dataset. The total length of the tibia is 159.56 mm, and the diaphyseal length is 136.37 mm measured along the anterior margin. This specimen comes from a mature animal, as the epiphyses are fully ossified to the diaphysis and the sutural lines are no longer visible. The proximal articular end is very slightly wider anteroposteriorly (28.78 mm) than it is mediolaterally (28.48 mm). The lateral condyle is only slightly larger than the medial condyle. Both condyles are ovate with the long axes of the ovals directed anteriomedially. The intercondylar area is relatively well-defined. The lateral intercondylar tubercle is a raised bump with a rounded apex. It is intersected by the medial intercondylar tubercle, which takes the form of a raised crest along which the long axis is directed almost mediolaterally. When viewed anteriorly, the distal half of the diaphysis is fairly straight with a very slight lateral convexity. The inflection point of the convexity occurs approximately at the mid-point of the diaphysis where the convexity is now medial. When viewed medially or laterally, the shaft is straight with a slight flaring in the proximal of the diaphysis. The tibial tuberosity is a prominent feature that follows the convexity of the proximal of the shaft. Just as in many other specimens in this dataset, the tuberosity grades into the distal shaft making an accurate length measurement impossible. The proximal of the tuberosity is roughened indicating

a site of muscle attachment. The medial and interosseous margins are fairly well-defined, and the popliteal line is represented by a bifurcated, raised, and roughened crest of bone angled slightly medially across the posterior face. There is only a slight fossa on the posterior face. Articular facets for the fibula are located on the proximal articular end very close to the interosseous margin and distally, the facet is elongated along the interosseous margin and terminates at the distal articular end. The distal articular end is wider mediolaterally (18.95 mm) than it is anteroposteriorly (16.63 mm). The medial malleolus is U-shaped and is flanked on the posterior side by a slight malleolar groove.

Microstructural arrangement of the left tibia: The center of the cortical bone shows a continuous width of secondary bone that is bounded by equal widths of primary bone on both the periosteal and endosteal surfaces (Figure 4.4 B, C). The secondary bone occupies the middle one millimeter of the cortex and is circumferentially continuous around the diaphysis. Secondary osteons in this area overlap one another, indicating that there have been at least two episodes of remodeling. Primary vasculature is rare, but when present, is sub-circular in cross-section, an indication that the vasculature is approximately parallel to the long axis of the diaphysis.

Felis rufus

Family: Felidae

Common name: Bobcat

Accession number: NCSM not cataloged/EC

Description of the left tibia (Figure 4.5 A). The bone is slightly robust relative to the other mammal tibiae in this sampling. The total length of the bone is 155 mm, with a diaphyseal length of 133.67 mm measured along the anterior margin. Closed sutural lines between both the proximal and distal epiphyses and the diaphysis indicate that this specimen is from a mature animal. The proximal and distal articular ends are very slightly offset from vertical alignment as the medial malleolus protrudes more medially than does the medial condyle of the proximal articular surface. The

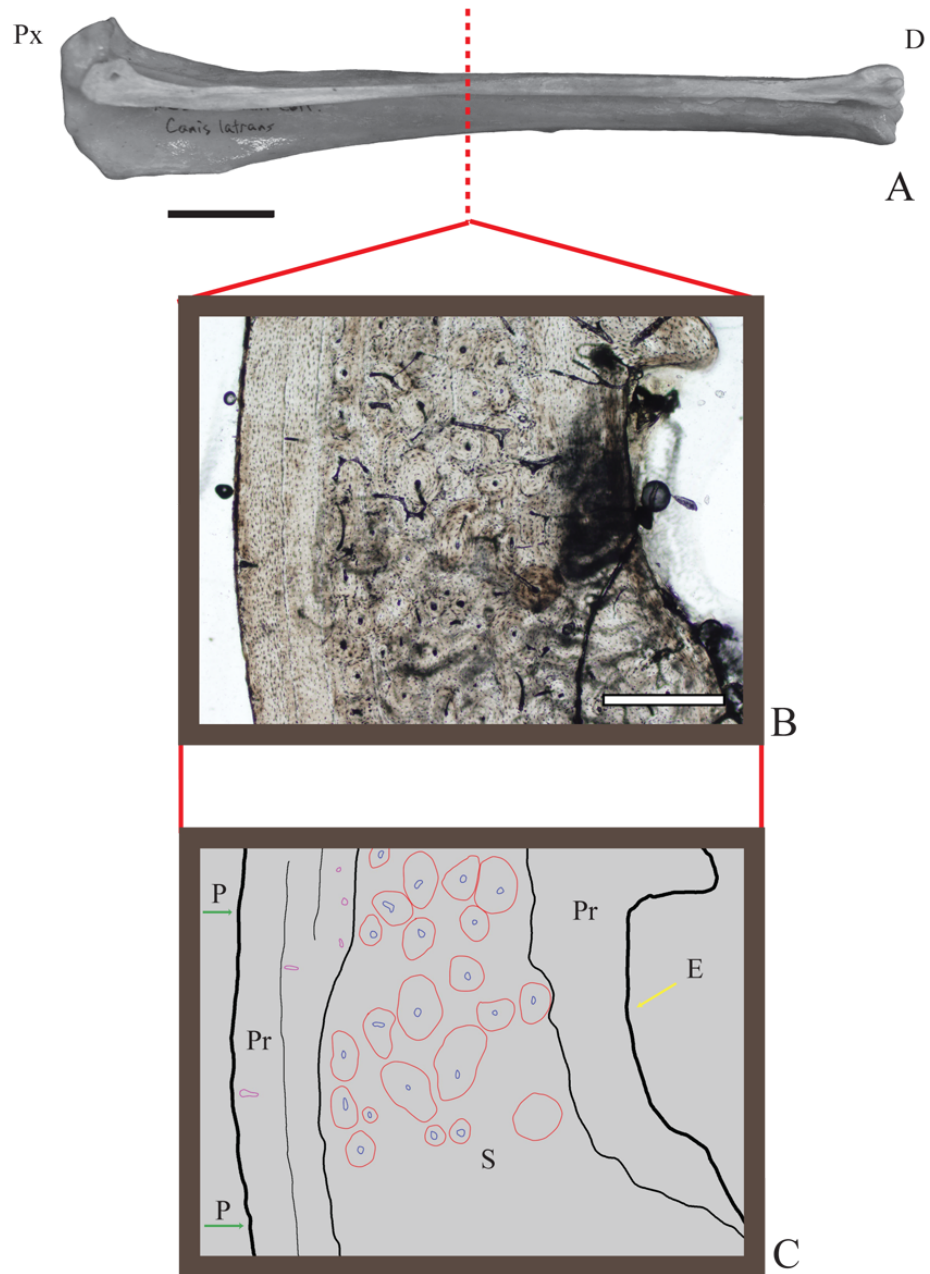


Figure 4.4: *Canis latrans* (Coyote) tibia (A) with a corresponding micrograph showing representative microstructural arrangement (B) and schematic (C). A continuous layer of secondary bone is bounded on both sides by primary bone along the periosteal and endosteal surfaces. Scale for (A) = 2cm. Scale for (B,C) = 0.5mm.

distal half of the shaft is straight. The shaft begins to curve slightly at the mid-point of the diaphysis. When viewed anteriorly, the curve of the proximal part of the shaft is convex medially. When viewed laterally, the shaft is convex anteriorly. The distal end is twisted slightly clockwise relative to the proximal end about the long axis of the diaphysis. The tibial tuberosity follows both the convexity and twisting of the shaft and blends with the diaphysis. The proximal articular end is wider mediolaterally (31.32 mm) than it is anteroposteriorly (25.79 mm) and the lateral condyle is slightly larger than the medial condyle. The lateral condyle is sub-circular with a slightly longer axis oriented anteriomedially. The medial condyle is oval with its long axis oriented directly anterior. A clearly delimited intercondylar sulcus separates the condyles. Intercondylar tubercles define the medial and lateral border of the intercondylar sulcus and take the form of distinct crests of bone oriented anteroposteriorly.

The medial and interosseous margins of the tibia are marked by a distinctly raised and sharp crest of bone representing muscle attachments. The sharpest and most proximally placed muscle attachment is referable to the popliteal line. There are no fossae between muscle attachments, and all of the latter generally follow the convexity of the bone. Approximately at the mid-point of the tibial tuberosity is a robust, roughened area that also appears to be a site of muscle attachment. Articular facets for the fibula are found on the proximal and distal articular ends very close to the interosseous margin. In life, the fibula would have run parallel to the interosseous margin. The distal articular end is wider mediolaterally (20.59mm) than it is anteroposteriorly (17.08mm). The medial malleolus is relatively robust, the morphology of which follows a wide U-shape when viewed medially. The malleolar groove is very prominent and well-defined.

Microstructural arrangement of the left tibia: The center of the cortical bone shows secondary bone of varying width that is bounded by approximately 1.5 millimeters of primary bone on the periosteal surface and approximately 0.25 millimeters of primary bone on the endosteal surface (Figure 4.5 B, C). The secondary bone, with widths varying from 0.5 to 1.5 millimeters, occupies the middle of the cortex, and is circumferentially continuous around the diaphysis. Secondary osteons in this area do not overlap one another to a great degree, indicating that remodeling has been limited in this bone during the animal's life. Primary vasculature is rare, but when present,

shows a bimodal distribution among sub-circular canals and longitudinal canals. The split indicates that the most likely orientation for the primary vasculature is either parallel or perpendicular to the longitudinal axis of the diaphysis.

Procyon lotor

Family: Procyonidae

Common name: Raccoon

Accession number: NCSM 2674

The left tibia of *P. lotor* is suspected to come from a more mature animal than others in the Primary Dataset. No remnants of a suture line are visible between the distal epiphysis and the diaphysis (Figure 4.6 A). Although the bone is fully ossified, the suture line is slightly visible where the proximal epiphysis articulates with the diaphysis. The total length of the tibia is 116mm, with a diaphysis of approximately 100mm measured along the anterior-most edge of the anterior margin of the bone. The lateral side of the bone is slightly concave as is the posterior edge. The medial side is slightly convex. Most of the “bend” in the tibia is located in the proximal end of the bone above the mid-diaphysis. Below the mid-diaphysis, the shaft straightens from all angles. The proximal articular end is greatly expanded relative to the distal articular end. The proximal end is slightly wider mediolaterally than it is anteroposteriorly. The medial and lateral condyles are approximately equal in size: the medial condyle is slightly longer anteroposteriorly than the lateral condyle, whereas the lateral condyle is wider mediolaterally than the medial condyle. Both condyles have a slightly concave bowl shape. There is a pronounced medial intercondylar tubercle on the lateral side of the medial condyle. There is a raised area on the medial side of the lateral condyle that represents the lateral intercondylar tubercle, but it is smooth and not as pronounced as the medial intercondylar tubercle. Along the anterior margin is the tibial tuberosity with a length of 28.59mm along the diaphysis. This prominent structure ends before the mid-point of the diaphysis, and is angled towards the medial side of the shaft. Just medial to the tibial tuberosity is a prominent muscle attachment site 18.06mm in length. The medial margin is marked by a thin, elongate crest palpable on the distal end of the diaphysis that becomes more rounded proximally. Posterior to the medial



Figure 4.5: *Felis rufus* (Bobcat) tibia (A) with a corresponding micrograph showing representative microstructural arrangement (B) and schematic (C). Secondary bone of varying width occurs in the endosteal region of the cortex, bounded by a wide layer of primary bone on the periosteal surface and a thin layer along the endosteal surface. Scale for (A) = 2cm. Scale for (B,C) = 0.5mm.

margin is a distinct soleal line on the proximal end of the shaft. It is approximately 21.39mm in length and it angled with the distal-most end pointing slightly medially. There is a small, elongate fossa that separates the soleal line from the interosseous margin. The interosseous margin is marked by a thin, distinct ridge that originates underneath the lateral condyle and spirals anteriorly to terminate at the fibular notch. On the distal articular end the medial malleolus is wide and U-shaped when viewed from the medial side of the bone. The malleolar groove is bordered dorsally and ventrally by distinct ridges of bone that do not extend onto the shaft. The middle of the groove shows a small, smooth, raised ridge that follows the attitude of the two larger ridges on each side of the groove. The groove for the flexor hallucis longus is relatively large and flat. The distal articular end is wider mediolaterally (13.54mm) than it is anteroposteriorly (10.44mm).

Microstructural arrangement of the left tibia: The width of the cortex shows distinct, alternating areas of primary and secondary bone formation, beginning and ending with primary bone along the periosteal and endosteal surfaces, respectively. Maximum width of secondary bone formation is 0.5 millimeters (Figure 4.6 B, C), and the layers of primary and secondary bone continue circumferentially around the diaphysis. Secondary osteons do not overlap one another to a great degree, indicating that remodeling has been limited in this bone during the animal's life. Primary vasculature is of medium abundance compared to that of the other carnivores in this study. When present, it shows highly elliptical shape in cross-section. This indicates that the orientation for the primary vasculature is at some angle relative to the longitudinal axis of the diaphysis.

Ursus americanus

Family: Ursidae

Common name: Black bear

Accession number: NCSM 5363

Description of the left tibia: This is the most robust bone relative to its length of all of the specimens in the dataset (Figure 4.7 A). The proximal and distal epiphyses



Figure 4.6: *Procyon lotor* (Raccoon) tibia (A) with a corresponding micrograph showing representative microstructural arrangement (B) and schematic (C). Areas of secondary and primary bone alternate across the width of the cortex, beginning and ending with primary bone of the periosteal and endosteal surfaces, respectively. Scale for (A) = 2cm. Scale for (B,C) = 0.5mm.

are missing from the specimen so the total length could not be obtained. However, the length of the diaphysis is 172.62mm measured along the anterior margin. This is presumably a younger animal, because the epiphyses are not ossified to the diaphysis. The proximal articular end is wider mediolaterally (47.41mm) than it is anteroposteriorly (35.78mm). The tibial tuberosity is not particularly prominent relative to the overall robusticity of the diaphysis. The morphology of the proximal first fourth of the tuberosity is obscured because of the missing proximal epiphysis. The second fourth of the tuberosity shows a large roughened patch referable to a muscle attachment that ends slightly above the mid-point of the diaphysis. The diaphysis is fairly straight. However, there is a very slight medial convexity in the proximal half of the shaft. When viewed medially or laterally, the shaft is convex towards the anterior. The medial and interosseous margins are fairly nondistinct, and there is no popliteal line or fossa located along the posterior face. The only indications that there may have been muscle attachment sites along the posterior face are slightly roughened lines that angle slightly medially. The only feature on the posterior face is a large nutrient foramen located of the length of the shaft down from the proximal border of the diaphysis. The distal end of the diaphysis is wider mediolaterally (34.13mm) than it is anteroposteriorly (27.37mm).

Microstructural arrangement of the left tibia: The width of the cortex shows intermingling areas of primary and secondary bone formation. No regular pattern of remodeling is evident and, unlike other carnivores, the secondary bone continues to the edge of the endosteal surface (Figure 4.7 B, C). Continuous primary bone along the periosteal surface measures from 0.5 millimeters to 1.5 millimeters. Secondary osteons do not overlap one another to a great degree, indicating that remodeling was limited in this bone during the animal's life. Primary vasculature is rare, but when present, shows highly elliptical shape in cross-section. This indicates that the orientation for the primary vasculature is at some angle relative to the longitudinal axis of the diaphysis.

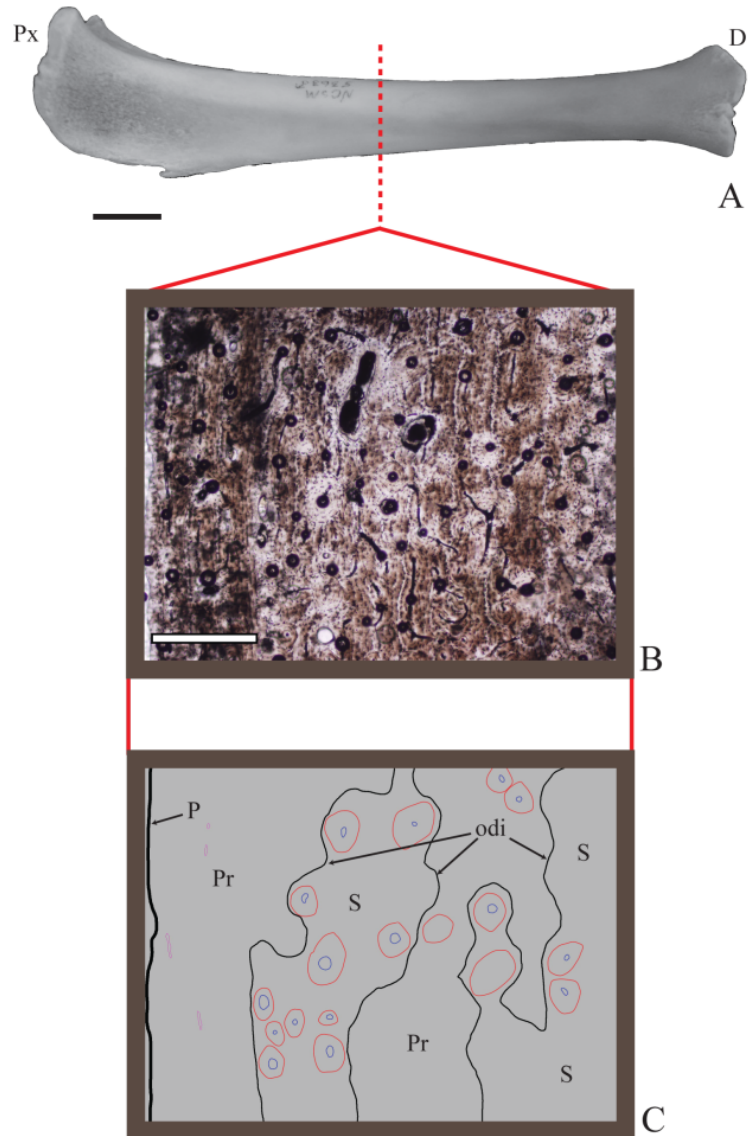


Figure 4.7: *Ursus americanus* (Black bear) tibia (A) with a corresponding micrograph showing representative microstructural arrangement (B) and schematic (C). Areas of secondary and primary bone intermingle along the width of the cortex, with secondary bone present to the edge of the endosteal surface. Scale for (A) = 2cm. Scale for (B,C) = 0.5mm.

4.4.3 Order Rodentia

Marmota monax

Family: Sciuridae

Common name: Groundhog

Accession number: NCSM, not cataloged

Description of the left tibia: The tibia of the groundhog represents a skeletal form in this dataset that is mid-way between gracile and robust. The suture line connecting the diaphysis with the distal epiphysis is fully ossified, but is still visible (Figure 4.8 A). The suture connecting the diaphysis with the proximal articular end is not fully ossified and is still very distinct around the entirety of the bone. The total length of the bone is 76.92mm, and the length of the diaphysis is 61.95mm measured along the anterior margin. The shaft of the bone is slightly concave along the interosseous margin and greatly concave along the dorsal margin. The medial side of the bone is slightly convex while the anterior/ventral margin of the bone is more convex relative to the medial margin. When viewed anteriorly, the greatest “bend” in the bone occurs above the mid-point of the diaphysis. However, when viewed laterally or medially, the arch in the bone is continuous from the proximal to the distal end. The proximal articular end is 1.65 times the mediolateral width of the distal articular end. The proximal articular end is slightly wider mediolaterally (16.17mm) than it is anteroposteriorly (12.91). The lateral condyle is markedly larger than the medial condyle. The lateral condyle has approximately the same anteroposterior length as the medial condyle, but is wider mediolaterally. The lateral condyle shows a distinct saddle shape. The lateral intercondylar tubercle comprises the inner, smooth, upturned lip of the lateral condylar “saddle”, which drops off abruptly into the continuous, U-shaped valley between the condyles. The U-shaped valley includes both the anterior and posterior intercondylar areas. The tibial tuberosity is present along the anterior margin of the diaphysis. The length of the tibial tuberosity is 20.77mm measured from the sutural line between the proximal epiphysis and the shaft to the termination of the feature just above the mid-point of the diaphysis. The tuberosity follows the medially convex curvature of the shaft. The medial margin is marked by

a thin crest of bone that is more prominent proximally. Along the proximal section of the crest is a roughened and slightly thickened area most likely serving as the origin of the soleus muscle. There is no distinct soleal line as occurs in many other mammal tibiae. Between the medial and interosseous margins there is a shallow fossa that terminates just above the mid-point of the diaphysis and just below a nutrient foramen. The interosseous margin is similar to the medial margin, as the crest of bone becomes more prominent proximally. However, the proximal portion of the interosseous margin does not show a thickening for muscle attachment. The fibular notch at the distal end of the interosseous margin is a distinct, elongated, triangular roughened area. There are two distinct lobes of bone extending downward from the medial side of the distal articular end. The smaller of these lobes is the medial malleolus, which is positioned medially. The larger lobe is positioned posteriomedially and is flanked on the medial side by a relatively large crest of bone probably corresponding to the attachment site of the flexor hallucis longus. Between the two lobes, there is a deep malleolar groove. The distal articular end is slightly wider mediolaterally (9.18mm) than it is anteroposteriorly (9.16mm).

Microstructural arrangement of the left tibia: The width of the cortex shows clear microstructural distinction between periosteal bone, primary bone, secondary bone, and endosteal bone, respectively. The primary and secondary bone occupy approximately equal widths in the cortex, whereas the periosteal and endosteal bone are thin layers on the outer and inner surfaces of the diaphysis, respectively (Figure 4.8 B, C). The coresponding layers continue circumferentially around the diaphysis. The area of secondary bone is dense with secondary osteons, indicating that there was a large amount of local remodeling during the animal's life. Primary vasculature is relatively abundant and shows highly elliptical shapes in cross-section. This indicates that the orientation of the primary vasculature is at a large angle relative to the longitudinal axis of the diaphysis.

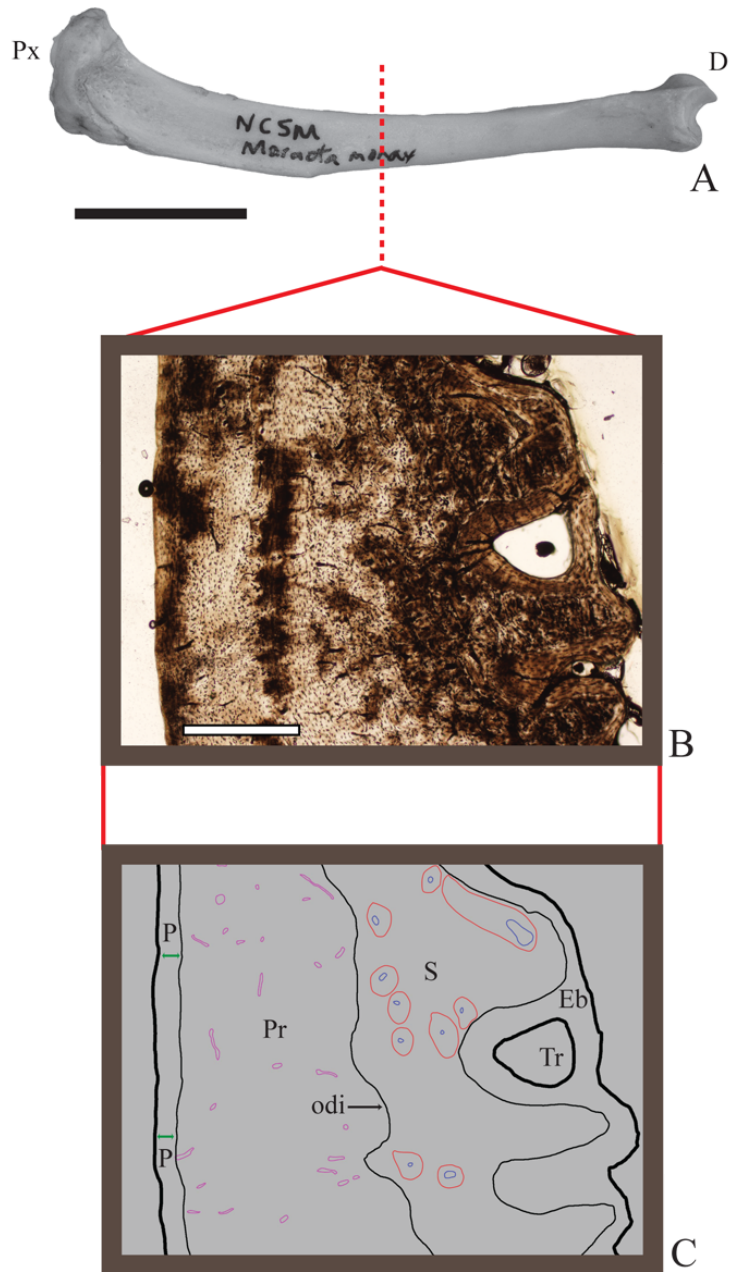


Figure 4.8: *Marmota monax* (Groundhog) tibia (A) with a corresponding micrograph showing representative microstructural arrangement (B) and schematic (C). There is an optically distinct interface between the bone of the periosteal surface, primary bone, secondary bone, and endosteal bone. Scale for (A) = 2cm. Scale for (B,C) = 0.5mm.

Castor canadensis

Family: Castoridae

Common name: American beaver

Accession number: NCSM, not cataloged

Description of the left tibia: The tibia of the beaver is an overall robust bone (Figure 4.9 A). In this specimen the total length could not be measured because the proximal epiphysis is not present. The length of the diaphysis is 107.23mm measured along the anterior margin. The open suture between the diaphysis and the distal epiphysis and the absence of the proximal epiphysis indicate a more juvenile animal. When viewed anteriorly/ventrally, the diaphysis is convex medially. The lateral side of the shaft between the anterior and interosseous margins is strongly concave, and there is a shallow fossa between the anterior and interosseous margins proximally. Viewing the shaft medially, the bone is highly convex anteriorly along the proximal half of the shaft and then becomes convex posteriorly along the second half of the diaphysis. The alternation of convexity creates a slight S-shaped curve in the shaft. The existing bone, measured at the sutural line is slightly wider mediolaterally (24.00mm) than it is anteroposteriorly (21.95mm). The tibial tuberosity is present along the anterior margin of the shaft and has a length of 58.9mm, thus terminating below the mid-point of the diaphysis. In addition to creating the anterior border for a shallow fossa on the more lateral face, the tuberosity also follows the curvature of the shaft. The medial and interosseous margins are very distinct crests of bone proximally that eventually blend into the shaft below the mid-point of the diaphysis. There is an elongate, raised, and roughened muscle attachment site located just anterior to the medial margin. This muscle attachment is suspected as the soleal line, despite the different position relative to other tibiae in this dataset. Between the medial and interosseous margins is a deep fossa that shallows below the mid-point of the diaphysis. The fibular notch is an elongate feature at the distal end of the interosseous margin. The fibular notch measures 31.76mm in length. The distal articular end is wider mediolaterally (17.76mm) than it is anteroposteriorly (16.05mm). There are two malleoli flanking the medial side of the articular surface. There seems to be no proper medial malleolus, but instead there is an anterior malleolus and a posterior malleolus. The anterior malleolus is wide and U-shaped and extends only slightly distally. The posterior

malleolus is not as wide as the anterior malleolus and extends also farther distally than that bone. The two structures are separated by a relatively deep sulcus of uniform width. This is assumed to be the malleolar groove. The anterior edge of the posterior malleolus consists of a raised but rounded portion of bone that flattens out abruptly posteriorly to give a larger surface for the attachment of flexor hallucis longus.

Microstructural arrangement of the left tibia: The width of the cortex shows clear microstructural distinction between periosteal bone, primary bone, and secondary bone. However, there is no endosteal bone present, and the secondary bone continues to the inner edge of the diaphysis. The primary bone occupies the majority of the width of the cortex. Periosteal bone appears as a distinct, thin layer along the periosteal surface. Bone remodeling is locally rare (Figure 4.9 B, C). Primary vasculature is relatively abundant, showing highly elliptical shapes in cross-section. This indicates that the orientation of the primary vasculature is at some high angle relative to the longitudinal axis of the diaphysis.

4.4.4 Order Didelphimorphia

Didelphis virginianus

Family: Didelphidae

Common name: Opossum

Accession number: NCSM 8368

Description of the left tibia: The tibia of the opossum is an overall gracile bone (Figure 4.10 A). The total length of the bone is 88.56mm. The length of the diaphysis is 74.35mm measured along the anterior margin. This specimen appears to be a sub-adult animal as evidenced by the open sutures between the diaphysis and both the proximal and distal epiphyses. When viewed anteriorly/ventrally, the shaft shows a slight S-shape. Proximally, the shaft is convex medially. The inflection point of the curvature is slightly above the mid-point of the diaphysis such that, at the mid-point of the diaphysis, the shaft is convex laterally. The proximal and distal articular ends

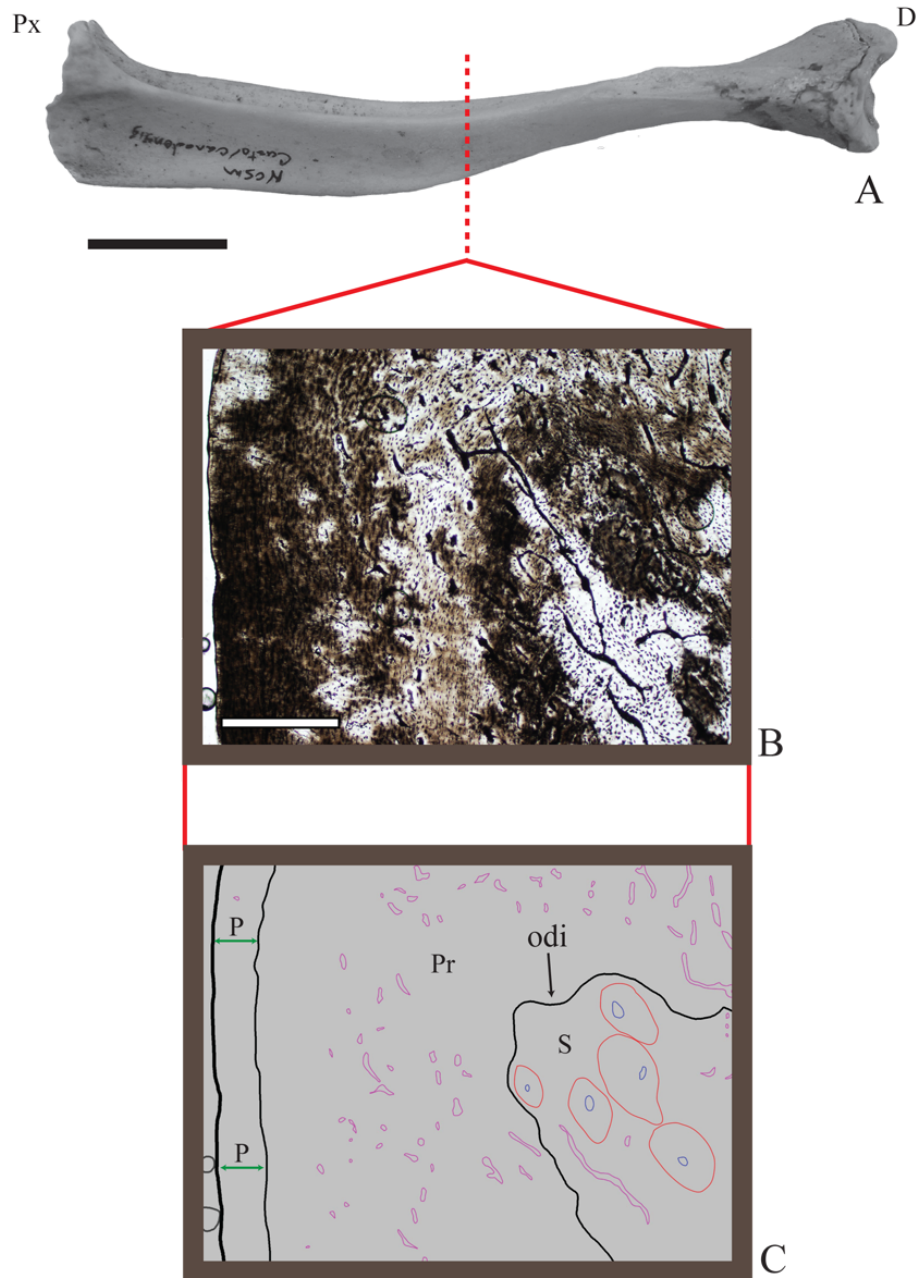


Figure 4.9: *Castor canadensis* (Beaver) tibia (A) with a corresponding micrograph showing representative microstructural arrangement (B) and schematic (C). There is an optically distinct interface between the bone of the periosteal surface, primary bone, and secondary bone; no endosteal bone is present. Scale for (A) = 2cm. Scale for (B,C) = 0.5mm.

are not off-set from each other. The proximal articular end is wider mediolaterally (13.69mm) than it is anteroposteriorly (11.57mm). The lateral condyle is slightly larger than is the medial condyle. The lateral condyle is sub-circular, whereas the medial condyle is oval with the long axis directed anteromedially. The lateral and medial intercondylar tubercles seem to have merged into one, sub-central tubercle raised into a rounded dome. There are no distinct anterior or posterior intercondylar areas. Although the tibial tuberosity is present along the anterior margin, it is not distinct from the majority of the shaft. It grades imperceptibly into the adjacent bone, which is why it cannot be measured definitively. The morphologies of the medial and interosseous margins are similar to that of the anterior margin. As in most mammals, there are distinct faces of the tibia, but they are not defined by prominent crests of bone. The proximal head of the fibula articulates in a shallow fossa between the medial and interosseous margins, and it twists slightly to articulate distally just anterior to the medial margin. The medial malleolus is a robust feature that descends in a wide U-shape. The distal articular end is wider anteroposteriorly (8.5mm) than it is mediolaterally (6.94mm).

Microstructural arrangement of the left tibia: The width of the cortex is dominated by primary bone and is divided by a visually distinct boundary. Secondary structures are rare, this section showing only a small number of secondary osteons along the endosteal surface. Periosteal bone appears as a distinct, thin layer along the periosteal surface (Figure 4.10 B, C). There is no distinct endosteal bone present in this cross-section. Primary vasculature is abundant, represented by a distinctive radial pattern of the canals around the entire circumference of the diaphysis.

4.4.5 Order Lagomorpha

Lepus americanus

Family: Leporidae

Common name: Snowshoe hare

Accession number: MCZ 60888

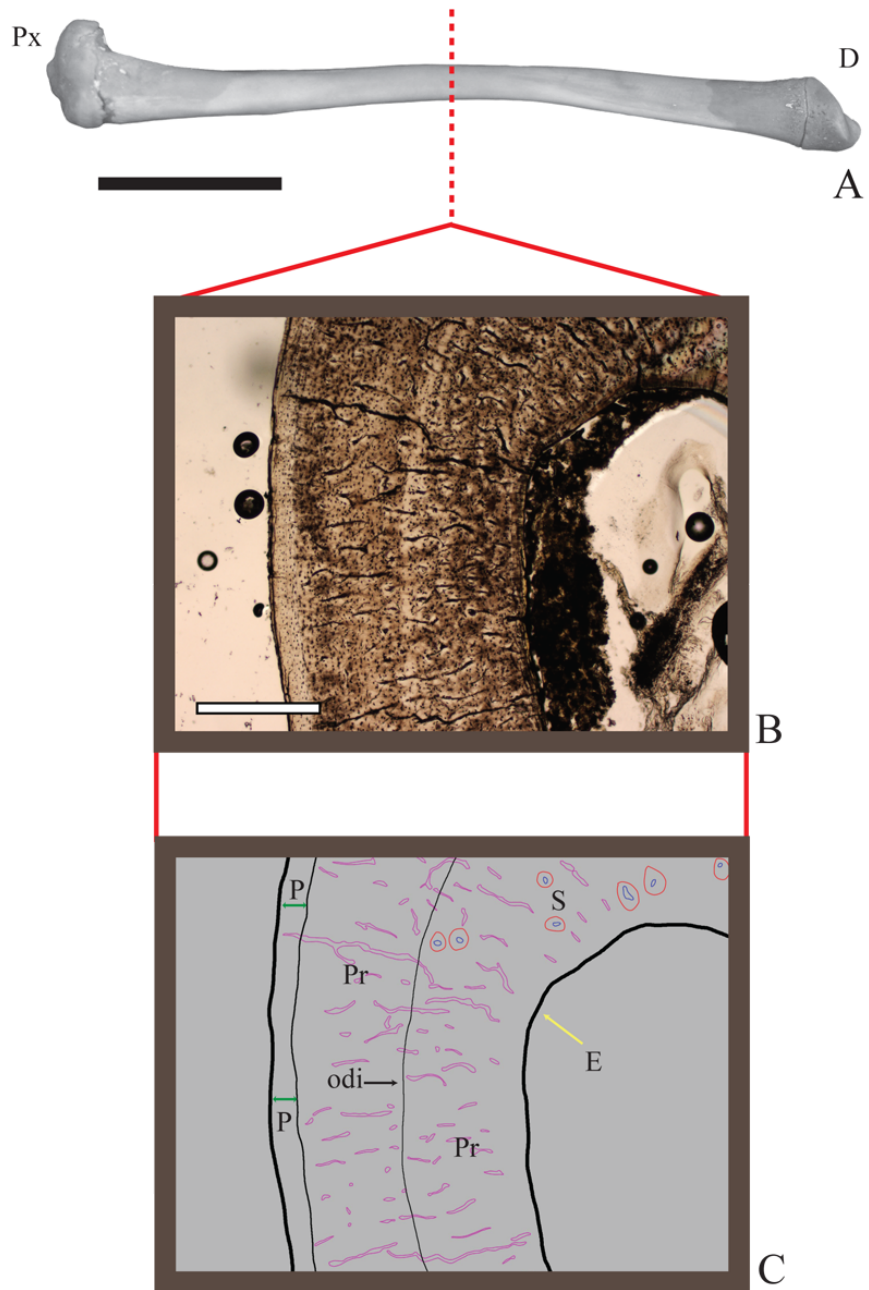


Figure 4.10: *Didelphis virginianus* (Opossum) tibia (A) with a corresponding micrograph showing representative microstructural arrangement (B) and schematic (C). Primary bone with radial primary vasculature dominates the width of the cortex. Scale for (A) = 2cm. Scale for (B,C) = 0.5mm.

Description of the left tibia: The tibia is slender and quite gracile relative to the length of the bone (Figure 4.11 A). The overall length of the tibia is 114mm, with a diaphyseal length of 102.04mm measured along the anterior margin. This specimen is mature, as the suture lines between the diaphysis and the proximal and distal epiphyses are completely obliterated. In dorsal/ventral and in medial/lateral views, the shaft is straight and generally tapers distally. The proximal and distal ends are not offset from one another. The proximal articular end is wider mediolaterally (14.31mm) than it is anteroposteriorly (13.66mm). The lateral condyle of the proximal articular end is significantly larger than the medial condyle. Both condyles are sub-ovate with long axes tilted toward the sagittal plane of the tibia. The lateral condyle shows an extended posterior lip that allows for attachment of the proximal fibula. Medial and lateral intercondylar tubercles are present and distinct as rounded ridges of bone bordering the connected anterior and posterior intercondylar areas. The lateral intercondylar tubercle is slightly larger than the medial, and the tubercles are generally directed anteroposteriorly. The tibial tuberosity is a distinct flare of bone extending 16.31mm along the proximal shaft. Immediately below the distinct flare, the tuberosity blends into the diaphysis. The anterior, medial, and interosseus margins create the typical triangular form of the tibia. Each margin is represented by a distinct ridge of bone. Along the proximal part of the posterior face of the diaphysis, there is a long, slightly raised ridge of bone that represents the soleal line. The fibula is fused to the tibia along the interosseus margin; the distal end of the fibula terminates just above the midpoint of the diaphysis. The distal articular end of the tibia is wider mediolaterally (12.14mm) than it is anteroposteriorly (8.38mm). The distal end is, thus far, distinct from that of other specimens in that it does not show a typical mammalian medial malleolus.

Microstructural arrangement of the left tibia: The secondary bone is continuous along the endosteal surface and has over-printed any primary endosteal bone that may have been present (Figure 4.11 B, C). The width of the secondary bone is not constant around the circumference of the diaphysis, and it frequently appears to be projecting as lobes into primary bone. The primary bone is highly vascularized with canals that are elliptical in shape. Secondary structures are dense, but do not appear to overlap each other greatly. Periosteal bone appears as a distinct, thin layer along the periosteal surface. There is no distinct endosteal bone present in this cross-section.

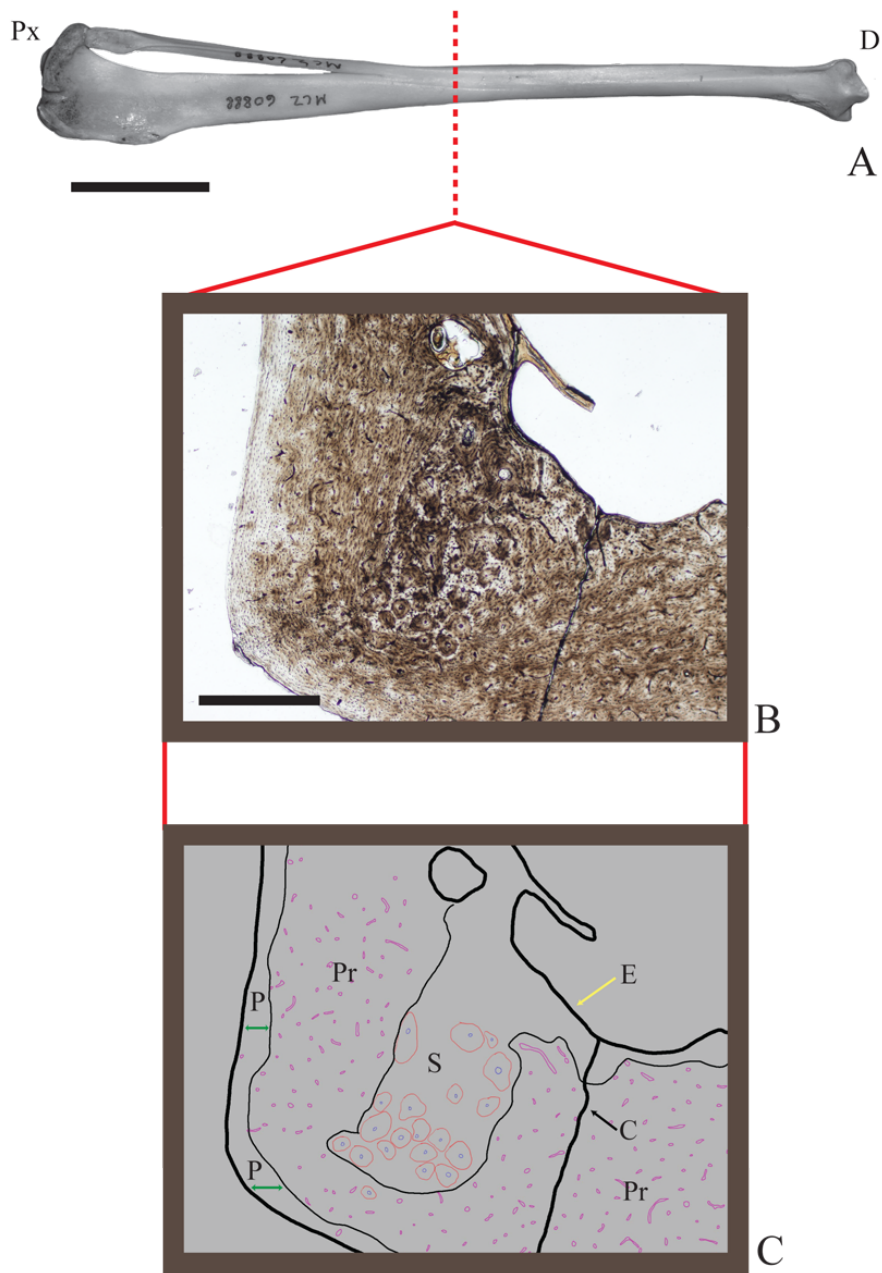


Figure 4.11: *Lepus americanus* (Snowshoe hare) tibia (A) with a corresponding micrograph showing representative microstructural arrangement (B) and schematic (C). Secondary bone is continuous along the endosteal surface, but is not constant in width; it intermingles with primary bone of the outer cortex. Scale for (A) = 2cm. Scale for (B,C) = 0.5mm.

4.4.6 Order Primates

Varecia variagata variagata

Family: Strepsirrhini

Common name: Ruffed lemur

Accession number: MCZ 59274

Description of the left tibia: The shaft is slender and of approximately equal circumference along its length (Figure 4.12 A). The shaft only changes width at the proximal and distal ends to accommodate the epiphyses. The total length of the tibia is 137.32mm, with a diaphyseal length of 116.55mm measured along the anterior margin. No suture lines are visible, indicating that this specimen is mature. In a ventral/dorsal view the shaft is straight, but a medial/lateral view shows the tibia is convex toward the anterior margin. The proximal and distal epiphyses are not offset from one another. The proximal articular end is wider mediolaterally (19.24mm) than it is dorsoventrally (16.26mm). The medial condyle of the proximal articular end is significantly larger than the lateral condyle. Both condyles are sub-ovate, with their long axes tilted toward the sagittal plane of the tibia. Whereas the medial condyle is convex for articulation with the femur, the lateral condyle is only slightly convex. The medial and lateral intercondylar tubercles have merged together to form one tubercle located centrally between the condyles. The tubercle is a raised, rounded bump of bone that separates the distinct anterior and posterior intercondylar areas. The tibial tuberosity is not prominent on the diaphysis, the tuberosity taking the form of a slightly raised, flattened surface for muscle attachment. Whereas the anterior margin of the tibia is distinguished by a sharp ridge of bone, the medial and interosseous margins are less distinctive and highly rounded. On the proximal, posterior part of the shaft, the soleal line is visible as a slightly raised, sharp ridge of bone tilted such that the proximal extent of the muscle scar points medially. The distal articular end is wider mediolaterally (13.48mm) than it is dorsoventrally (11.02mm). The medial malleolus is a prominent, U-shaped, distal extension of bone. The malleolar groove is shallow. On the lateral side of the distal articular end there is a distinct, fibular notch in the shape of a half-circle.

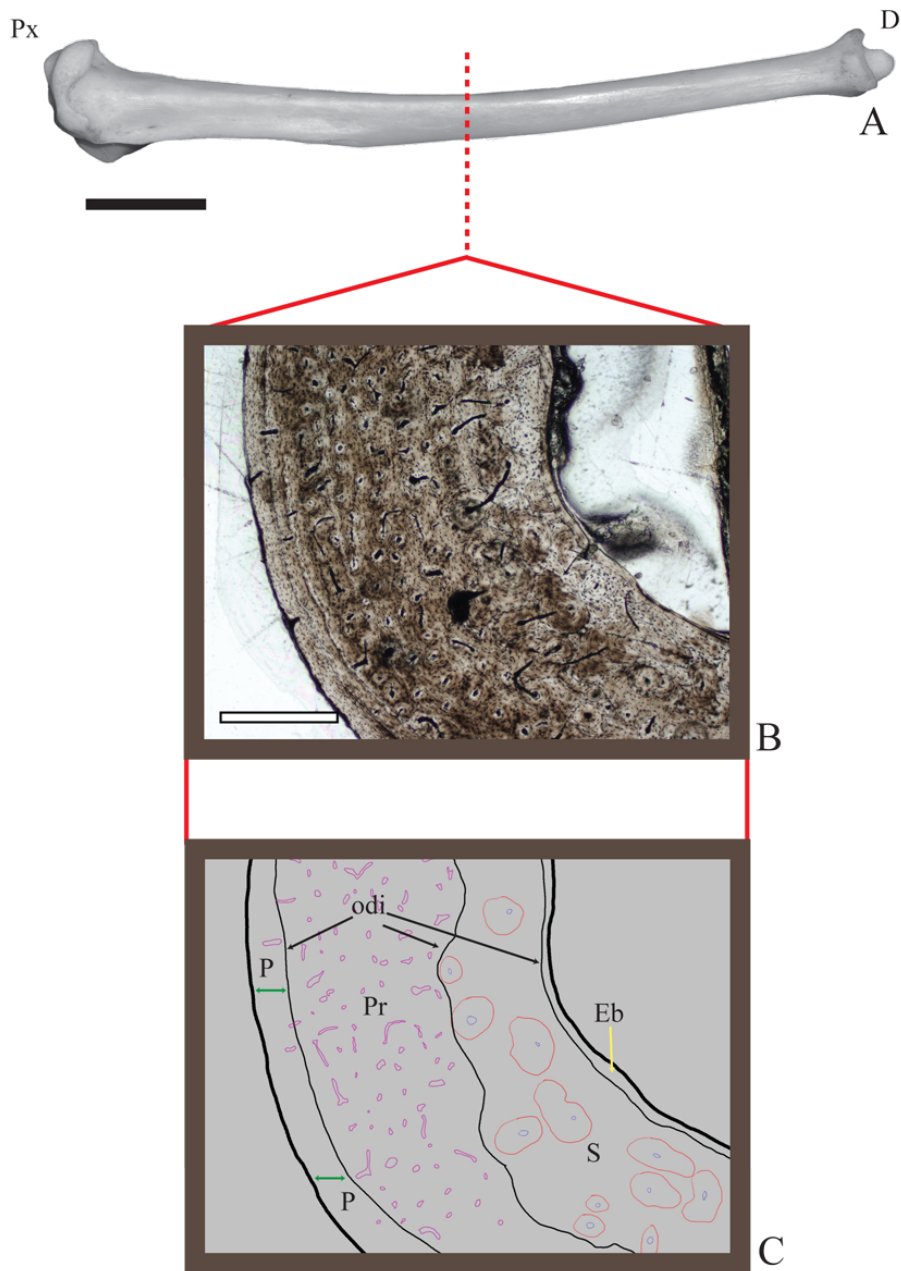


Figure 4.12: *Varecia variegata variegata* (Lemur) tibia (A) with a corresponding micrograph showing representative microstructural arrangement (B) and schematic (C). Showing almost a quintessential “textbook” bone microstructural arrangement, a thin layer of periosteal bone flanks the outer edge of the diaphysis followed inwardly by regular widths of primary, secondary, and endosteal bone. Scale for (A) = 2cm. Scale for (B,C) = 0.5mm.

Microstructural arrangement of the left tibia: The microstructural arrangement in the lemur has a very “textbook” appearance (Figure 4.12 B, C). Along the outer edge of the diaphyseal cross-section, a thin layer of periosteal bone signals continuing bone growth. This feature is separated distinctly from primary bone, which is approximately 0.5mm thick. An equal width of secondary bone is just inside of the primary layer, and the endosteal surface is bounded by a thin layer of endosteal bone. All layers continue circumferentially around the cortex, maintaining the same arrangement. The primary bone is highly vascularized, with canals that are of various shapes. Secondary structures are dense, and show some overlap with each other.

Macaca mulatta

Family: Cercopithecidae

Common name: Rhesus monkey

Accession number: MCZ 64360, First Series

Description of the left tibia: The shaft is of approximately equal circumference along its length, but tapers slightly towards the distal end (Figure 4.13 A). The total length of the tibia is 134.77mm, with a diaphyseal length of 107.67mm measured along the anterior margin. Faint suture lines are still visible on the distal end, although the distal epiphysis is fully ossified to the diaphysis. In contrast, the epiphysis is not fully ossified to the diaphysis at the proximal end, indicating that this is a sub-mature specimen. In a dorsal/ventral view, the shaft is convex towards the medial side. In a lateral/medial view, the shaft is convex ventrally (anteriorly). The proximal and distal articular ends are slightly offset from one another because of this shaft curvature. The proximal articular end is wider mediolaterally (21.39mm) than it is dorsoventrally (15.58mm). The lateral condyle is only slightly larger than the medial condyle due to its more circular shape as compared to the ovate form of the medial condyle. Both condyles show a concave articular surface and condyle long axes that are dorsoventral in orientation. The lateral and medial intercondylar tubercles are of the same morphology on both the medial and lateral condyles. They show raised, sharp ridges of bone directed dorsoventrally and connected across the intercondylar sulcus by a ridge of bone perpendicular to them. The ridges of bone

create an “H”. There are distinct anterior and posterior intercondylar areas. The tibial tuberosity lies close to the shaft and emerges from the proximal articular end as an anteriorly flattened feature. The muscle scarring is distinct and follows the curve of the shaft. The scarring terminates 43.76mm from the proximal articular end. The interosseus margin is the most distinct of all margins, shown by a raised ridge of bone. The anterior and medial margins are clearly identifiable, but are rounded in form. The soleal line is very faint, extending distally to terminate at the midpoint of the diaphysis. The medial malleolus is prominent and square, with the anterior and distal-most corner slightly longer than the other corner. The malleolar groove is shallow. On the lateral side of the distal articular end a shallow groove is present for the articulation of the fibula.

Microstructural arrangement of the left tibia: There is a single layer each of primary and secondary bone of almost equal widths ($\tilde{0}.5$ millimeters) in cross-section (Figure 4.13B, C). The primary bone is located along the periosteal edge, but no periosteal bone is evident. In contrast, a thin layer of endosteal bone bounds the endosteal surface. All layers, in the same arrangement, continue circumferentially around the cortex. The primary vascularization is rare, only six canals evident in this cross-section. Secondary structures are dense, and show some overlap with each other.

Cebus sp.

Family: Cebidae

Common name: Capuchin monkey

Accession number: MCZ BOM 438

Description of the left tibia: The left tibia of BOM 438 has attached to it the distal epiphysis of the femur, accompanied by extensive remnants of cartilage and ligaments (Figure 4.14 A). The morphology of the proximal articular end of the tibia is masked by the presence of the femoral epiphysis. Museum guidelines prohibit additional destructive altering of specimens beyond what was agreed upon when the loan was granted. The removal of the femoral epiphysis would violate the terms of the loan

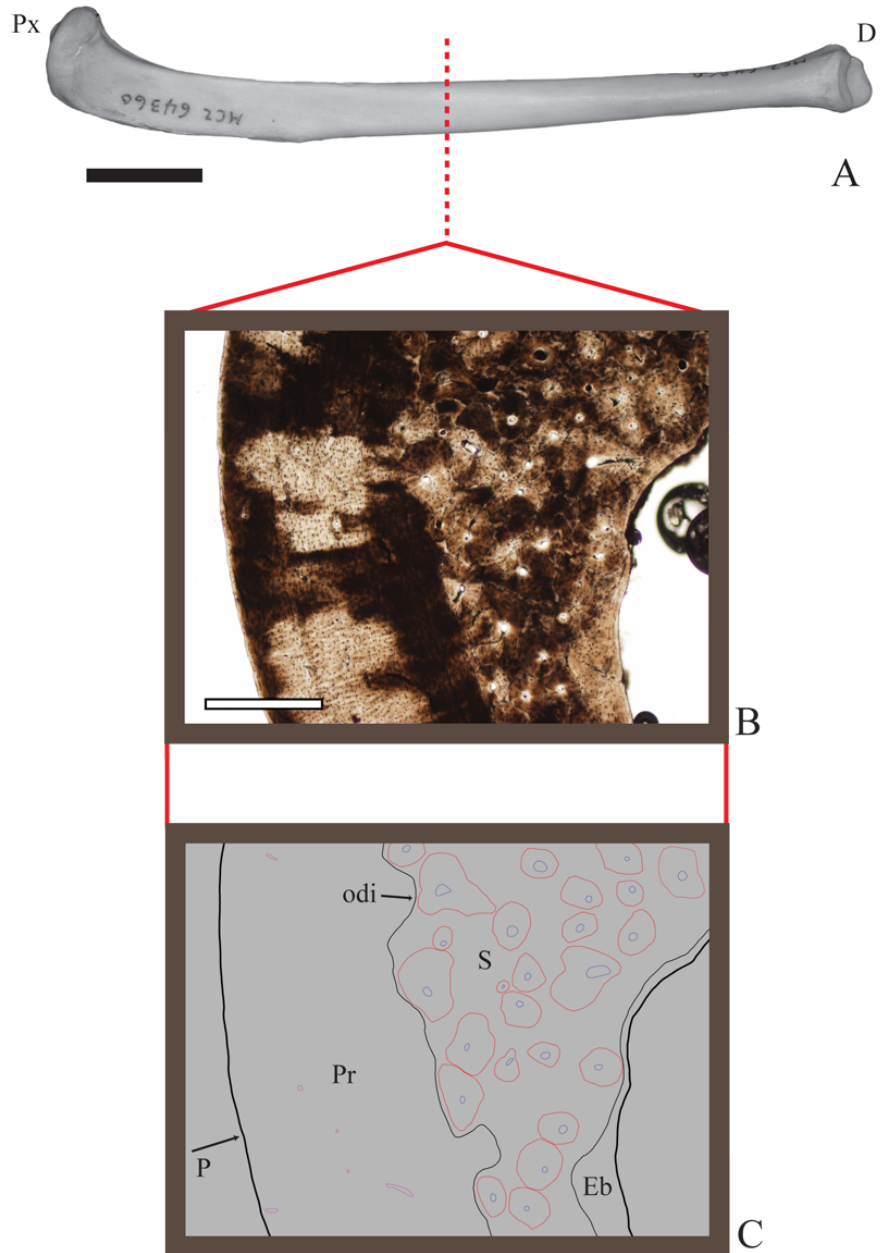


Figure 4.13: *Macaca mulatto* (Rhesus monkey) tibia (A) with a corresponding micrograph showing representative microstructural arrangement (B) and schematic (C). A single layer each of primary and secondary bone dominate the thin-section. A thin layer of endosteal bone flanks the inner edge of the diaphysis, but there is not a distinct layer of periosteal bone on the outer edge of the cortex. Scale for (A) = 2cm. Scale for (B,C) = 0.5mm.

agreement. For the description of *Cebus sp.*, the morphology of the proximal articular end of the tibia will be described from the right tibia. All other parts of the description, including that of the distal articular end, are sourced from the left tibia.

The gracile tibial shaft tapers gradually toward the distal end. The total length of the tibia is 103.86mm, with a diaphyseal length of 84.58mm measured along the anterior margin. Suture lines are prominent on the proximal and distal ends, indicating that this is a sub-mature specimen. In a dorsal/ventral view the shaft is convex towards the medial side. The proximal and distal articular ends are slightly offset from one another because of this shaft curvature. In a lateral/medial view the shaft is convex ventrally (anteriorly). The proximal articular end of the left tibia is wider mediolaterally (17.51mm) than it is dorsoventrally (13.42mm). On the right tibia, the proximal lateral condyle is slightly larger than the medial condyle. Both condyles show ovate, concave articular surfaces. The long axes of the medial and lateral condyle are oriented dorsoventrally. The intercondylar tubercles are not visible on the right tibia because of remnant cartilage and ligaments. However, distinct anterior and posterior intercondylar areas are visible as shallow fossae that define a portion of the condyle borders. The tibial tuberosity is not prominent and blends into the shaft, emerging from the proximal articular end as an anteriorly flattened feature. The total length of the tuberosity is approximately 1/4 the total shaft length. The interosseus margin is the most distinct of all margins, shown by a raised ridge of bone. The anterior and medial margins are clearly identifiable, but are rounded in form. There is no evidence of a soleal line. The medial malleolus is prominent and quadrilateral with the anterior and distal-most corner slightly longer than the other corner. On the lateral side of the distal articular end, a shallow, crescent-shaped groove is present for the articulation of the fibula.

Microstructural arrangement of the left tibia: The microstructural arrangement in the capuchin monkey tibia has a very “textbook” appearance, similar to that of the ruffed lemur (Figure 4.14 B, C). Along the outer edge of the diaphyseal cross-section, a thin layer of periosteal bone flanks the outer edge of the cortex, followed inwardly by approximately equal widths of primary and secondary bone. Unlike in the lemur, the microstructural arrangement here does not have an optically discernable interface between the primary and secondary bone layers. On the inner edge of the cortex, the endosteal surface is bounded by a thin layer of endosteal bone. All layers, in

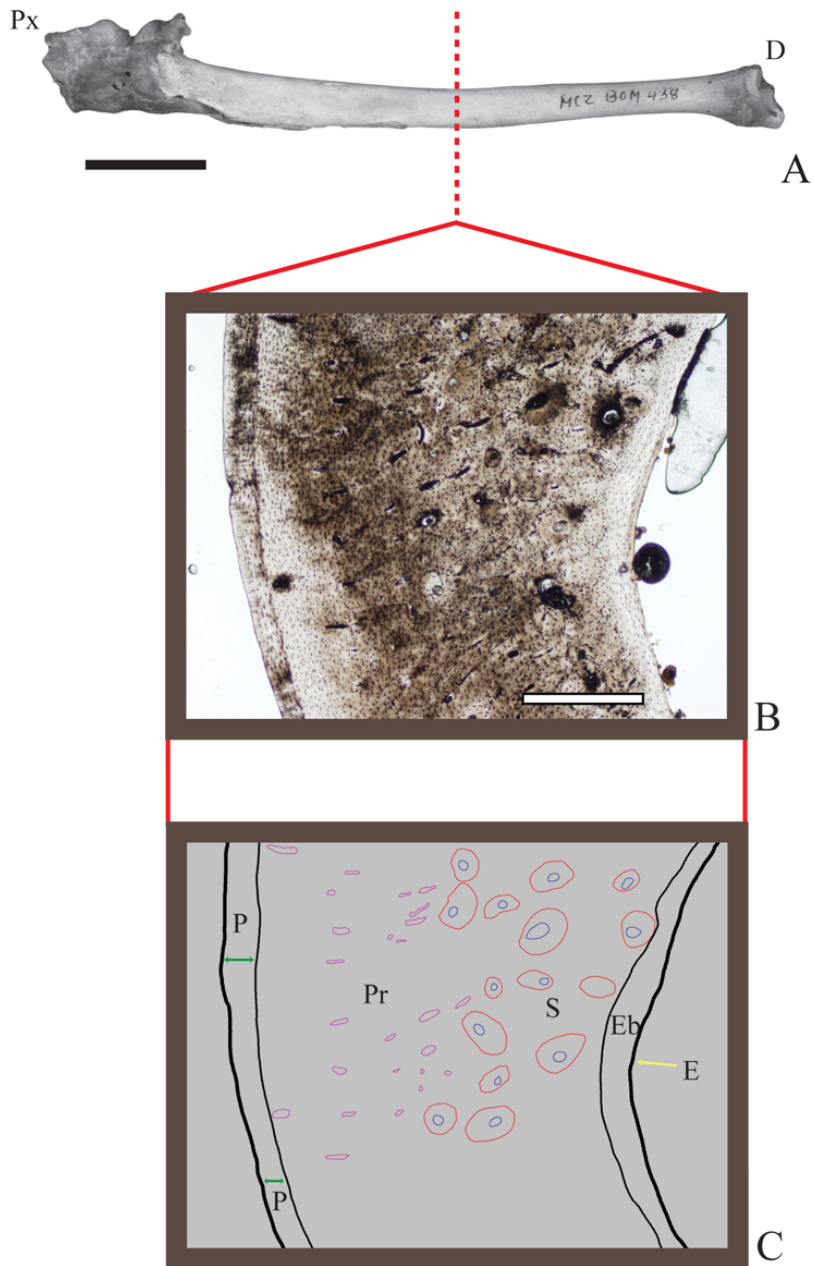


Figure 4.14: *Cebus sp.* (Capuchin monkey) tibia (A) with a corresponding micrograph showing representative microstructural arrangement (B) and schematic (C). There is a “textbook” example of mammalian microstructural arrangement. A distinct layer of periosteal bone caps the outer edge of the cortex, followed inwardly by equal widths of primary and secondary bone, without an optically distinct interface between. A thin layer of endosteal bone flanks the inner edge of the diaphysis. Scale for (A) = 2cm. Scale for (B,C) = 0.5mm.

their arrangements continue circumferentially around the cortex. The primary bone is highly vascularized, revealing canals that are of mainly elliptical shapes, which signals that the primary vasculature is at some high angle to the longitudinal axis of the diaphysis. Secondary structures are numerous, but do show overlap with each other.

4.5 Intra-skeletal and Intra-bone Variation

The previous comparisons of 11 mammals focused on the same selected bone in all specimens. The next-order question is whether the cortex of any or all bones in the skeleton would yield the same taxon-specific signature in its bone microstructure. The literature review presented in Chapter 1 revealed that there is little known about the microstructural variation within a single skeleton or within a single bone (Enlow and Brown, 1956, 1957, 1958). Whereas some innate variation is expected within the skeletal elements of a particular taxon, too much variation could seriously limit the use of the method presented in this dissertation in future endeavors. Comprehensive analysis of variation within a single skeleton is a huge undertaking and beyond the scope of this project. Instead, two case-studies in skeletal variation were developed to address the critical issues in intra-skeletal variation discussed above. The full skeleton of a wild extant mammal was desired, but could not be obtained on loan through a museum. The author therefore acquired from the Missouri Department of Transportation a specimen of *Odocoileus virginianus* (white-tailed deer).

4.5.1 *Odocoileus virginianus*

Order: Artiodactyla

Family: Cervidae

Common name: White-tailed deer

It is estimated that there are over 1 million white-tailed deer in Missouri (Figure 4.3), a portion of which have contributed to over 3000 deer-vehicular accidents each year.

A young doe killed in a highway collision in November, 2005 satisfied the necessity for a complete mammalian specimen that would allow analysis of intra-skeletal and intra-bone microstructural variation (see Chapter 7) to augment the Primary Dataset.

The deer was prepared by the author at Tyson Research Center at Washington University in Saint Louis. Preparation included skinning, gutting, and removal of desired bones. Only the appendicular skeleton, ribs, and mandible were retained (Figure 4.15, Figure 4.16, Figure 4.17, and Figure 4.18). Additional treatment of the skeleton included submersing the bones in simmering water for four hours to remove any remaining tissue and fat on and within the bone. Whereas this is a gentle process and does not affect the bone microstructure, failure to do so would result in bone rancidity. After simmering, bones were air-dried for one week before being moved to appropriate storage and labeled. Unfortunately, the only damage to the skeleton as a result of the vehicular accident was to the left tibia, preventing the deer from inclusion in the Primary Dataset.

The doe was determined to be approximately two years old by mandibular tooth pattern analysis (Figure-Mandible) and was subsequently categorized as a young adult. The age of two years was indicated by fully erupted permanent molars I-III, the loss of the “milk” premolars, and the eruption of permanent premolar III. Full eruption of premolars I-III occurs at an age of two and one-half years.

Complete skeletal and microstructural descriptions of the specimen are beyond the scope of this dissertation. Instead, only the arrangement of the microstructural features of the bones used in the case-studies for intra-bone and intra-skeletal variation are described in detail. The bones that are not addressed in this thesis will be used in future analyses of bone microstructural variation.

4.5.2 Variation Datasets

The datasets analyzed in the case studies of intra-skeletal and intra-bone microstructural variation are focused on the ribs of *Odocoileus virginianus*. The ribs were chosen for analysis because (1) during formation, the ribs undergo intramembranous ossification, unlike the bones of the appendicular skeleton, such as the tibiae in the Primary

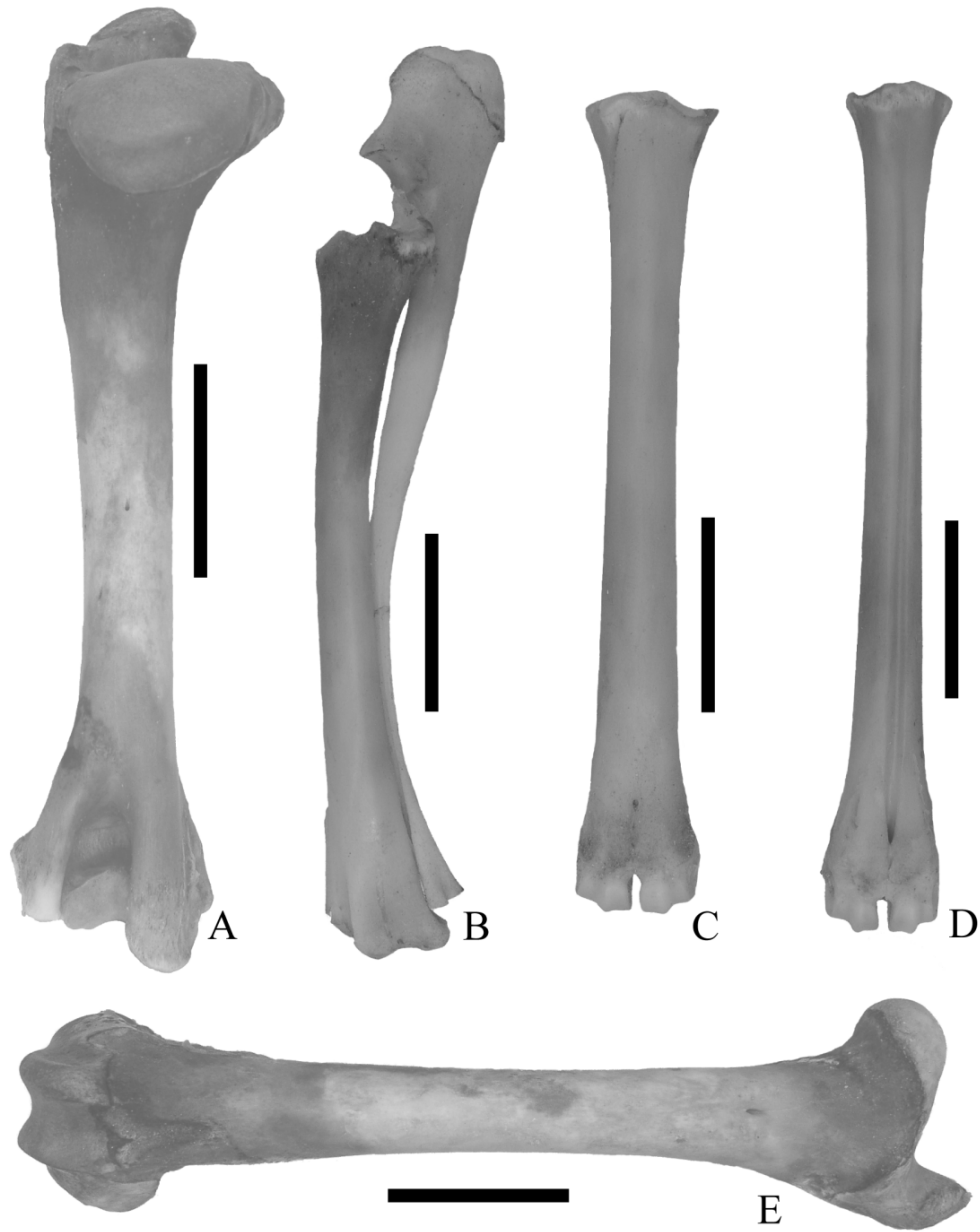


Figure 4.15: The long bones of the left portion of the appendicular skeleton of the specimen of *Odocoileus virginianus* used in this study. The forelimb includes the humerus (A), radius and ulna (B), and metacarpal (C). The hindlimb includes the metatarsal (D) and femur (E). The left tibia was shattered in the deer-vehicular accident. Scale = 5cm.

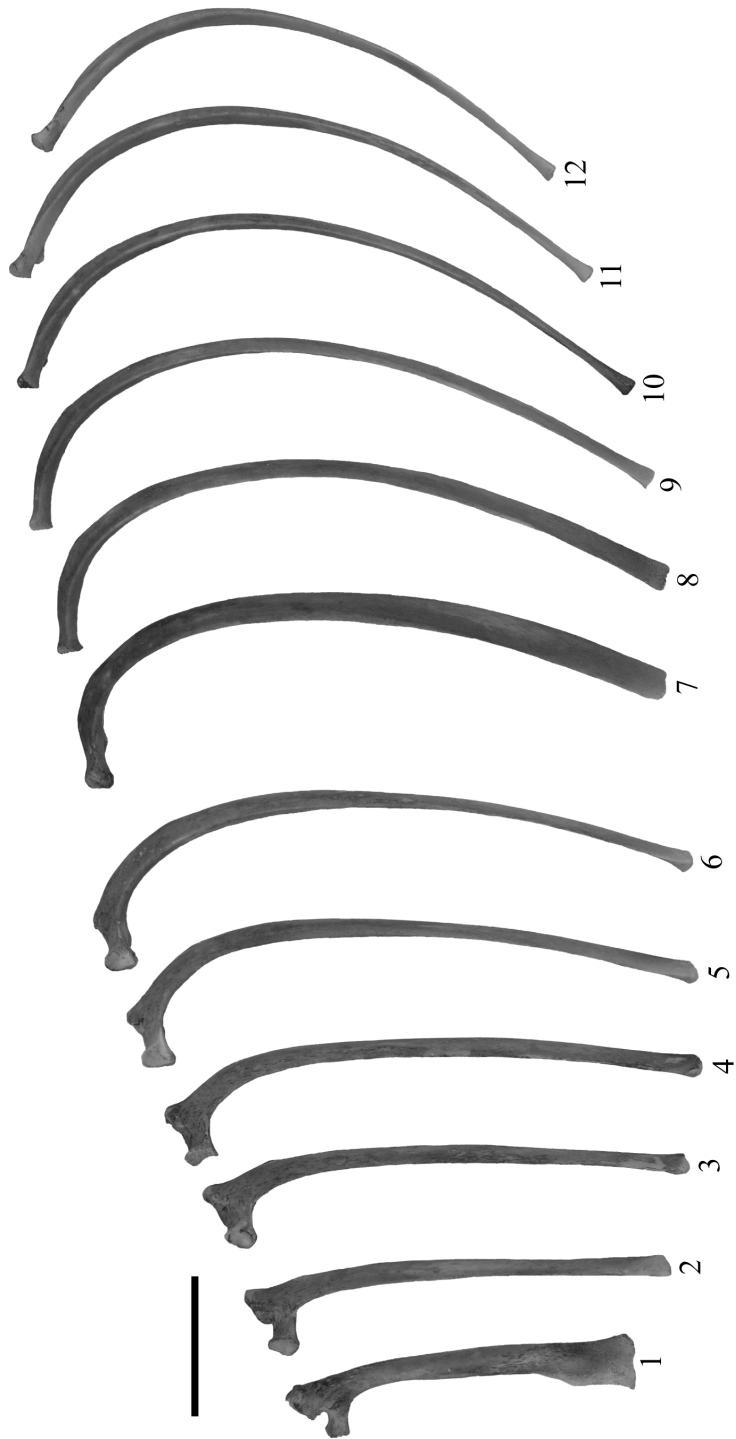


Figure 4.16: Left ribs of the *Odocoileus virginianus* specimen used in the current study. Rib 1 is the anterior-most rib in the series. Scale = 5cm.

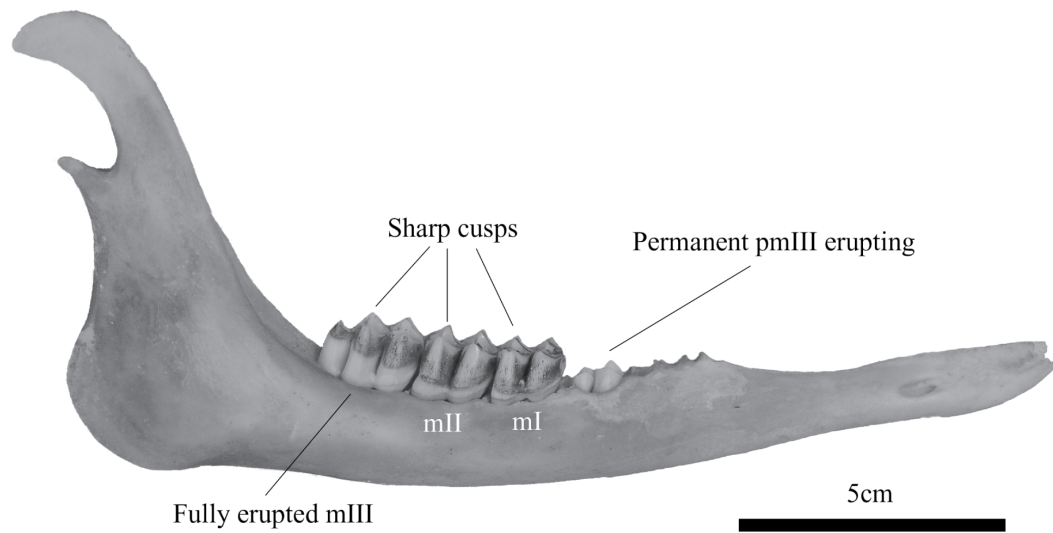


Figure 4.17: Right mandible of the *Odocoileus virginianus* specimen used in this study. The tooth patterning indicates that the specimen was approximately 2 years old at the time of death, as evidenced by fully erupted molars I-III with sharp cusps, the loss of the “milk” premolars, and the not yet fully erupted permanent premolar III.

Element	Side	Length (mm)	Element	Side	Length (mm)
Humerus	left	142	Rib1	left	122
	right	141		right	122
Radius	left	191	Rib 2	left	149
	right	189		right	149
Ulna	left	218	Rib 3	left	171
	right	218		right	171
Metacarpal	left	177	Rib 4	left	188.5
	right	176		right	190
Forelimb phalanx I	lateral	36	Rib 5	left	210
	medial	38		right	213
Forelimb phalanx II	lateral	23	Rib 6	left	231
	medial	26.5		right	231
Forelimb phalanx I	lateral	38	Rib 7	left	253
	medial	38		right	252
Forelimb phalanx II	lateral	23	Rib 8	left	266
	medial	23		right	264
Femur	left	207	Rib 9	left	270
	right	206.5		right	268.5
Tibia	left	broken	Rib 10	left	245
	right	240		right	258
Metatarsal	left	211	Rib 11	left	220
	right	212		right	247
Hindlimb phalanx I	lateral	41	Rib 12	left	178.5
Left	medial	41		right	223.5
Hindlimb phalanx II	lateral	28			
Left	medial	25			
Hindlimb phalanx I	lateral	40			
Right	medial	41			
Hindlimb phalanx II	lateral	26			
Right	medial	28			

Figure 4.18: Rib body and diaphyseal measurements of the appendicular skeleton of the *Odocoileus virginianus* specimen used in the current project. The diaphyses of long bones were measured between the proximal and distal epiphyseal sutures along the anterior portion of the bone shaft.

Dataset, which form by endochondral ossification, (2) ribs do not bear weight, (3) the ribs are serially repeated bones, and (4) ribs and rib fragments are abundant in the fossil record, yet have been deemed of little taxonomic value. Analysis of the ribs for microstructural variation acknowledges the possibility of microstructural differences between bones of different formation processes as well as between weight-bearing and non-weight-bearing bones. As serially repeated skeletal elements, ribs offer the chance to examine “closely related” bones in order to detect any variation. For example, if there is a great amount of variation among the ribs of the white-tailed deer, it would be reasonable to hypothesize that a comparison between the other bones in the skeleton would likewise yield high microstructural variability. Ribs are of particular interest to the current study because of the abundance of this skeletal element in the fossil record. The gross morphology of the rib body shows a “piscis” or pointed oval geometry in cross-section, allowing even small fragments to be identified as ribs. Unfortunately, the gross morphology of even a complete rib holds little taxonomic value, and the rib rarely can be identified taxonomically in the absence of more distinctive skeletal elements. The outcome of the current study on the variation of bone microstructure within the deer ribs will indicate the applicability of the microstructural technique to fossil rib fragments and guide the continuation of intra-skeletal analysis of microstructural variation.

All rib bodies were measured to determine where the bones would be cut (Figure 4.19 A). The mid-body of the rib was determined as equidistant from the proximal and distal ends of the bone (Figure 4.19 B) and four additional cuts divided the remaining rib body into equal sections.

Dataset I: Intra-skeletal Variation

Microstructural features from the mid-body (cut 3) of left ribs 2-12 were compared in order evaluate intra-skeletal variation. The distribution, proportions, and arrangement of the microstructural features within the primary and secondary bone of each mid-body thin-section was similar. A representative sample is illustrated using left rib 7 in Figure 4.20. In all micrographs, the periosteal surface of the rib appears on the left side of the micrograph.

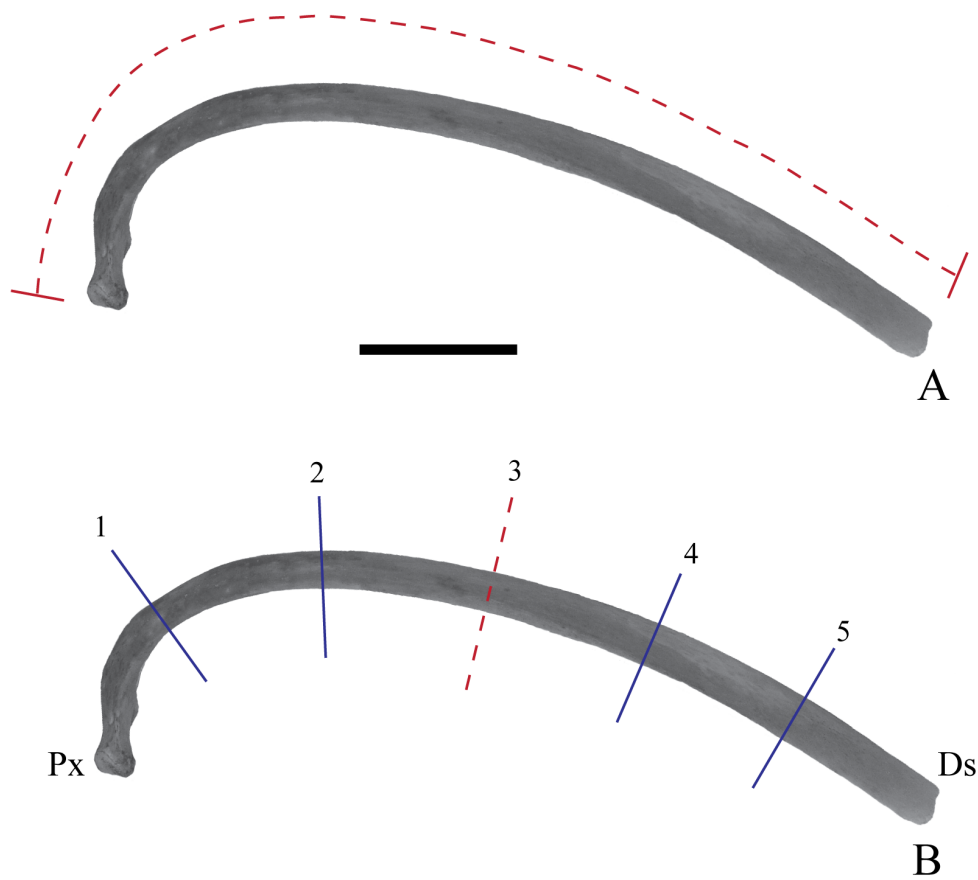


Figure 4.19: *Odocoileus virginianus* left rib 7. The total length of the rib body (red, dotted line) was measured before determination of cut placement (A). Cut three is the mid-point of the rib body, equidistant from the proximal and distal ends (B). The other four cuts divide the rib equally and are made perpendicular to the rib body. Scale = 5cm.

Microstructural arrangement of *Odocoileus virginianus* left Rib 7, Cut 3: Primary and secondary bone occupy equal widths within the cortex. There is no distinct periosteal bone along the outer edge of the rib body cross-section, although primary bone is clearly identifiable on the outer part of the cortex. There are two visually distinct interfaces in the cross-section, one within the primary bone and the other between the primary and secondary bone layers. All layers and their arrangement continue circumferentially around the cortex. The primary bone is moderately vascularized with canals that are mainly circular and somewhat elliptical, signaling that the primary vasculature is at some small angle to the longitudinal axis of the rib body. Secondary structures are numerous, but do not overlap each other.

Dataset II: Intra-bone Variation

Arrays of microstructural features in the thin-sections made from the five cuts along *Odocoileus virginianus* left rib 7 were compared in order to evaluate intra-bone variation. The arrangement of the microstructural features throughout left rib 7 are described below.

Microstructural arrangement of *Odocoileus virginianus* left Rib 7, Cut 1: Primary and secondary bone occupy equal widths within the cortex (Figure 4.21 B,C). There is no distinct periosteal bone along the outer edge of the rib body cross-section, although primary bone is identified on the outer part of the cortex. There is one visually distinct interface in the cross-section, which divides the primary from the secondary bone layer. All layers and their arrangement continue circumferentially around the cortex. The primary bone is moderately vascularized with canals that are mainly circular to slightly elliptical, signaling that the primary vasculature is at some small angle to the longitudinal axis of the rib body. Secondary structures are numerous and show significant overlap with each other.

Microstructural arrangement of *Odocoileus virginianus* left Rib 7, Cut 2: The secondary bone occupies double the width that the primary bone does (Figure 4.22 B,C). There is no distinct periosteal bone along the outer edge of the rib body cross-section, although primary bone is identified on the outer part of the cortex. All layers and their arrangement continue circumferentially around the cortex. The primary bone is

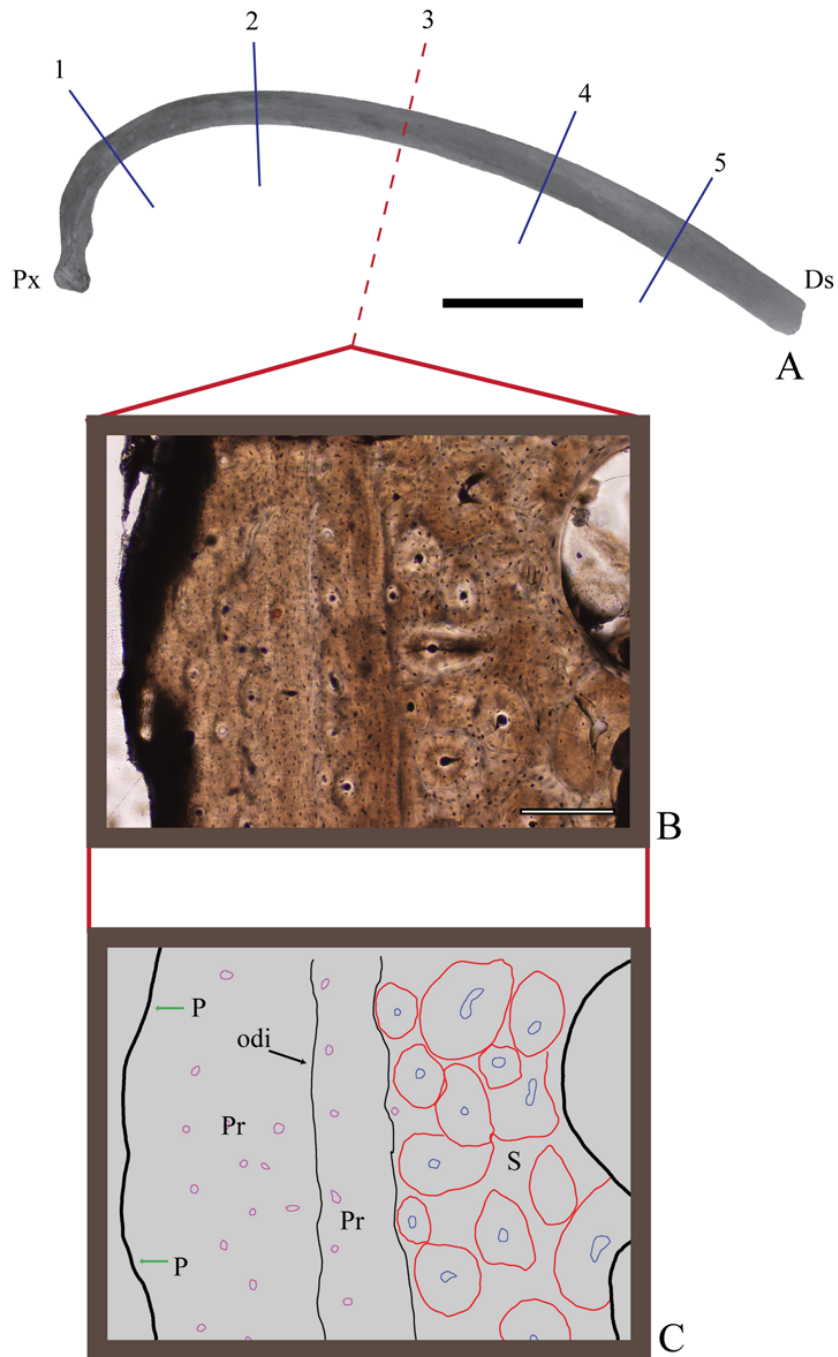


Figure 4.20: *Odocoileus virginianus* left rib 7 (A) with a corresponding micrograph showing representative microstructural arrangement of Cut 3 (B) and a schematic (C). Sub-equal widths of primary and secondary bone occupy the cortex. The cortex is generally very vascularized. Scale for (A) = 5cm. Scale for (B,C) = 0.2mm.

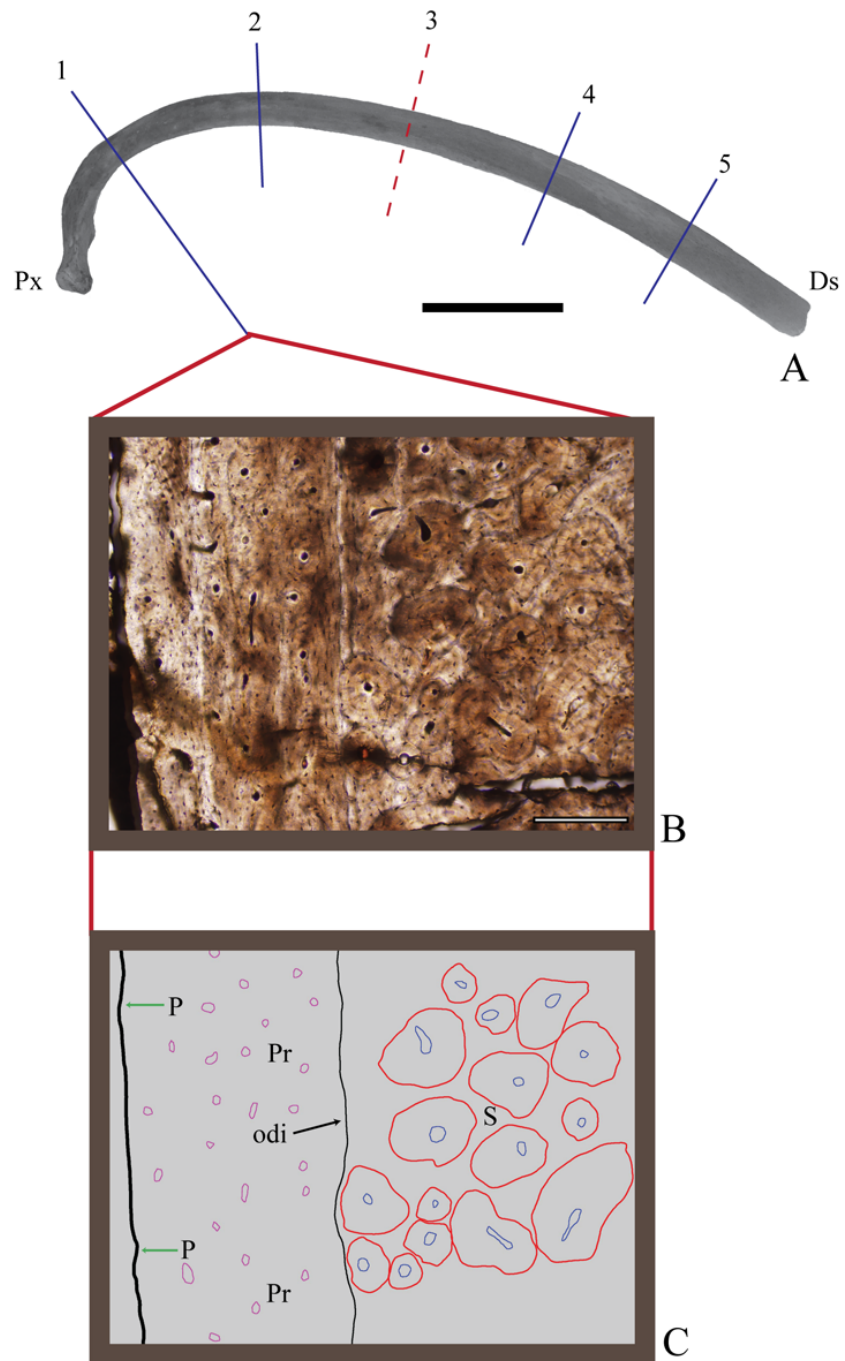


Figure 4.21: *Odocoileus virginianus* left rib 7, (A) with a corresponding micrograph showing representative microstructural arrangement of Cut 1(B) and a schematic (C). Sub-equal widths of primary and secondary bone occupy the cortex. There is no distinct periosteal bone. Scale for (A) = 5cm. Scale for (B,C) = 0.2 mm.

poorly vascularized, with canals that are mainly circular, signaling that the primary vasculature is parallel to the longitudinal axis of the rib body. Secondary osteons are numerous and show significant overlap with each other.

Microstructural arrangement of *Odocoileus virginianus* left rib 7, cut 3: see subsection: Intra-skeletal variation and Figure 4.20.

Microstructural arrangement of *Odocoileus virginianus* left rib 7, cut 4: Primary and secondary bone occupy equal widths within the cortex (Figure 4.23 B,C). There is no distinct periosteal bone along the outer edge of the rib body cross-section, although primary bone is identified on the outer part of the cortex. There is one visually distinct interface in the cross-section, which divides the primary from the secondary bone layer. All layers and the arrangement continue circumferentially around the cortex. The primary bone is moderately to highly vascularized, with canals that are mainly circular, signaling that the primary vasculature is parallel to the longitudinal axis of the rib body. Secondary structures are present, but do not overlap each other.

Microstructural arrangement of *Odocoileus virginianus* left rib 7, cut 5: Primary and secondary bone occupy equal widths within the cortex (Figure 4.24 B,C). There is no distinct periosteal bone along the outer edge of the rib body cross-section, although primary bone is identifiable on the outer part of the cortex. All layers and the arrangement continue circumferentially around the cortex. The primary bone is poorly vascularized. Secondary osteons are present, but do not overlap each other.

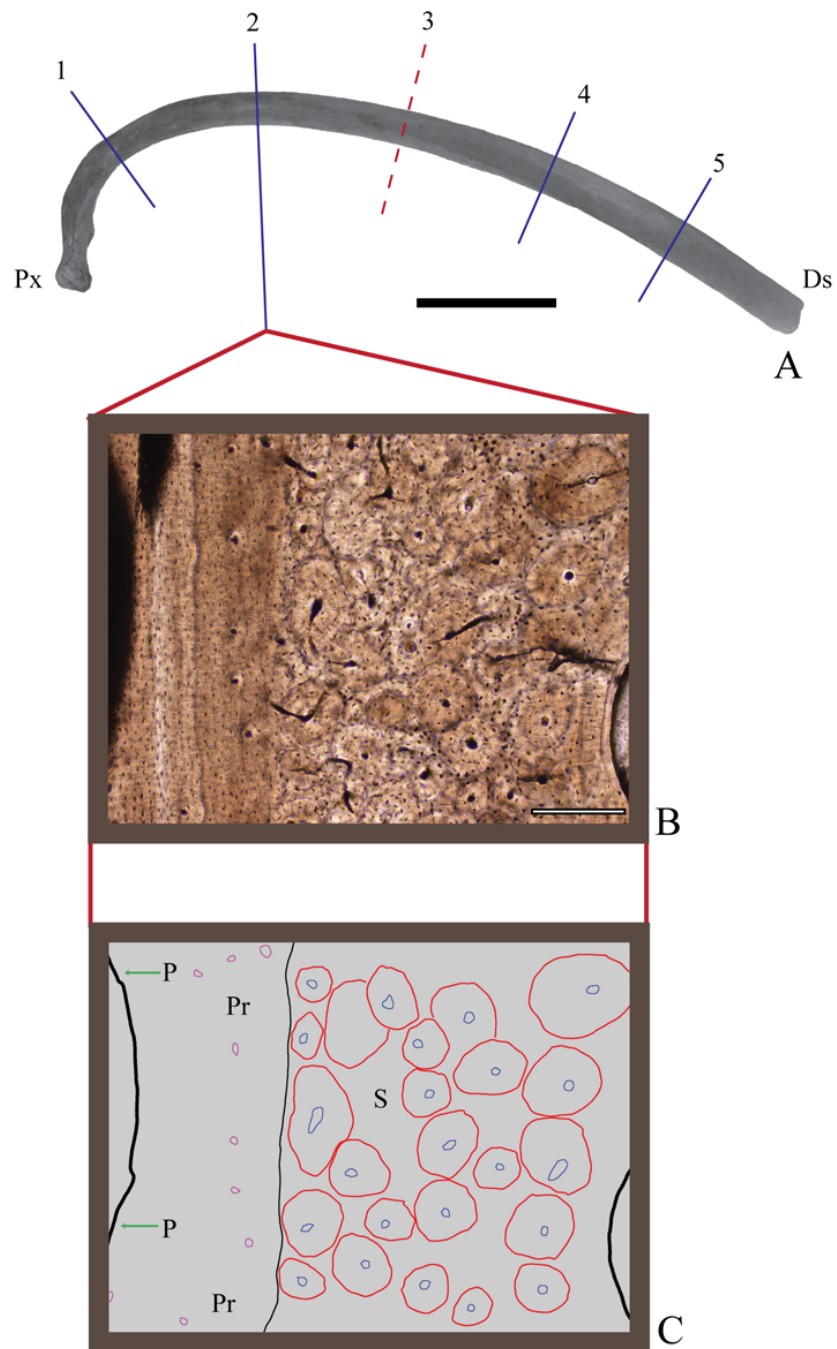


Figure 4.22: *Odocoileus virginianus* left Rib 7 (A) with a corresponding micrograph showing representative microstructural arrangement of Cut 2 (B) and a schematic (C). Secondary bone makes up double the width of the primary bone. Scale for (A) = 5cm. Scale for (B,C) = 0.2mm.

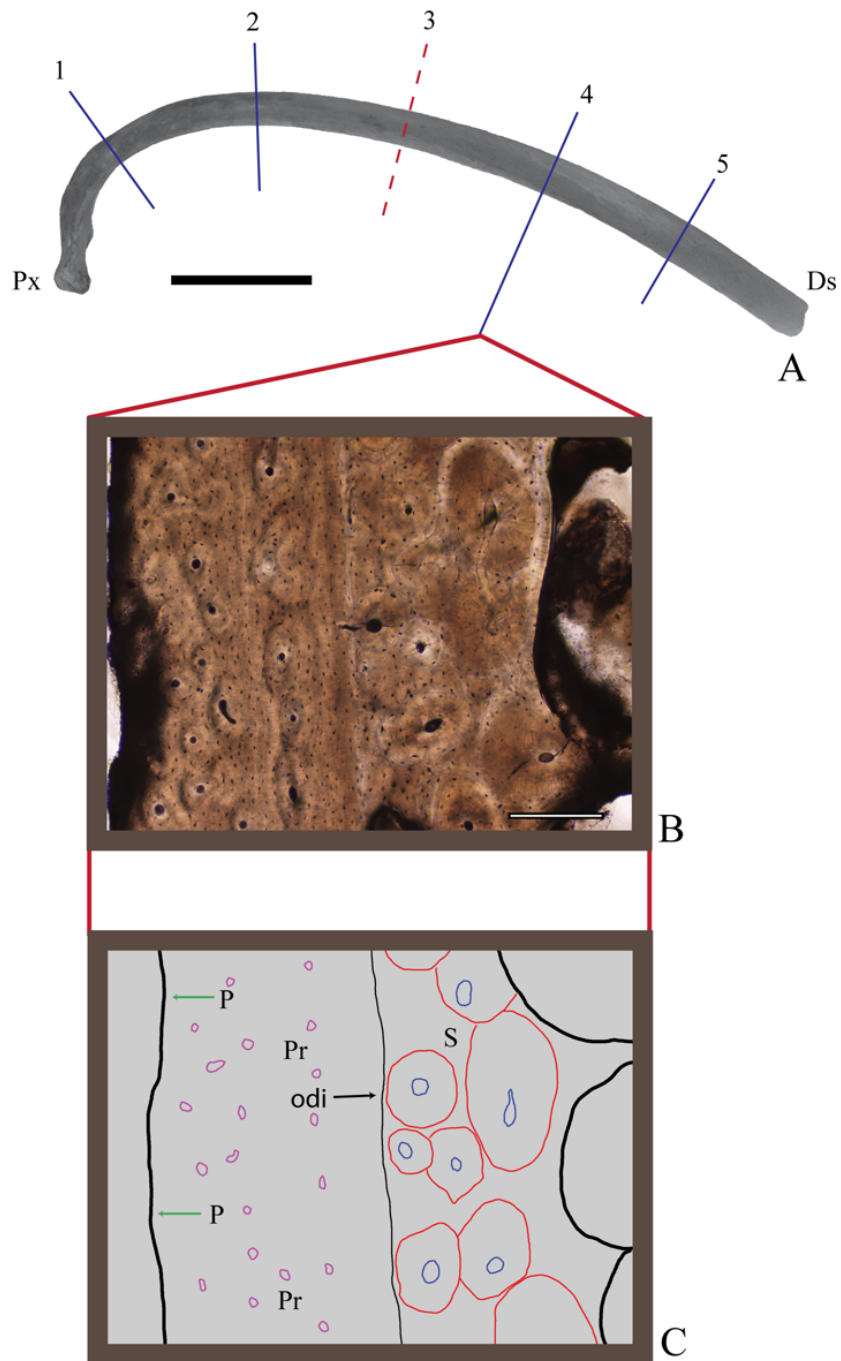


Figure 4.23: *Odocoileus virginianus* left Rib 7 (A) with a corresponding micrograph showing representative microstructural arrangement of Cut 4 (B) and a schematic (C). Sub-equal widths of primary and secondary bone make up the cortex. There is no distinct periosteal bone. Scale for (A) = 5cm. Scale for (B,C) = 0.2mm.

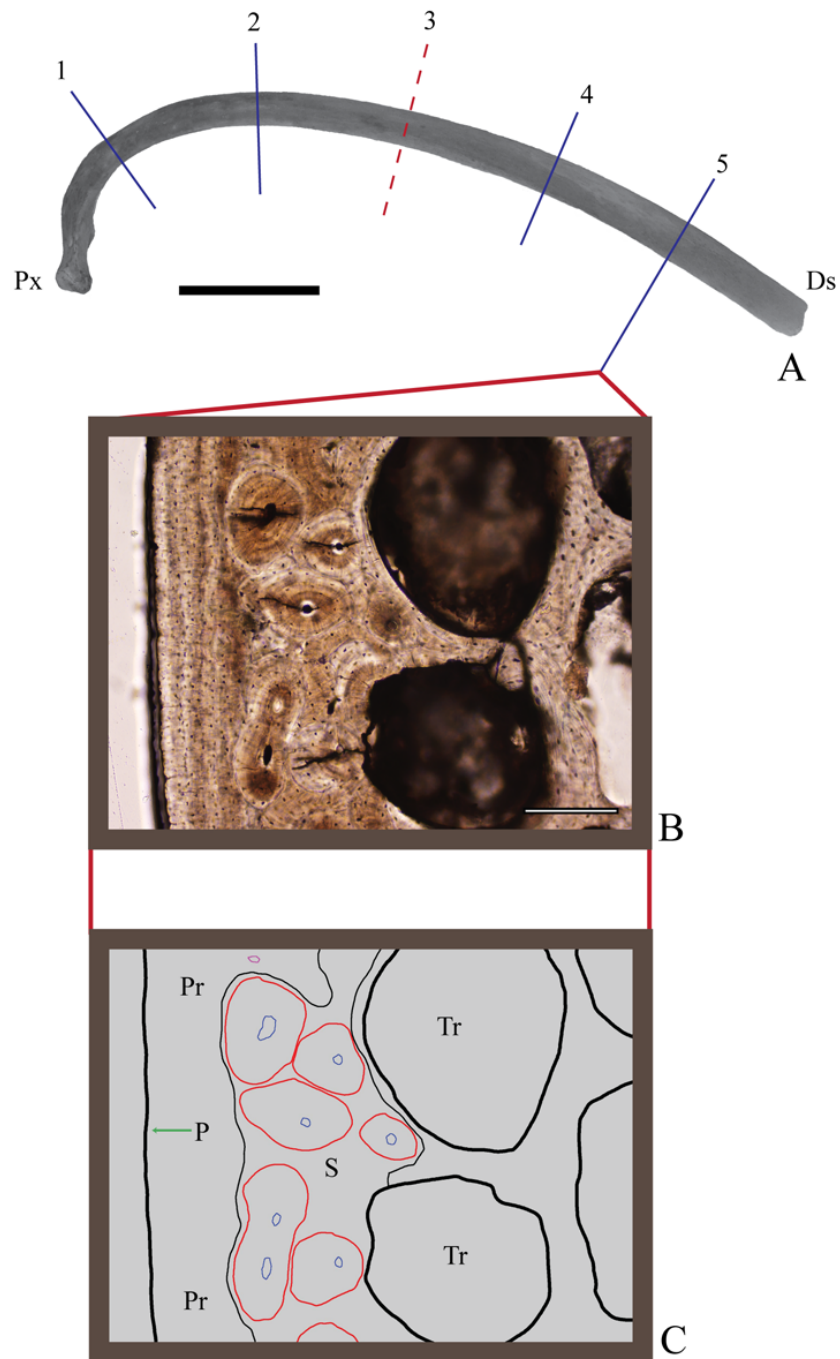


Figure 4.24: *Odocoileus virginianus* left Rib 7 (A) with a corresponding micrograph showing representative microstructural arrangement of Cut 5 (B) and a schematic (C). Sub-equal widths of primary and secondary bone make up the cortex. The primary bone shows a low density of vascularization. Scale for (A) = 5cm. Scale for (B,C) = 0.2mm.

Chapter 5

Principal Components Analysis of the Primary Dataset and Dataset Modeling

5.1 Introduction

The Primary Dataset, consisting of the 11 mammalian taxa described in Chapter 4, is used as the first evaluation of the new method presented in this dissertation. The Primary Dataset serves as a representative sample of taxa for the evaluation of the degree to which the metrics separate the taxa. These measurements also establish the first dataset dedicated to quantitative taxonomy. In viewing the tests of this hypothesis as a pyramid, the present dissertation represents the wide base of the pyramid upon which all other test depends. The base should not only be wide in scope, but should also represent a broad overview of microstructural variation. The decision to populate the Primary Dataset with mammals from a variety of Orders ensured broad phylogenetic, habitat, and locomotive separation, hypothetically also ensuring wide variation in the bone microstructure. Proven ability to separate taxa on the basis of bone microstructure at the Order level would suggest that additional datasets be considered in the future. Such sets would be more tightly honed for determining, for instance, to what taxonomic level the method can be effective, the variation within species, and an evaluation of taxa from more specific environments (i.e., moving towards the apex of the pyramid).

The exploratory nature of this dissertation makes it necessary to document the details of each step that was taken in order to assure the validity of the results and future repeatability. There are no prior tests for comparison, no published standards for data collection, and no analogous course of research. The first iterations of such tests are established and analyzed here. Although this chapter is mainly concerned with the presentation of statistical output, it is equally important to address the specific data preparation and configuration that preceded any statistical analysis. In order to give a comprehensive overview of the treatment of the Primary Dataset, Chapter 5 will address (1) data collection and measurement, (2) data manipulation, (3) an overview of each statistical technique with reference to the Primary Dataset, (4) input structure of the Dataset for each statistical analysis, (5) results for each statistical analysis, (5) the meaning of the results, and (6) future outlook for this method in quantitative taxonomy.

5.2 Collection of Microstructural Data

In this chapter, the collection of data refers to the treatment of the microstructures after the thin-sectioning procedure was completed. “Data collection” actually began during the selection of mammal tibiae, the harvesting of the mid-diaphysis, and the making of a thin-section for each mammal tibia. A detailed account of bone harvesting and thin-section procedure is outlined in Chapter 3. With those procedures now established, focus is shifted to the determination of an optimal procedure to collect and organize microstructural data.

The Primary Dataset presents an interesting situation because, without prior knowledge of microstructural variation within and between taxa, optimizing data collection becomes difficult. It is essentially a “best guess” of experimental set-up that will be refined later after statistical analysis. How would the differences in the number of microstructures among data subsets be considered in analysis? How many microstructures would have to be measured for each taxon in order to detect reliable and reproducible differences between taxa? Because the microstructures are on the micrometer scale, what magnification should be used for each micrograph to ensure that the features can be measured accurately? Based on the above questions,

a specific approach was adopted, and all measurable microstructures within the 11 cross-sections were considered in the analysis.

5.2.1 Dataset Hierarchy

The measurements made on each microstructural feature were designed to be straightforward and repeatable. Regardless of where the feature is located in the cortex, it is always measured identically using the fundamental principals of geometry detailed in Chapter 3. The method does not consider the overarching feature “microstructural arrangement” as a variable to distinguish taxa. However, the density of the microstructures changes along the circumference of the cortex. In other words, there are numerous levels of variation inherent in each sample that must be accounted for in this first test of the method. For instance, not only can there be variation between mammal specimens, but there is also microstructural variation within one cross-section, etc. To account for any variation within a single specimen and to enhance the ability to scrutinize the data more closely if necessary, the Primary Dataset was organized in a hierarchy with increasing specificity at each successive tier. The tiers range in specificity from the whole tibia at the broadest level, Tier I, to a single microstructural measurement at the most specific level (Tier V) (Figure 5.1). Using the groundhog as an example in Figure-Hierarchy, Tier I refers to the broadest data-level, occupied in this dataset by the left tibia. Tier II is occupied by the mid-diaphyseal cross-section taken from the tibia and is followed by the individual micrograph images in Tier III, taken from the mid-diaphyseal cross-section. Within each micrograph, represented as Tier IV, are five measurable microstructural types (primary vasculature, secondary osteons, Haversian canals, primary lacunae, and secondary lacunae). Each of the five microstructural types is then subject to a series of measurements and calculations, represented in Tier V. By organizing the data in this way, the microstructural variation in each level can be explored and then taken into account for future dataset organization and treatment. Tiers I and II are presented in detail in Chapter 3. The following sections will address the treatment of the dataset with regard to Tiers III, IV, and V.

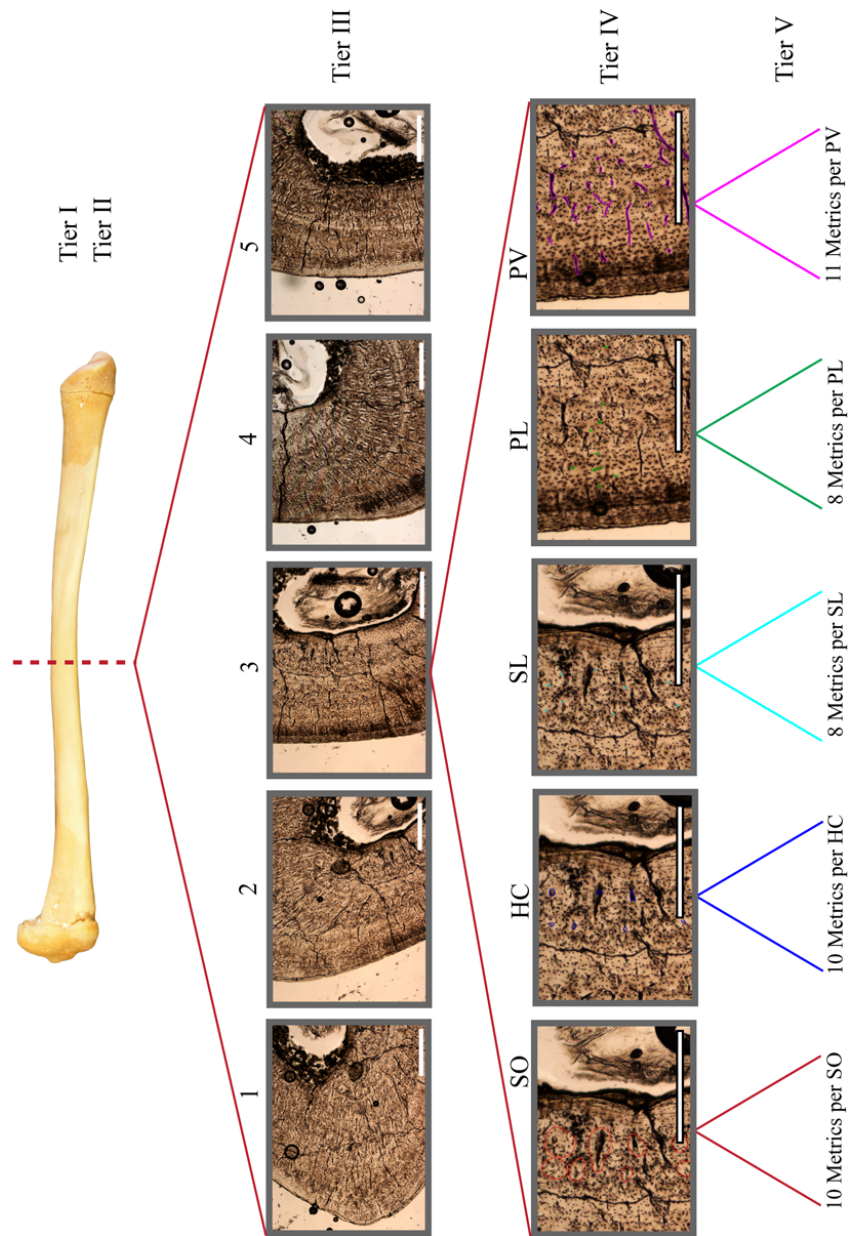


Figure 5.1: The five hierarchical levels of data specificity are illustrated here using the Groundhog tibia as an example. Tiers I and II correspond to the entire tibia and the single cross-section taken from the mid-diaphysis for microstructural analysis. Tier III is represented by each micrograph in the cross section. Tier IV refers to each of the five microstructural types (secondary osteon, Haversian canal, secondary lacunae, primary lacunae, primary vasculature). Tier V is represented by the series of specific metrics used to characterize each of the types of microstructures in the cross-section. The number of measurements made depends on the type of microstructure.

Micrographs - Tier III

The size, shape, and cortical thickness of each tibia in the Primary Dataset were unique to the taxon (for details see Chapter 4). The transverse cross-section made from the tibia also reflected these morphological differences. For instance, a larger cross-section was generally associated with larger cortical area. There were three main concerns when deciding how the micrographs should be taken: (1) the magnification of the microstructures must be sufficient to allow accurate marking of the features prior to measurement in the Welsh Computer Program, (2) all the micrographs must be taken at the same magnification despite the size differences of the cross-section to enable the Welsh Computer Program to output directly comparable measurements, and (3) all microstructures in the cross-section should be measured only once.

Micrographs of the cross-sections were taken using the 5x objective at a resolution of 2040 x 1536 pixels per micrograph. At this magnification and resolution, the micrographs could be “zoomed to” 300% of their original size and retain enough resolution to accurately mark the smallest microstructures, the lacunae. Each original micrograph has an area of 1.5mm × 1.5mm. However, the dimensions of each micrograph as a “sample of bone” change slightly depending on the thickness of the cortex. Different bone microstructural types are found in different sections of the cortex (see Chapter for an overview of the cortices of the Primary Dataset). If the cortical thickness of a tibial specimen exceeds the width of a single micrograph (1.5mm) the number and type of microstructures in that image will be different than in a micrograph that shows the entire cortical width (i.e., secondary osteons are likely to be found on the endosteal surface; if the micrograph only shows the periosteal half of the cortex, then the sampling becomes biased). For instance, the bear has a cortex that is wider than 1.5mm. This means that a typical micrograph “sample” for the bear cross-section might be 1.5mm in height and 3.0mm in width, whereas mammals with cortical widths less than 1.5mm will have micrograph “sample” dimensions of 1.5mm in height and 1.0mm in width. Each micrograph has a height of approximately 1.5mm. To compensate for the differences in cortical thickness of the tibial samples in the Primary Dataset, consecutive micrographs were taken by moving the field-of view radially across the cortex. The micrographs were then combined into a panoramic view in Adobe Photoshop. The differences in cortical thickness are taken into account in the metric “CT” (see below). Also because each micrograph was taken at the same

magnification, the different sizes of the tibial cross-sections yielded a different number of micrographs per specimen. The number of micrographs per cross-section ranged from 5 for the opossum to 32 for the bear (Figure 5.2) for a total of 161 micrographs for all mammalian specimens in the Primary Dataset.

TAXON	# of MICROGRAPHS	Secondary Osteons	Haversian Canals	Primary Lacunae	Secondary Lacunae	Primary Vasculature	TOTAL
Bobcat	21	687	701	402	350	231	2371
Bear	32	1742	1760	311	675	663	5151
Beaver	19	75	75	219	137	709	1215
Capuchin	9	112	114	91	76	106	499
Coyote	20	261	261	164	218	133	1037
Groundhog	8	31	31	81	59	81	283
Hare	10	54	54	199	114	1126	1547
Lemur	11	103	102	218	211	492	1126
Opossum	5	32	33	50	46	233	394
Raccoon	12	184	181	120	120	539	1144
Rhesus	14	309	305	142	138	84	978
TOTAL	161	3590	3617	1997	2144	4397	15745

Figure 5.2: Tabulation of the number of microstructural units of each of the five types measured within all 161 micrographs. The total number of microstructural units is dominated by the number of measured primary vascular canals, the majority of which were measured from the Hare. The number of micrographs per cross-section ranged from 5 to 32, from which 15,745 microstructural units were measured in total.

To ensure that each microstructural unit was measured only once, the first micrograph was taken from the anterior-most point of each cross-section. In addition to the radial images taken across the cortical width of each cross-section, sequential images were also taken by rotating the cross-section in a counterclockwise direction following the bone cortex. Each micrograph overlapped slightly, serving a dual purpose. The overlap ensured that all data (microstructures) were measured and that no microstructures were measured twice. A double-check of this was then made when marking the micrographs.

Microstructures - Tier IV

The microstructural types marked and measured, as discussed in Chapter 3, included individual examples of all primary vasculature, secondary osteons, and Haversian

canals from each tibial cross-section. Samples of approximately 10 primary and 10 secondary lacunae were taken from each microscope field-of view ((1.5 x 1.5)mm²). Note here that the number of measured primary and secondary lacunae also vary by cortical width. For instance, if the cortical thickness of a specimen could be captured in two fields-o-view, then the total number of secondary lacunae measured would be 20. The 161 micrographs yielded 15,745 microstructural units (Figure 5.2) that were marked by hand and then measured automatically using the Welsh algorithm. Just as there were differences in the number of micrographs per cross-section, the number of units of each type of microstructure also differed per micrograph as well as per cross-section. Summaries of these data for each taxon can be found in Figure 5.3 through Figure 5.13. These tables organize the data to show the breakdown (and totals) of number and type of microstructures measured from each micrograph. The tables for each taxon, as well as the summary table (Figure 5.2), show that the number of measured secondary osteons and Haversian canals is similar. This is expected because only those Haversian canals that were within measured secondary osteons were included in the dataset. The slight difference in the numbers of measured secondary osteons and Haversian canals results from several occurrences of two or more Haversian canals within the reversal line of one secondary osteon (Figure 5.14 (A)). It is important to note here that the criterion for marking a secondary osteon for measurement was that the entire circumference of the reversal line must be visible. The remodeling of cortical bone throughout the life of an animal, however, results in overprinting of early secondary osteons by later ones (Figure 5.14 (B)). The secondary osteons whose reversal lines were obscured by later bone remodeling were not considered in this analysis. Differences between the number of primary lacunae and secondary lacunae are a result of the type of bone (primary vs. secondary) present in the cross-section. For example, the bear cross-section (Figure 5.3) was almost entirely composed of secondary bone, leaving only a few opportunities to collect measurements on primary structures. All measured microstructural units (15,745) are used in the statistical analysis.

Microstructure measurements - Tier V

The goal of the principal component analyses and the multiple discriminant analyses (6) in this dissertation is to record variation in bone microstructural morphology

TAXON	MICROGRAPH #	Secondary Osteons	Haversian Canals	Primary Lacunae	Secondary Lacunae	Primary Vasculature	TOTAL
Bear	NCMS 5363 01	193	197	20	30	8	448
Bear	NCMS 5363 02	75	74	10	20	25	204
Bear	NCMS 5363 03	43	46	1	20	0	110
Bear	NCMS 5363 04	39	38	9	20	0	106
Bear	NCMS 5363 05	34	36	10	20	25	125
Bear	NCMS 5363 06	3	3	10	10	40	66
Bear	NCMS 5363 07	14	14	20	20	78	212
Bear	NCMS 5363 08	13	13	10	10	0	46
Bear	NCMS 5363 09	18	16	10	10	21	75
Bear	NCMS 5363 10	37	32	20	20	18	127
Bear	NCMS 5363 11	31	27	20	20	35	133
Bear	NCMS 5363 12	45	44	21	20	47	177
Bear	NCMS 5363 13	20	20	10	10	55	115
Bear	NCMS 5363 14	50	52	20	20	31	173
Bear	NCMS 5363 16	72	72	10	30	28	212
Bear	NCMS 5363 17	73	72	10	30	26	211
Bear	NCMS 5363 18	47	47	0	21	33	148
Bear	NCMS 5363 19	11	11	10	10	25	67
Bear	NCMS 5363 20	14	14	0	10	35	73
Bear	NCMS 5363 21	81	79	0	30	18	208
Bear	NCMS 5363 22	49	50	11	30	0	140
Bear	NCMS 5363 23	24	24	0	20	0	68
Bear	NCMS 5363 24	53	55	8	30	13	159
Bear	NCMS 5363 25	42	44	20	30	17	153
Bear	NCMS 5363 26	25	25	10	25	20	105
Bear	NCMS 5363 27	35	36	9	20	22	122
Bear	NCMS 5363 28	43	43	10	20	22	138
Bear	NCMS 5363 29	72	74	0	30	7	183
Bear	NCMS 5363 30	54	58	0	10	0	122
Bear	NCMS 5363 31	161	163	12	30	6	372
Bear	NCMS 5363 32	167	180	0	29	8	384
Bear	NCMS 5363 33	104	101	10	20	0	235
TOTAL	32	1742	1760	311	675	663	5151

Figure 5.3: The number of microstructural units measured per micrograph ranged from 46 to 448 and was dominated by secondary osteons and Haversian canals. The bear had the highest number of microstructural units measured in one cross-section, 5151.

TAXON	MICROGRAPH #	Secondary Osteons	Haversian Canals	Primary Lacunae	Secondary Lacunae	Primary Vasculature	TOTAL
Beaver	NCSM C canadensis 01	0	0	10	0	53	63
Beaver	NCSM C canadensis 02	0	0	10	0	58	68
Beaver	NCSM C canadensis 03	5	5	21	10	74	115
Beaver	NCSM C canadensis 04	9	9	21	19	49	107
Beaver	NCSM C canadensis 05	0	0	10	0	58	68
Beaver	NCSM C canadensis 06	0	0	10	0	28	38
Beaver	NCSM C canadensis 07	0	0	13	0	55	68
Beaver	NCSM C canadensis 08	5	5	10	10	71	101
Beaver	NCSM C canadensis 09	3	3	10	9	21	46
Beaver	NCSM C canadensis 10	1	1	10	10	74	96
Beaver	NCSM C canadensis 11	4	4	10	10	37	65
Beaver	NCSM C canadensis 12	1	1	10	10	50	72
Beaver	NCSM C canadensis 13	0	0	10	0	49	59
Beaver	NCSM C canadensis 15	11	10	11	10	0	42
Beaver	NCSM C canadensis 16	6	6	10	9	0	31
Beaver	NCSM C canadensis 20	5	6	10	9	0	30
Beaver	NCSM C canadensis 21	10	10	11	10	0	41
Beaver	NCSM C canadensis 22	12	12	11	11	18	64
Beaver	NCSM C canadensis 23	3	3	11	10	14	41
TOTAL	19	75	75	219	137	709	1215

Figure 5.4: The number of microstructural units measured per micrograph ranged from 30 to 101 and was dominated by primary vascular canals. This microstructural dominance is evident in the totals per microstructural type, showing the primary vasculature with a total of 709 measured units in the Beaver cross-section compared to only 75 units each for secondary osteons and Haversian canals.

TAXON	MICROGRAPH #	Secondary Osteons	Haversian Canals	Primary Lacunae	Secondary Lacunae	Primary Vasculature	TOTAL
Bobcat	F rufus 1	69	69	20	20	0	178
Bobcat	F rufus 02	72	64	21	20	0	177
Bobcat	F rufus 03	49	47	20	19	0	135
Bobcat	F rufus 04	16	16	21	10	12	75
Bobcat	F rufus 05	8	8	20	10	23	69
Bobcat	F rufus 06	7	7	20	10	28	72
Bobcat	F rufus 07	23	23	20	20	34	120
Bobcat	F rufus 08	33	36	20	20	0	109
Bobcat	F rufus 09	36	40	20	20	11	127
Bobcat	F rufus 10	31	33	20	20	14	118
Bobcat	F rufus 11	56	59	20	20	0	155
Bobcat	F rufus 12	28	34	10	10	0	82
Bobcat	F rufus 13	30	32	20	21	7	110
Bobcat	F rufus 14	39	39	20	20	10	128
Bobcat	F rufus 15	20	20	20	20	23	103
Bobcat	F rufus 16	20	21	20	20	4	85
Bobcat	F rufus 17	13	13	20	10	13	69
Bobcat	F rufus 18	6	6	20	10	33	75
Bobcat	F rufus 19	29	31	20	20	19	119
Bobcat	F rufus 20	64	64	20	20	0	168
Bobcat	F rufus 21	38	39	10	10	0	97
TOTAL	21	687	701	402	350	231	2371

Figure 5.5: The bobcat cross-section is dominated by secondary osteons (687) and Haversian canals (701) compared to the primary vasculature (231). The total number of microstructural units measured per micrograph ranged from 69 to 178.

TAXON	MICROGRAPH #	Secondary Osteons	Haversian Canals	Primary Lacunae	Secondary Lacunae	Primary Vasculature	TOTAL
Capuchin	MCZ 438 01	25	26	10	10	0	71
Capuchin	MCZ 438 02	2	2	10	6	0	20
Capuchin	MCZ 438 03	0	0	10	0	0	10
Capuchin	MCZ 438 04	5	5	10	10	14	44
Capuchin	MCZ 438 05	22	23	11	10	12	78
Capuchin	MCZ 438 06	15	16	10	10	27	78
Capuchin	MCZ 438 07	15	14	10	10	25	74
Capuchin	MCZ 438 08	21	21	10	10	28	90
Capuchin	MCZ 438 09	7	7	10	10	0	34
TOTAL	9	112	114	91	76	106	499

Figure 5.6: Summary table of the microstructural units measured in the Capuchin monkey cross-section. Despite large differences in the number of microstructural units measured per micrograph, i.e., 10 to 90, the total number of measured secondary osteons, Haversian canals, and primary vascular canals is close to equal.

TAXON	MICROGRAPH #	Secondary Osteons	Haversian Canals	Primary Lacunae	Secondary Lacunae	Primary Vasculature	TOTAL
Coyote	NCSM C latrans 01	3	3	0	10	0	16
Coyote	NCSM C latrans 02	21	21	0	20	0	62
Coyote	NCSM C latrans 03	7	6	0	10	0	23
Coyote	NCSM C latrans 04	1	1	10	9	0	21
Coyote	NCSM C latrans 05	9	9	10	9	5	42
Coyote	NCSM C latrans 06	8	8	10	10	4	40
Coyote	NCSM C latrans 07	17	17	10	10	10	64
Coyote	NCSM C latrans 08	11	11	10	10	12	54
Coyote	NCSM C latrans 09	6	6	10	10	32	64
Coyote	NCSM C latrans 10	4	3	10	10	19	46
Coyote	NCSM C latrans 11	17	18	9	10	7	61
Coyote	NCSM C latrans 12	15	15	10	10	8	58
Coyote	NCSM C latrans 13	13	13	10	10	0	46
Coyote	NCSM C latrans 14	20	20	10	10	10	70
Coyote	NCSM C latrans 15	22	22	12	10	16	82
Coyote	NCSM C latrans 16	20	22	10	10	3	65
Coyote	NCSM C latrans 17	22	21	11	10	6	70
Coyote	NCSM C latrans 18	20	20	10	10	1	61
Coyote	NCSM C latrans 19	7	7	11	20	0	45
Coyote	NCSM C latrans 20	18	18	1	10	0	47
TOTAL	20	261	261	164	218	133	1037

Figure 5.7: The coyote cross-section is dominated by secondary structures. Many of the micrographs do not show any primary vascular canals. The accompanying absence of primary lacunae indicates that the lack of primary vascular canals was due to bone remodeling rather than simple lack of vascularization in the primary bone. Total microstructural units measured per micrograph ranged from 16 to 82.

TAXON	MICROGRAPH #	Secondary Osteons	Haversian Canals	Primary Lacunae	Secondary Lacunae	Primary Vasculature	TOTAL
Groundhog	Marmota 01	2	2	10	5	3	22
Groundhog	Marmota 03	1	1	10	4	3	19
Groundhog	Marmota 04	3	3	10	10	8	34
Groundhog	Marmota 05	6	6	10	10	11	43
Groundhog	Marmota 06	5	5	10	10	7	37
Groundhog	Marmota 07	10	10	10	9	26	65
Groundhog	Marmota 09	3	3	10	10	4	30
Groundhog	Marmota 10	1	1	11	1	19	33
TOTAL	8	31	31	81	59	81	283

Figure 5.8: The total number of microstructural units measured per micrograph ranges from 19 to 65. The partitioning of the microstructures into types reveals that there were many more primary vascular canals in the cross section (81) than secondary osteons and Haversian canals (31 each).

TAXON	MICROGRAPH #	Secondary Osteons	Haversian Canals	Primary Lacunae	Secondary Lacunae	Primary Vasculature	TOTAL
Hare	MCZ 60888 01	11	10	20	20	49	110
Hare	MCZ 60888 02	4	4	20	17	148	193
Hare	MCZ 60888 03	0	0	20	0	118	138
Hare	MCZ 60888 04	0	0	20	0	105	125
Hare	MCZ 60888 05	19	20	20	19	185	263
Hare	MCZ 60888 06	3	3	20	19	95	140
Hare	MCZ 60888 07	0	0	19	0	102	121
Hare	MCZ 60888 08	0	0	20	0	75	95
Hare	MCZ 60888 09	3	3	20	19	125	170
Hare	MCZ 60888 10	14	14	20	20	124	192
TOTAL	10	54	54	199	114	1126	1547

Figure 5.9: In contrast to the Bear (Figure 5.3), the cross-section of the Hare is dominated by primary vascular canals (1126) and has a dearth of secondary osteons (54) and Haversian canals (54). Given the size of the cross-section, there was a relatively large number of microstructural units measured per micrograph, ranging from 95 to 263.

TAXON	MICROGRAPH #	Secondary Osteons	Haversian Canals	Primary Lacunae	Secondary Lacunae	Primary Vasculature	TOTAL
Lemur	MCZ 59274 01	16	15	20	20	48	119
Lemur	MCZ 59274 02	10	9	19	20	21	79
Lemur	MCZ 59274 03	5	6	20	20	17	68
Lemur	MCZ 59274 04	5	6	20	21	23	75
Lemur	MCZ 59274 05	14	14	20	20	63	131
Lemur	MCZ 59274 06	12	11	20	20	99	162
Lemur	MCZ 59274 07	12	12	20	20	84	148
Lemur	MCZ 59274 08	7	7	20	20	61	115
Lemur	MCZ 59274 09	1	1	20	10	39	71
Lemur	MCZ 59274 10	8	8	20	20	17	73
Lemur	MCZ 59274 11	13	13	19	20	20	85
TOTAL	11	103	102	218	211	492	1126

Figure 5.10: The lemur cross-section is dominated by primary vascular canals (492) rather than secondary osteons (103) and Haversian canals (102). The number of microstructural units measured per micrograph ranged from 71 to 162.

TAXON	MICROGRAPH #	Secondary Osteons	Haversian Canals	Primary Lacunae	Secondary Lacunae	Primary Vasculature	TOTAL
Opossum	NCSM 8368 01	1	1	10	9	11	32
Opossum	NCSM 8368 02	4	4	10	9	0	27
Opossum	NCSM 8368 03	11	12	10	10	51	94
Opossum	NCSM 8368 05	9	9	10	10	92	130
Opossum	NCSM 8368 07	7	7	10	8	79	111
TOTAL	5	32	33	50	46	233	394

Figure 5.11: The opossum has the lowest number of micrographs per tibial cross-section. The cross-section shows many more primary vascular canals (233) than secondary osteons (32) and Haversian canals (33). The number of microstructural units measured per micrograph range from 32 to 130.

TAXON	MICROGRAPH #	Secondary Osteons	Haversian Canals	Primary Lacunae	Secondary Lacunae	Primary Vasculature	TOTAL
Raccoon	NCSM 2674 01	21	21	10	10	77	139
Raccoon	NCSM 2674 02	22	23	10	9	49	113
Raccoon	NCSM 2674 03	30	29	9	10	19	97
Raccoon	NCSM 2674 04	15	15	11	10	46	97
Raccoon	NCSM 2674 05	17	17	10	10	26	80
Raccoon	NCSM 2674 06	14	14	10	10	34	82
Raccoon	NCSM 2674 07	17	17	10	10	27	81
Raccoon	NCSM 2674 08	6	6	10	10	44	76
Raccoon	NCSM 2674 09	13	13	10	10	47	93
Raccoon	NCSM 2674 10	9	9	10	10	62	100
Raccoon	NCSM 2674 11	3	3	10	10	42	68
Raccoon	NCSM 2674 12	17	14	10	11	66	118
TOTAL	12	184	181	120	120	539	1144

Figure 5.12: The raccoon cross-section shows many more primary vascular canals (539) than secondary osteons (184) and Haversian canals (181). The number of microstructural units measured per micrograph ranged from 68 to 139.

TAXON	MICROGRAPH #	Secondary Osteons	Haversian Canals	Primary Lacunae	Secondary Lacunae	Primary Vasculature	TOTAL
Rhesus	MCZ 64360 01	44	44	10	10	0	108
Rhesus	MCZ 64360 02	25	25	10	10	7	77
Rhesus	MCZ 64360 03	6	5	10	10	9	40
Rhesus	MCZ 64360 04	2	2	10	10	9	33
Rhesus	MCZ 64360 05	8	9	10	10	5	42
Rhesus	MCZ 64360 06	33	33	11	10	8	95
Rhesus	MCZ 64360 07	23	21	10	9	0	63
Rhesus	MCZ 64360 08	26	25	10	10	0	71
Rhesus	MCZ 64360 09	17	17	12	10	0	56
Rhesus	MCZ 64360 10	10	9	7	10	17	53
Rhesus	MCZ 64360 11	11	11	10	10	11	53
Rhesus	MCZ 64360 12	23	23	10	10	14	80
Rhesus	MCZ 64360 13	39	38	10	10	4	101
Rhesus	MCZ 64360 14	42	43	12	9	0	106
TOTAL	14	309	305	142	138	84	978

Figure 5.13: The cross-section of the rhesus monkey showed more secondary osteons (309) and Haversian canals (309) than primary vasculature(84). Given the abundance of primary lacunae (about the same for the secondary lacunae), it appears that although primary bone was present, it was not highly vascularized. The number of microstructural units measured per micrograph ranged from 33 to 108.

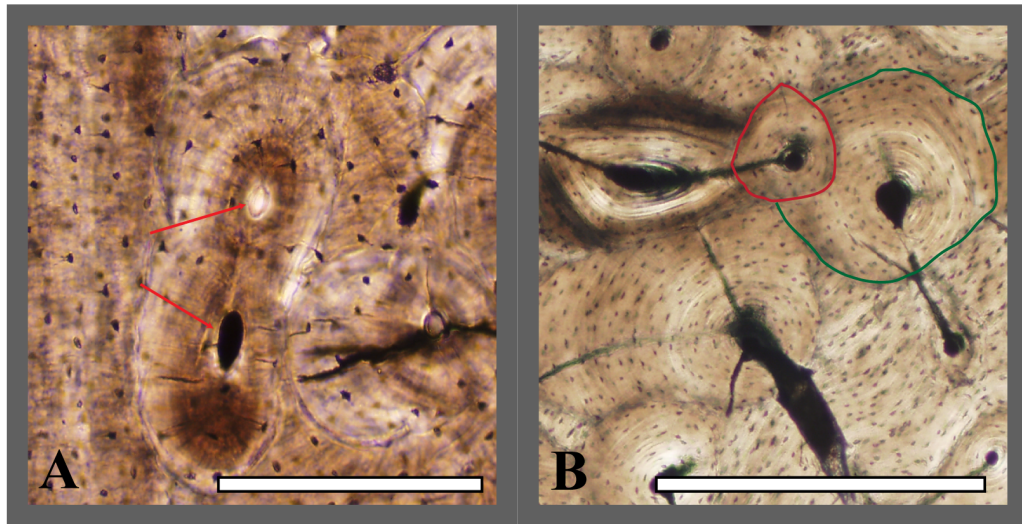


Figure 5.14: In the simplest case, the number of secondary osteons equals that of Haversian canals. Some deviation from this equality is due to the occurrence of two or more Haversian canals within a single osteon (A, red arrows). Only those secondary osteons showing the entire circumference of the reversal line (B, red outline) were marked for measurement. The secondary osteon outlined in green has been partly overprinted and is not considered in the analysis. Examples sourced from *O. virginianus* rib (A) and *F. rufus* tibia. Scale for A = 0.2mm. Scale for B = 0.5mm.

within a single taxon (cross-section) so as to recognize differences between taxa in the Primary Dataset. The answer to the question “Can tetrapods be distinguished on the basis of bone microstructural morphology?” relies simply on size, shape, and orientation of the microstructural units. Figure 5.15 provides a list of the specific measurements (metrics) and their abbreviations.

The geometry of the direct measurements is described in Chapter 3. In addition to those direct measurements, several other metrics were derived to show the relationships among certain measurements and microstructural types in the dataset (Figure 5.16). The five derived metrics include (1) the ratio of the major and minor axes of the bounding ellipse (i.e. the ellipse generated by the Welsh algorithm that fully encompasses the real microstructural unit), (2) the ratio of the microstructural unit’s circumference to the circumference of its bounding ellipse, (3) the ratio of the secondary osteon’s circumference to its Haversian canal’s circumference, (4) the ratio of the primary lacuna’s circumference to the secondary lacuna’s circumference, and (5) the ratio of the primary vascular canal’s circumference to the Haversian canal’s circumference. Each metric listed describes a certain relationship between the sizes and shapes of microstructural types that may not otherwise be detected during statistical analysis. The ratio of the major and minor axes of the bounding ellipse (1) reflects the shape of the ellipse regardless of its absolute size. The comparison of the microstructural unit’s circumference with the circumference of the bounding ellipse (2) captures the departure from an elliptical shape. Whereas much of the phenotypic expression of bone formation and remodeling has been documented in direct measurements, there are still certain relationships, such as the difference in size between primary and secondary lacunae, that have yet to be explored. The metric comparing the circumferences of the primary and secondary lacunae (4) will address any difference in size. The ratio of circumferences of the primary and secondary (Haversian) vasculature (5) reveals whether the vascular channels that originated during the primary formation of the bone are the same size as those formed as result a remodeling process. Interpretation of the size of the Haversian canal presents a challenge in the absence of information on whether the canal was at its final size. Remodeling of bone is a continuous process. It is possible that some of the variation in the sizes of the Haversian canals is due to the cessation of remodeling forced by the animal’s death rather than as the result of completion of the remodeling process. In addition to the

		Primary Vasculature	Primary Lacunae	Secondary Osteons	Haversian Canals	Secondary Lacunae	OSTEOLOGICAL FEATURE
		Magenta	Green	Red	Blue	Cyan	COLOR LABEL
METRIC	ABBREVIATION	PV	PL	SO	HC	SL	ABBREVIATION
Microstructural Unit Circumference	C	PVC	PLC	SOC	HCC	SLC	
Microstructural Unit Area	A	PVA	PLA	SOA	HCA	SLA	
Bounding Ellipse Major Axis Length	Maj	PVMaj	PLMaj	SOMaj	HCMaj	SLMaj	
Bounding Ellipse Minor Axis Length	Min	PVMin	PLMin	SOMin	HCmin	SLMin	
Bounding Ellipse Major/Minor Ratio	MMR	PVMMR	PLMMR	SOMMR	HCMMR	SLMMR	
Bounding Ellipse Circumference	CEllipse	PVCEllipse	PLCEllipse	SOCEllipse	HCEllipse	SLCEllipse	
Bounding Ellipse Area	AEllipse	PVAEllipse	PLAEllipse	SOCEllipse	HCAEllipse	SLAEllipse	
Microstructure/ Bounding Ellipse Circumference Ratio	R	PVR	PLR	SOR	HCR	SLR	
Orientation with respect to Longitudinal Axis of Diaphysis	Long	PVLong	/	SOLong	HCLong	/	
Nearest Bounding Ellipse Centroid	Centroid	PVCentroid	PLCentroid	/	/	SLCentroid	
Orientation with respect to Periosteal Surface	Peri	PVPeri	/	SOPeri	HCPeri	/	

A

METRIC	ABBREVIATION
Secondary Osteon/Haversian Canal Circumference Ratio	SOHCR
Primary Lacuna/Secondary Lacuna Circumference Ratio	PLSLR
Primary Vascular/Haversian Canal Circumference Ratio	PVHCR
Cortical Thickness	CT

B

Figure 5.15: Each metric used in Runs 1, 2, and 3 is represented by an abbreviation that refers to the type of microstructure and the specific measurement being applied to it.

derived measurements described above, cortical thickness (CT) was also measured for each micrograph sample.

5.3 Statistical Methods: Selection and Application

The goals of the statistical treatment of the datasets presented in this dissertation are (1) to evaluate whether the variation in the size, shape, and orientation in the microstructural types can be attributed to taxonomic differences, (2) to gain insight into the metrics that account for the microstructural differences between taxa, (3) to evaluate the variance within each taxon of the data described above, (4) to test a series of “knowns” against a model of the Primary Dataset, and (5) to provide a statistical basis for construction of future databases. The first and second goals are accomplished through the use of Principal Components Analysis (PCA). The fourth goal is accomplished by using the method of Soft Independent Modeling of Class Analogy (SIMCA). The fifth goal is accomplished by the combination of the statistical techniques used here. The continuation of this project will eventually see the introduction of additional statistical analyses more appropriate for group classification and model generation, such as Discriminant Function Analysis and Partial Least Squares Regression. The following section provides background for PCA and SIMCA and details of the application of both methods to the Primary Dataset.

5.3.1 Principal Components Analysis

Principal Components Analysis (PCA) is an exploratory multivariate statistical technique for identifying meaningful trends in complex datasets. The method is a statistical tool for transforming a set of multiple variables (from actual measurements) that may be correlated into a new set of characteristics/variables that are not correlated. These new variables are called principal components, which conceptually plot along orthogonal axes. These orthogonal axes are chosen for their ability to represent

		Microstructural Type				
		Primary Vasculature	Primary Lacunae	Secondary Osteons	Haversian Canals	Secondary Lacunae
Metric	Microstructural Unit Circumference	✓	✓	✓	✓	✓
	Microstructural Unit Area	✓	✓	✓	✓	✓
	Bounding Ellipse Major Axis Length	✓	✓	✓	✓	✓
	Bounding Ellipse Minor Axis Length	✓	✓	✓	✓	✓
	Bounding Ellipse Major/Minor Ratio	✓	✓	✓	✓	✓
	Bounding Ellipse Circumference	✓	✓	✓	✓	✓
	Bounding Ellipse Area	✓	✓	✓	✓	✓
	Microstructure/ Bounding Ellipse Circumference Ratio	✓	✓	✓	✓	✓
	Orientation with Longitudinal Axis of Diaphysis	✓	/	✓	✓	/
	Nearest Bounding Ellipse Centroid	✓	✗	/	/	✗
	Orientation of Major Axis with Periosteal Surface	✓	/	✓	✓	/

Secondary Osteon/Haversian Canal Circumference Ratio	✓	✓ Included in analysis ✗ Not included in analysis / Not applicable to microstructure
Primary Lacuna/Secondary Lacuna Circumference Ratio	✓	
Primary Vascular/Haversian Canal Circumference Ratio	✓	
Cortical Thickness	✓	

Figure 5.16: When microstructural measurements are averaged for a cross-section, additional arithmetic functions can be applied to the direct measurements in order to derive additional relationships among microstructures of different types.

the maximum amount of variance in the samples' data (i.e., what variable or combination of variables are responsible for the statistical dispersion of the data), using eigenvector/eigenvalue analysis (or a similar formulation of singular value decomposition). Thus, the input to a PCA effort is a set of measurement data, annotated with classifications and categories. The output from the PCA model is a set of new axes and how they are related to the original variables (representing microstructural metrics in this dissertation) having the greatest variance. The first principal component encompasses the greatest amount of variance, with the succeeding components accounting for incrementally less variance.

Within the class of linear methods, PCA is considered the mathematically optimal information-preserving transformation (Basilevsky, 1994; Everitt and Dunn, 1992; Jolliffe, 1986). PCA simplifies the interactions of multiple variables through reduction in the dimensionality of the dataset. This reduction is accomplished through a mathematical projection transformation, determined in this dissertation by eigenvector/eigenvalue analysis of a covariance matrix. The transformation results in a new set of variables, the principal components, which represent the features of the data with reference to a set of input variables. PCA has been shown to facilitate many types of multivariate analysis including gene clustering expression (Yueng and Ruzzo, 2001), temporal variation of meteorological fields (Horel, 1981), facial recognition (Kim et al., 2002), and data visualization (Siedlicki et al., 1988).

Powerful commercial PCA tools exist, and these are routinely applied to large and diverse data sets in many industries and academic settings, ranging from pharmaceuticals to econometrics. PCA is a thoroughly validated, mathematically optimal solution to the problem of identifying which variables in a data set have greatest explanatory value. Relevant aspects of PCA will be discussed in the context of analyzing bone microstructural features, but a thorough discussion of the statistical validity of PCA is beyond the scope of this dissertation; for more detail, see the reference by Jolliffe 1986.

The challenge in applying PCA to a problem or set of questions involving measurements is not deriving an accurate PCA formulation (the formulation is complete) or justifying a PCA analysis (the output is mathematically optimal, based on the variance within the data). Rather, the challenge is to formulate the input data such

that the most information will be extracted by the principal components analysis, and then to properly interpret the results in the context of the system. PCA is a powerful tool for identifying trends in a data set; the task of making sense of the reported trends is for the scientist.

Underlying the hypothesis that taxa can be differentiated on the basis of bone microstructural morphology is an assumed ability to target those variables that will contribute to the greatest diagnostic power, resulting in the largest amount of taxonomic separation of variables. The variables responsible for any separation of taxa are revealed by generating a PCA model and projecting the data onto the newly derived axes. The large size and complexity of the datasets in the current study require treatment with a statistical technique capable of multivariate analysis. This is essential, not only to determine the variables that have the greatest positive effect on taxonomic discrimination, but also to detect variables that contain redundant information, and to prevent biased overweighting of variables. It is also important to identify those variables that contribute little variability to the actual system under consideration. These variables have meager explanatory value. At best, they contribute nothing to the hypothesis. At worst, they add “noise” to the statistical signal arising from the diagnostic features, which, if unchecked, swamp out meaningful output. In addition, since the bone microstructure methodology is novel, the variability in the data set and the identification of explanatory variables had to be addressed through the course of the analysis. Such tasks are standard practice in PCA.

5.3.2 PCA of the Primary Dataset

In order to facilitate an understanding of basic PCA, a summary of the preparation of the dataset and the analysis technique is given here in the context of the Primary Dataset currently under study in this chapter. PCA is able to evaluate large datasets consisting of multiple variables. However, appropriate treatment of the data before analysis will ensure valid, reproducible results that then can be fully interpreted for meaning and impact. The goal of PCA is to reduce the dimensionality of the data matrix by identifying r new variables (the number of principal components) based on the original dataset, which incorporates a number of observations, m , made on a number of variables, n . The complete set of principal components (r) accounts

for as much of the variance in the original variables (n) as possible, while remaining uncorrelated and orthogonal. The structure of the imported data, then, directly affects the outcome of the analysis. This section outlines the specific treatment of the Primary Dataset prior to PCA and during post-processing of the output through discussion and examples of (1) raw data output from the Welsh computer program, (2) the configuration of the dataset that will undergo PCA, (3) the PCA output matrices, and (4) the discarding and retention of variables. The “Welsh computer program” refers to the software developed to automatically measure the microstructures that were digitally hand-marked on the micrographs. A detailed discussion of the program is found in Chapter 3.

5.3.3 Input

Raw Data

Input for the principal components analysis comes from the output of the Welsh program. The output from the Welsh computer program consisted of two files: (1) a duplicate of the digital micrograph, highlighting the measured microstructural units as overprinted with their corresponding points of axis-ellipse intersections and centroid locations (see Chapter 3 Figure 3.9) and (2) a data table containing the raw measurements and derived calculations from each microstructural unit marked on the micrograph. An example of the data table output from the Welsh program is given in Figure 5.17. It is important to note that the spreadsheet presented here has not been modified from the actual algorithm output. As a result, some of the terminology labeling each column is different than the terminology used throughout the body of this dissertation. The original output terminology is preserved here as a reference in the event that the algorithm should be used by another party. The proper terms used in this dissertation are in parentheses. Each color in the Feature (microstructural type) column represents one of the five types of microstructure. The shape# (unit) assigns a number to each microstructural unit that then may be located on the micrograph according to the unit’s centroid or top left X- and Y-coordinates (blue highlight). Total shape# (Total Unit#) gives the total number of units of that type in the micrograph view. Direct measurements and derived

calculations (green highlight) are given for each microstructural unit. A summary of the units in the micrograph (yellow highlight) compiles the total number of units of each microstructure type and the averages of all of the derived measurements. The raw microstructure data from each micrograph were reorganized into input matrices for PCA, and column labels were changed to reflect metric abbreviations. Details of each data matrix used for the Primary Dataset are described below.

Dataset Organization

Data from the Primary Dataset were organized into three configurations to facilitate multiple analyses for principal components—Run 1, Run 2, and Run 3 (Figure 5.18). The structure of the input matrices ($n \times m$) is different for each configuration. Simple examples of the matrices for Runs 1, 2 and 3 are shown in Figures 5.19 through 5.22. Each measurement in the matrix is coded for the type of microstructure (column headings in highlighted in green) and is represented by an abbreviation (Figure 5.15). The first analysis of the Primary Dataset, Run 1, is organized such that each microstructure is a separate datapoint (i.e., there is no averaging of values). For the input matrix of Run 1, each row corresponds to one microstructural unit, and each column corresponds to one microstructural metric (Figure 5.19). Within Run 1, each type of microstructure (secondary osteons, Haversian canals, primary lacunae, secondary lacunae, and primary vasculature) is analyzed separately to determine its individual influence over taxonomic separation in the Primary Dataset. These analyses are denoted as Runs 1A through 1E (Figure 5.18). Each microstructural unit is considered here to be one “sample” of data (m). Because of the different cortical sizes of the mid-tibial sections, some taxa are represented by a larger number of microstructural units. In addition, each of the five analyses in Run 1 has a different number of microstructural metrics depending on the type of microstructure. PCA of the primary vasculature evaluates 11 original microstructural metrics, Haversian canals 10 metrics, secondary osteons 10 metrics, primary lacunae 8 metrics, and secondary lacunae 8 metrics (Figure 5.20).

For the principal components analysis of Primary Dataset Run 2, metric values for each type of microstructure are averaged per micrograph. For the Run 2 input matrix, each row corresponds to one micrograph (one micrograph is 1.5mm in height and the

Feature	Shape#	Total Shape#	Centroid X	Centroid Y	TopLeft X	TopLeft Y	Shape Circumference	Shape Area	Ellipse Major Axis Length	Ellipse Minor Axis Length
red	NA	20	NA	NA	NA	NA	566.627649	24789.7	219.770912	139.252822
blue	NA	22	NA	NA	NA	NA	91.067267	643.954545	34.896914	22.167391
green	NA	10	NA	NA	NA	NA	41.648275	110.8	16.397066	8.860041
cyan	NA	10	NA	NA	NA	NA	31.892029	69	11.764597	7.562983
magenta	NA	13	NA	NA	NA	NA	107.672388	886	44.115031	22.925404
red	1	20	1636	90	1639	33	355.344248	10263	129.063403	101.718618
red	2	20	1099	233	1092	72	787.972841	43123	332.785543	165.868255
red	3	20	713	161	684	109	345.169008	9391	131.092548	91.607058
red	4	20	1759	359	1744	254	593.928752	28794	208.101096	177.595982
red	5	20	1466	445	1534	326	678.863735	33648	286.784088	151.918888
red	6	20	1912	419	1911	337	475.227793	18229	176.663171	131.848055
red	7	20	874	453	856	351	587.271882	27053	207.528089	170.537684
red	8	20	1854	631	1813	558	439.388337	15351	173.804196	112.933207
red	9	20	1257	645	1223	562	622.746164	30526	226.591201	173.00726
red	10	20	1668	729	1665	643	486.410381	19577	163.451361	154.256717
red	11	20	619	761	586	672	437.198401	12510	187.554594	85.21043
red	12	20	1792	827	1786	753	484.380988	19251	165.83716	148.031335
red	13	20	1670	926	1598	801	718.703191	38717	290.680384	173.565073
red	14	20	998	919	979	815	563.417729	25413	211.110308	153.99798
red	15	20	1232	969	1225	874	507.06725	21169	181.74951	149.193211
red	16	20	423	1219	310	887	1517.4714	84160	654.756084	198.316378
red	17	20	1876	1048	1889	990	387.811181	11863	129.651472	117.541175
red	18	20	1317	1139	1279	1045	567.812297	23258	241.355586	126.690307
red	19	20	1371	1294	1317	1244	356.497443	9443	142.233272	84.854532
red	20	20	1433	1410	1423	1342	419.869966	14055	154.625169	116.364286
...

Figure 5.17: An example of the raw output from the Welsh computer program using a portion of the data obtained from the periosteal portion of sample 10 (micrograph) of the bobcat thin-section. The three dots in each of the sections of the last row and column signify the continuation of data. Please refer to the text for further details

RUN		SAMPLE TYPE	# OF SAMPLES
1	A	Secondary Osteons	3580
	B	Haversian Canals	3610
	C	Primary Lacunae	1992
	D	Secondary Lacunae	2141
	E	Primary Vasculature	4343
2	N/A	Per Micrograph	161
3	N/A	Per Cross-section	11

Figure 5.18: A summary table of PCA Runs 1, 2, and 3 of the Primary Dataset.

total width of the cortex) from part of the one thin-section made for each of the 11 mammalian taxa (Figure 5.21). Each column in the PCA matrix corresponds to a microstructural metric, and the value that appears in the box is the average value of that metric within the specified micrograph. Each micrograph is considered here to be one “sample” of data, for a total of 161 samples (m). Because of the size difference in the cortex of the mid-tibial sections of these mammals, some taxa are represented by more micrographs (samples) than others (Figure 5.2). For the columns corresponding to microstructural metrics, the analysis of Run 2 begins with 11 metric values (see chapter 3 and above) for the primary vasculature, followed by 10 metrics for the Haversian canals, 10 metrics for the secondary osteons, 8 metrics for the primary lacunae, 8 metrics for the secondary lacunae, 1 metric describing cortical thickness, and an additional 3 metrics comparing measurements of certain microstructural features (Figure 5.16), for a total of 51 metrics (n).

For principal component analysis Run 3 of the Primary Dataset, the metric values for each type of microstructure are averaged over each complete tibial cross-section. In the Run 3 input matrix, each row corresponds to one tibia cross-section (Figure 5.22), i.e., also one taxon. Each cross-section is considered one “sample”, for a total of 11 samples (m). Each column corresponds to a microstructural metric. The analysis of Run 3 begins with 11 metric values (see chapter 3 and above) for the primary vasculature, 10 metrics for the Haversian canals, 10 metrics for the secondary osteons, 8 metrics for the primary lacunae, 8 metrics for the secondary lacunae, 1 metric

Micrograph #	Microstructural unit#	Taxon	SOC	SOA	SOMaj	SOMin	SOMMR	SOCEllipse	SOAEllipse	SOR	SOLong	SOPeri
NCSM 05363 33	1	Bear	337.0085	9658	119.2866	103.4817	1.152731	350.364028	9694.935109	0.961881	29.83001	60.76927
NCSM 05363 33	2	Bear	380.6874	11334	152.3915	94.84375	1.606764	393.634634	11351.65915	0.967109	51.51066	58.97462
NCSM 05363 33	3	Bear	322.4827	7756	125.8795	79.36574	1.586069	326.551477	7846.536687	0.98754	50.91374	67.8471
NCSM 05363 33	4	Bear	385.6506	11482	133.4601	111.5163	1.196755	385.58335	11689.27491	1.000175	33.32236	134.1246
...
NCSM C. canadensis 23	4516	Beaver	924.9372	69404	323.6953	273.7144	1.182602	940.051746	69586.32516	0.983922	32.26449	34.34433
NCSM C. canadensis 23	4517	Beaver	690.8196	37789	233.9624	210.2897	1.112572	698.325099	38641.50693	0.989252	25.9968	144.4169
NCSM C. canadensis 23	4518	Beaver	911.4188	67596	310.46	280.3331	1.107468	928.619003	68354.9384	0.981478	25.44999	43.37824
NCSM C. canadensis 22	4519	Beaver	452.7021	16398	157.3348	133.2158	1.181053	457.182422	16461.53859	0.9902	32.14522	98.87157
...
F rufus 02	5732	Bobcat	250.5992	5015	85.33613	75.67918	1.127604	253.149759	5072.233842	0.989925	27.52164	50.55964
F rufus 02	5733	Bobcat	407.8406	13323	147.0436	115.8085	1.269714	414.345938	13374.46123	0.9843	38.04016	171.3592
F rufus 02	5734	Bobcat	488.5856	15314	219.5612	89.47772	2.453808	507.189207	15429.80246	0.96332	65.95025	120.438
F rufus 02	5735	Bobcat	314.1323	8180	108.122	96.50716	1.120352	321.689624	8195.271657	0.976507	26.80114	170.163
...
MCZ 0438 06	8089	Capuchin	379.5048	11804	129.4506	116.3955	1.112162	386.446537	11833.96691	0.982037	25.95345	13.69308
MCZ 0438 06	8090	Capuchin	344.0158	9806	123.0499	102.1854	1.204183	354.558091	9875.515006	0.970266	33.85618	96.2007
MCZ 0438 06	8091	Capuchin	268.7744	5855	92.74592	80.55732	1.151304	272.560833	5867.99451	0.986108	29.70588	153.0821
MCZ 0438 06	8092	Capuchin	869.4188	30942	308.3963	145.6986	2.116673	736.372159	35290.23565	1.180679	61.80723	96.53863
...

Figure 5.19: A portion of the data input for Run 1 of the Primary Dataset showing individual data points used to illustrate the spreadsheet structure. Cells containing three dots symbolize the continuation of data. Only columns for the 10 metrics of the secondary osteons are shown. All metrics shown in Figure 5.20 appear here as columns.

		Microstructural Type				
		Primary Vasculature	Primary Lacunae	Secondary Osteons	Haversian Canals	Secondary Lacunae
Metric	Microstructural Unit Circumference	✓	✓	✓	✓	✓
	Microstructural Unit Area	✓	✓	✓	✓	✓
	Bounding Ellipse Major Axis Length	✓	✓	✓	✓	✓
	Bounding Ellipse Minor Axis Length	✓	✓	✓	✓	✓
	Bounding Ellipse Major/Minor Ratio	✓	✓	✓	✓	✓
	Bounding Ellipse Circumference	✓	✓	✓	✓	✓
	Bounding Ellipse Area	✓	✓	✓	✓	✓
	Microstructure/ Bounding Ellipse Circumference Ratio	✓	✓	✓	✓	✓
	Orientation with Longitudinal Axis of Diaphysis	✓	/	✓	✓	/
	Nearest Bounding Ellipse Centroid	✓	✗	/	/	✗
	Orientation of Major Axis with Periosteal Surface	✓	/	✓	✓	/
	Total # of metrics	11	8	10	10	8

Secondary Osteon/Haversian Canal Circumference Ratio	✗
Primary Lacuna/Secondary Lacuna Circumference Ratio	✗
Primary Vascular/Haversian Canal Circumference Ratio	✗
Cortical Thickness	✗

✓ Included in analysis
 ✗ Not included in analysis
 / Not applicable to microstructure

Figure 5.20: The metrics that can be applied to individual measurements with no averaging are denoted with check-marks. Only these measurements are used in Run 1 of the Primary Dataset.

Micrograph #	Taxon	SOC	SOA	SOMaj	SOMin	HCC	HCA	HCMaj	HCMin	PLC	PLA	PLMaj	PLMin	...
Marmota 01	groundhog	470.8044	15267.5	177.7116	116.0759	...	82.62069	531.5	29.52271	23.44276	53.47315	177.1	22.42601	10.29281
Marmota 03	groundhog	312.4827	7701	118.1107	83.73212	...	110.0441	769	43.75851	23.68329	57.47021	195.6	23.96356	10.64469
Marmota 04	groundhog	398.921	13659.67	146.5727	112.7723	...	96.37497	741.3333	36.00374	25.9644	47.98553	146.3	19.78505	9.703855
Marmota 05	groundhog	286.8427	6867.333	104.4432	78.49958	...	62.05615	318.6667	22.96022	16.59871	49.60011	157.9	20.04262	10.18764
MCZ 438 01	capuchin	438.3704	15693.48	161.9114	117.4	...	130.2822	1491.462	46.45349	37.56016	46.52131	148.6	18.81683	10.19511
MCZ 438 02	capuchin	572.0819	24285	221.9837	140.6033	...	143.0735	1510.5	58.46305	32.84468	53.40158	171.9	22.20776	10.14128
MCZ 438 03	capuchin	48.22058	150.8	19.67395	9.944629
MCZ 438 04	capuchin	417.0874	14277.4	146.7952	121.9346	...	116.8909	1071	44.14654	30.88806	52.45415	173.9	21.81013	10.4586
...
MCZ 59274 01	lemur	556.0538	26314.81	205.2123	153.8712	...	106.5327	812.2	43.73832	22.36497	37.05263	86.55	14.66359	7.618444
MCZ 59274 02	lemur	528.6673	23066.2	196.9736	144.3684	...	70.06344	367	26.05597	18.10618	39.21407	96.57895	15.73393	7.973996
MCZ 59274 03	lemur	607.4295	29787.6	226.9116	160.9193	...	89.09026	510.1667	36.89639	17.84274	39.93731	99.9	16.04647	8.015973
MCZ 59274 04	lemur	577.1405	24004.4	217.9318	140.9627	...	78.14132	453.5	28.5829	20.4469	37.14387	85.8	14.85873	7.499714
...

Figure 5.21: A portion of the data input for Run 2 of the Primary Dataset using micrographs as “samples.” Cells containing three dots symbolize the continuation of data.

describing cortical thickness, and an additional 3 metrics comparing measurements of certain microstructural features (Figure 5.16), for a total of 51 metrics (n).

The number of principal components calculated for each Run is different depending on the type of input matrix. Three principal components are calculated for each analysis in Run 1 (5 total analyses). Fifteen principal components are calculated for Run 2, and 11 principal components for Run 3. The number of principal components that may be calculated depends on the number of variables and observations. The total number of possible principal components is one less than the number of variables or observations, whichever is the lower number. In Run 2 there are 51 variables and 161 observations, making the number of possible principal components 50. In Run 3, there are 51 variables and 12 observations, making the number of possible principal components 11. Most of the variance is usually accounted for in the first three components. Extending the analyses of Runs 2 and 3 to 15 and 11 components, respectively, simply offers a better analytical view of the data, but may not offer additional information. This issue will be discussed in a later section.

For initial exploration of the data, it was very important to retain all input variables and microstructural data points before assuming that the input should be modified in some way for enhanced analysis. The actual numbers of samples for each taxon in Run 1 were retained (i.e., not normalized to a standard number of samples) because the difference in the number of samples provides additional information that could be used. For instance, if one cross-section contains a greater density of primary vascular canals than another cross-section, this observation could be a separating feature at some taxonomic level. Normalizing the data to equal numbers of primary vascular canals per cross-section would eliminate this distinction. For the same reason, the different numbers of micrograph samples in Run 2 (Figure 5.2) per cross-section were not normalized across taxa (i.e., the number of micrographs per cross-section is an indicator of the size of the tibial specimen). To calculate the principal components of the variables in Runs 1, 2, and 3, $n \times m$ covariance matrices are used to calculate n eigenvalues and their corresponding eigenvectors.

TAXON	SOC	SOA	SOMaj	SOMin	...	HCC	HCA	HCMaj	HCMin	...
Bobcat	505.597	21274.8	187.69	130.643	...	79.9021	521.006	30.1711	20.0684	...
Bear	397.159	12631.6	145.748	106.074	...	96.6312	781.92	35.8959	25.7165	...
Beaver	589.545	29720.5	218.18	160.557	...	133.75	1763.08	49.3656	36.2215	...
Capuchin	432.934	15285.5	158.652	116.863	...	132.095	1482.07	47.9677	36.9836	...
Coyote	405.47	14005.2	149.83	110.39	...	91.5424	681.057	34.3137	23.6682	...
Groundhog	389.261	12433.2	149.643	97.6736	...	87.6715	681.931	33.6942	21.9926	...
Hare	264.209	5502.94	96.74	69.5959	...	64.6798	329.426	23.1766	15.9002	...
Lemur	497.761	20635.5	184.646	133.997	...	85.058	529.382	33.0572	19.8127	...
Opossum	258.583	5636	93.9168	71.0731	...	79.4685	495.242	29.3587	20.9727	...
Raccoon	410.688	13720.9	151.384	109.127	...	87.1615	663.519	33.3866	21.7605	...
Rhesus	538.933	26475.4	197.815	147.069	...	118.972	1320.15	43.3771	32.5547	...

Figure 5.22: A portion of the data input for Run 3 of the Primary Dataset using the entire cross-section of each taxon as a “sample.” The values listed are averaged over an entire thin-section. Cells containing three dots symbolize the continuation of data.

5.3.4 Retention and Discarding of Principal Components

Hypothetically, as stated above, the PCA output would transform the data with a resulting output of n eigenvalues. The variance accounted for by each of the principal components is represented by its associated eigenvalue. In this study, an eigenvalue represents the variance of a component over all taxa. An eigenvalue is a scalar value that corresponds to each eigenvector of the linear transformation (such as any combination of stretching, rotation, reflection, compression, or shear) of a vector space. Each eigenvector defines a principal component. The eigenvectors with large eigenvalues are those that contribute most strongly to the PCA model; eigenvectors with small eigenvalues contain very little to no information and may be considered “noise”. Determining the true dimensionality of the data is a balance between retaining and discarding components. The goal is to retain enough principal components to capture the meaningful trends in the data set, while discarding those components that are neither meaningful nor statistically relevant. There are several strategies that have been proposed to determine the number of components to retain after principal components analysis of a correlation matrix. The Kaiser-Guttman rule and the Cattell scree test are well-studied techniques used for this purpose (Browne, 1968; Cattell, 1966, 1978; Guttman, 1954; Hakistan et al., 1982; Kaiser, 1960; Linn, 1968). The Kaiser-Guttman rule maintains that it does not make sense to retain components in the analysis with eigenvalues values less than one. Eigenvalues less than one indicate that the component explains less variance than the original, standardized variables in the data set. Using this rule, all components with eigenvalues greater than or equal to one are retained. The Cattell scree test is a graphical method that determines the number of components that will be retained based on visual inspection of a change in slope. By graphing the components’ eigenvalues against the component number and joining all of the points, a sharp break in the slope of the curve is used to indicate the number of components to retain, as illustrated later in the chapter. Choosing an optimal eigenvalue cutoff is a subject of some debate amongst statistical theorists; these debates are clearly beyond the scope of this dissertation. The Kaiser-Guttman rule sometimes retains too many components, whereas the Cattell scree test sometimes does not retain enough components. However, both tests offer intuitive interpretation, and will be shown to produce robust and meaningful results in the context of

bone microstructure. Both techniques are used in this dissertation and the results compared.

5.3.5 Output

The software package Evince (Umbio, 2009) was used to facilitate PCA analysis. Evince is a program for PCA, written and marketed by Umbio, a spin-off of the Wold group at Umea University, Sweden; Herman and Svante Wold are the forefathers of modern PCA and PLS analysis, having published the non-linear iterative partial least squares (NIPALS) and partial least squares (PLS) algorithms beginning in 1966. Evince combines rigorous statistical analysis and easy visual display of data, variables, loadings, and PCA models.

The PCA implementation provides the mathematically optimal factorization of the $n \times m$ matrix into two matrices: T , the scores matrix (dimensionality: $n \times f$) and P , the loadings matrix (dimensionality: $m \times f$), where f is the number of factors. The factors, f , are linear combinations of the original variables and are referred to as principal components in PCA.

Scores: T

The T matrix provides information on the variables that explain the greatest amount of variance in the dataset and that contribute to the separation of taxa according to principal component axes. This provides an intuitive visual output for the optimal score for a given loading matrix. The visual output of the T matrices for Run 1 is configured in two dimensions using principal components 1 and 2 as the X- and Y-axes, respectively (for an example of this plot, refer to Figure 5.25 presented later in this chapter). The visual plot of T matrices for Runs 2 and 3 of the Primary Dataset are configured in three dimensions using principal components 1, 2, and 3 as the X-, Y-, and Z- axes. Examples of these plots are presented later in this chapter in context of the principal components analysis in Figure 5.38 and Figure 5.47. The numerical values on each of the axes correspond to the scalar quantities of the eigenvector

representing each component. All data are centered about the origin as a result of data normalization (i.e., subtracting the mean from each value).

The scores plot can be referred to as a map of samples. The 3D plots of T matrix results are organized according to taxon. Each sample (i.e., each micrograph or each taxon) is represented by a sphere. The color of each sphere corresponds to the taxon (Figure 5.38). The size of the colored spheres indicates perspective on that particular graph and has no further meaning. The variables that are most responsible for the organization of the data in the scores matrix (T) are given in the P matrix.

Loadings: P

The loadings matrix (P) provides information on those original variables that account for the greatest amount of variance in the scores (T) and that contribute to the separation of taxa. Like the values of the PCA scores, the loadings can be plotted with axes defined by principal components (e.g. Figure 5.25 B). The loadings plot can be referred to as a map of variables.

Because each principal component is a combination of the original variables, it is possible to ascribe physical meaning to what the components represent. This relationship also allows for the recognition of variables that do not contribute to the variance of the data and that therefore could be excluded from future analyses without loss of information. PCA provides a powerful paradigm for converging upon a minimal set of variables that still maintain optimal diagnostic power. First, a full data set is analyzed, and score and loading matrices are calculated. On the first iteration, the input data likely contain redundant information and information of low variance, which can be pruned from consideration in the PCA model by examining their relative (weighted percentage) contribution in the loading matrix, P .

For example, consider the bone microstructure measurements for the circumference of an actual microstructural unit and the circumference of its best-fit ellipse. It is clear from visual examination of many bone microstructure micrographs that the measured features tend toward elliptical shapes. However, it was not known *a priori* to what degree ellipticity would be diagnostic. Clearly, some shapes are well-fit by an ideal two-axis ellipse, while other shapes (like curving primary vascular canals; Figure 5.23)

are better fit by a numerical pixel-by-pixel shape descriptor. Combining knowledge of the system and the PCA loadings, it is possible to reasonably judge whether shape circumference and ellipse circumference were reporting redundant information to the PCA model. If these two measurements were found to correlate strongly, the ellipse circumference might be removed from consideration in the next iteration of the PCA model, to prevent redundant information in the loading matrix.

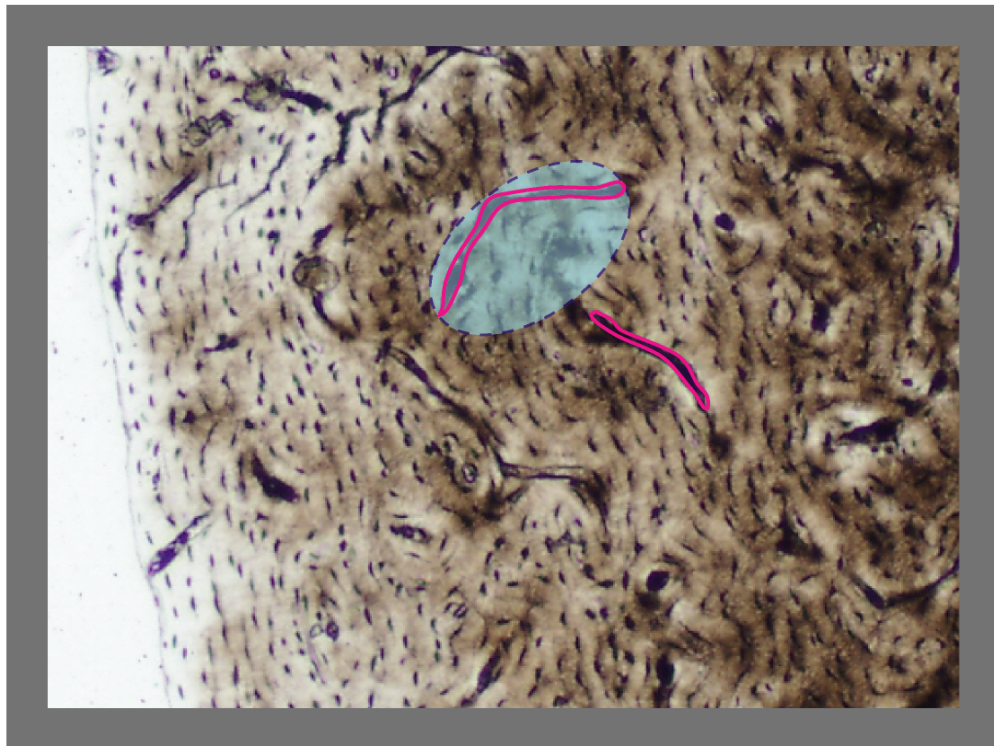


Figure 5.23: The primary vascular canal outlined in red in this figure deviates from the expected “elliptical” shape, making measurement by best-fit ellipse (blue shading) subject to greater error in representation. Measurement of the actual shape outline will give a better representation of the “real” circumference.

It is also important to consider those variables that may contribute little diagnostic power to the model. Regardless of the weighting, it is not possible to derive meaningful distinctions from variables that do not change much across experimental samples (i.e., they have a small global experimental variance). For example, consider the bone microstructure measurements for the angle of orientation of the primary vascular

canals with respect to the periosteal surface (PVPeri). In Run 1E, this variable contributed very little to the loading matrix (see Figure 5.30), with a value almost at the origin (0, 0), meaning that the variance in the measurements of the angle of orientation of the primary vascular canals with respect to periosteal surface did not contribute to the separation of taxa. Therefore, this variable may be removed from the the PCA model, because no matter the weighting, it cannot contribute any useful signal, only noise. In this way, a PCA of the entire dataset iteratively verges toward a PCA model having only meaningful diagnostic variables. This kind of iterative data pruning is entirely self-consistent and unbiased as long as unique variables having diagnostic power are maintained in the set.

Eliminating the low-variance components, while reducing “noise”, also discards some amount of information, so it is necessary to strike a balance between reducing dimensionality and capturing meaningful data. It is preferable to retain too many principal components than to retain too few. Retaining too many components leads to a situation where there is unnecessary noise in the data set, but since the principal components are loaded according to the ranked P matrix, the contribution of “noisy” components is minimized. The explanatory power estimates for the first few principal components should be accurate. Retaining too few components is more dangerous, because significant but unaccounted-for principal components may not contribute to loadings in the P matrix, thereby leading to erroneous estimates of the significance of the first components. Detailed results of the scores and loadings matrices from the present analyses are discussed below.

The variables are distributed on the P matrix plots according to their contribution to each principal component (e.g., Figure 5.30). The scalar values on the X- and Y- axes do not correspond to the “amount” of variance explained by a variable. Rather, what is important in the P-plot is the position of the variable relative to the origin of the graph. The closer a variable is to the origin of the graph, the less effect it has on the variance, whereas the farther the variable is from the origin (either in the positive or negative direction) the more effect it has. Variables that plot on the same principal component axis but that are associated with opposite signs (-/+) on the graph, are inversely correlated. Variables that plot within the quadrants of the graphs indicate their covariance with respect to the two principal components.

5.4 Results of Principal Components Analyses

5.4.1 Run 1

Run 1 evaluated the variance of each type of microstructure measured throughout the taxa of the Primary Dataset. By partitioning the microstructures by type (i.e., secondary osteons, Haversian canals, primary lacunae, secondary lacunae, and primary vasculature) into five separate analyses, individual variation within each type of microstructure could be evaluated within the set of taxa. The analyses lend themselves to direct questions. Could the taxa be separated on the basis of a suite of measurements made on a single type of microstructural feature (i.e., can the taxa in the Primary Dataset be distinguished using only the differences in the secondary osteons)?

No more than three principal components were retained for each analysis in Run 1 (Figure 5.24). Principal components with eigenvalues greater than or equal to one were retained based on the Kaiser-Guttman rule.

Secondary Osteons: 1A

PCA of the secondary osteons (Run 1A) resulted in two principal components that account for 79% of the variance in the dataset (Figure 5.24). Principal component 1 (PC1) shows that most of variance is due to the size of the secondary osteon (Figure 5.25 B). The measurements of the actual microstructures (e.g., SOC) track with estimations of the best-fit ellipse estimations (e.g., SOCEllipse). This relationship can be interpreted in two ways: (1) the secondary osteons in the Primary Dataset, regardless of taxon, have an overall elliptical shape or (2) the measurements of the actual microstructure and the best-fit ellipse are different, but equally important in explaining the variance. The metric that compares the ratio of the actual secondary osteon circumference with the circumference of the best-fit ellipse (SOR) was created to make this distinction. On the loadings plot, SOR plots in the upper right quadrant and therefore shows covariance between PC1 and PC2; SOR also is positioned far from those metrics related to osteon size, which are grouped on PC1. This suggests that

Secondary Osteons

Principal Component	r^2	r^2 Cumulative	Eigenvalue
1	0.599	0.599	5.9906
2	0.1877	0.7868	1.8779
3	0.09973	0.8865	0.9973

Haversian Canals

Before removal of outliers

Principal Component	r^2	r^2 Cumulative	Eigenvalue
1	0.5539	0.5539	5.5398
2	0.1887	0.7427	1.8878
3	0.1232	0.8659	1.2323

After removal of outliers

Principal Component	r^2	r^2 Cumulative	Eigenvalue
1	0.5792	0.5792	5.7925
2	0.1942	0.7734	1.9424
3	0.1002	0.8737	1.0022

Primary Lacunae

Principal Component	r^2	r^2 Cumulative	Eigenvalue
1	0.7233	0.7233	5.7871
2	0.1769	0.9003	1.4152
3	0.09455	0.9948	0.7564

Secondary Lacunae

Principal Component	r^2	r^2 Cumulative	Eigenvalue
1	0.7298	0.7298	5.8385
2	0.1717	0.9015	1.3742
3	0.09239	0.9939	0.7391

Primary Vasculature

Principal Component	r^2	r^2 Cumulative	Eigenvalue
1	0.5468	0.5468	6.0148
2	0.1725	0.7193	1.8985
3	0.09293	0.8123	1.0222

Figure 5.24: The eigenvalues and r^2 values for each of the five principal components analyses of the Primary Dataset included in Run 1. Using the Kaiser-Guttman rule (eigenvalue must be ≥ 1.0), PCA of the secondary osteons, primary lacunae, and secondary lacunae results in two informative principal components, whereas analyses of the Haversian canals and primary vasculature result in three principal components to explain the variance in the dataset.

there are indeed some secondary osteons in the Primary Dataset that differ from an elliptical shape and that this shape deviation explains some of the variance in the taxa. In a second example, the orientation of the secondary osteons with respect to the periosteal surface (SOPeri), plotting close to the origin of the graph, explains the least amount of variance on PC1 and PC2. No metrics plot on or very near to the axis for PC2. The variance in principal component 2 (PC2) therefore can be explained best by the longitudinal orientation of the secondary osteons (SOLong). SOLong tracks with SOMMR, plotting at the top of the NE quadrant. This is an expected relationship, because both metrics are calculated using the relationship of the major and minor axes of the secondary osteon, which are major players in PC1. The scores plot (Figure 5.25 A) shows how the taxa are arranged with respect to their differences in secondary osteon morphology. The central cloud of bear secondary osteons on the graph shows equal weighting on PC1 and PC2, the variance in the secondary osteons accounted for almost equally by size and longitudinal orientation. However, the bobcat and lemur, whose data clusters extend to a greater degree along PC1, show that the variance in their secondary osteons is mostly a result of size.

Haversian Canals: 1B

The PCA of the Haversian canals (Run 1B) resulted in three principal components that account for 87% of the variance (Figure 5.24). The variance in PC1 (Figure 5.26 A) is explained by the size of the Haversian canal, and PC2 is explained by the ratio of the major and minor axis lengths (HCMMR) and the ratio of the actual Haversian canal circumference to the best-fit ellipse circumference (HCR). The orientation of the Haversian canal with respect to the periosteal surface (HCPeri), located at the origin, does not explain any of the variance in PC1 or PC2, similar to the results from Run 1A. The actual size measurements of the Haversian canals track with the measurements of the elliptical estimations, also like the secondary osteons. However, the variance on PC2 is explained to a greater extent by the ratio of the actual Haversian canal circumference to the circumference of the best-fit ellipse estimation (HCR) than the equivalent metric of the secondary osteons (SOR). The loadings of the Haversian canals were expected to be similar to those of the secondary osteons because they are related, nested microstructures that form in the same remodeling process.

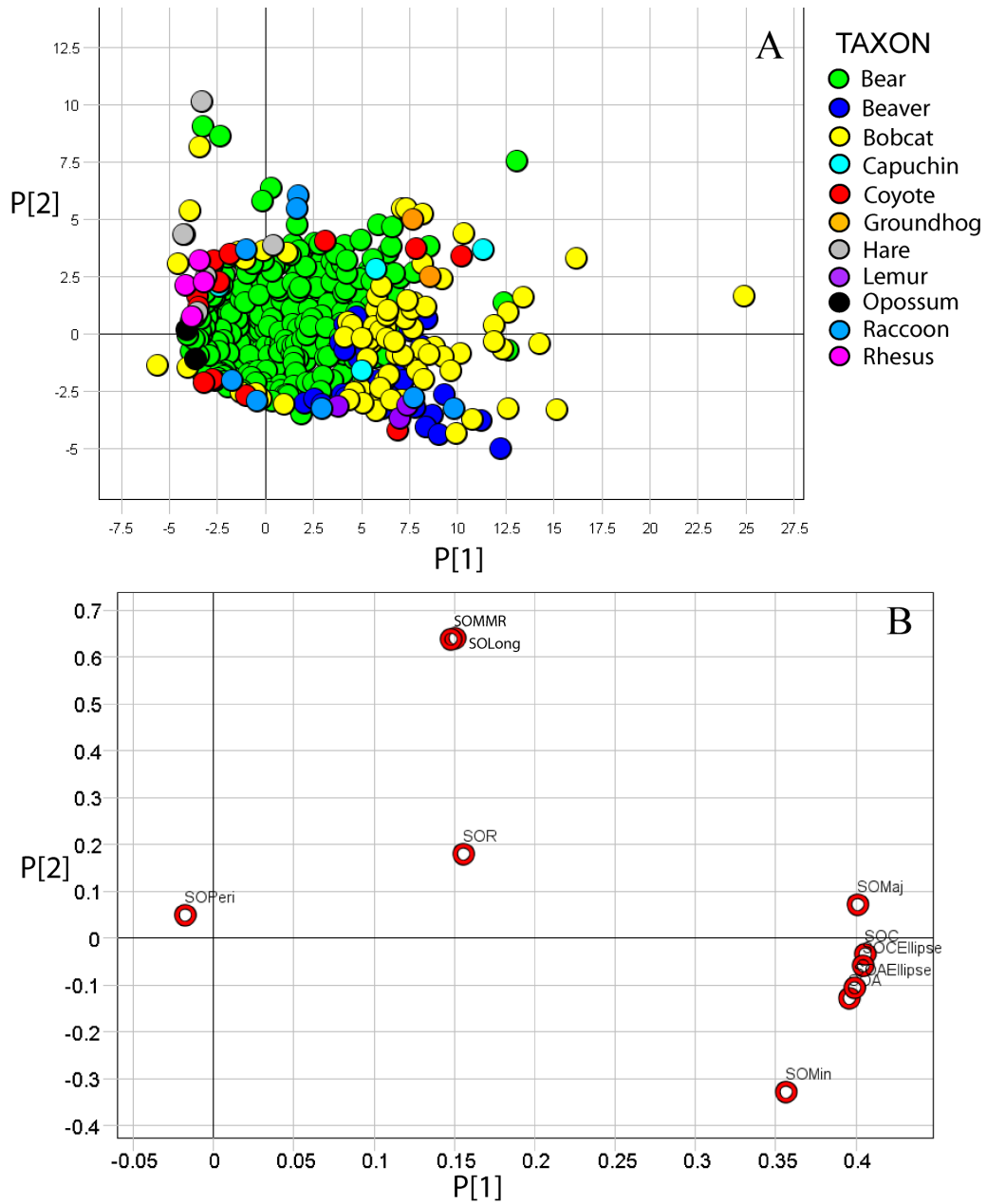


Figure 5.25: The scores (A) and loadings (B) plots for PCA of the Primary Dataset using only microstructural metrics of secondary osteons. Principal component 1 is graphed on the x-axis and principal component 2 on the y-axis.

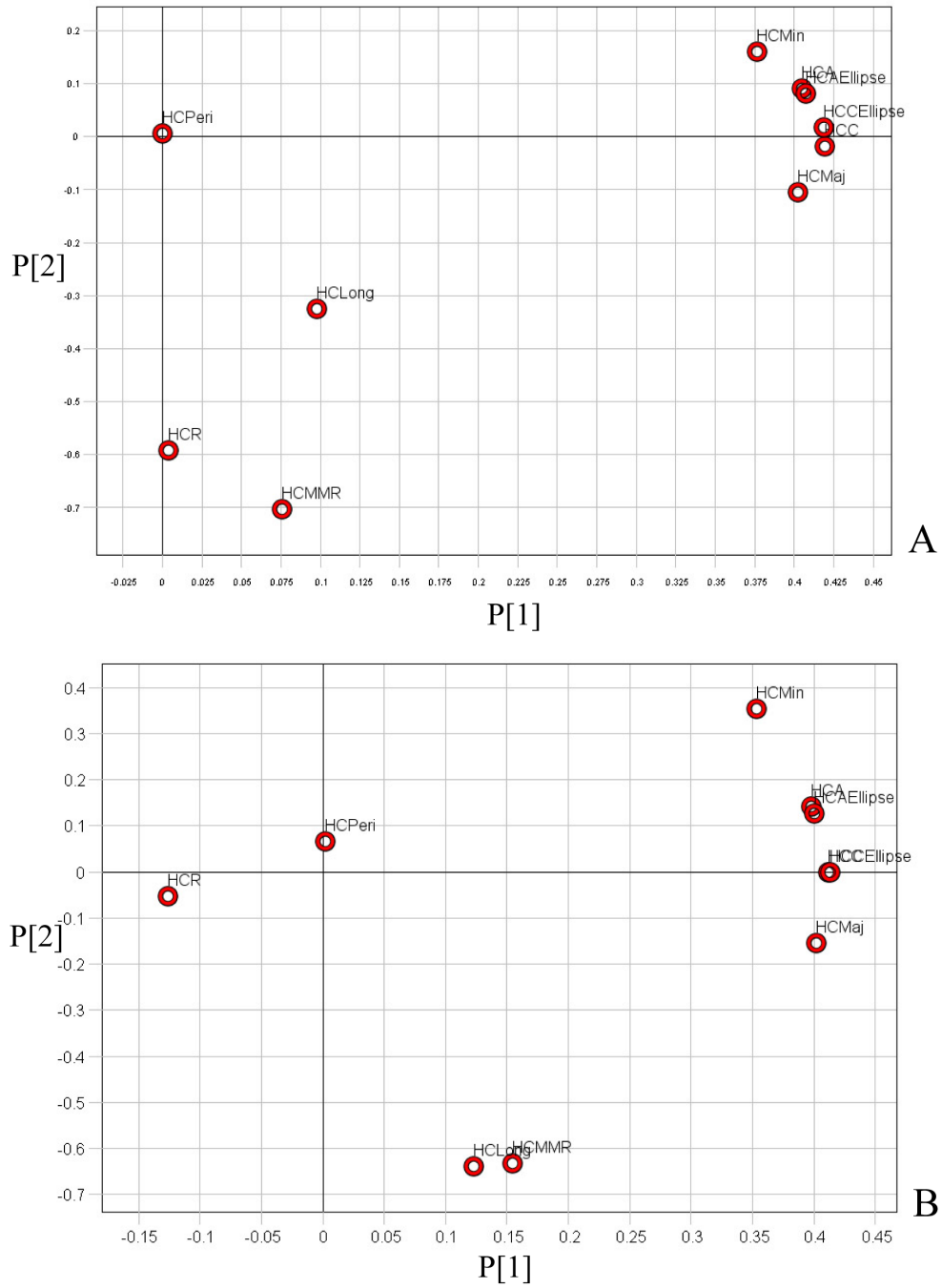


Figure 5.26: The loadings plots for PCA of the Primary Dataset using only microstructural metrics of the Haversian canals. Before removal of 6 outliers (A) and after the removal of 6 outliers (B).

Unlike the scores plot from Run 1A on the secondary osteons, the initial scores plot for the Haversian canals (Figure 5.27) showed a tight grouping of points about the origin and only a few outliers on the graph. The outliers were dictating a lot of the variance in the sample, thus decreasing the resolution among the other data points to lack resolution on the graph. Six outliers were removed to gain resolution among the other data points. The outliers removed represent six Haversian canals measured from bear micrographs 24 (1.9628, -56.72), 32 (-0.915, -28.3), and 07 (-0.721, -23.27), raccoon micrograph 11 (33.991, 5.33847), and beaver micrographs 22 (26.973, 4.318) and 23 (27.729, 4.813). A “before” and “after” comparison of the datapoints in Figure 5.27 A,B reveals the difference in point-cloud resolution and the large amount of the variance attributed to the six datapoints. The eigenvalues change slightly after removal of the six datapoints, the result being three principal components explaining 87% of the data (Figure 5.24). The influence of each variable also changed slightly as a result of outlier removal. The new loadings plot (Figure 5.26 B) shows Haversian canal size metrics to be anti-correlated with HCR along PC1, instead of HCR accounting for most of the variance along PC2. The longitudinal orientation metric explains most of the variance along PC2. The variables HCLong and HCMMR are now shown to track with each other, similar to the loadings of the secondary osteons described above. Although HCPeri shifted slightly from the origin, it still contributes the least to explaining the variance in the samples.

Primary Lacunae: 1C

The PCA of the Primary Lacunae (Run 1C) resulted in two principal components explaining 90% of the variance in the dataset (Figure 5.24). The loadings plot (Figure 5.28 B) shows that PC1 can be explained by the size of the primary lacunae. The actual measurements of the primary lacunae track with the best-fit ellipse measurements. The metric PLR, however, is anti-correlated with the size measurements along PC1. There are no variables close to PC2 (coordinates [0, Y-value]). However, metrics PLMMR and PLMin show covariance between PC1 and PC2. The shape of lacunae, discussed in detail in Chapter 3, is ellipsoidal with different lengths and ratios of major and minor axes. The influence of PLMMR on the variance in the primary lacunar dataset is an indication that the ratio of the major and minor lacunar axes may be specific to taxon. The scores plot (Figure 5.28 A) shows reasonably good

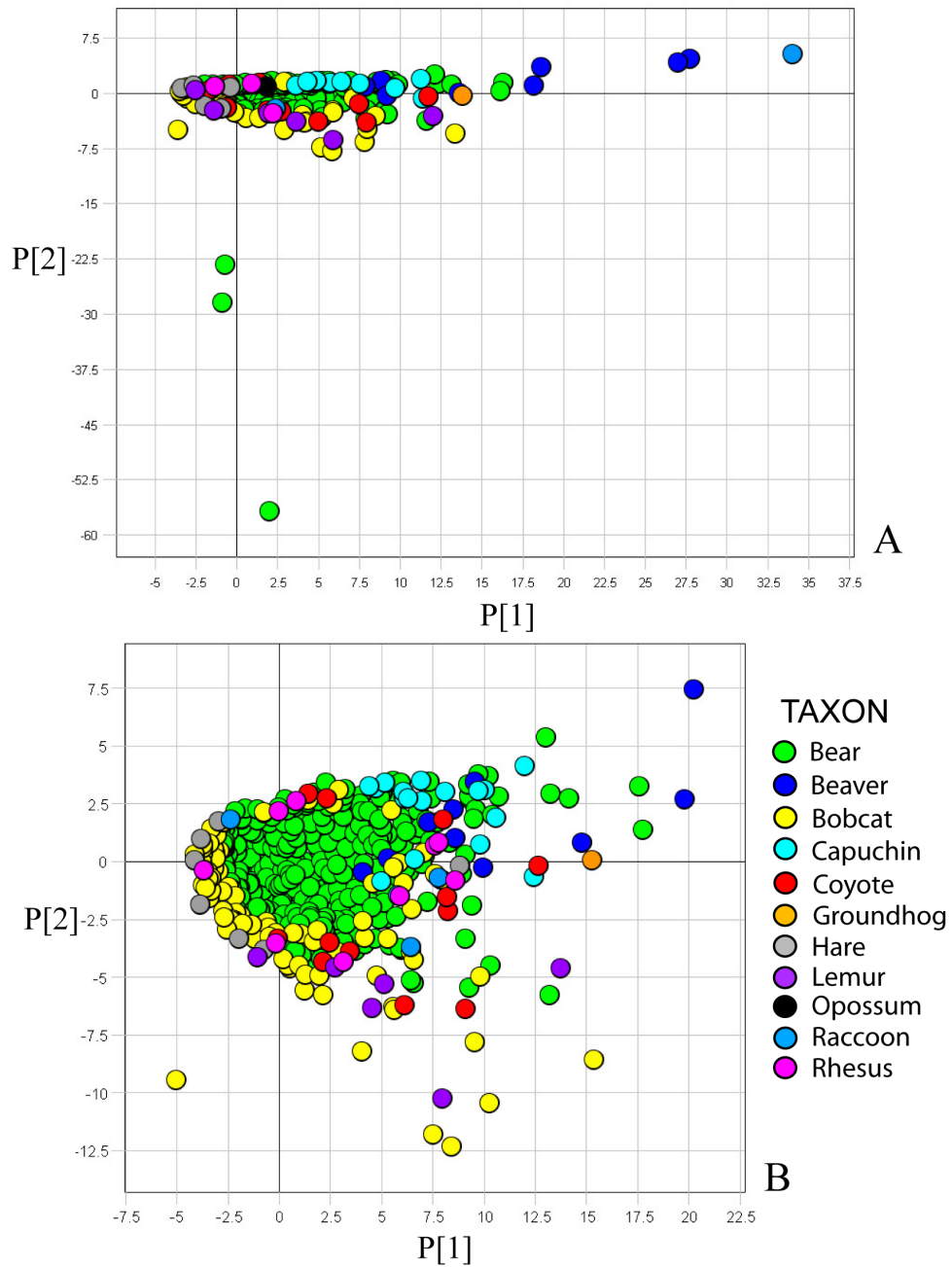


Figure 5.27: The scores plots for PCA of the Primary Dataset using only microstructural metrics of the Haversian canals (A) Before removal of 6 outliers and (B) after the removal of 6 outliers.

grouping of taxon samples. The primary lacunar samples from the bobcat, bear, and beaver form individual, tight groups in comparison with other taxa, such as the rhesus monkey and raccoon. The lemur, even though the samples are not tightly grouped, shows a diagonal trend between PC1 and PC2. This distribution suggests that, in the lemur, there is covariance between PC1 and PC2, but there is also variation in primary lacunar measurements depending on the portion of the cross-section from which they were measured.

Secondary Lacunae: 1D

The PCA of the secondary lacunae (Run 1D) resulted in two principal components explaining 90% of the variance in the dataset (Figure 5.24). The loading plot for the secondary lacunae (Figure 5.29 B) is essentially identical to the loadings for the primary lacunae (Figure 5.28 B). This result is not surprising, because the function and biology of the structures are the same. The main difference is that secondary lacunae are formed during bone remodeling and primary lacunae are formed during initial bone formation. The scores plot (Figure 5.29 A) shows a configuration of samples similar to that of the scores plot for the primary lacunae. Secondary lacunar samples from the bobcat and bear are tightly grouped. The lemur does not show as much sample spread as in the primary lacunae, whereas the rhesus monkey shows a greater amount of sample spread. The variance in the lemur is explained mostly by SLMMR.

Primary Vasculature: 1E

The PCA of the primary vasculature (Run1E) resulted in three principal components explaining 81% of the variance in the dataset (Figure 5.24). The loadings plot (Figure 5.30 B) shows that the variance in PC1 can be explained by the size of the primary vasculature. Compared to the other microstructural types, the size measurements of the actual primary vascular canals do not track as tightly with the best-fit ellipse measurements. The area of the primary vasculature bounding ellipse (PVAEllipse) is different from that of the actual shape (PVA), both showing covariance between PC1 and PC2. Different values for the measurements of the actual shapes compared

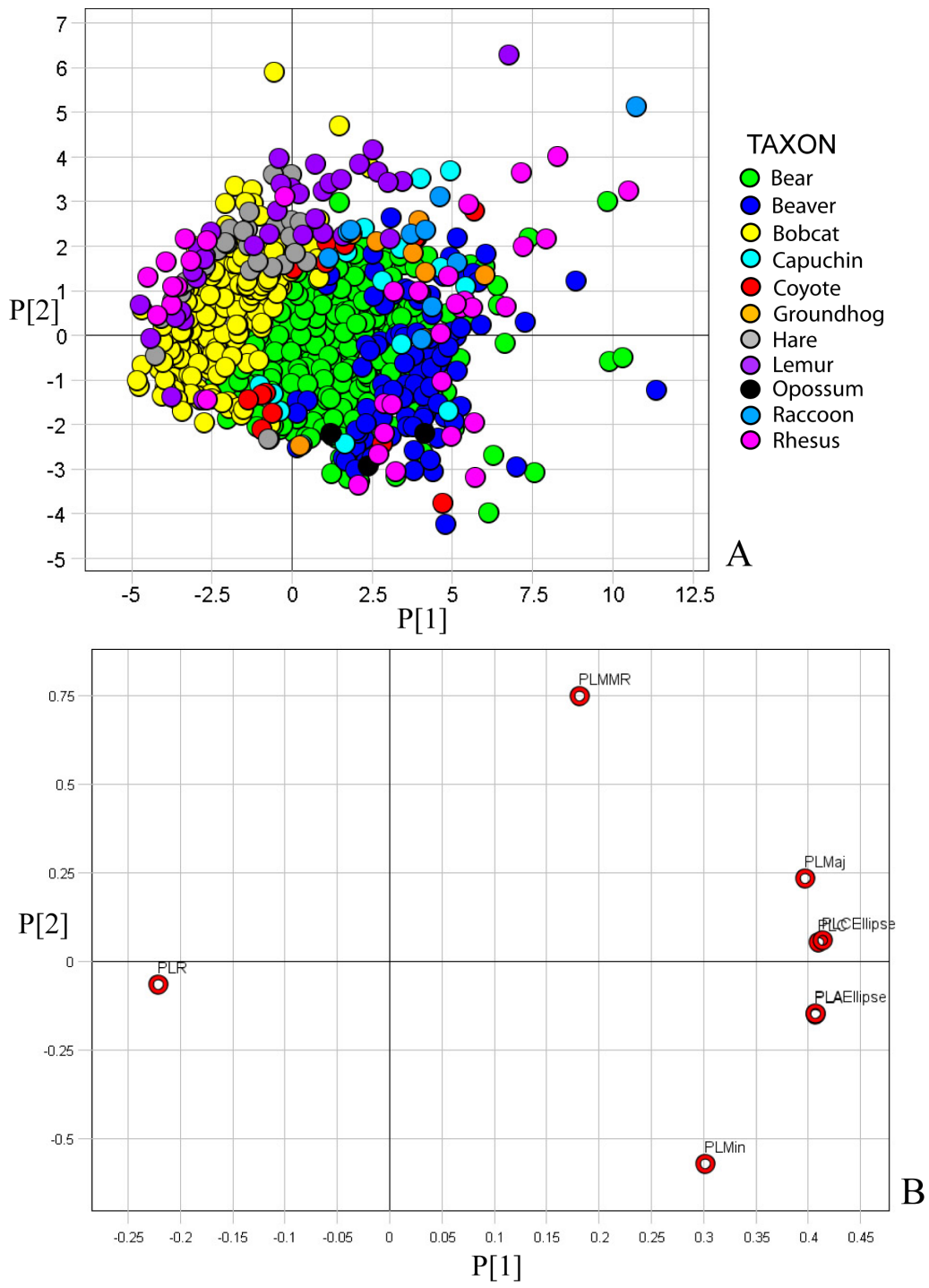


Figure 5.28: The scores (A) and loadings (B) plots for PCA of the Primary Dataset using only microstructural metrics of primary lacunae. Principal component 1 is graphed on the x-axis and principal component 2 on the y-axis

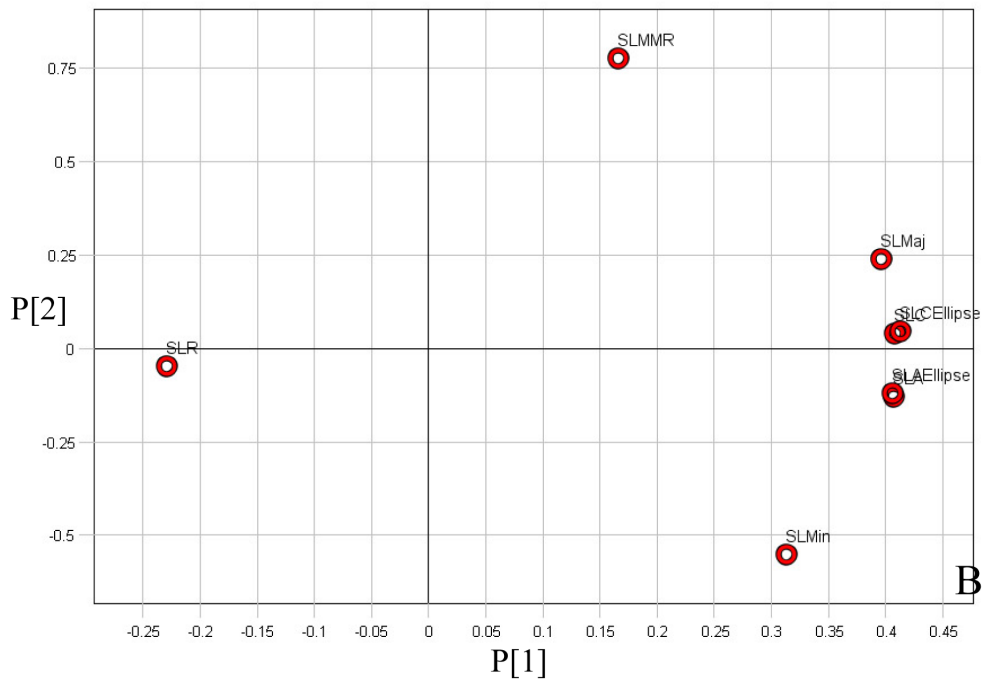
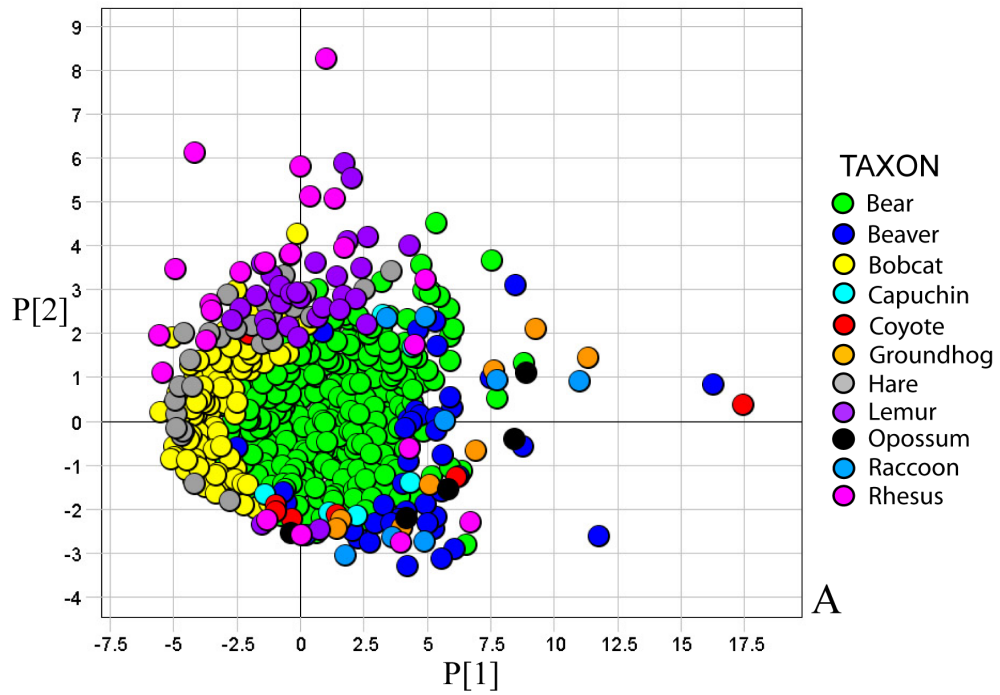


Figure 5.29: The scores (A) and loadings (B) plots for PCA of the Primary Dataset using only microstructural metrics of secondary lacunae. Principal component 1 is graphed on the x-axis and principal component 2 on the y-axis

to those of the best-fit ellipse suggest that the shapes of primary vascular canals deviate from an elliptical shape (see Figure 5.23). The longitudinal orientation of the primary vascular canals (PVLong) and the ratio of the minimum and maximum axis lengths (PVMMR) show covariance between PC1 and PC2. Most of the variance on PC2 is explained by the ratio of the actual primary vascular circumference to the circumference of the best-fit ellipse. The distance from the centroid of each primary vascular canal to the centroid of its closest neighbor (PVCentroid) and the orientation of the primary vascular with respect to the periosteal surface (PVPeri) explain the least amount of variance in the dataset. The scores plot (Figure 5.30 A) does not show much separation of taxa. Primary vascular samples from the beaver are grouped most closely.

Summary: Run 1

In summary, each PCA in Run 1 (A-E) shows that the size of the microstructural features explains the most variance in PC1 in all of the microstructural types. The shape and longitudinal orientation explain most of the variance on PC2. Microstructural orientation with respect to the periosteal surface (Peri) did not explain much of the variance in the samples. The results of the five principal component analyses in Run 1 suggest that taxa cannot be differentiated effectively on the basis of the combined size, shape, and orientation characteristics of a single type of microstructure.

5.4.2 Run 2

As discussed above, PCA Run 2 uses averaged values of each metric per micrograph as “samples” (Tier III in dataset hierarchy). Therefore, each micrograph is considered as one sample, rather than individual microstructural units as in Run 1. The results from the PCAs of Run 1 suggested that taxa could not be differentiated on the basis of size, shape, and orientation of a single type of bone microstructure. PCA of Run 2 explores the taxonomic differentiation of the Primary Dataset further by combining all metrics from the five microstructural types (secondary osteons, Haversian canals, primary lacunae, secondary lacunae, and primary vasculature). By using the averaged values for each microstructural measurement from each micrograph, the PCA of Run

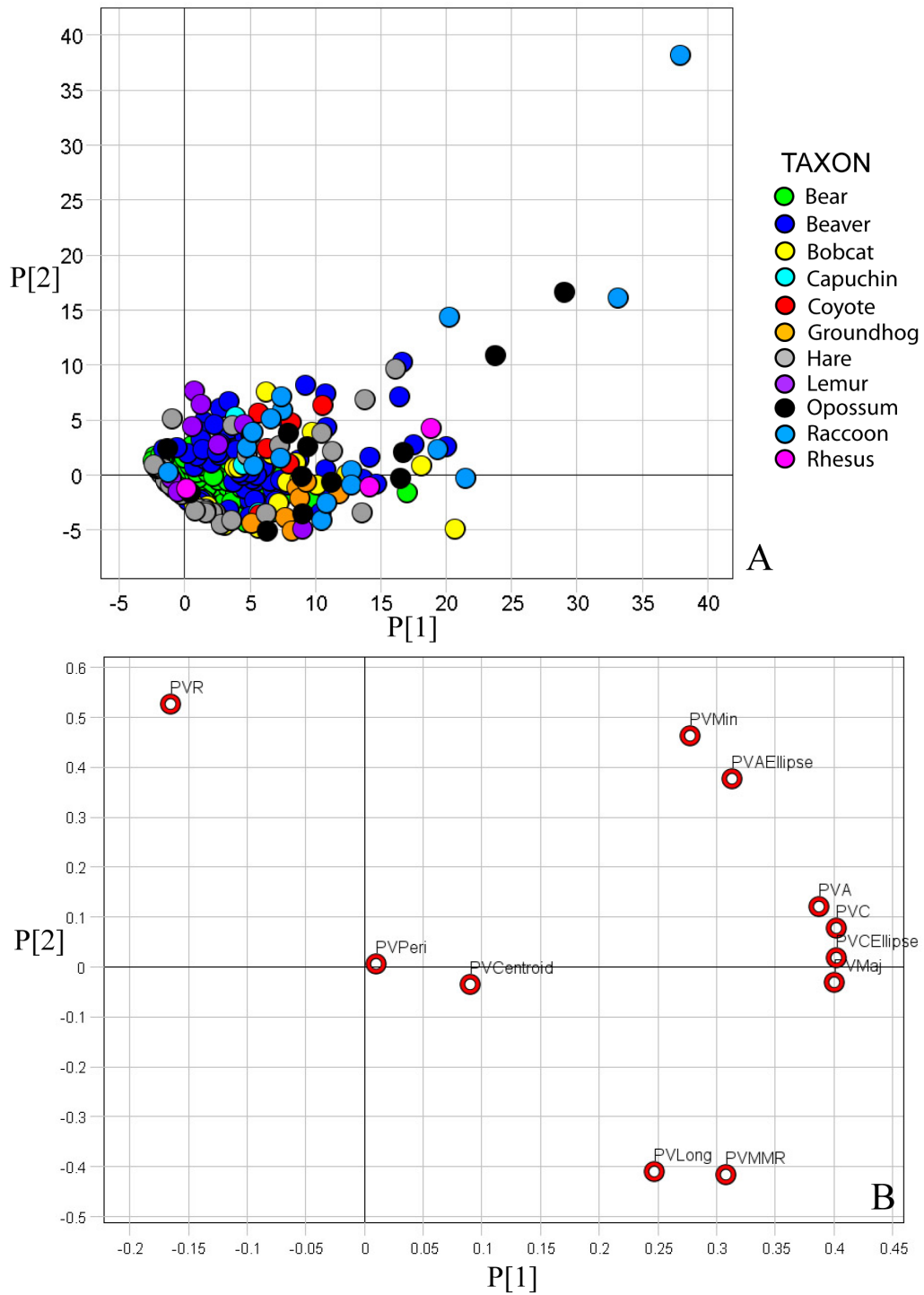


Figure 5.30: The scores (A) and loadings (B) plots for PCA of the Primary Dataset using only microstructural metrics of primary vascular canals. Principal component 1 is graphed on the x-axis and principal component 2 on the y-axis

2 provided a means to explore 1) the ability of this method to separate taxa and 2) the variance within each bone cross-section.

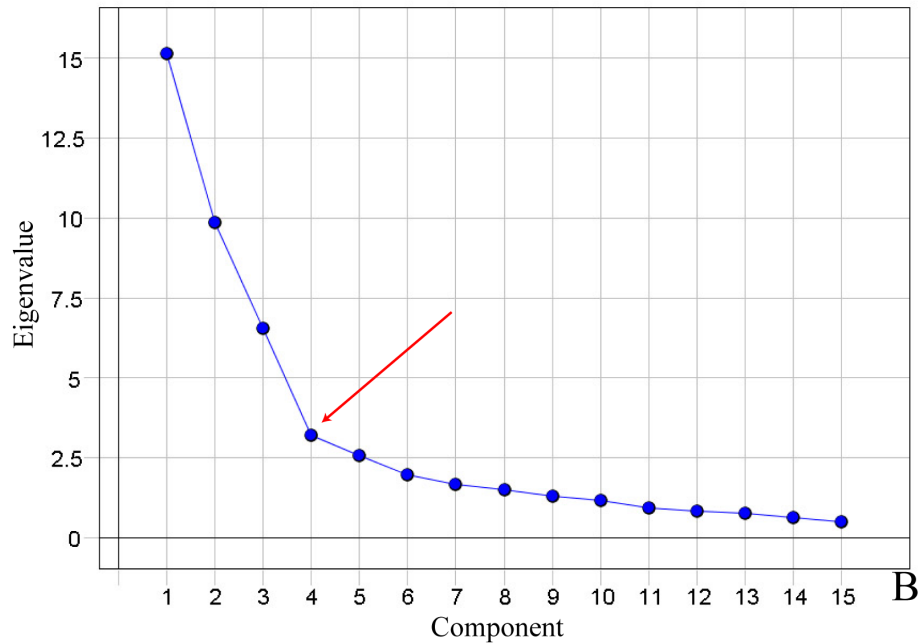
Prior to PCA of Run 2, Capuchin monkey micrograph 03 was removed from the analysis because this micrograph had the greatest number of missing metric values compared to other micrographs in the dataset. The Kaiser-Guttman rule suggests the retention of 10 principal components for Run 2 (Figure 5.31 (A)), explaining 88% of the variance in the dataset. Considering the large number of variables, i.e. 51 bone microstructural metrics, capturing this degree of variance in the first 10 components is good. However, a scree plot of the eigenvalues shows the “elbow” of the slope at principal component 4 (Figure 5.31 (B)). According to the Cattell’s Scree Test, three principal components should be retained for Run 2. The difference in the number of principal components per the Kaiser-Guttman rule and the Cattell Scree Test is large. Per the definition of PCA, the first three principal components account for the majority of the variance in the data, approximately 62%. The variance that is explained for each of the principal components after PC3 is small, indicated by r^2 values of less than 7% each for PC4 through PC15. For Run 2, therefore, PC1 through PC3 are retained as indicated by the Cattell Scree Test.

The PCA of Run 2 resulted in three principal components explaining 62% of variance in the dataset (Figure 5.31). The plot of the P values for PC1 and PC2 is more complex than for Run 1. As shown in Figure 5.32, the least amount of variance in PC1 and PC2 is explained by the orientation of the major axis with respect to the periosteal surface in the primary vascular canals (PVPeri), secondary osteons (SOPeri), and Haversian canals (HCPeri). All other metrics show more explanatory power. The variance along PC1 can be best explained by the size metrics of the primary lacunae and secondary lacunae (Figure 5.33), size metrics of the Haversian canals (Figure 5.34), and the ratio of the shape circumference to best-fit ellipse circumference of the Haversian canals (HCR), primary lacunae (PLR), and secondary lacunae (SLR) (Figure 5.35). The variance along PC2 is best explained by the ratio of the actual shape circumference of the primary vasculature to the best-fit ellipse circumference (PVR) (Figure 5.36), size metrics of the secondary osteons, and size metrics of the primary vasculature (Figure 5.37). The variance in PC3 (not shown) is explained by the longitudinal orientations of the secondary osteons (SOLong) and the Haversian canals (HCLong).

Principal Component	r^2		Eigenvalue
	r^2	Cumulative	
1	0.2968	0.2968	15.139
2	0.1934	0.4902	9.8649
3	0.1285	0.6188	6.5547
4	0.06303	0.6818	3.2148
5	0.05052	0.7323	2.5769
6	0.03878	0.7711	1.978
7	0.03248	0.8036	1.6568
8	0.02941	0.833	1.5003
9	0.0255	0.8585	1.3007
10	0.0225	0.881	1.1475
11	0.01798	0.899	0.9171
12	0.01648	0.9155	0.8405
13	0.01515	0.9307	0.7731
14	0.01207	0.9427	0.616
15	0.00979	0.9525	0.4992



A



B

Figure 5.31: A table (A) and plot (B) of the eigenvalues for Run 2 of the Primary Dataset. The red star represents the cut-off for the valid eigenvalues as determined by the Kaiser-Guttman criterion. The red arrow is the eigenvalue cut-off using the Cattell Scree Test.

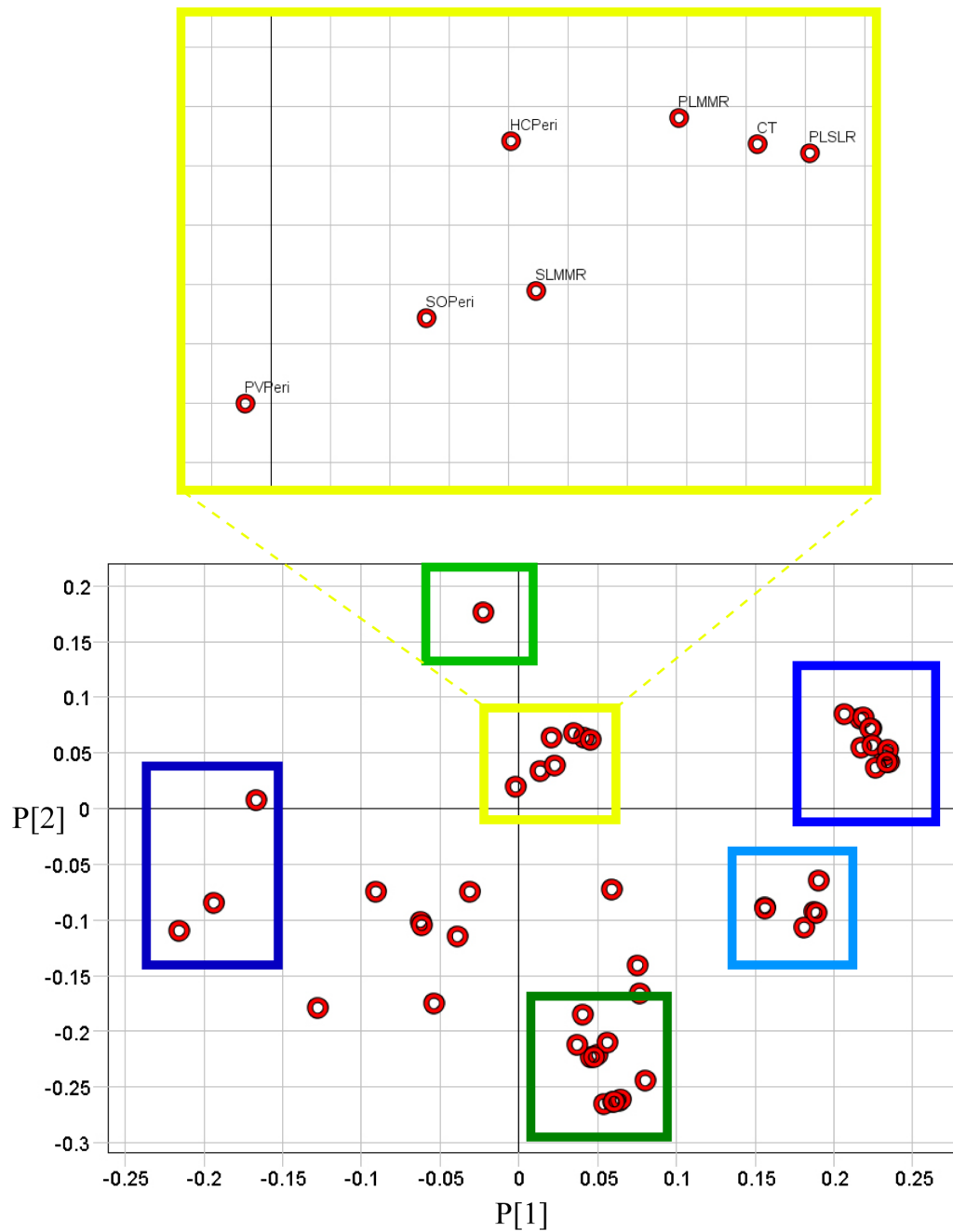


Figure 5.32: The loadings plot for Run 2 of the Primary Dataset, showing an enlarged view of the variables that explain the least amount of variance in the PC1-PC2 plane.

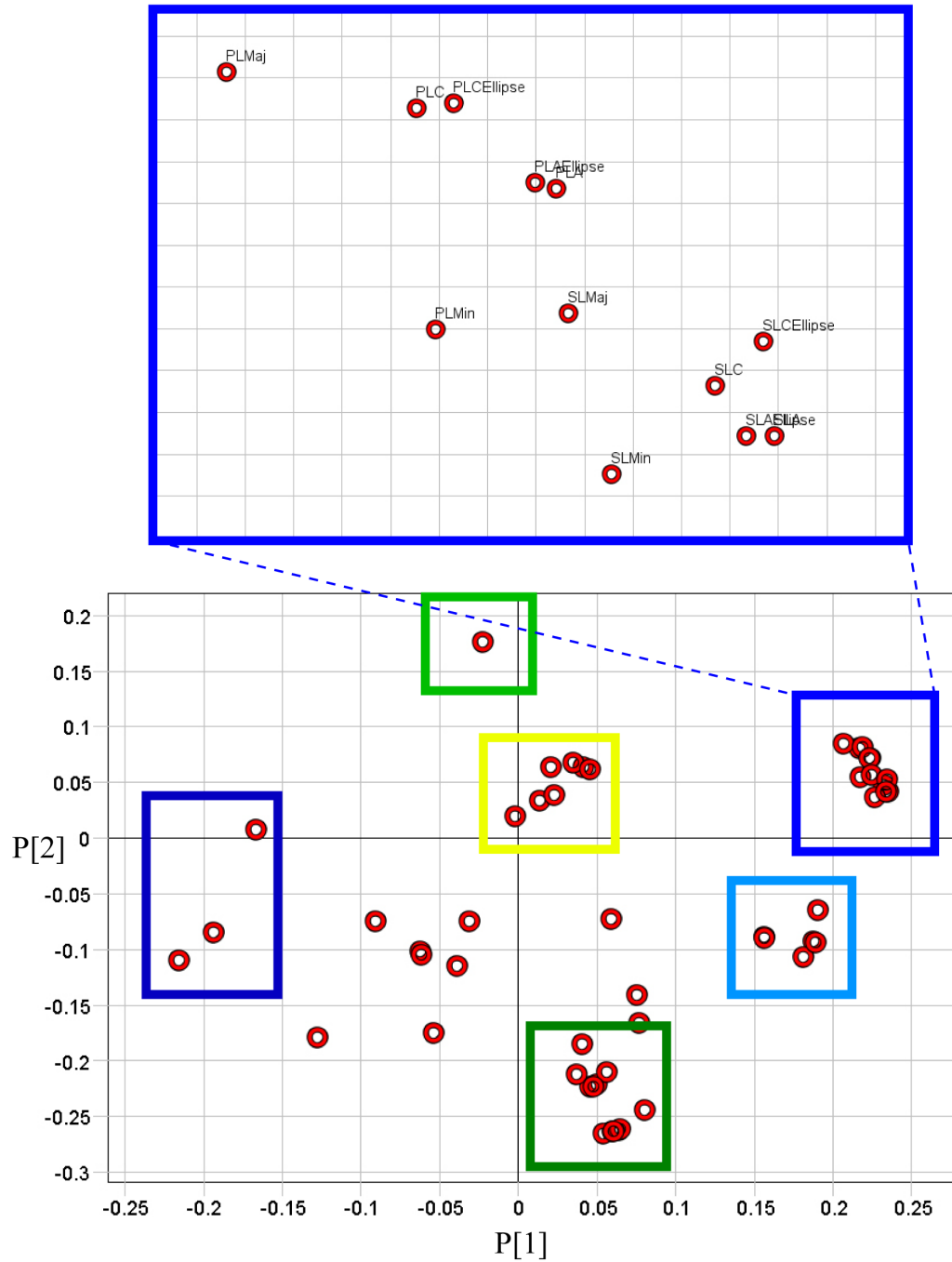


Figure 5.33: The loadings plot for Run 2 of the Primary Dataset, showing an enlarged view of the variables that explain a large amount of variance along positive principal component 1. There is a small amount of covariance with positive PC2.

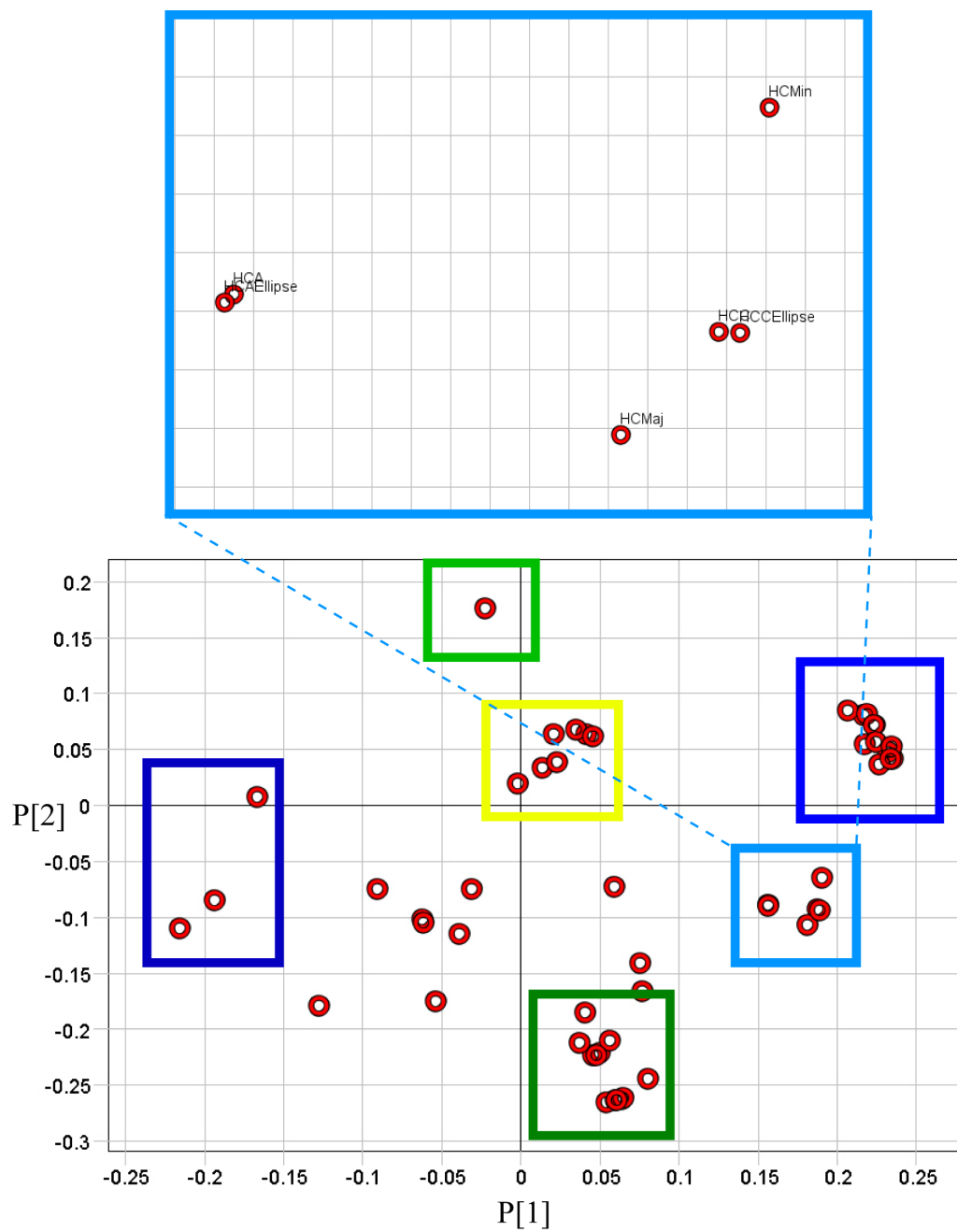


Figure 5.34: The loadings plot for Run 2 of the Primary Dataset, showing an enlarged view of the variables that explain a large amount of variance along positive principal component 1. There is a small amount of covariance with negative PC2.

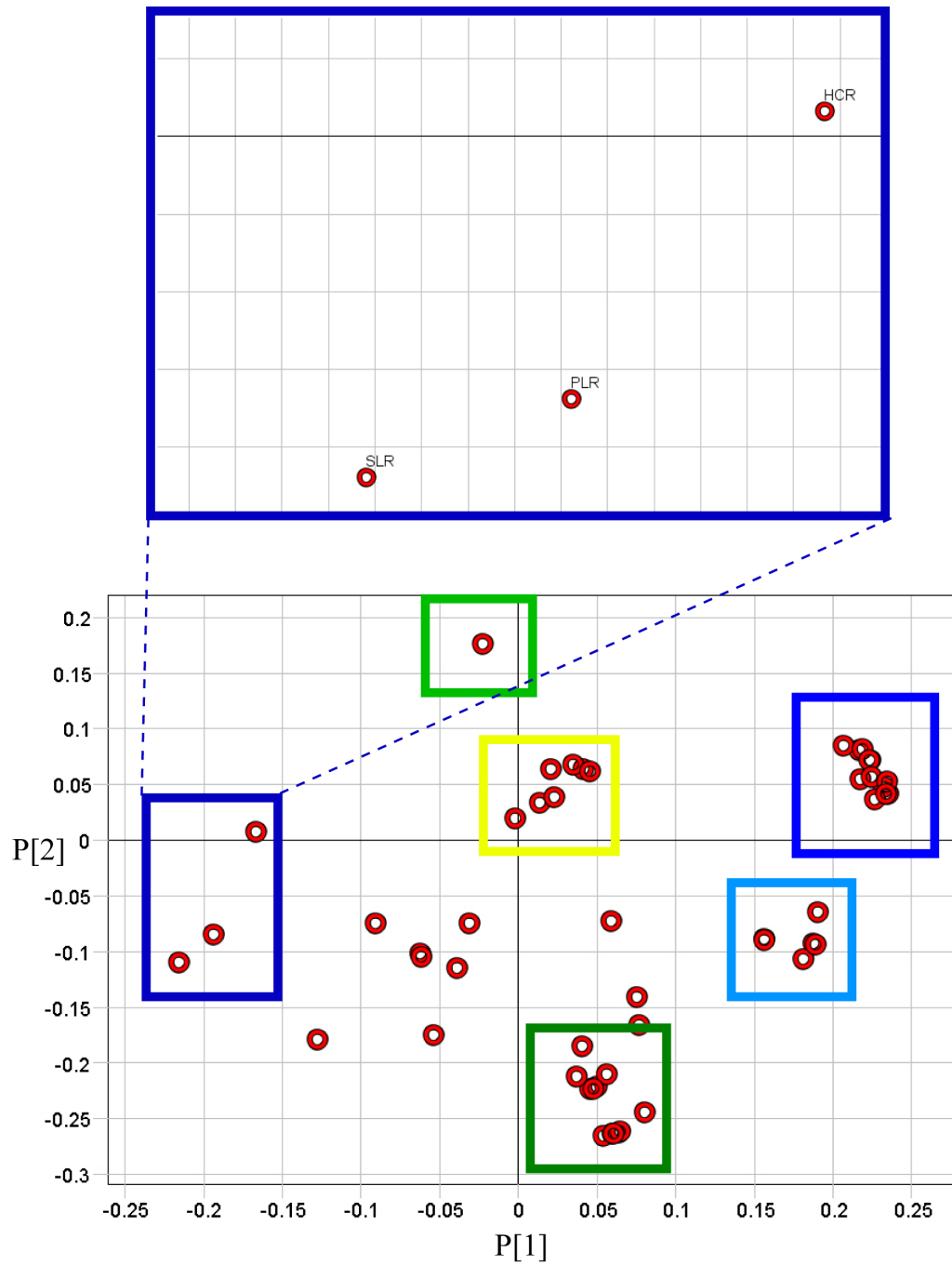


Figure 5.35: The loadings plot for Run 2 of the Primary Dataset, showing an enlarged view of the variables that explain a large amount of variance along negative principal component 1.

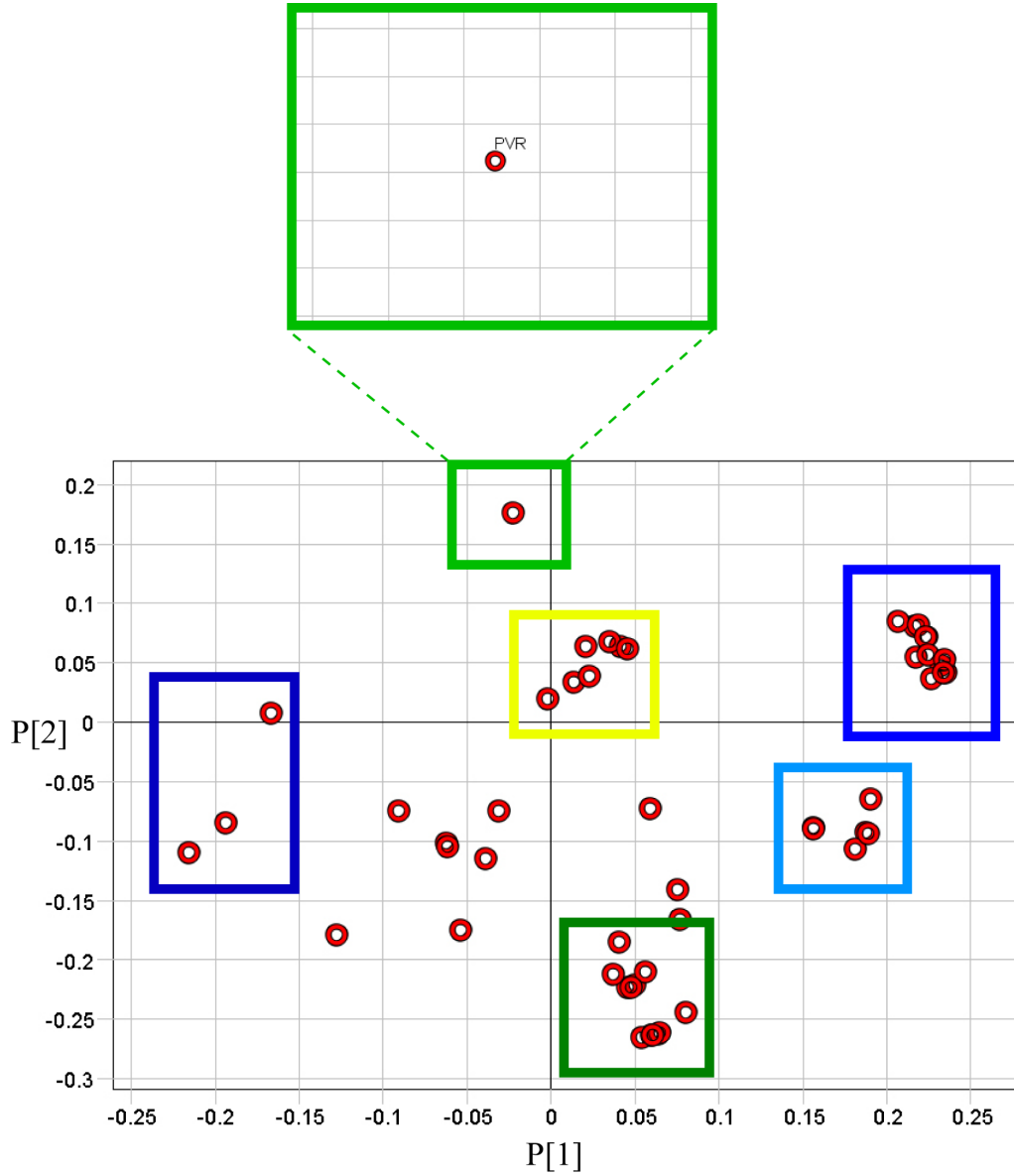


Figure 5.36: The loadings plot for Run 2 of the Primary Dataset, showing an enlarged view of the variable that explains a large amount of variance along positive principal component 2.

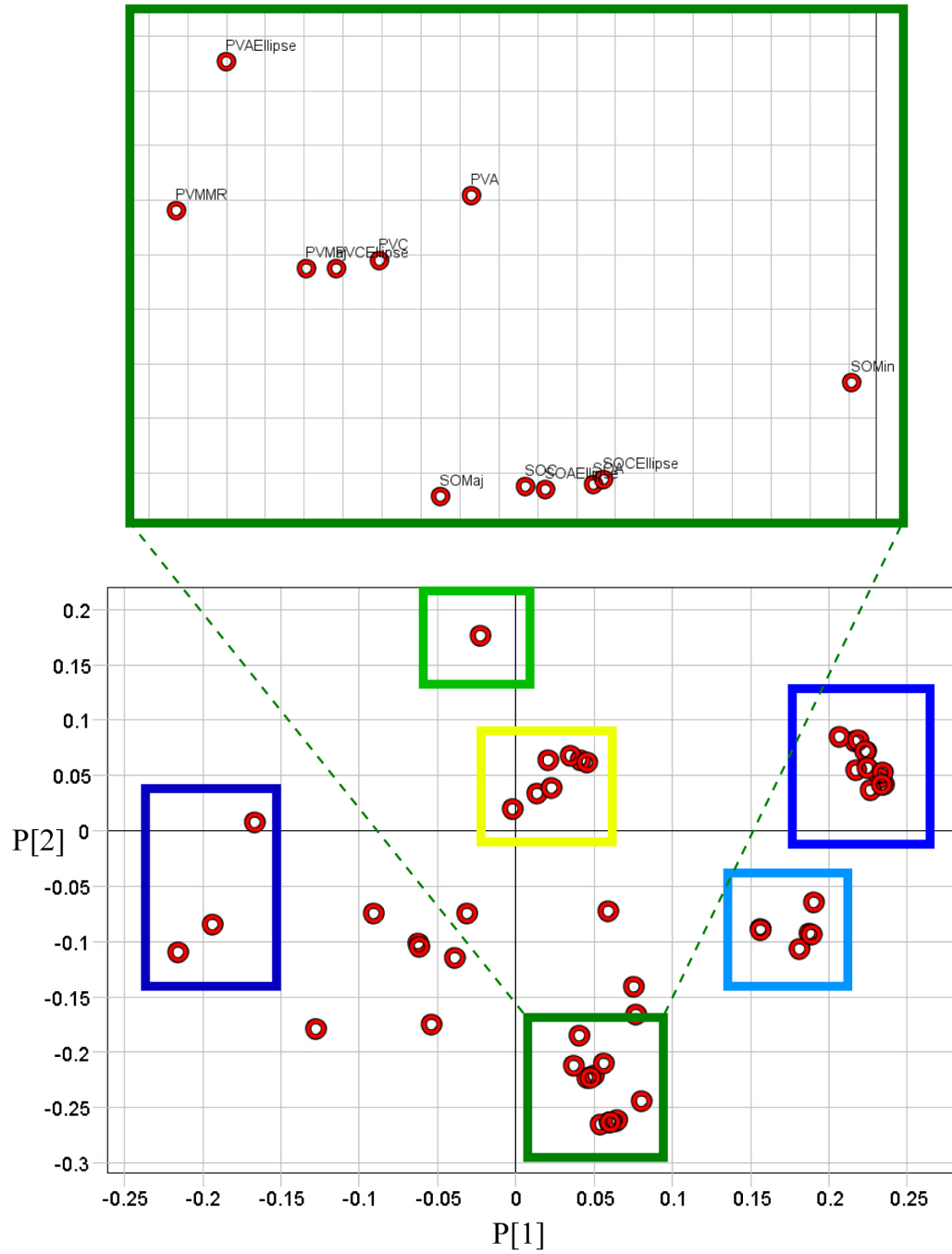


Figure 5.37: The loadings plot for Run 2 of the Primary Dataset, showing an enlarged view of the variable that explains a large amount of variance along negative principal component 2.

The scores plot (Figure 5.38) from Run 2 shows that 1) the micrographs from each taxon generally group together and 2) the taxa separate to some degree according to taxon. There are two distinct groupings of taxa along PC1 (X-axis) and PC2 (Y-axis).

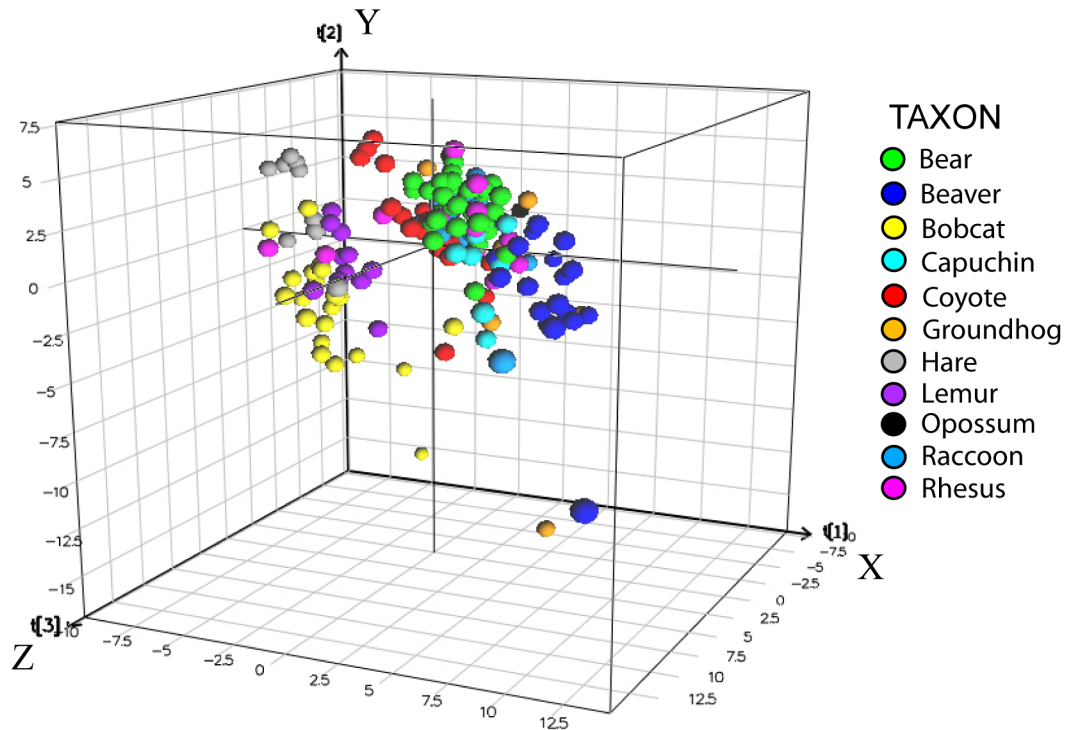


Figure 5.38: The scores plot for Run2 of the Primary Dataset showing clustering and separation of data points (each representing one micrograph) according to taxon.

The two groupings of taxa are most clearly distinguished in the PC1-PC2 (X-Y) plane when viewed orthogonally along the positive and negative Z-axis (PC3). Orthogonal views down the positive and negative Z-axis are shown in Figure 5.39 and Figure 5.40, respectively. Group 1 contains samples from the bobcat, lemur, and hare. Group 2 contains samples from the coyote, bear, opossum, raccoon, beaver, capuchin and groundhog. The rhesus monkey shows samples that occur in both groups. Although the samples from each taxon are generally grouped together, there is some overlap of samples from different taxa in each of the two groups. It is highly likely, however, that the taxa in Group 1 would be distinguished from those in Group 2.

PCA of Run 2 suggests that taxa may be distinguished from each other to a certain degree on the basis of the size, shape, and orientation of microstructural features. Additional statistical treatment of these data is presented in Chapter 6 in order to evaluate the significance in the variance and clustering shown by PCA.

5.4.3 Run 3

The principal component analysis of Run 3 uses the averaged value for each metric (Tier IV in dataset hierarchy) per cross-section. Therefore, each taxon is considered as one sample, rather than each micrograph in Run 2, or each individual microstructural unit, as in Run 1. The results from the PCA of Run 2 suggest that taxa could be differentiated on the combined basis of the size, shape, and orientation of the five types of bone microstructures measured for these analyses. PCA of Run 3 explores the Primary Dataset to gain information on 1) where the taxa lie in microstructure-variable space relative to one another and 2) whether there is any obvious phenotypic (megascopic), general locomotive, and/or phylogenetic pattern to where the 11 mammals lie in space relative to one another and to the component axes.

The Cattell Scree Test and the Kaiser-Guttman test both supported the retention of three principal components (Figure 5.41), explaining 77% of the variance in the dataset.

The loadings of PC1 are similar to those from Run 2, as shown in Figures 5.42 and 5.43. However, the variables explaining the variance on PC2 are different from those of Run 2. Explaining the greatest amount of variance on positive values of PC2 in Run 3 is the ratio of the circumference of the primary vascular canal to the circumference of the Haversian canal (PVHCR) (Figure 5.44). As seen in Figure 5.45, the ratio of the major to the minor axes of the primary lacunae (PLMMR) and the ratio of the major to the minor axes of the secondary lacunae (SLMMR) explain the largest amount of the variance along the negative values of PC2 and are anti-correlated with PVHCR on PC2. As seen in Figure 5.46, there is also a large amount of covariance in the size and orientation variables of the Haversian canals between PC1 and PC2.

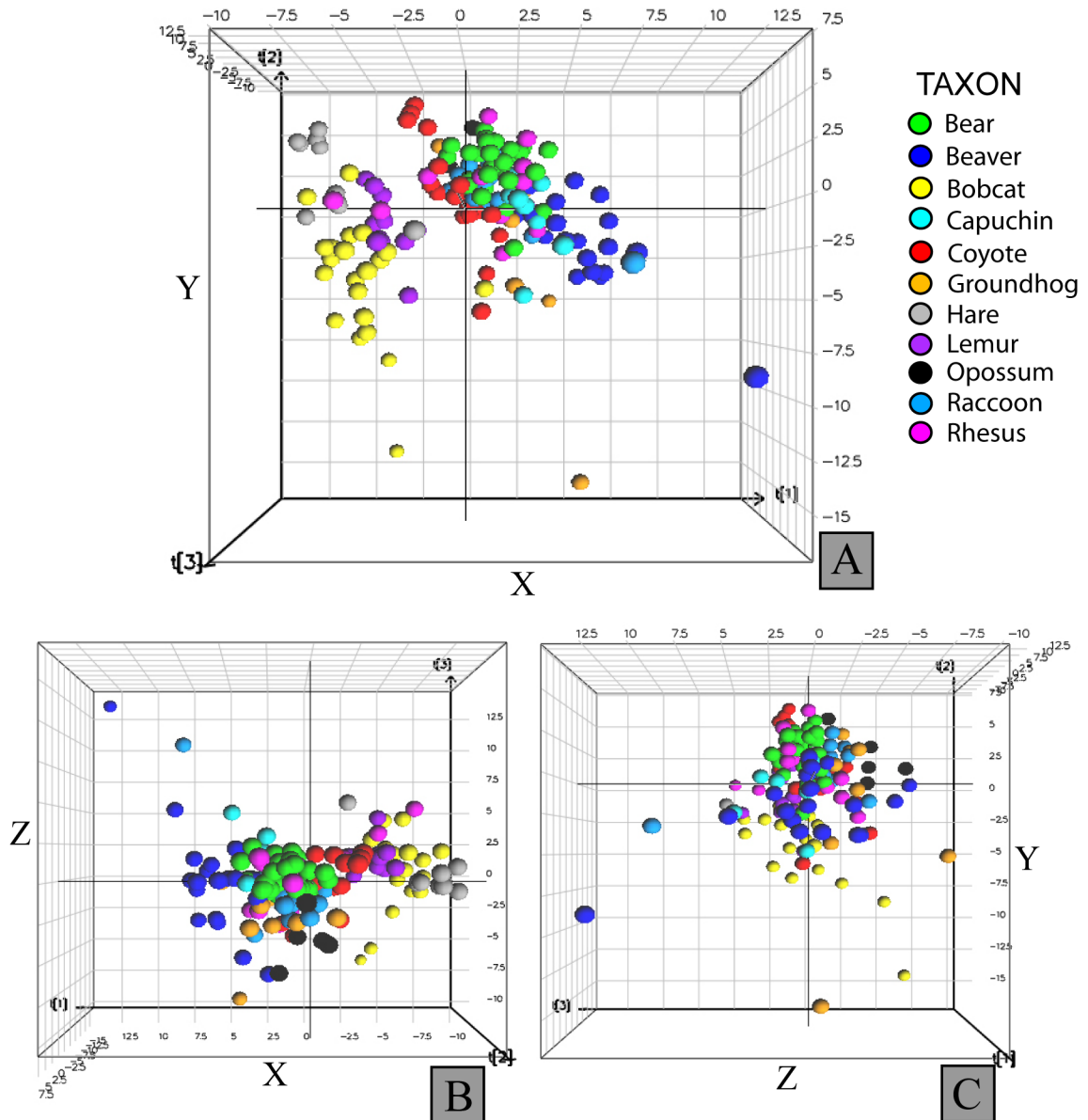


Figure 5.39: Orthogonal views of the Primary Dataset in Run 2 looking at the X-Y plane down the positive Z-axis (A), the X-Z plane down the positive Y-axis (B), and the Y-Z plane down the positive X-axis (C).

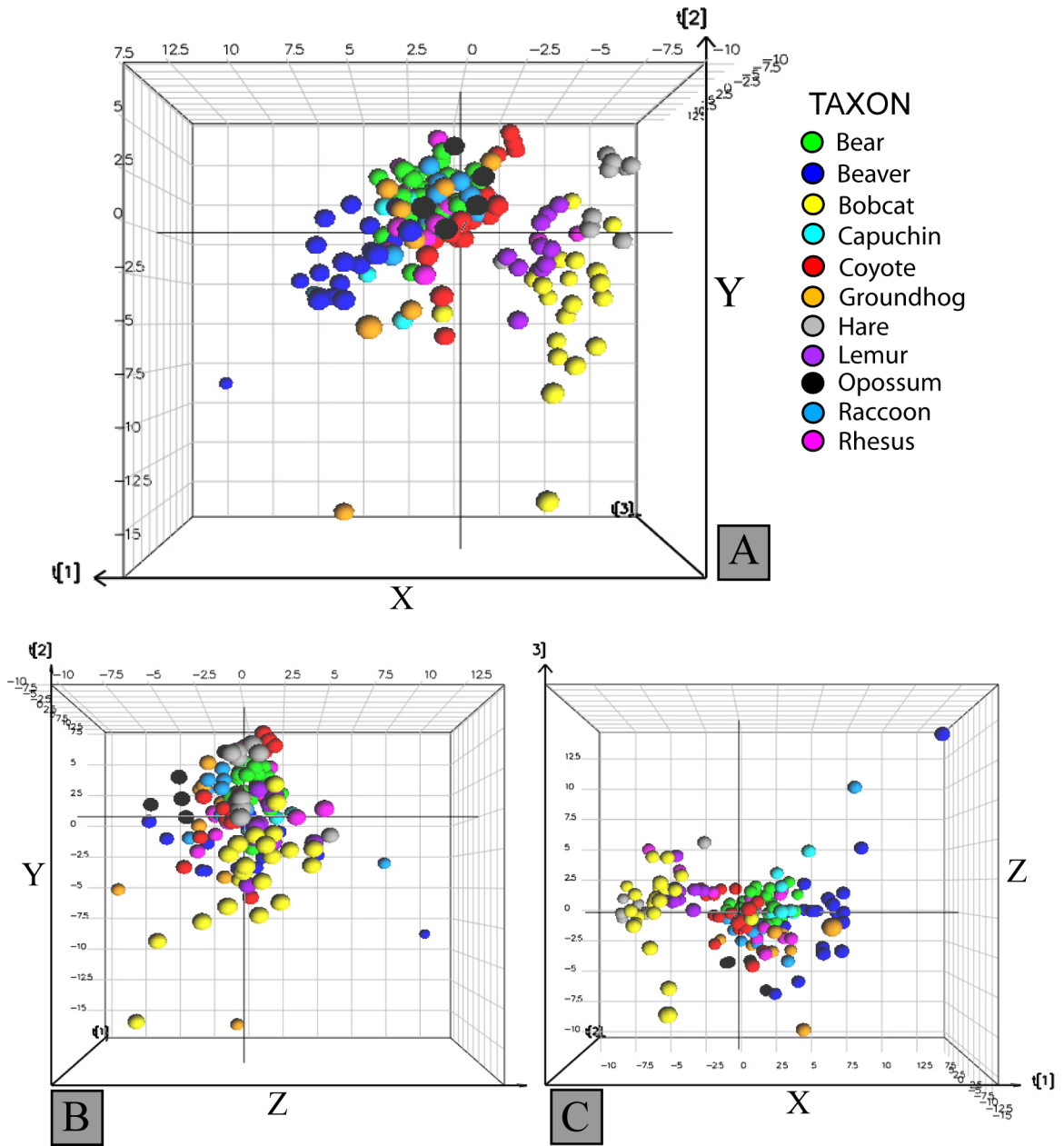


Figure 5.40: Orthogonal views of the Primary Dataset in Run 2 looking at the X-Y plane down the negative Z-axis (A), the Y-Z plane down the negative Y-axis (B), and the X-Z plane down the negative X-axis (C).

Principal Component	r^2	r^2 Cumulative	Eigenvalue
1	0.4397	0.4397	4.8375
2	0.2101	0.6499	2.3116
3	0.1224	0.7723	1.3465
4	0.07191	0.8442	0.791
5	0.05563	0.8998	0.612
6	0.04027	0.9401	0.443
7	0.02373	0.9638	0.261
8	0.01616	0.98	0.1777
9	0.01396	0.994	0.1535
10	5.98E-03	0.9999	0.06574
11	2.22E-16	0.9999	2.44E-15

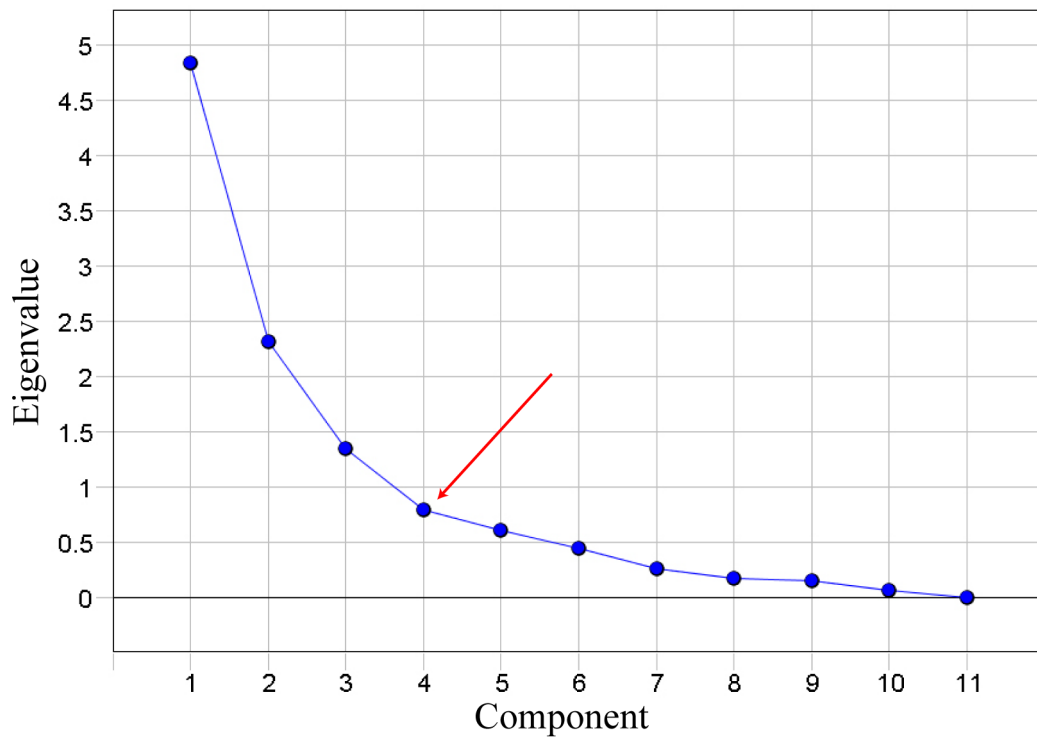


Figure 5.41: A table (A) and plot (B) of the eigenvalues for Run 3 of the Primary Dataset. The red star represents the cut-off for the valid eigenvalues as determined by the Kaiser-Guttman criterion. The red arrow is the eigenvalue cut-off using the Cattell Scree Test.

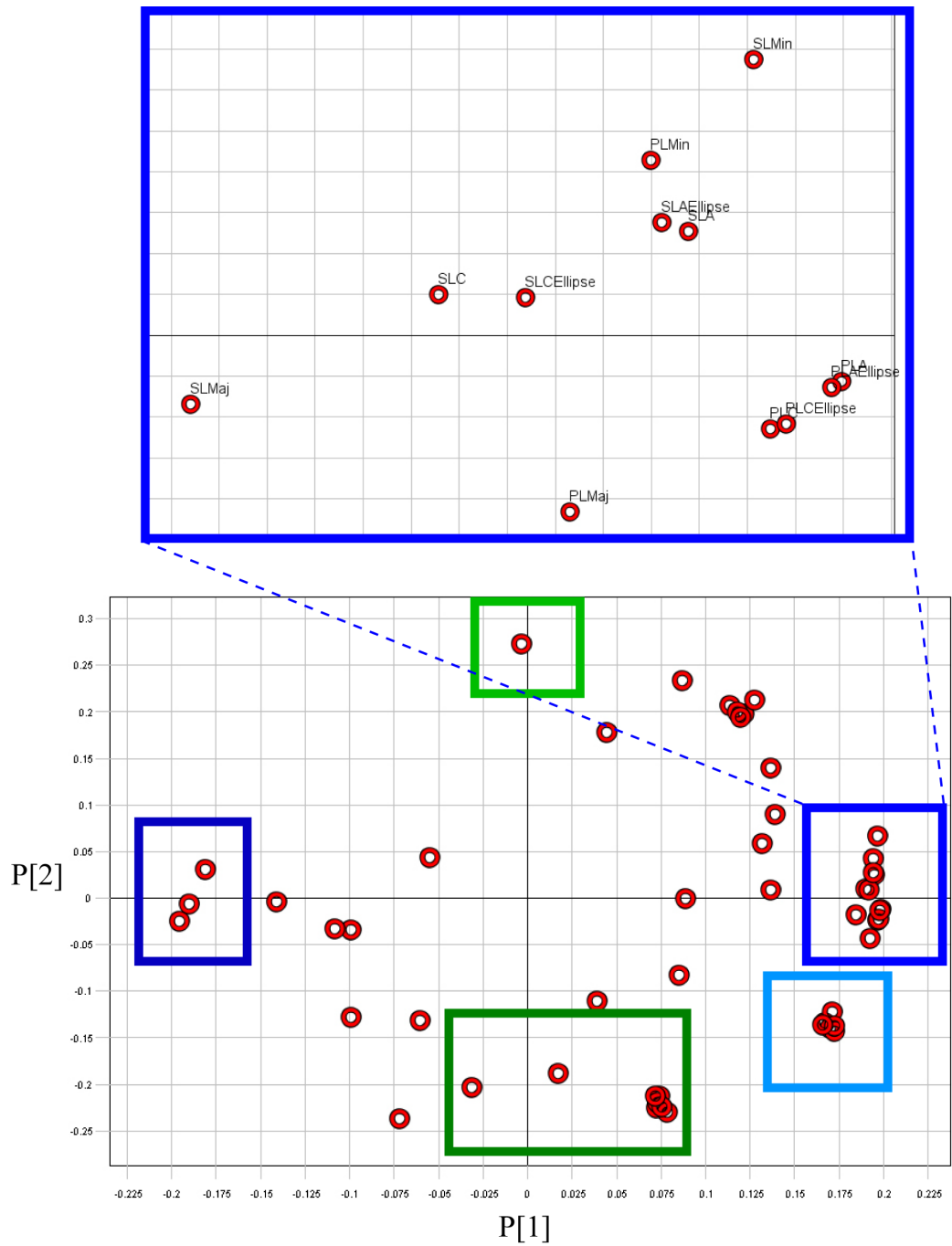


Figure 5.42: The loadings plot for Run 3 of the Primary Dataset, showing an enlarged view of the variables that explain the greatest amount of variance along positive principal component 1.

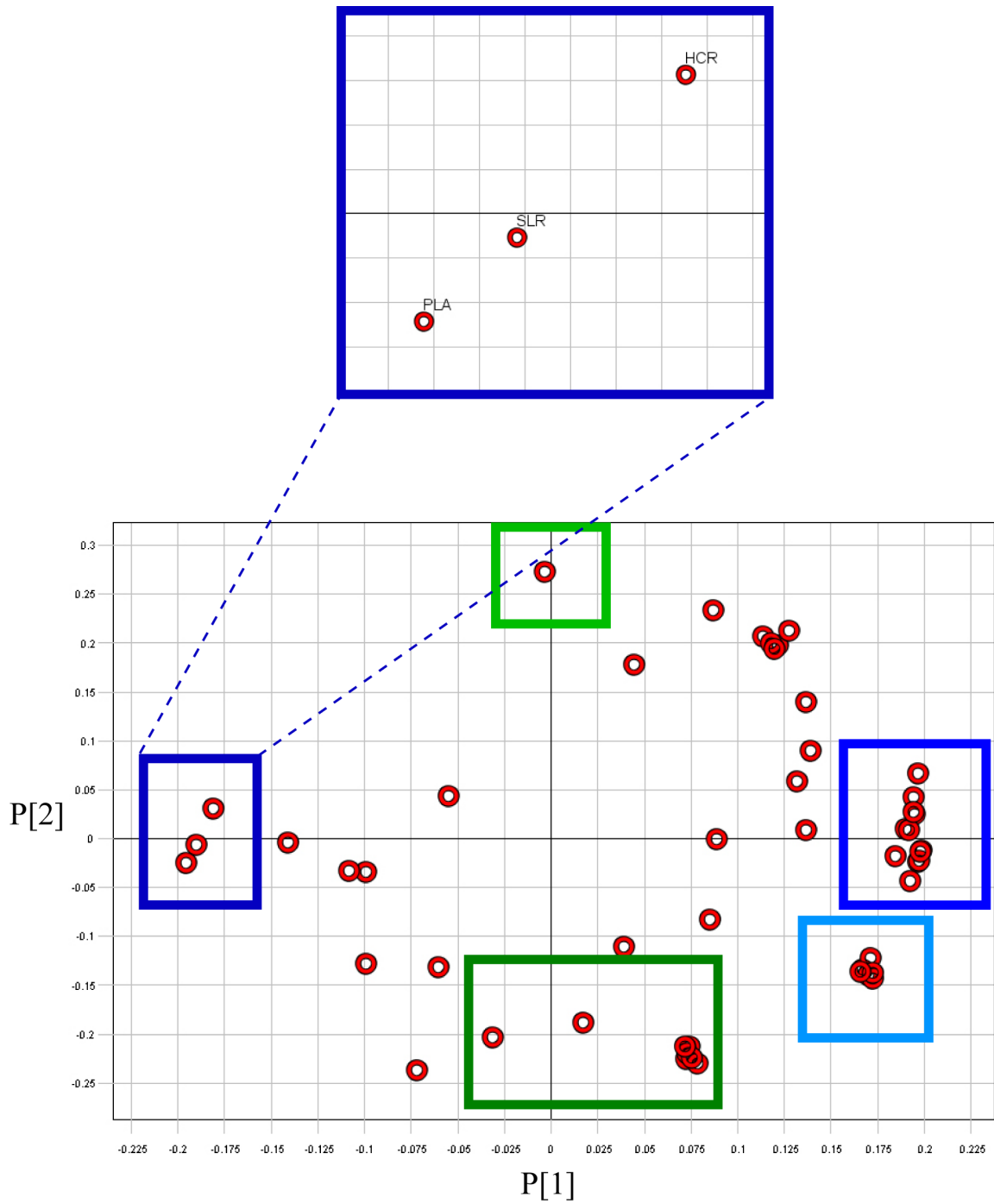


Figure 5.43: The loadings plot for Run 3 of the Primary Dataset, showing an enlarged view of the variables that explain the greatest amount of variance along negative principal component 1.

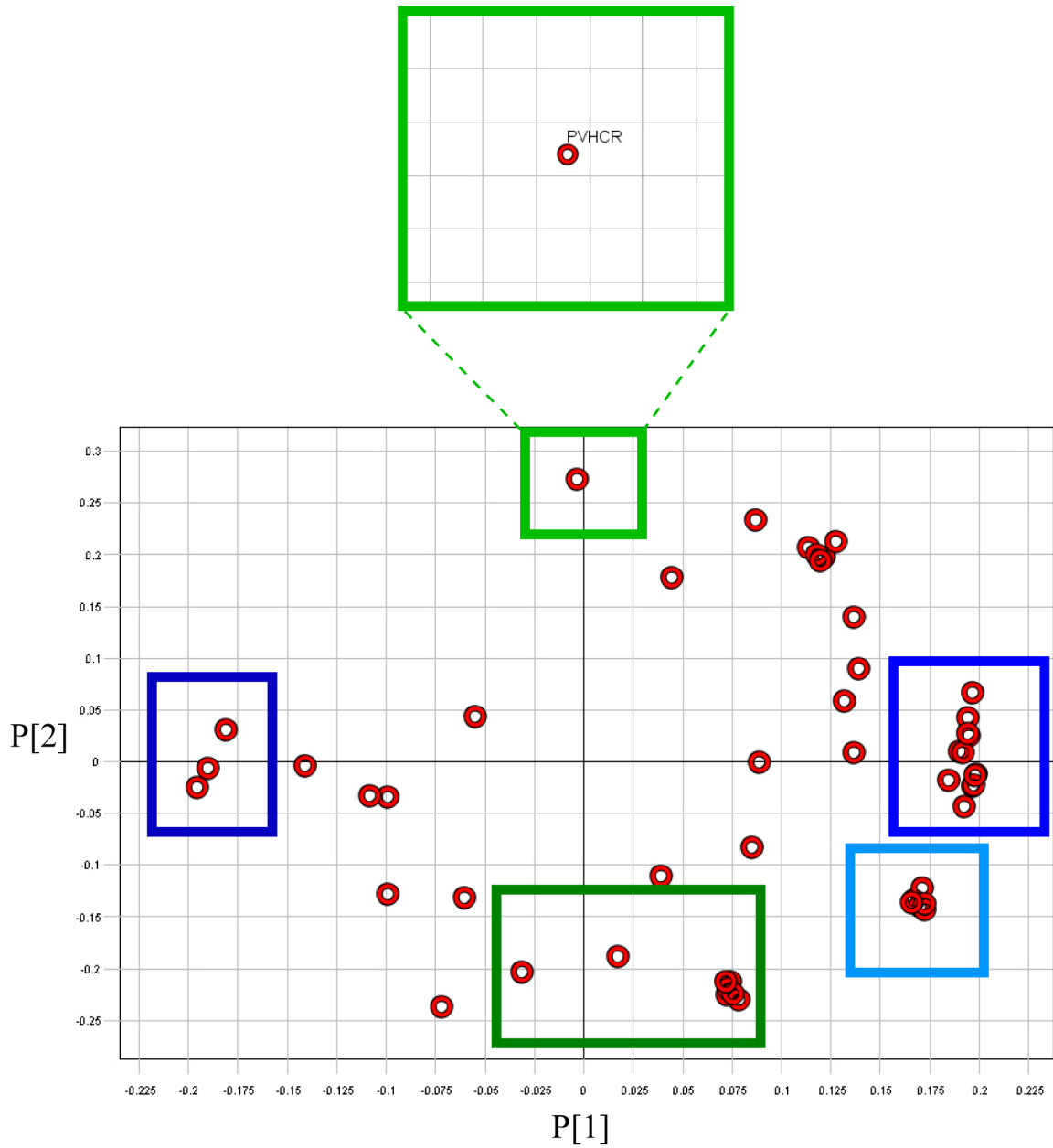


Figure 5.44: The loadings plot for Run 3 of the Primary Dataset, showing an enlarged view of the variable that explains the greatest amount of variance along positive principal component 2.

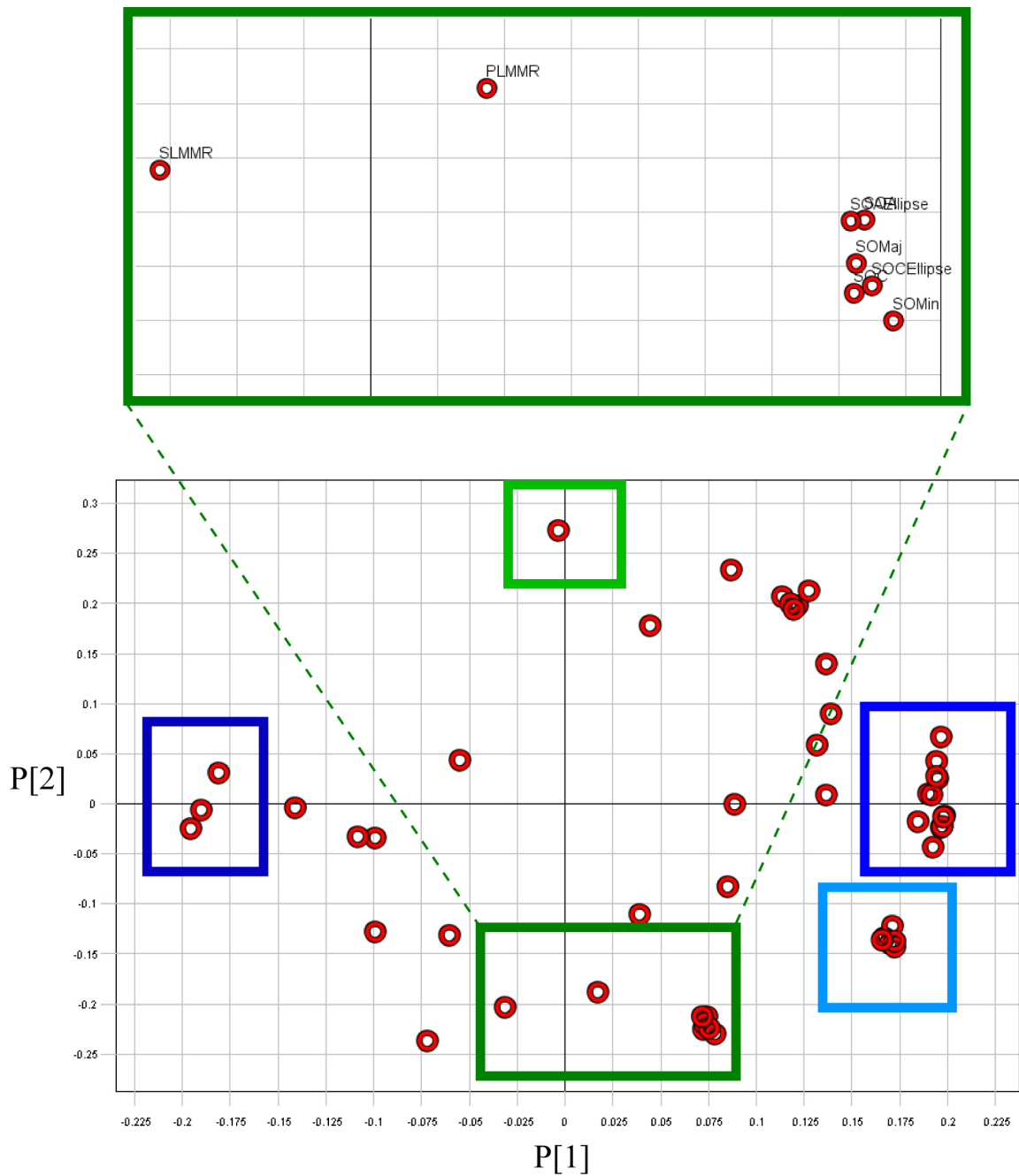


Figure 5.45: The loadings plot for Run 3 of the Primary Dataset, showing an enlarged view of the variable that explains the greatest amount of variance along negative principal component 2.

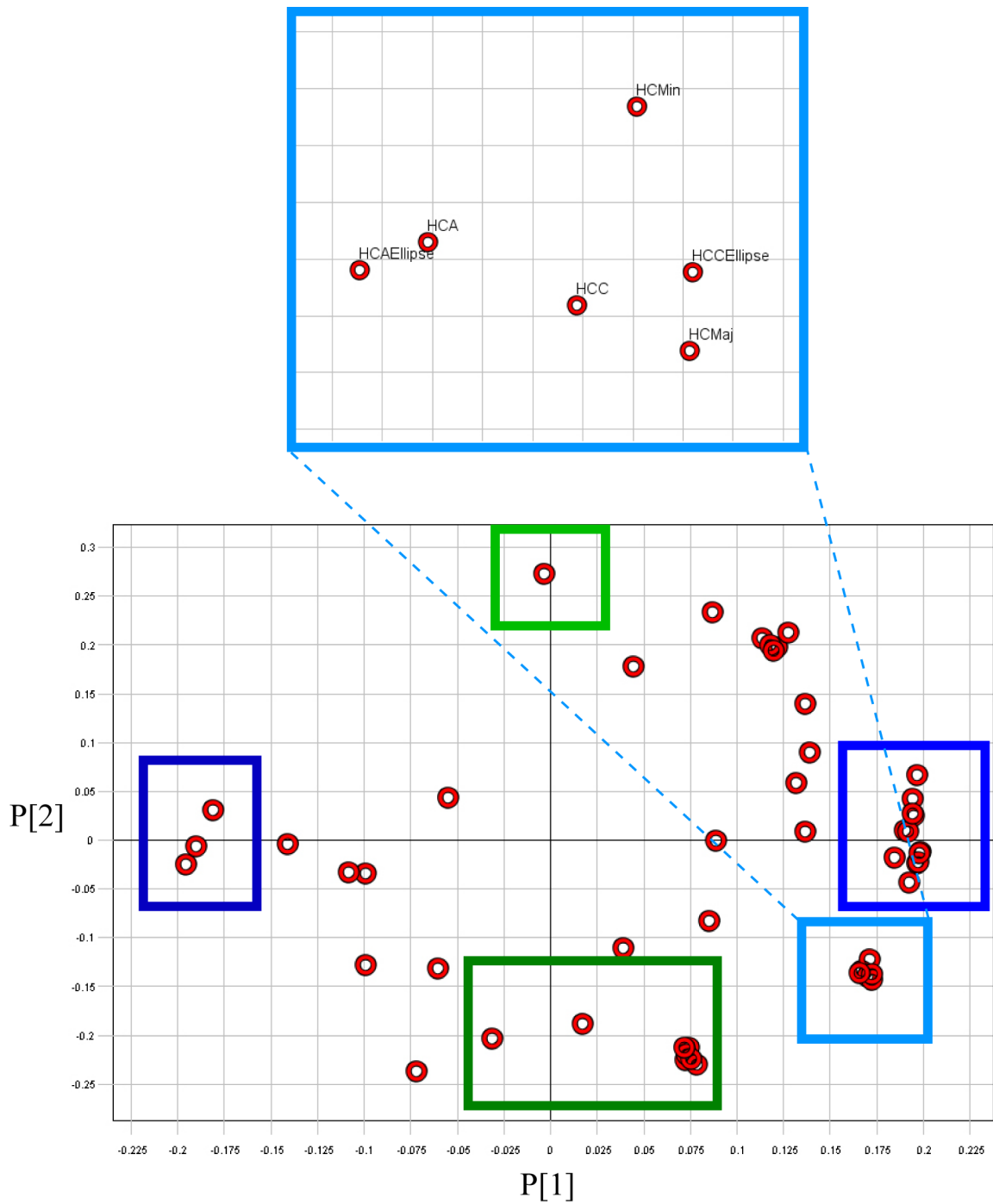


Figure 5.46: The loadings plot for Run 3 of the Primary Dataset highlighting the variables that explain the greatest amount of the variance along positive principal component 1. There is a small amount of covariance with negative PC2.

The second goal of Run 3 was to find out whether microstructural morphology differed according to any phylogenetic, locomotive, or other obvious phenotypic character of the specimens in the Primary Dataset. Although the Primary Dataset does not have multiple specimens of any taxon, the dataset is populated with four specimens from the Carnivora (bear, bobcat, raccoon, coyote) and three specimens from the Primates (rhesus, capuchin, and lemur). The scores plot of Run 3, represented in a perspective view in Figure 5.47, shows that the points representing the specimens from each of those two groups do not cluster together.

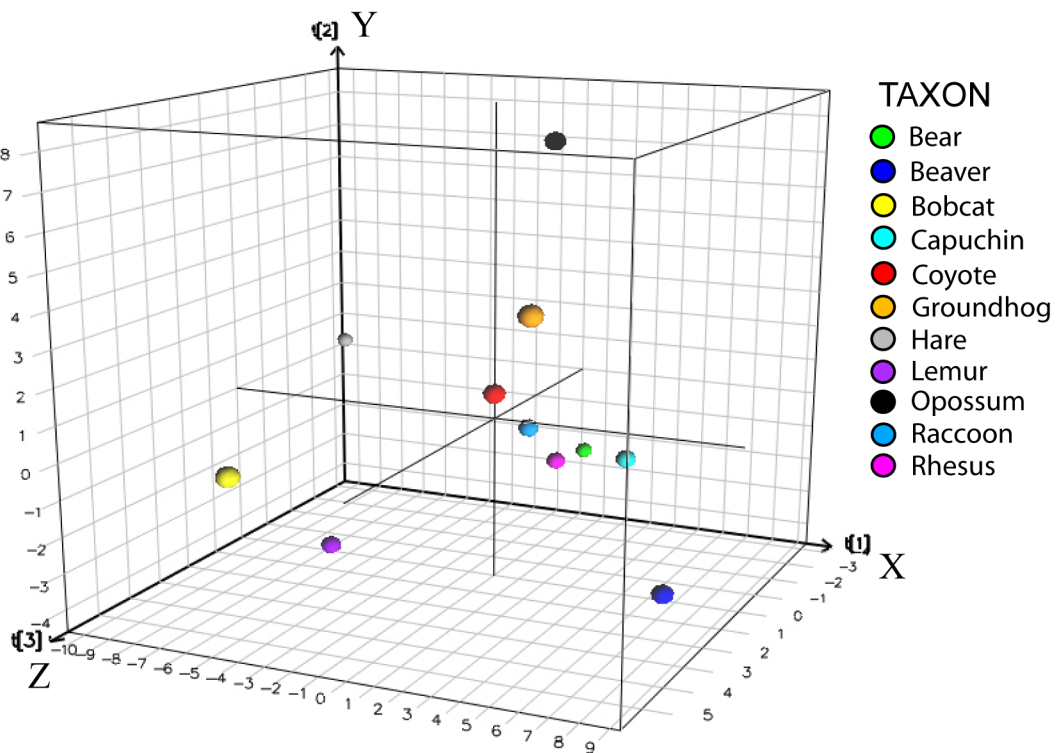


Figure 5.47: The scores plot for Run 3, where each sample is one taxon, of the Primary Dataset showing the separation of the taxa in 3D space.

However, when the X-Y (PC1-PC2) plane is viewed from the orthogonal Z-axis (PC3) (Figure 5.48, red dotted line), all of the Primates are oriented along a diagonal line. A comparison of the distribution of the Primate datapoints in the scores plot with the loadings plot (Figure 5.45) suggests that the most of the variance in those taxa can be explained by variables along PC1 and, to some extent, the size and shape of the secondary osteons. In the PC1-PC2 (X-Y) plane, the points representing the

bear, raccoon, and coyote also lie along a diagonal line (Figure 5.48, blue dotted line), but one that is perpendicular to that defined by the Primate datapoints. The three Carnivora taxa are also distributed along a diagonal line in the PC1-PC3 and PC2-PC3 planes. The loading plots (Figure 5.44 and Figure 5.45) suggest that the distribution of the Carnivora data points in the PC1-PC2 plane can be explained by the variables along PC2 (PVHCR, PLMMR, and SLMMR). In the PC1-PC3 plane, the variables that explain the variance in the aligned Carnivora points are along PC3 (PVHCR, PLMMR, SLMMR, and CT). In the PC2-PC3 plane of the scores plot, the variables that explain the variance in the three Carnivora specimens are also along PC3. In this plane, the variables relate to the size and shape of the primary and secondary lacunae. Note that the bobcat plots far from the diagonal line representing the other Carnivora specimens. Other than the tentative grouping according to taxonomic order, described above, the point distribution does not seem to correlate with other megascopic biological signals. The lack of biological explanation for taxa separation is not problematic. As discussed in the last section of Chapter 1, the purpose of the development and testing of this method is to identify the animals by their bone microstructure (the equivalent of identifying people by their fingerprints), not to reconstruct a phylogenetic history.

This configuration of data, i.e., taking an average value of each microstructural metric over an entire cross-section, will be the approach to datasets developed in future analyses. Further testing of the methodology presented in this dissertation requires more than one specimen of each taxon to populate the dataset. Unfortunately, the acquisition of multiple samples of each taxon in order to test the method here was impossible. This lack prohibits a test of whether the microstructural values from two specimens of the same taxon would plot in similar space. More than one specimen of each taxon is needed in order to build a dataset in which samples of “known”, and eventually “unknown”, taxonomic origin can be tested.

A training model of the Primary Dataset, i.e, a synthetic analogue to the situation in which multiple samples of the same taxon are compared, is presented in the next section using the information in Run 3. The training model is tested against the metric values from individual micrographs (the test set) in order (1) to explore the robustness of the results showing the separation of taxa in Run 2 (i.e., individual micrographs properly reassigned to their respective taxon based on the model) and

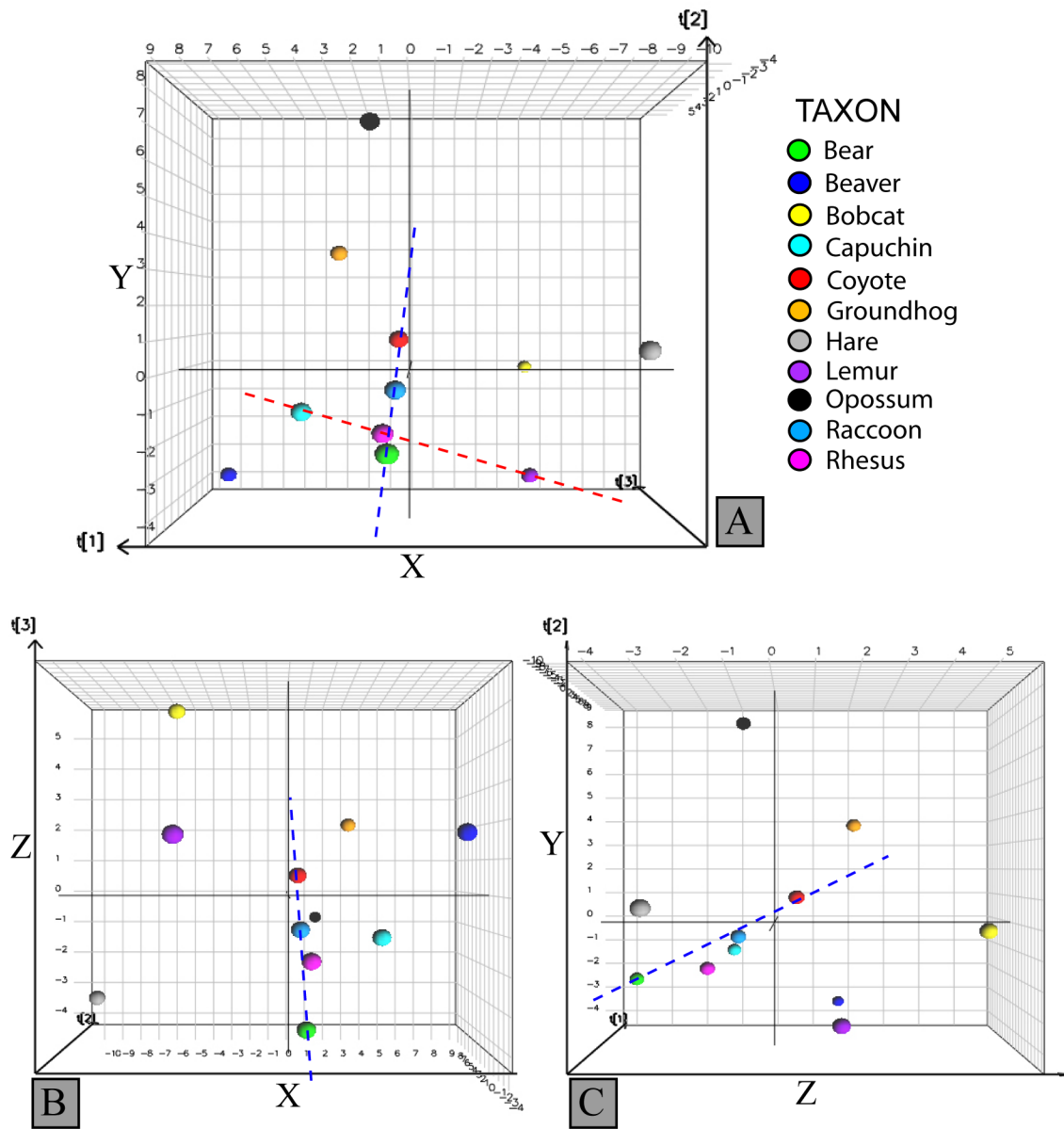


Figure 5.48: Orthogonal views of the Primary Dataset in Run 3 looking at the X-Y plane down the negative Z-axis (A), the X-Z plane down the negative Y-axis (B), and the Y-Z plane down the negative X-axis (C). The red dotted-line represents the diagonal distribution of the Primates in PC space, and the blue-dotted line likewise connects the Carnivora bear, coyote, and raccoon along a differently oriented diagonal line.

(2) to establish a base method for taxonomic comparison of specimens (both “known” and “unknown samples”) in future datasets.

Based on the scores plot of Run 3, several predictions can be made regarding the outcome of the training model as individual micrographs are tested for reassignment to their respective taxon. There are two main situations that will contribute to the ability of the model to predict to which taxon each micrograph belongs. (1) The closer the variance in a single micrograph is to the average variance in the cross-section [model], the more likely it is that the micrograph will be reassigned to the taxon of origin. (2) The more separation a taxon has from all other taxa in space, the more likely the micrographs from that taxon will be reassigned correctly. For example, in vector space, the bobcat lies farthest from the bear, beaver, opossum, and hare. Based on that information, a prediction can be made that the bobcat micrographs will not be incorrectly reassigned to those other animals. Likewise, it could be predicted that the micrographs of the rhesus monkey may be reassigned incorrectly to the raccoon, capuchin monkey, bear, or coyote because of the close proximity of those points to the rhesus point.

5.5 Soft Independent Modeling of Class Analogy

Soft Independent Modeling of Class Analogy (SIMCA) is a classification approach used to identify local models in a dataset and to predict probable class membership, which enables identification of new observations/measurements (Wold, 1976). For high-dimensional data (such as the datasets used in this dissertation), local models are created through principal component analysis of each defined class (taxon) in the dataset. This differs from other classification approaches, such as Canonical Variates Analysis (CVA), that combine all of the data into a single principal component analysis of the whole dataset. In SIMCA, each local model occupies its own principal components space. As in all PCA, the analysis of each class retains a certain number of principal components that explain most of the variation within the class. Cross-validation of the PCA model of the class ensures that the model has minimum prediction error and ensures a high signal-to-noise ratio.

After the creation of local class models, new observations or new types of measurements can be introduced into the dataset to facilitate classification. Classification is based on the best-fit (distance) of a new observation to a respective local model. The distance from the new sample to the established local models is determined by two measurements, (1) the Euclidian distance (e_i) from the sample to the model in the variable space, and (2) the Mahalanobis distance (h_i) between the sample and model in principal component space (Davies and Fearn, 2008) (Figure 5.49). The Mahalanobis distance differs from the Euclidean distance by taking into account correlations in the dataset; it is not related to a scale of measurement (but it is a scalar value). Mahalanobis distances are commonly used in statistical analyses to determine the similarity of an unknown sample to a set of known samples. They are calculated as the distance from a new sample to the local model centroid. New “unknown” samples that are similar to the samples represented by the local model will map near to that model’s principal component space.

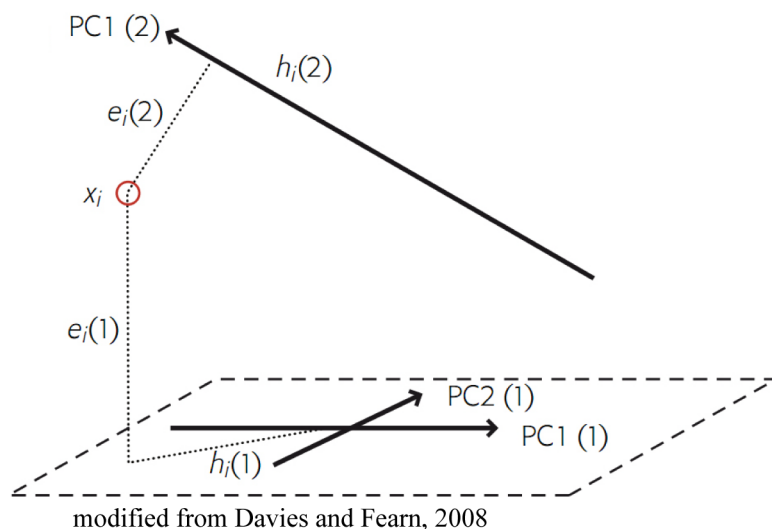


Figure 5.49: The open red circle represents a test sample. The Euclidean distances from the test sample to the two models PC1 (1) and PC1 (2) are $e_i(1)$ and $e_i(2)$, respectively. The Mahalanobis distance from the test sample to PC1 (1) is $h_i(1)$.

The results of a SIMCA analysis can be assessed by a “Coomans’ Plot” and a “Membership Plot”. The Coomans’ Plot compares the Euclidean distances between the new samples and the local models. Because SIMCA uses different principal component models for each class, the Euclidean distances between the new samples and

the local models cannot be viewed in one plot. Instead, Coomans' Plots allow for pairwise comparisons. For comprehensive results, all possible pairs must be taken into account. The Membership plots give the results for the Mahalanobis distances between new (test) samples and local models. One membership plot is created for each local model; it displays the distances of all of the new (test) samples from one local class model's centroid.

The variance that describes the signal in the class model is called the modeled variance, whereas the variance that is not accounted for in the model is called the residual variance. It is possible to get a measure of similarity between a test sample and the local class by comparing the average residual variance of the class with that of the unknown sample. This comparison can be used to fit the unknown test sample with a local class model. SIMCA analysis will only assign a new sample to a class for which the new sample has a high probability of belonging, meaning that unknown samples are not forced into one of the local models in the dataset. If the residual variance of the unknown sample is greater than the maximum residual variance in every local model, the unknown sample will remain unassigned. It is possible that an unassigned sample could be an outlier of one of the classes or that it may not belong to any of the classes in the dataset.

There is no limit to the number of measurement variables that can be used in SIMCA; the dimensionality is reduced in PCA. However, the minimum number of observations for which SIMCA will give good results is 10 samples per class. In the absence of multiple specimens of each taxon in the Primary Dataset of this dissertation, the SIMCA approach implemented here uses the multiple micrographs of each cross-section to create "training" and "test" sets. SIMCA is used (1) to explore local models that characterize the cross-sections of each taxon in the Primary Dataset (e.g., "bobcat-ness" and "bear-ness"), (2) to predict whether micrographs of "known" taxonomic origin can be reassigned to the correct taxonomic model, and (3) to establish a procedure for treatment of future datasets that have more than one sample of each taxon.

5.5.1 Data organization

For SIMCA, the Primary Dataset is organized identically to that in PCA Run 2 (Figure 5.21). There needs to be a set of samples designated/treated as a “training set” and a set of samples that makes up a “test set”. There are no unknown samples of taxonomic affinity in the Primary Dataset. In order to test the local models (training sets), one “known” sample (i.e., micrograph) was removed from each taxon’s dataset to make up the “test set”. The sample removed was chosen using a random number generator (www.random.org) based on atmospheric noise. The remaining samples from each taxon comprised the “training set.” The test set samples were removed before the PCA was done and before the local model was determined for each taxon. In other words, the test samples were not included in the principal component analysis used to create each local class model. The software package Evince was also used to facilitate the SIMCA.

5.5.2 Results: PCA by class

Several iterations of SIMCA were explored for the Primary Dataset. Because there is a minimum number of 10 samples per class in SIMCA, the capuchin monkey, groundhog, hare, and opossum data were removed from the dataset. The hare originally had 10 micrographs, but one would have to be removed for the test set, thus bringing the total to just under the SIMCA threshold. Modeling and testing of the remaining taxa revealed that taxa consisting of less than 20 samples were unreliable in creating a local model that would allow a test sample to be reassigned to the correct taxon. Based on this, the lemur, raccoon, and rhesus monkey were removed from the analysis. The beaver (19 samples) was included in the final SIMCA analysis because of the higher sample count relative to the other taxa that were removed. The final SIMCA treatment/analysis consisted of micrograph samples from the bear, bobcat, coyote, and beaver.

The micrographs chosen at random to comprise the test set were bear 21, bobcat 15, beaver 7, and coyote 9. The principal component models of the training set included three principal components for each taxon. Results of the principal component analyses explore the variables that explain most of the variance in the micrograph samples

of each tibial cross-section. PCA of the bear (with micrograph 21 removed) resulted in three principal components that accounted for 61% of the variance in the tibial cross-section (Figure 5.50).

The loadings plot in Figure 5.51 shows that the variance on PC1 can be explained by size of the secondary osteons and Haversian canals, as well as by the ratio of the actual primary vasculature circumference to the circumference of the Haversian canals (PVHCR) and the minimum axis length of the primary vascular canals (PVMin). The variance in PC2 of the bear is best explained by the size of the primary lacunae and the ratio of the circumference of the primary lacunae to the secondary lacunae (PLSLR). Variables explaining the least amount of variance in the local dataset are PVMMR, SLR, and SOPeri, which sit close to the graphical origin. These variables that do not explain much of the variance in a taxon are extremely important to SIMCA, as they make up the residual variance of each local model. By taking into account the residual variance, SIMCA can classify known and unknown samples, as described above.

Principal component analysis of the bobcat (with micrograph 15 removed) included three principal components explaining 68% of the variance in the cross-section (Figure 5.50). The variables that explain most of the variance on PC1 (Figure Loadings-SIMCA-bobcat) are all related to the size, shape, and orientation of the primary vasculature, PVR, and PVHCR (Figure 5.52). The loadings plot of PC2 shows that PLSLR, CT, PLMMR, and the size metrics of the secondary osteons explain most of the variance along the PC2 axis. Explaining the least amount of the variance are the variables SOR and SOMMR.

Three principal components were also retained for the beaver (with micrograph 7 removed), which explained 69% of the variance in the tibial cross-section (Figure 5.50). The loadings plot shows a large amount of covariance between the variables in PC1 and PC2 (Figure 5.53). However, explaining most of the variance on PC1 is the size of the secondary osteons, the size of the primary vasculature, PVHCR, and HCR. The variables that explain most of the variance along PC2 are those associated with the size of the secondary lacunae and, along the negative PC2, the longitudinal orientation of the primary vasculature. Explaining the least amount of variance in the sample are CT and PVCentroid.

Bear

Principal Component	r^2	r^2 Cumulative	Eigenvalue
1	0.2954	0.2954	9.1581
2	0.1649	0.4604	5.1148
3	0.1505	0.611	4.6685

Beaver

Principal Component	r^2	r^2 Cumulative	Eigenvalue
1	0.3806	0.3806	6.8515
2	0.2091	0.5897	3.7644
3	0.08427	0.674	1.5168

Bobcat

Principal Component	r^2	r^2 Cumulative	Eigenvalue
1	0.3857	0.3857	7.7154
2	0.1908	0.5766	3.8171
3	0.0983	0.6749	1.9661

Coyote

Principal Component	r^2	r^2 Cumulative	Eigenvalue
1	0.3902	0.3902	7.4145
2	0.1903	0.5806	3.6172
3	0.1261	0.7067	2.3972

Figure 5.50: Eigenvalues and the variance (r^2) explained by each local taxon model in SIMCA analysis.

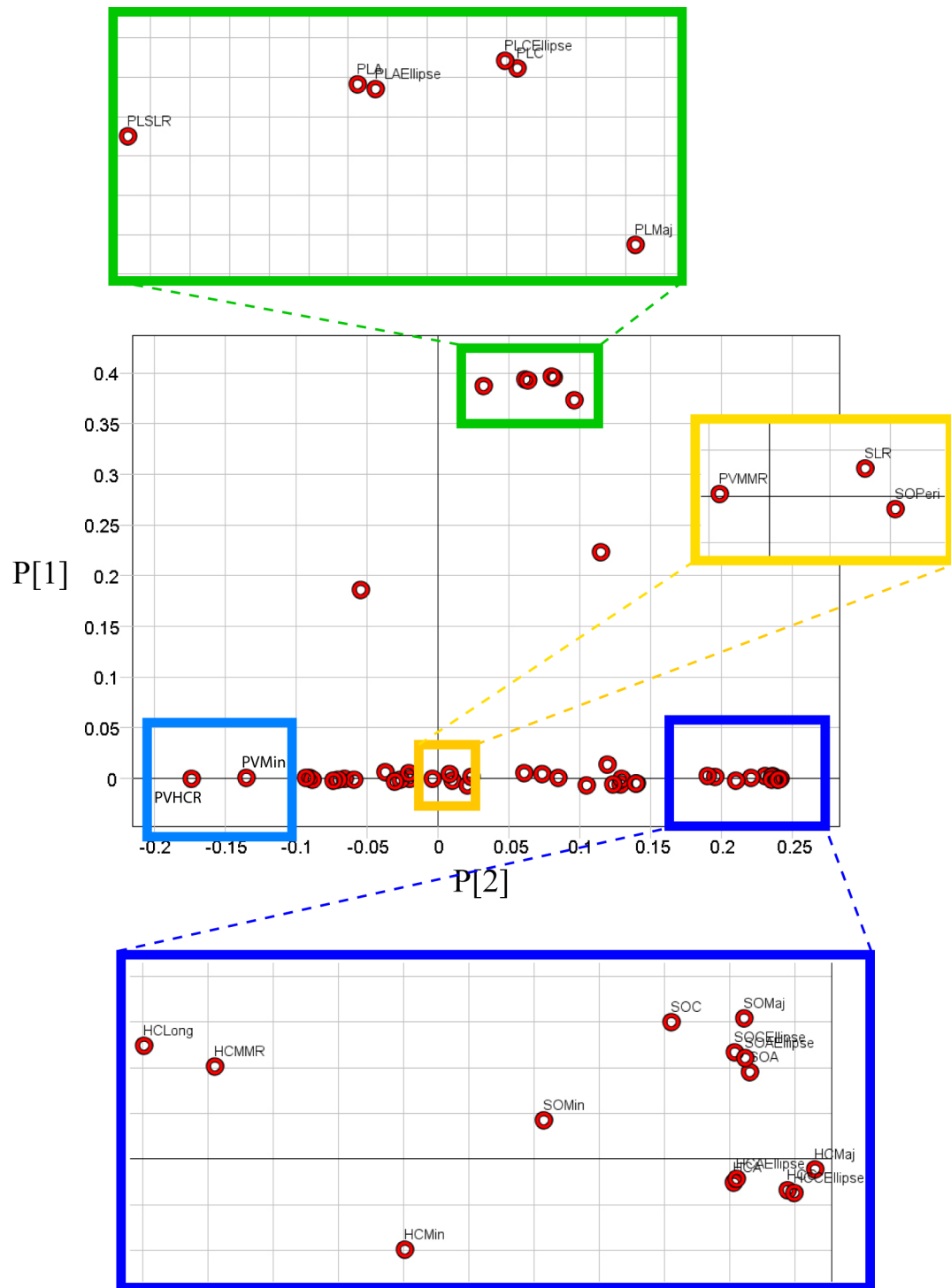


Figure 5.51: The loadings plot for the Bear local model in SIMCA analysis.

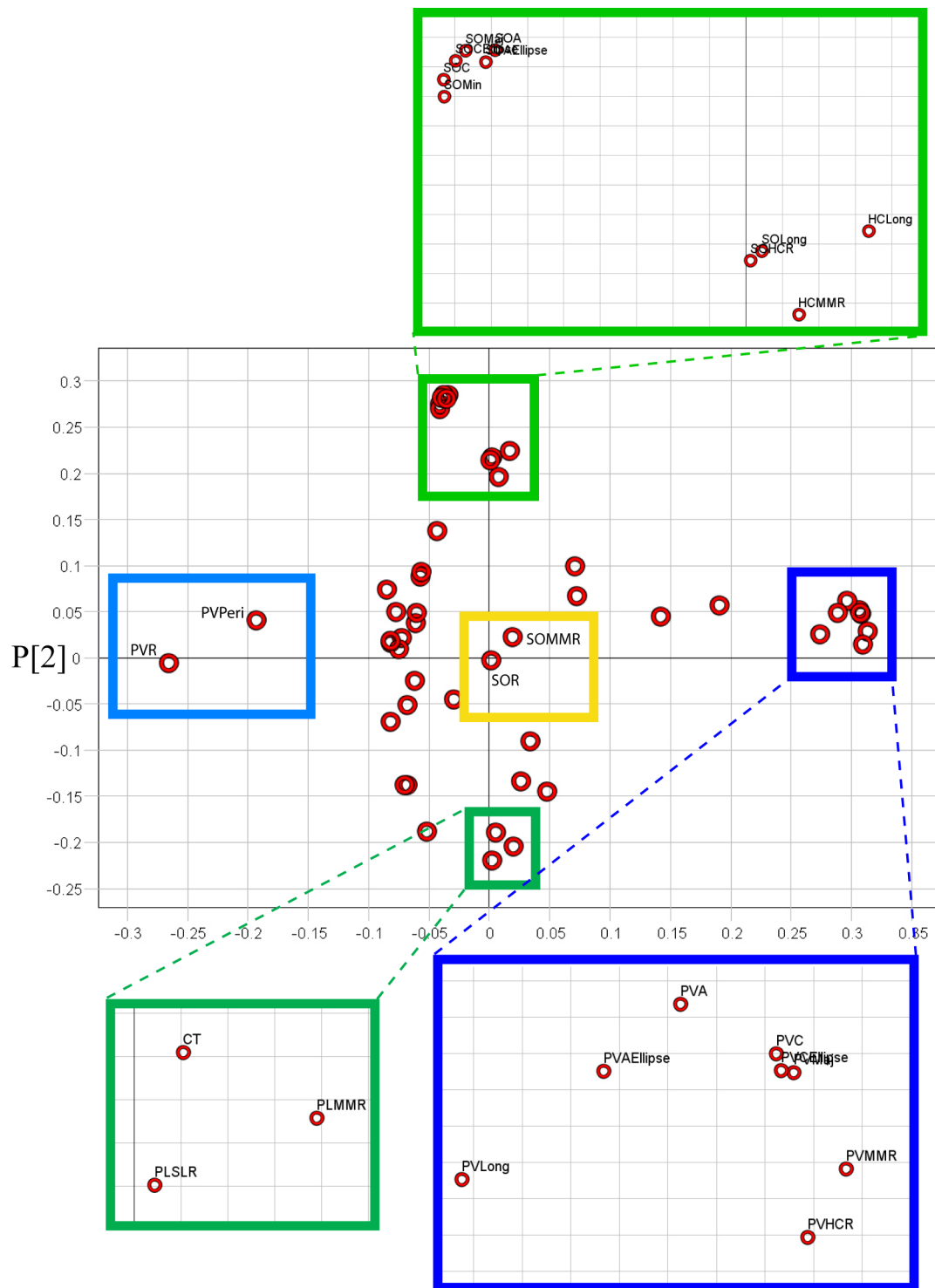


Figure 5.52: The loadings plot for the Bobcat local model in SIMCA analysis.

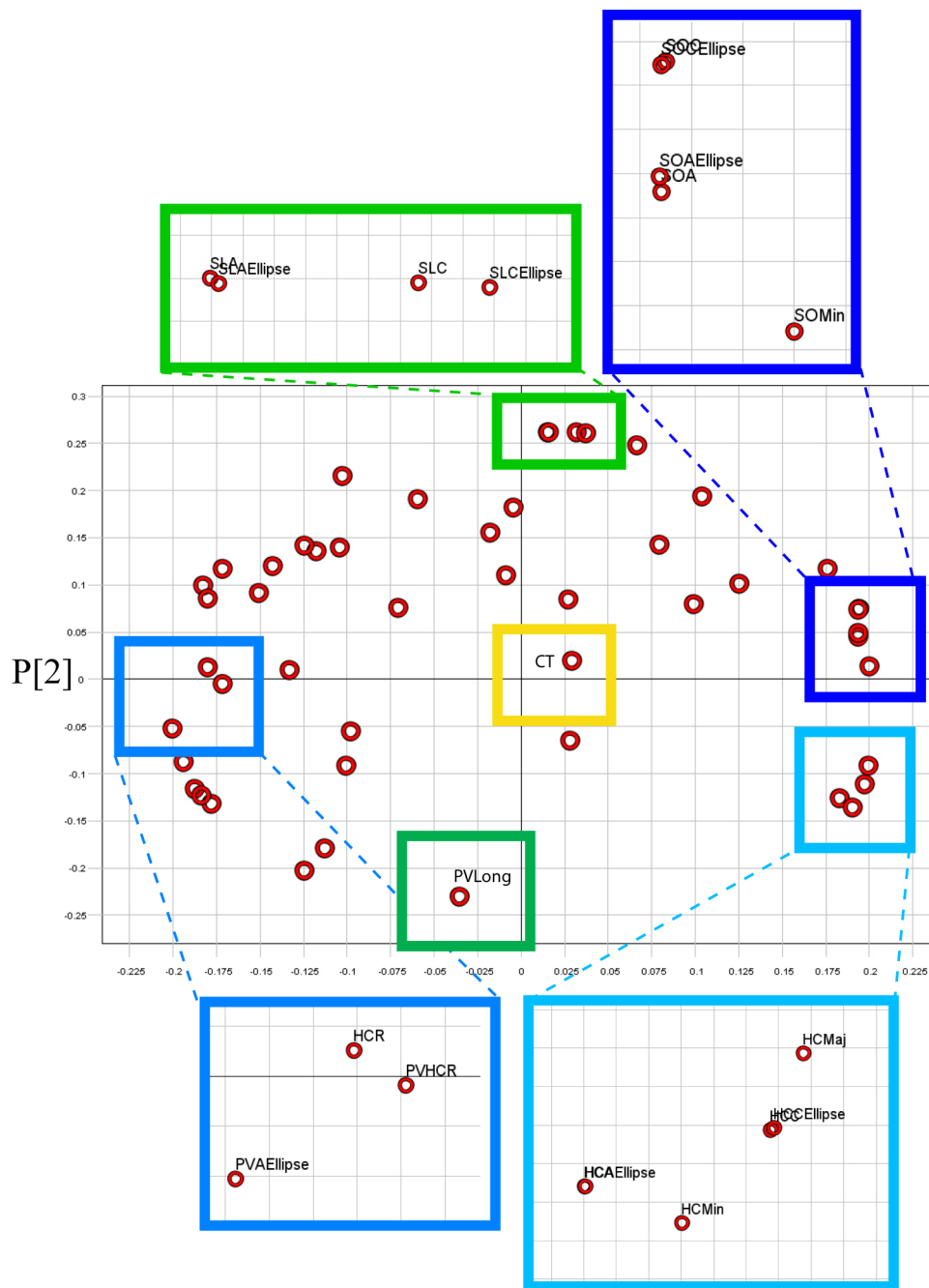


Figure 5.53: The loadings plot for the Beaver local model in SIMCA analysis.

The three principal components of the coyote (with micrograph 9 removed) explained 71% of the variance in the tibial cross-section (Figure 5.50). The variables of the coyote also show a large amount of covariance between PC1 and PC2. Most of the variance along PC1 (Figure 5.54) can be explained by the variables relating to the size of the secondary osteons, HCLong, SOR, PVHCR, and PVMin. The variables that show covariance in the all-positive PC1-PC2 quadrant are those that are related to the size of primary lacunae and the size of the Haversian canal. Variables that show covariance in the positive PC1 and negative PC2 quadrant are those related to the size of the secondary lacunae. Explaining the least amount of variance in the cross-section, and thus of most importance to this part of the study, are PVCentroid, PVPeri, PVR, and PLR.

5.5.3 Results: SIMCA

The test set, consisting of one micrograph chosen at random from each taxon (bear, beaver, bobcat, coyote), was tested against the training set (local models of each taxon) with 100% success. Each test micrograph was reassigned to the correct taxon. The Coomans' Plots in Figure 5.55 and Figure 5.56 show each possible pair of classes (taxa) in the dataset and the relationship of the Euclidean distances of each test sample. If the test sample is within a critical value (distance) of a class, then it is assigned to that class (horizontal and vertical red lines). For example, in the top plot of Figure 5.56, in which the "beaveriness" plots on the Y-axis and the "bobcatness" plots along the X-axis, the blue test point has a value of approximately 0.3 Y-units less than the critical value for the beaver (1.49 units). This makes it match to the beaver class. Likewise, the yellow point is approximately 0.4 X-units less than the critical value for the bobcat (1.56), also making it a match.

If there were test samples that could not be classified, they would appear as red dots in the upper right corner of the plot. Dots are colored by their predicted class membership and they are labeled by their actual class membership. Because an "unclassified" sample will be colored red, the color of the coyote was changed to magenta for SIMCA. All other taxon colors are consistent with previous sections of this chapter. In this iteration of SIMCA, the predicted and actual class membership matches correctly. The membership plots in Figure 5.57 show that the test sample

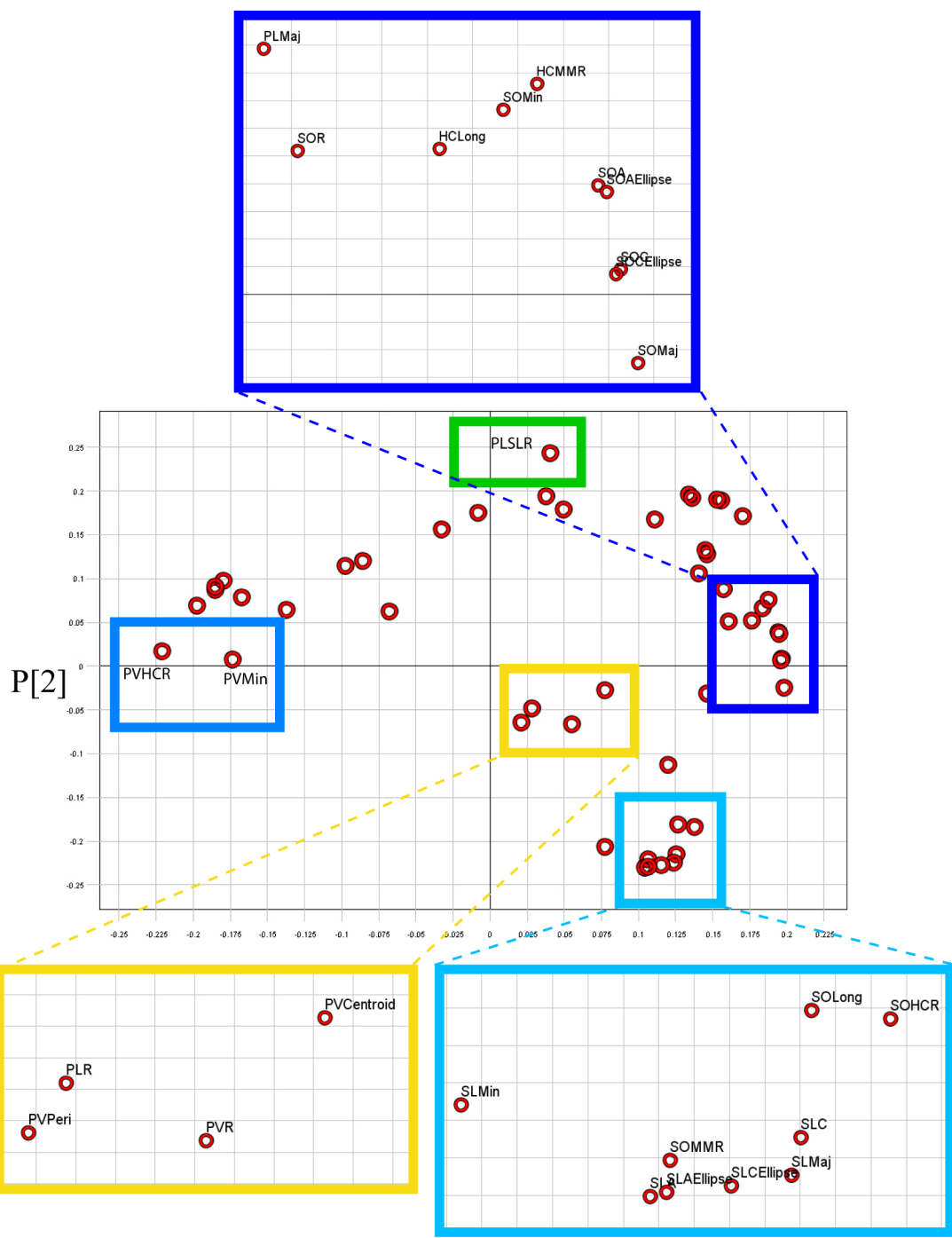


Figure 5.54: The loadings plot for the Coyote local model in SIMCA analysis.

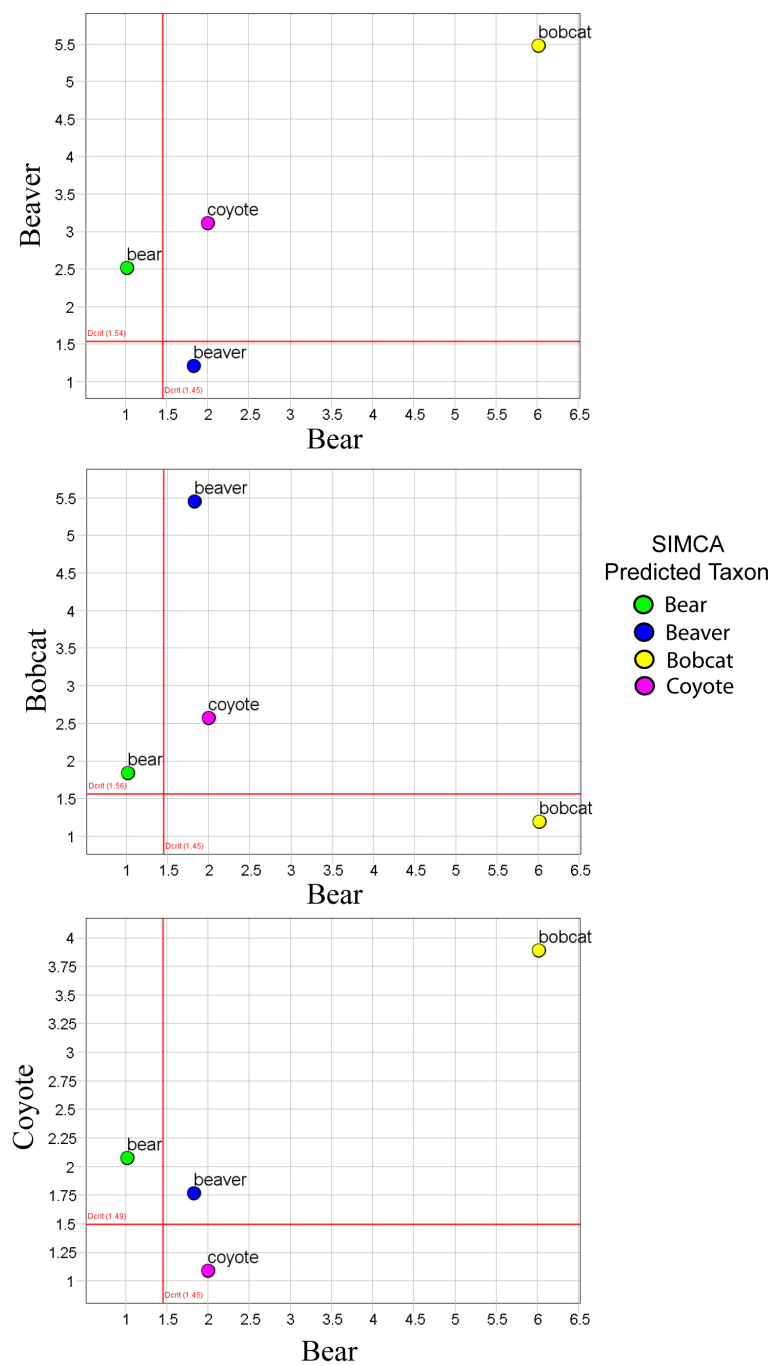


Figure 5.55: A series of Coomans' plots showing pairwise comparisons between taxa and the critical values associated with the local model of each taxon (red lines). The colors of the points refer to the SIMCA-predicted taxon and the labels refer to the actual taxonomic origin of the datapoint. Additional pairwise plots are found in Figure 5.56.

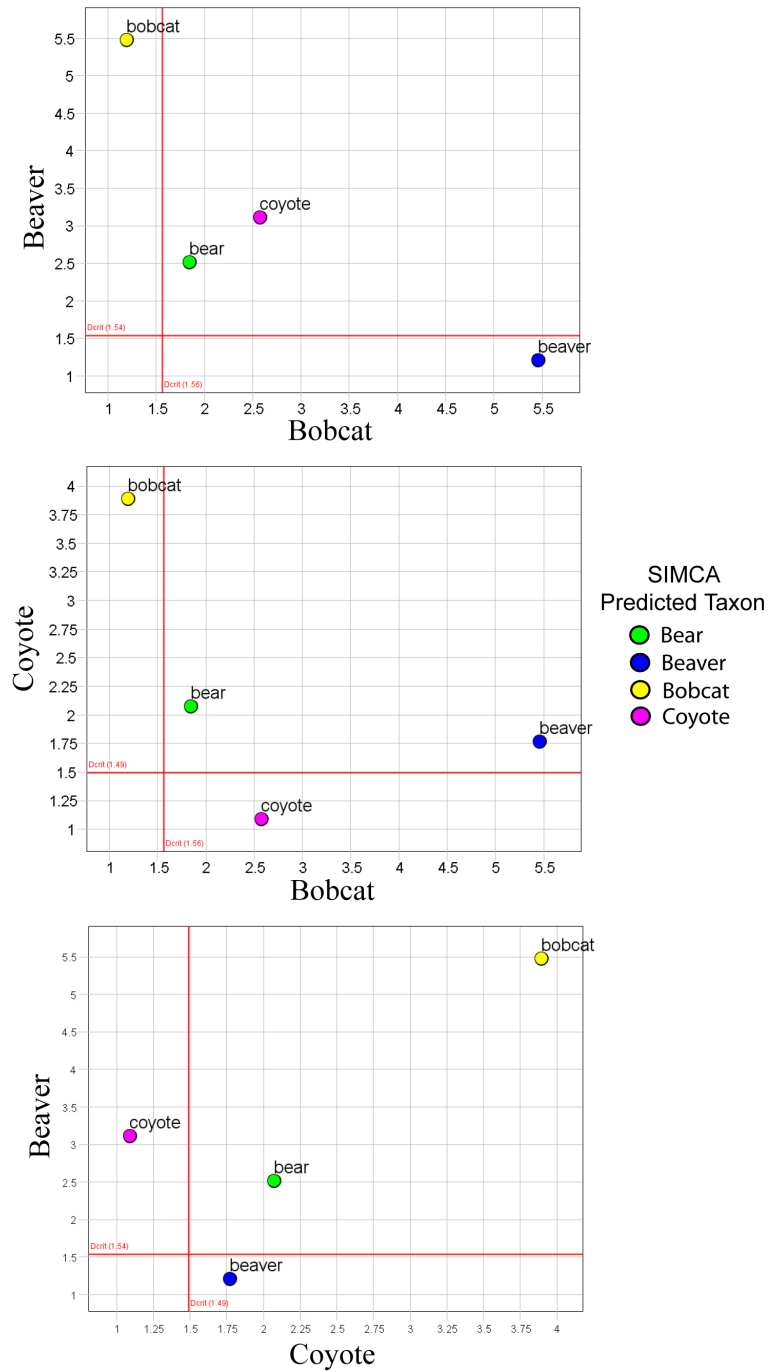


Figure 5.56: A series of Coomans' plots showing pairwise comparisons between taxa and the critical values associated with the local model of each taxon (red lines). The colors of the points refer to the SIMCA-predicted taxon and the labels refer to the actual taxonomic origin of the datapoint. Additional pairwise plots are found in Figure 5.55.

with the shortest Mahalanobis distance to the centroid of the local taxon model is assigned to that class.

The reassignment to the correct taxa of the randomly chosen samples in the test set is a promising outcome. This result suggests that the variation in microstructural morphology within a single bone cross-section is small enough that a single sample (micrograph) from that cross-section can still be recognized as having the microstructural fingerprint of a “bobcat”, “bear”, “coyote”, or “beaver”. The results also suggest that the variance between the taxa is large enough that the taxa can be separated.

Unfortunately, many of the taxa in the Primary Dataset could not undergo SIMCA analysis due to their low number of samples (micrographs). However, it is interesting to compare the outcome of this four-taxon SIMCA analysis with the results from PCA Run 2 on the whole Primary Dataset. The scores plot of Run 2 (Figure 5.38) shows clustering of samples according to taxon as well as two, larger-scale clusters of taxa, Group 1 and Group 2. Group 1 contained the bobcat, hare, and lemur, whereas Group 2 contained the coyote, bear, opossum, raccoon, beaver, capuchin and groundhog . The rhesus monkey has samples that overlapped with both groups. Based on the scores from Run 2, one might predict that bobcat samples (Group 1) could be distinguished from those of the bear (Group 2), because the centroids are farther apart in space between Groups 1 and 2 than within groups. SIMCA analysis confirms the ease of the bear-bobcat differentiation. The successful classification via SIMCA analysis of the bear, coyote, and beaver test samples was unexpected. However, a closer look at the sample points in Figure 5.39 (A,B) show that the data fields for the bear, bobcat, and beaver are closely adjacent to one another, but do not overlap much. Because of this, the SIMCA local models (and centroids) of each taxon were unique, and allowed the successful reassignment of test samples. The Mahalanobis distances of each taxon from one other shown in Figure 5.57 indicate that the centroids of the local models of the bear, beaver, and coyote are closer in space than that of the local model of the bobcat to each of those taxa.

The first test set chosen at random represents only one such test of the ability of the local taxon models to reassign samples to their respective taxon. What if the above samples chosen at random were the only samples that could be properly reclassified?

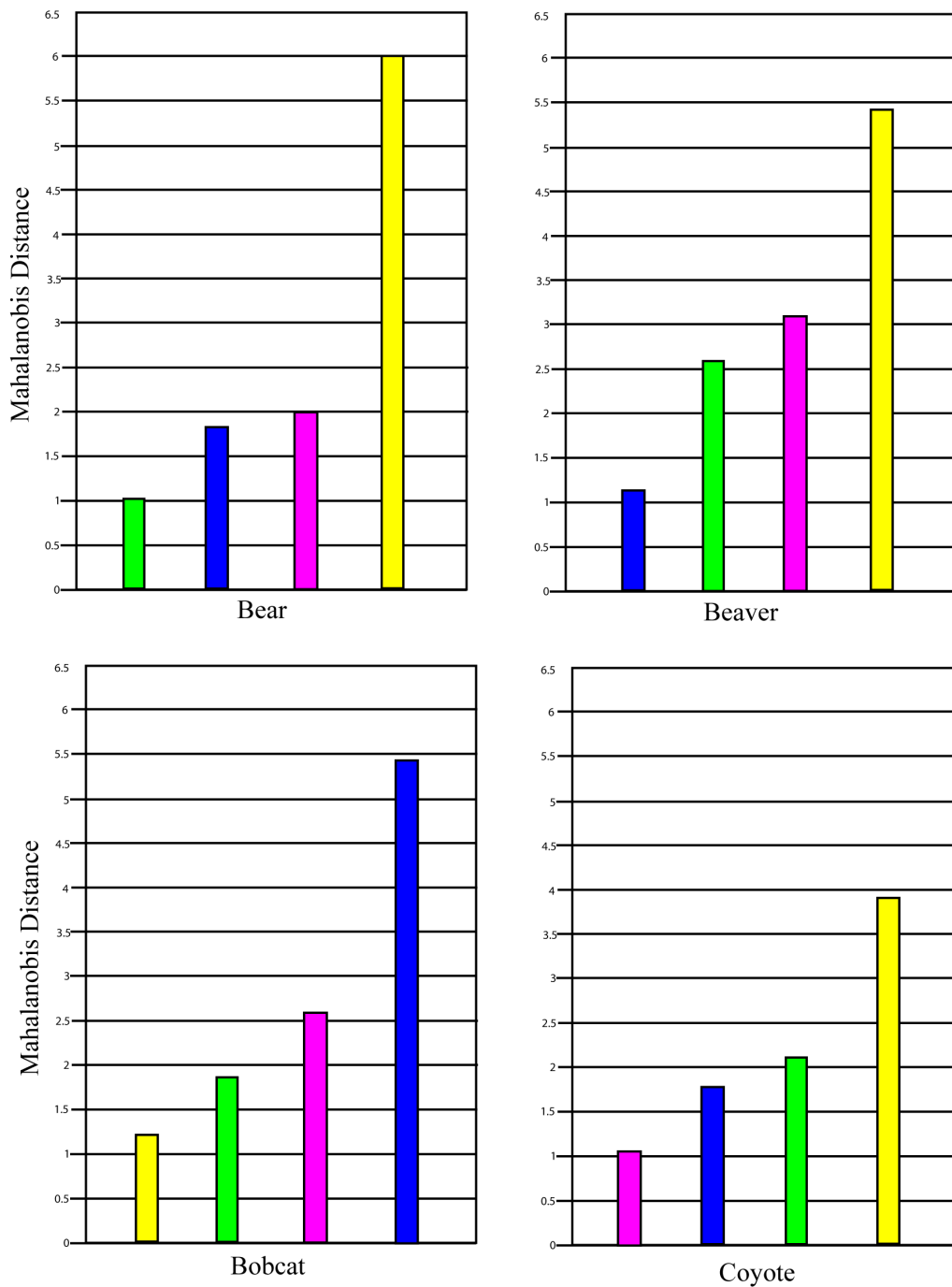


Figure 5.57: The membership plots for each taxon in the SIMCA analysis show the Mahalanobis distances to each local model (labeled on x-axis) represented. For a test sample to be assigned to a taxon, it must have the shortest Mahalanobis distance to that taxon.

If each sample were removed in a “leave-one-out” type of analysis, would each be reassigned correctly? How many samples can be removed from the training set before the local models become unable to predict the class membership of the test samples? Answering these questions is not trivial, especially considering the number of possible sample combinations in the bear/bobcat/beaver/coyote dataset. The bobcat was used as a case study to further test the robustness of the method and as an attempt to address the questions above. In this case study, the samples of the bear, beaver, and coyote included in the test set remained the same as those used above and stayed constant throughout the bobcat test. Further testing of the bobcat samples showed that Sample 15 was not the only sample that could be reassigned correctly to the local model. Determining the number of samples that could be reassigned correctly was accomplished by reinserting Sample 15 into the training set, removing another sample, recalculating the local model, and testing the newly removed sample for reassignment. This procedure was repeated for all 21 bobcat samples. All samples were classified correctly to the bobcat except for bobcat Samples 3, 12, 16, and 21. Rather than being assigned to the bear, beaver, or coyote, those samples were labeled as “not classified”. This means that the residual variance in those bobcat samples exceeded the residual variance for all other local models. Inspection of the input data matrix revealed that bobcat Samples 3, 12, and 21 were lacking in all measurement values for the primary vasculature. Visual inspection of the micrographs confirmed that there were no primary vascular canals. Most of the variance in principal component 1 of the bobcat, however, can be explained by the size and shape of the primary vascular canals. Whereas bobcat Sample 16 does show measured primary vascular canals, the shape, size, and orientation of these features are very different (long, thin, radial orientation) from those of other primary canals in other parts of the cross-section (generally short with a variable orientation). The results here indicate that the missing PV values contributed to the non-classification of three samples and further suggest that treatment of missing metrics could be very important in future microstructural datasets. The non-classification of Sample 16 may have been simply due to the difference in the size, shape and orientation of the primary canals compared to the same structures in other micrographs. These data must be included in order to fully characterize the microstructural morphology of the bobcat and cannot be further “dealt with”, such as by removal from the dataset.

The final evaluation of the bobcat case study was aimed at determining how many bobcat samples could be removed before collapse of the local model (the point at which too little information about the “bobcat-ness” of the cross-section was present by which to classify test samples). Beginning with Sample 15 as the test set, another sample was added sequentially to the test set after each SIMCA analysis. Each time a sample was added to the test set, the local model was recalculated. No samples were reinserted into the local class model after they had been removed. A total of 12 samples were transferred from the local model of the bobcat (training set) to the test set before the model could not classify some of the samples in the test set (Figure 5.58). This success with down to 9 samples in the training set confirms the stated requirement of the SIMCA analysis for at least ten samples of each class in the training set. The results of the enhanced bobcat analysis suggest that (1) given 9 or 10 samples/micrographs of the size treated here, the over-all characterization of bobcat microstructure is similar regardless of location in the cross-section from which the microstructures are measured, (2) it may have been possible to mark and measure a smaller number of microstructures of each type to get the same result, and (3) the methodology is robust in capturing the microstructural characteristics of different taxa.

5.6 Conclusions

Many conclusions can be drawn from the results of the principal component analyses and SIMCA modeling of the Primary Dataset. However, most germane to this dissertation is whether taxa can be separated/distinguished on the basis of bone microstructural morphology. The results of this chapter show that tetrapods can be distinguished taxonomically based on the quantitative measurement of the size, shape, and orientation of their bone microstructures. In addition, the results of PCA and SIMCA suggest that the variance of the microstructures within one cross-section is less than the variance between taxa, that the variables that explain the microstructural variance differ among the taxa, and that assurance of no missing metric values is very important to the correct characterization of the overall bone microstructure of a taxon.

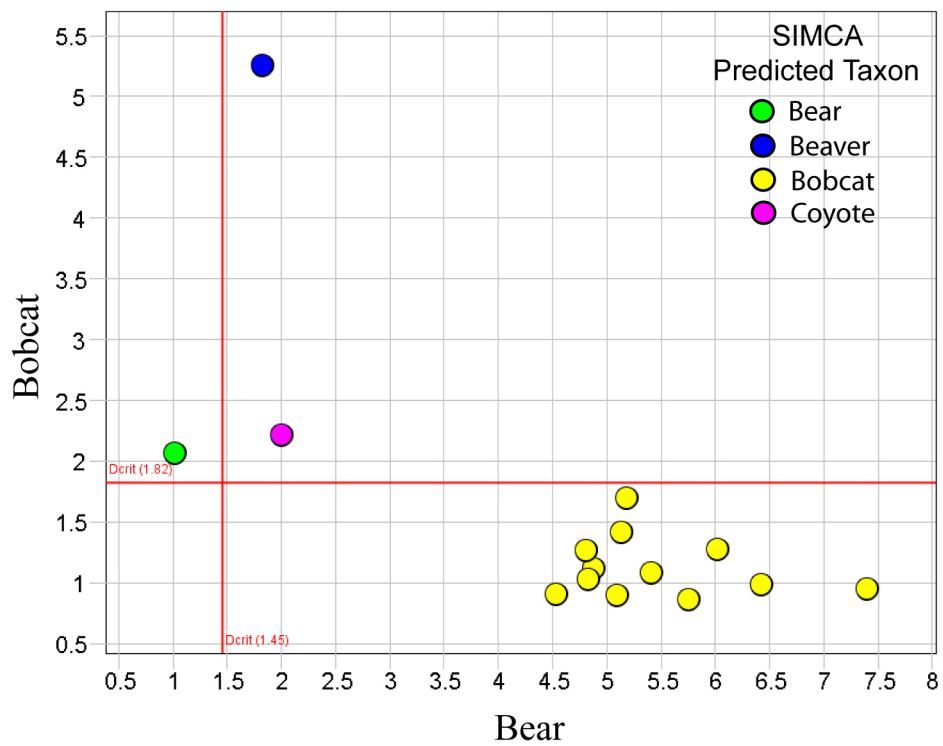


Figure 5.58: A Coomans' plot showing the twelve test samples that were assigned correctly to the bobcat local model whose training set had been depleted to only nine samples.

Chapter 6

Multiple Discriminant Analysis and Significance Tests of the Primary Dataset

6.1 Introduction

Whereas the main goal of the overall project is to differentiate taxa based on the morphology of bone microstructure, this dissertation represents an exploratory stage of the project. Chapter 5 presented detailed principals component analyses (PCA) and a Soft Independent Modeling of Class Analogy (SIMCA) analysis of the Primary Dataset. The results suggested that (1) taxa can be distinguished on the basis of the size, shape, and orientation of cortical bone microstructures, (2) taxonomic separation is the result of a combination of measurements from different microstructural types, and (3) the variance of microstructural morphology was greater between taxa than it was within one bone cross-section. In the present chapter, confidence in the discrimination between taxa undergoes its final test through Multiple Discriminant Analysis (MDA) of the PCA scores.

Multiple discriminant analysis (alternatively called discriminant function analysis, discriminant factor analysis, or canonical discriminant analysis) is an extension of discriminant analysis (DA), in that it is able to accommodate more than two categorical dependent variables. The main purpose of MDA is to classify cases into groups, to investigate the differences between groups, to determine the most parsimonious way to distinguish between groups, and to assess the relative importance of independent

variables in classifying the dependent variables. A good review of MDA can be found in Huberty (1994). Multiple discriminant analysis is used here to test the significance of the PCA results presented in Chapter 5. The PCA-MDA combination is found throughout the literature (Park et al., 2006; Sirieix and Downey, 1993) and is used, in part, to test the validity of data point configuration (in this case, clustering and separation of taxa) as a result of PCA. There are no significance values assigned to PCA results, which can lead to over-interpretation of the results. Principal components analysis will always provide an amount of variance that is explained by the variables in the dataset, the loadings values that explain the variance, and the scores values that show where the points lie in vector space. Depending on the question to be answered, however, the way that data points are situated in space can be misleading. As an example, it is good to review Run 3 of Chapter 5 (Figure 5.47). Each point in the scores plots represents a single taxon. From the scores plot, it seems that the taxa are widely separated in space. This situation would make identification of an “unknown” sample seem easy. It also gives the impression that the bone microstructural morphologies are unique to each specimen. Because the results are in line with the hypothesis of this dissertation, they are very alluring. However, PCA will always show separation of data points in the scores plot. What is important and what is being validated here is whether that data point separation is “significant” and if the results support the hypothesis of taxonomic separation due to bone microstructural morphology.

Significance testing of the principal components can be performed through multiple discriminant analysis, using the scores values for each component. The values of the scores represent the product of each observed variable and the j^{th} principal component’s eigenvector. Therefore, scores can be used either as (1) measures of latent variables in statistical analysis, used to identify factors that explain their variability (as dependent variables) or (2) measures of factors that act as explanatory (independent) variables. In this chapter, the principal component scores are treated as the latter. A series of multiple discriminant analyses is performed using the principal component scores to test the significance of the data compression arising from PCA of the Primary Dataset.

The organization of this chapter is similar to that of Chapter 5. Multiple discriminant analysis will be performed on the scores from PCA of the datasets in Run 1 and Run

2 presented in Chapter 5. The scores values included in each MDA are from those principal components retained in each Run as determined by the Kaiser-Guttman Criterion. The two steps of the MDA proceed with (1) an F-test (Wilke's Lambda), which is used to test the overall significance of the model, and (2) a test of each independent variable (in this case, PCA scores) to see which variables' means differ significantly from one another, as a method of determining if the overall model is significant. Those independent variables whose means differ significantly are used to classify the dependent variable. It should be noted here that, although an overall PCA model may be significant, this does not mean that the model supports the hypothesis that taxa may be discriminated based on the morphology of their cortical microstructure. The real test provided by the MDA (and, thus, PCA) is whether the independent samples can be re-classified to their respective dependent variables (Taxa). Unlike PCA, which does not assume class membership before analysis take place, MDA offers optimal separation of pre-defined groups. For example, if the class membership of each sample is already known before the analysis takes place, all of the "bobcat" samples are "binned" as such, and the MDA will attempt to fit all of those bobcat samples into the "bobcat" vector space. Although this method can be a disadvantage as a first step in exploratory analysis of a dataset, it will be an advantage here in the final test of significance. The taxonomic grouping and separation by microstructural datapoints have been pre-defined by PCA. The true test of significance will be whether those points (represented here as PCA scores rather than the original sample values) can be reassigned to their respective taxa. The larger the number of data points that can be reassigned to the correct taxon, the more powerful the principal components are, and, thus, the variables, in distinguishing between taxa in the Primary Dataset.

Unlike PCA plots, the output of MDA refers to each taxon as a number. The taxa are numbered according to their alphabetical order. The abbreviations for plots in Chapter 6 are as follows: Bear (**1**); Beaver (**2**), Bobcat (**3**), Capuchin (**4**), Coyote (**5**), Groundhog (**6**), Hare (**7**), Lemur (**8**), Opossum (**9**), Raccoon (**10**), Rhesus (**11**).

6.2 Multiple Discriminant Analysis: Run 1

Multiple discriminant analysis is performed on the PCA scores calculated for the five microstructural types (secondary osteons, Haversian canals, primary lacunae, secondary lacunae, and primary vasculature). The format will follow that of Run 1 in Chapter 5, and the significance of each PCA analysis will be addressed. The details of each dataset can be found in Chapter 5.

6.2.1 Run 1A: Secondary Osteons

The results of the MDA on the secondary osteons are shown in Figure 6.1 and Figure 6.2. For a total of 3580 cases (one secondary osteon is equal to one case), principal component 1 ($t[1]$) and principal component 2 ($t[2]$) are significant to a 95% confidence interval. In the Analysis of Variance (ANOVA) table (testing the equality of group means) in Figure 6.1, the smaller the value of Wilks' Lambda, the more important the independent variable is in the discriminant function. By definition, the first principal component should be the most important and should explain the greatest amount of variance in the dataset. The ANOVA table shows that this is the case, in that PC1 ([1]) has a smaller Wilks' Lambda value than PC2. The second test of the relative importance of the independent variables in predicting the dependent variables (Taxa) is shown in the Standardized Canonical Discriminant Function Coefficients table, also found in Figure 6.1. The coefficients in the table serve the same function as beta weights in a multiple regression analysis. The results of this latter test show that PC1 has the greatest influence in the first discriminant function (i.e., $t[1]$ has the highest value in the column under Function 1) and that PC2 has the most influence over the second discriminant function. This is an expected result and supports the validity of the PCA data compression. In the canonical discriminant function plot of the secondary osteons in Figure 6.1, the group centroids are defined by squared Mahalanobis distances. The plot shows that the centroids of all the taxa are tightly clustered. The clustering of the centroids based on the morphological characteristics of the secondary osteons indicates that it is not likely that taxa can be discriminated using only those microstructural characteristics. The data in Figure 6.2 support this conclusion, indicating that only 8.7% of the cases (secondary osteons from known

taxa) were correctly classified. This result is consistent with PCA results for secondary osteons, which also did not show strong separation of taxa.

6.2.2 Run 1B: Haversian Canals

The results of the MDA on the Haversian canals are shown in Figure 6.3 and Figure 6.4. For a total of 3610 cases (one Haversian canal is equal to one case), principal component 1 (t[1]), principal component 2 (t[2]), and principal component 3 (t[3]) are significant. The ANOVA table (testing the equality of group means) in Figure 6.3, shows that PC1 has the smallest value of Wilks' Lambda, which is as expected. For the same reason, it is expected that PC3 will have the largest value of Wilks' Lambda, but this is not the case. Instead, PC2 has the largest value. The Standardized Canonical Discriminant Function Coefficients table, also found in Figure MDA-blue1, reveals the same result, based on the influence of each principal component to predict the dependent variable. The results of this latter test show that PC1 has the greatest influence in the first discriminant function (i.e., highest value in the column for Function 1), but PC3 has the most influence over the second discriminant function and PC2 over the third discriminant function. In the canonical discriminant function plot of the Haversian canals in Figure 6.3, the positions of the group centroids are defined by squared Mahalanobis distances. The plot shows that the centroids of the taxa are tightly clustered. The clustering of the centroids based on the morphological characteristics of the Haversian canals indicates that it is not likely that taxa can be discriminated using only those microstructural characteristics. Figure 6.4 supports this conclusion, indicating that only 10.1% of cases were correctly classified. This result is consistent with PCA results for Haversian canals (Figure 5.27).

The discrepancy between the relative influences of the PC2 and PC3 over the discriminant functions is suspected to be a result of the different mathematical treatment of the data in PCA versus MDA. Whereas MDA adopts many of the same perspectives as PCA, the two methods are mathematically different in what they are maximizing. Whereas PCA maximizes the variance in all of the variables accounted for by the principal components, MDA maximizes the difference between values of the dependent variables in order to give optimal separation of pre-defined groups.

Analysis Case Processing Summary

Unweighted Cases		N	Percent
Valid		3580	100.0
Excluded	Missing or out-of-range group codes	0	.0
	At least one missing discriminating variable	0	.0
	Both missing or out-of-range group codes and at least one missing discriminating variable	0	.0
	Total	0	.0
Total		3580	100.0

Tests of Equality of Group Means (ANOVA)

	Wilks' Lambda	F	df1	df2	Sig.
t[1]	.867	54.879	10	3569	.000
t[2]	.976	8.921	10	3569	.000

Standardized Canonical Discriminant Function Coefficients

	Function	
	1	2
t[1]	.950	.316
t[2]	-.362	.933

Canonical Discriminant Functions

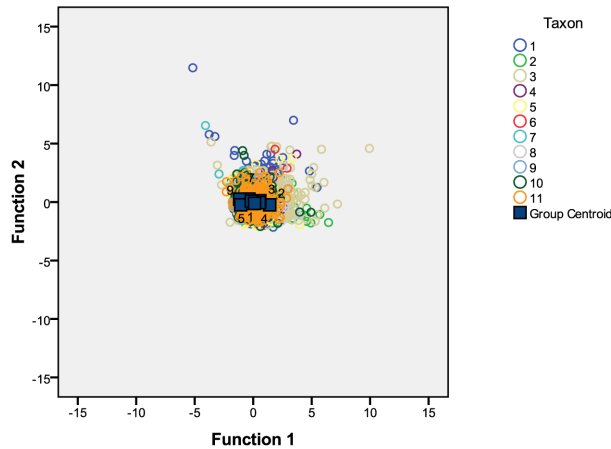


Figure 6.1: A series of tables and the canonical discriminant functions chart from the multiple discriminant analysis of the PCA scores of Run 1A (secondary osteons) of the Primary Dataset. The scores values for each principal component are significant to 95% confidence level.

Classification Results^a

Taxon	Predicted Group Membership											Total
	1	2	3	4	5	6	7	8	9	10	11	
Original Count	72	85	138	29	317	296	241	88	297	46	133	1742
	4	40	9	0	7	4	2	2	2	0	5	75
	14	212	78	3	52	81	60	39	71	9	58	677
	3	16	12	2	23	10	14	5	12	2	13	112
	8	32	20	4	29	40	26	14	59	8	21	261
	2	1	2	1	2	7	6	1	7	0	1	30
	0	0	2	0	1	4	23	0	24	0	0	54
	2	31	14	1	4	9	8	12	12	2	8	103
	2	0	1	0	0	1	6	0	21	0	1	32
	5	20	21	3	26	31	30	11	31	1	5	184
	9	49	37	0	48	40	16	33	40	10	28	310
%	4.1	4.9	7.9	1.7	18.2	17.0	13.8	5.1	17.0	2.6	7.6	100.0
	5.3	53.3	12.0	.0	9.3	5.3	2.7	2.7	2.7	.0	6.7	100.0
	2.1	31.3	11.5	.4	7.7	12.0	8.9	5.8	10.5	1.3	8.6	100.0
	2.7	14.3	10.7	1.8	20.5	8.9	12.5	4.5	10.7	1.8	11.6	100.0
	3.1	12.3	7.7	1.5	11.1	15.3	10.0	5.4	22.6	3.1	8.0	100.0
	6.7	3.3	6.7	3.3	6.7	23.3	20.0	3.3	23.3	.0	3.3	100.0
	.0	.0	3.7	.0	1.9	7.4	42.6	.0	44.4	.0	.0	100.0
	1.9	30.1	13.6	1.0	3.9	8.7	7.8	11.7	11.7	1.9	7.8	100.0
	6.3	.0	3.1	.0	.0	3.1	18.8	.0	65.6	.0	3.1	100.0
	2.7	10.9	11.4	1.6	14.1	16.8	16.3	6.0	16.8	.5	2.7	100.0
	2.9	15.8	11.9	.0	15.5	12.9	5.2	10.6	12.9	3.2	9.0	100.0

8.7% of cases in the original group are correctly classified

Figure 6.2: The classification results from the multiple discriminant analysis of the PCA scores values of Run 1A (secondary osteons) of the Primary Dataset.

Analysis Case Processing Summary

Unweighted Cases		N	Percent
Valid		3610	100.0
Excluded	Missing or out-of-range group codes	0	.0
	At least one missing discriminating variable	0	.0
	Both missing or out-of-range group codes and at least one missing discriminating variable	0	.0
	Total	0	.0
Total		3610	100.0

Tests of Equality of Group Means (ANOVA)

	Wilks' Lambda	F	df1	df2	Sig.
t[1]	.895	42.354	10	3599	.000
t[2]	.983	6.216	10	3599	.000
t[3]	.966	12.795	10	3599	.000

Standardized Canonical Discriminant Function Coefficients

	Function		
	1	2	3
t[1]	.857	-.519	-.018
t[2]	.339	.453	.826
t[3]	.474	.695	-.544

Canonical Discriminant Functions

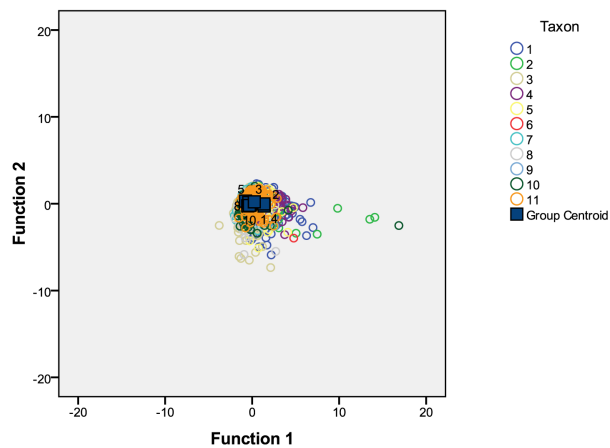


Figure 6.3: A series of tables and the canonical discriminant functions chart from the multiple discriminant analysis of the PCA scores of Run 1B (Haversian canals) of the Primary Dataset. The scores values for each principal component are significant to 95% confidence level.

		Classification Results ^a											Total
		Predicted Group Membership											
Taxo	Count	1	2	3	4	5	6	7	8	9	10	11	
1	104	147	58	141	34	40	189	352	138	95	462	1760	
2	7	20	1	12	0	1	3	8	2	4	14	72	
3	30	25	13	16	10	4	256	170	39	26	112	701	
4	4	29	1	39	2	1	0	1	3	8	26	114	
5	13	17	7	10	3	8	39	65	23	8	68	261	
6	3	1	1	0	0	0	6	11	4	1	3	30	
7	0	2	0	1	0	0	38	7	3	0	3	54	
8	1	5	4	0	3	2	32	33	4	2	16	102	
9	2	0	1	1	0	0	8	10	7	0	4	33	
10	7	7	9	3	2	4	46	64	11	5	23	181	
11	12	26	6	32	10	7	39	21	24	21	104	302	
%	5.9	8.4	3.3	8.0	1.9	2.3	10.7	20.0	7.8	5.4	26.3	100.0	
	9.7	27.8	1.4	16.7	.0	1.4	4.2	11.1	2.8	5.6	19.4	100.0	
	4.3	3.6	1.9	2.3	1.4	.6	36.5	24.3	5.6	3.7	16.0	100.0	
	3.5	25.4	.9	34.2	1.8	.9	.0	.9	2.6	7.0	22.8	100.0	
	5.0	6.5	2.7	3.8	1.1	3.1	14.9	24.9	8.8	3.1	26.1	100.0	
	10.0	3.3	3.3	.0	.0	.0	20.0	36.7	13.3	3.3	10.0	100.0	
	.0	3.7	.0	1.9	.0	.0	70.4	13.0	5.6	.0	5.6	100.0	
	1.0	4.9	3.9	.0	2.9	2.0	31.4	32.4	3.9	2.0	15.7	100.0	
	6.1	.0	3.0	3.0	.0	.0	24.2	30.3	21.2	.0	12.1	100.0	
	3.9	3.9	5.0	1.7	1.1	2.2	25.4	35.4	6.1	2.8	12.7	100.0	
	4.0	8.6	2.0	10.6	3.3	2.3	12.9	7.0	7.9	7.0	34.4	100.0	

10.1% of cases in the original group are correctly classified

Figure 6.4: The classification results from the multiple discriminant analysis of the PCA scores values of Run 1B (Haversian canals) of the Primary Dataset.

6.2.3 Run 1C: Primary Lacunae

The results of the MDA on the primary lacunae are shown in Figure 6.5 and Figure 6.6. For a total of 1992 cases (one primary lacuna is equal to one case), principal component 1 (t[1]) and principal component 2 (t[2]) are significant. The ANOVA table (testing the equality of group means) in Figure 6.5, shows that PC1 has the smaller value of Wilks' Lambda and PC2 the larger value. Thus, the principal components have the expected relative significance. The Standardized Canonical Discriminant Function Coefficients table, also found in Figure 6.5, shows the comparable result based on the influence of each principal component to predict the dependent variable. The results of this test show that PC1 has the greater influence over the first discriminant function and PC2 over the second discriminant function. In the canonical discriminant function plot of the primary lacunae in Figure 6.5, the group positions of centroids are defined by squared Mahalanobis distances. The plot shows that the centroids of the taxa are clustered, but clearly into two separated groups of taxa, reminiscent of the two taxon groups revealed in Run 2 of Chapter 5 (Figure 5.38). Figure 6.6 shows that the re-classification of cases based only on the primary lacunae is slightly more successful than reclassification by secondary osteons or Haversian canals, with 29.8% of cases correctly classified. Despite the increase in the number of cases correctly classified, the percentage is still not high enough to conclude that taxa can be discriminated based only on primary lacunae.

6.2.4 Run 1D: Secondary Lacunae

The results of the MDA on the secondary lacunae are shown in Figure 6.7 and Figure 6.8. For a total of 2141 cases (one secondary lacuna is equal to one case), principal component 1 (t[1]) and principal component 2 (t[2]) are significant. The ANOVA table (testing the equality of group means) in Figure 6.7, shows that PC1 has the smaller value of Wilks' Lambda and PC2 the larger value. The Standardized Canonical Discriminant Function Coefficients table, also found in Figure 6.7, reveals the same result based on the influence of each principal component to predict the dependent variable. The results of this test show that PC1 has the greater influence over the first discriminant function and PC2 over the second discriminant function. In the canonical

Analysis Case Processing Summary

Unweighted Cases		N	Percent
Valid		1992	100.0
Excluded	Missing or out-of-range group codes	0	.0
	At least one missing discriminating variable	0	.0
	Both missing or out-of-range group codes and at least one missing discriminating variable	0	.0
	Total	0	.0
Total		1992	100.0

Tests of Equality of Group Means (ANOVA)

	Wilks' Lambda	F	df1	df2	Sig.
t{1}	.449	243.115	10	1981	.000
t{2}	.878	27.615	10	1981	.000

Standardized Canonical Discriminant Function Coefficients

	Function	
	1	2
t{1}	1.023	.248
t{2}	-.554	.895

Canonical Discriminant Functions

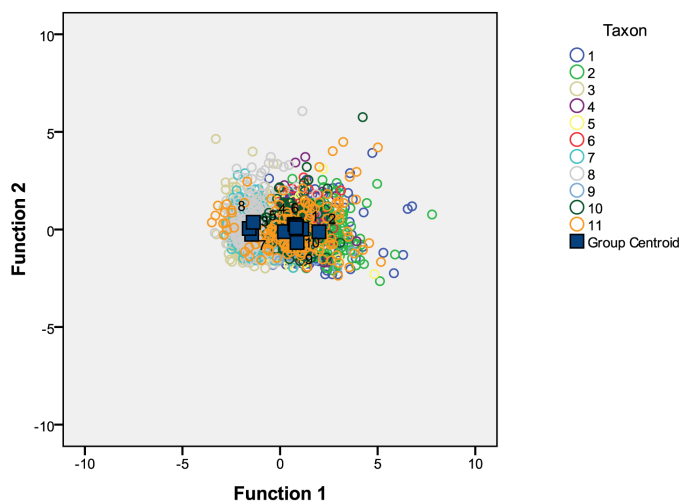


Figure 6.5: A series of tables and the canonical discriminant functions chart from the multiple discriminant analysis of the PCA scores of Run 1C (primary lacunae) of the Primary Dataset. The scores values for each principal component are significant to 95% confidence level.

Classification Results^a

Taxon	Predicted Group Membership											Total
	1	2	3	4	5	6	7	8	9	10	11	
Original	15	84	12	19	49	53	0	9	56	3	7	307
Count	27	125	0	8	2	18	0	0	33	4	2	219
	1	1	210	1	25	1	65	93	7	0	0	404
	6	11	2	3	25	22	0	2	14	3	3	91
	4	9	12	12	78	14	0	9	21	3	0	162
	9	10	0	8	25	17	0	0	10	0	2	81
	0	0	70	0	6	0	47	71	4	0	0	198
	0	0	66	4	11	9	51	73	4	0	0	218
	4	8	0	1	14	0	0	0	21	0	2	50
	7	19	2	10	19	24	0	5	29	3	2	120
	10	41	14	5	18	13	9	7	23	0	2	142
%	4.9	27.4	3.9	6.2	16.0	17.3	.0	2.9	18.2	1.0	2.3	100.0
	12.3	57.1	.0	3.7	.9	8.2	.0	.0	15.1	1.8	.9	100.0
	.2	.2	52.0	.2	6.2	.2	16.1	23.0	1.7	.0	.0	100.0
	6.6	12.1	2.2	3.3	27.5	24.2	.0	2.2	15.4	3.3	3.3	100.0
	2.5	5.6	7.4	7.4	48.1	8.6	.0	5.6	13.0	1.9	.0	100.0
	11.1	12.3	.0	9.9	30.9	21.0	.0	.0	12.3	.0	2.5	100.0
	.0	.0	35.4	.0	3.0	.0	23.7	35.9	2.0	.0	.0	100.0
	.0	.0	30.3	1.8	5.0	4.1	23.4	33.5	1.8	.0	.0	100.0
	8.0	16.0	.0	2.0	28.0	.0	.0	.0	42.0	.0	4.0	100.0
	5.8	15.8	1.7	8.3	15.8	20.0	.0	4.2	24.2	2.5	1.7	100.0
	7.0	28.9	9.9	3.5	12.7	9.2	6.3	4.9	16.2	.0	1.4	100.0

29.8% of cases in the original group are correctly classified

Figure 6.6: The classification results from the multiple discriminant analysis of the PCA scores values of Run 1C (primary lacunae) of the Primary Dataset.

discriminant function plot of the secondary lacunae in Figure 6.7, the positions of the group centroids are defined by squared Mahalanobis distances. The plot shows that the centroids of the taxa are clustered. The separation into two clusters of taxa, as seen in the canonical discriminant function plot for the primary lacunae, is not as prominent in this analysis. Figure 6.8 shows that the re-classification of cases based only on the secondary lacunae is the most successful of all of the microstructural types at distinguishing between taxa. A total of 46.3% of cases were reclassified correctly. This result is surprising given the relatively large percentage of taxonomic resolution achieved by the variables pertaining to the secondary lacunae. In the PCA of the Primary Dataset, the scores plot of the secondary lacunae (Figure 5.29) did not visually seem to show a greater amount of taxon clustering and/or separation than the other PCA in Run 1. The utility of MDA is shown here, in that these results suggest that the secondary lacunae could have a large taxonomic value even without the addition of other microstructural types in the analysis.

6.2.5 Run 1E: Primary Vasculature

The results of the MDA on the Haversian canals are shown in Figure 6.9 and Figure 6.10. For a total of 4393 cases (one Haversian canal is equal to one case), principal component 1 ($t[1]$), principal component 2 ($t[2]$), and principal component 3 ($t[3]$) are significant. The ANOVA table (testing the equality of group means) in Figure 6.9, shows that PC1 has the smallest value of Wilks' Lambda, confirming its greatest significance. It is expected that PC3 will have the largest value of Wilks' Lambda, but this is not the case. As in the discriminant analysis of the Haversian canals, PC2 is shown to have the largest value and, thus, the least significance. The Standardized Canonical Discriminant Function Coefficients table, also found in Figure 6.9, shows the comparable result based on the influence of each principal component to predict the dependent variable. The results of this test show that PC1 has the greatest influence in the first discriminant function, but PC2 has the most influence over the third discriminant function and PC3 over the second discriminant function. In the canonical discriminant function plot of the primary vascular canals in Figure 6.9, the positions of the group centroids are defined by squared Mahalanobis distances. The plot shows that the centroids of the taxa are tightly clustered as in the MDA of the

Analysis Case Processing Summary

Unweighted Cases		N	Percent
Valid		2141	100.0
Excluded	Missing or out-of-range group codes	0	.0
	At least one missing discriminating variable	0	.0
	Both missing or out-of-range group codes and at least one missing discriminating variable	0	.0
	Total	0	.0
Total		2141	100.0

Tests of Equality of Group Means (ANOVA)

	Wilks' Lambda	F	df1	df2	Sig.
t[1]	.527	191.065	10	2130	.000
t[2]	.878	29.595	10	2130	.000

Standardized Canonical Discriminant Function Coefficients

	Function	
	1	2
t[1]	.991	.235
t[2]	-.417	.929

Canonical Discriminant Functions

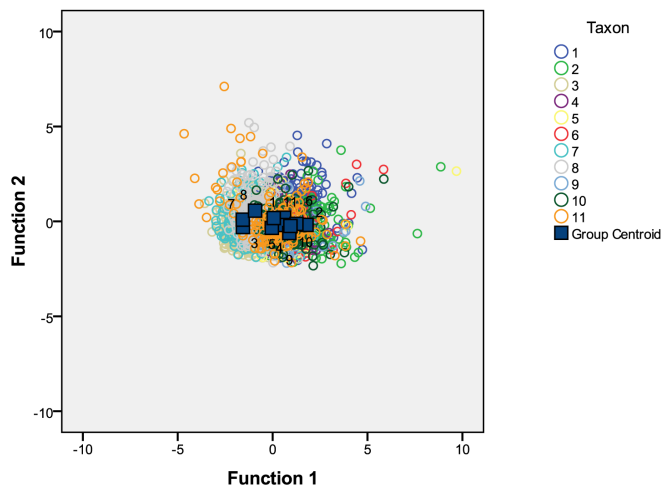


Figure 6.7: A series of tables and the canonical discriminant functions chart from the multiple discriminant analysis of the PCA scores of Run 1D (secondary lacunae) of the Primary Dataset. The scores values for each principal component are significant to 95% confidence level.

		Classification Results ^a											Total
		Predicted Group Membership											
Taxo	n	1	2	3	4	5	6	7	8	9	10	11	
Original	Count	615	20	33	0	1	0	0	6	0	0	0	675
		102	33	1	0	1	0	0	0	0	0	0	137
		30	0	292	0	2	0	0	24	0	0	0	348
		72	2	1	0	0	0	0	1	0	0	0	76
		154	3	55	0	2	0	0	4	0	0	0	218
		52	6	0	0	0	0	0	0	0	0	0	58
		14	0	85	0	0	0	0	15	0	0	0	114
		69	0	90	0	2	0	0	50	0	0	0	211
		37	6	3	0	0	0	0	0	0	0	0	46
		106	11	1	0	0	0	0	2	0	0	0	120
		94	7	24	0	1	0	0	12	0	0	0	138
%		91.1	3.0	4.9	.0	.1	.0	.0	.9	.0	.0	.0	100.0
		74.5	24.1	.7	.0	.7	.0	.0	.0	.0	.0	.0	100.0
		8.6	.0	83.9	.0	.6	.0	.0	6.9	.0	.0	.0	100.0
		94.7	2.6	1.3	.0	.0	.0	.0	1.3	.0	.0	.0	100.0
		70.6	1.4	25.2	.0	.9	.0	.0	1.8	.0	.0	.0	100.0
		89.7	10.3	.0	.0	.0	.0	.0	.0	.0	.0	.0	100.0
		12.3	.0	74.6	.0	.0	.0	.0	13.2	.0	.0	.0	100.0
		32.7	.0	42.7	.0	.9	.0	.0	23.7	.0	.0	.0	100.0
		80.4	13.0	6.5	.0	.0	.0	.0	.0	.0	.0	.0	100.0
		88.3	9.2	.8	.0	.0	.0	.0	1.7	.0	.0	.0	100.0
		68.1	5.1	17.4	.0	.7	.0	.0	8.7	.0	.0	.0	100.0

46.3% of cases in the original group are correctly classified

Figure 6.8: The classification results from the multiple discriminant analysis of the PCA scores values of Run 1D (secondary lacunae) of the Primary Dataset.

secondary osteons and the Haversian canals. The clustering of the centroids based on the morphological characteristics of the primary vasculature indicates that it is not likely that taxa can be discriminated using only those microstructural characteristics. Figure 6.10 supports this conclusion, indicating that only 19.5% of cases were correctly classified. This result is consistent with PCA results for the primary vasculature. As in the MDA of the Haversian canals, the discrepancy between the relative influences of the PC2 and PC3 over the discriminant functions is suspected to be a result of the different mathematical treatment of the data in PCA versus MDA. Whereas MDA adopts many of the same perspectives as PCA, the two methods are mathematically different in what they are maximizing. Whereas PCA maximizes the variance in all of the variables accounted for by the principal components, MDA maximizes the difference between values of the dependent variables in order to give optimal separation of pre-defined groups.

6.2.6 Run 1: Conclusions

Although all of the principal components in the Run 1 analysis were found to be significant at the 95% confidence interval based on MDA, a closer look revealed that the ability of the principal components to classify the cases of each microstructural type was poor. The results of the multiple discriminant function analyses of each microstructural type are consistent with the results of the PCA analyses, and the same conclusions are reached for each type. The most surprising result was the ability of the secondary lacunae to allow for the correct reclassification of 46.3% of the cases in the Primary Dataset. This result hints at elevated discriminatory power of the secondary lacunae with regard to taxon, which should be explored further in future datasets.

6.3 Multiple Discriminant Analysis: Run2

Multiple Discriminant Analysis was applied to Run 2 of the Primary Dataset. In this analysis, each case is equal to one micrograph. By running MDA with the scores from Run 2 of the Primary Dataset, the goal is to determine (1) if the results of the

Analysis Case Processing Summary

Unweighted Cases		N	Percent
Valid		4393	100.0
Excluded	Missing or out-of-range group codes	0	.0
	At least one missing discriminating variable	0	.0
	Both missing or out-of-range group codes and at least one missing discriminating variable	0	.0
	Total	0	.0
Total		4393	100.0

Tests of Equality of Group Means (ANOVA)

	Wilks' Lambda	F	df1	df2	Sig.
t{1}	.911	42.921	10	4382	.000
t{2}	.972	12.404	10	4382	.000
t{3}	.930	33.172	10	4382	.000

Standardized Canonical Discriminant Function Coefficients

	Function		
	1	2	3
t{1}	.851	.351	.393
t{2}	-.288	-.377	.881
t{3}	-.478	.854	.207

Canonical Discriminant Functions

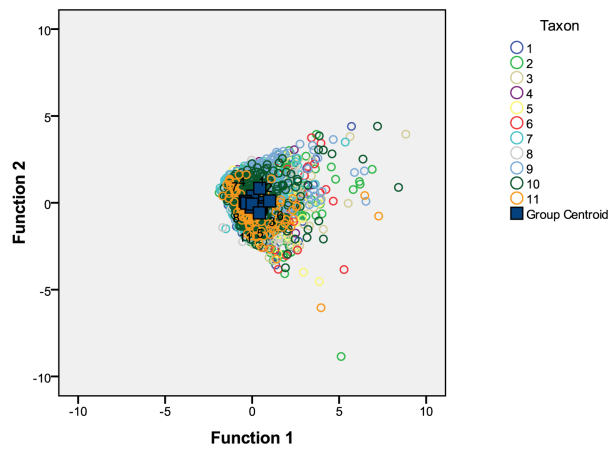


Figure 6.9: A series of tables and the canonical discriminant functions chart from the multiple discriminant analysis of the PCA scores of Run 1E (primary vasculature) of the Primary Dataset. The scores values for each principal component are significant to 95% confidence level.

		Classification Results ^a											Total
		Predicted Group Membership											
Taxo	n	1	2	3	4	5	6	7	8	9	10	11	
Original	Count	115	4	8	21	9	59	142	122	47	12	124	663
		35	10	6	66	45	113	85	79	116	14	140	709
		37	3	2	5	8	43	23	25	29	1	51	227
		4	3	1	16	1	7	14	15	29	3	13	106
		16	1	0	7	15	25	10	21	8	4	26	133
		5	0	0	4	1	21	12	3	19	0	16	81
		152	3	2	24	9	67	441	176	117	1	134	1126
		59	0	4	51	7	20	123	105	39	4	80	492
		3	1	1	21	2	36	34	12	98	1	24	233
		54	3	3	21	7	44	117	85	65	3	137	539
		8	0	1	2	0	16	15	8	4	0	30	84
%		17.3	.6	1.2	3.2	1.4	8.9	21.4	18.4	7.1	1.8	18.7	100.0
		4.9	1.4	.8	9.3	6.3	15.9	12.0	11.1	16.4	2.0	19.7	100.0
		16.3	1.3	.9	2.2	3.5	18.9	10.1	11.0	12.8	.4	22.5	100.0
		3.8	2.8	.9	15.1	.9	6.6	13.2	14.2	27.4	2.8	12.3	100.0
		12.0	.8	.0	5.3	11.3	18.8	7.5	15.8	6.0	3.0	19.5	100.0
		6.2	.0	.0	4.9	1.2	25.9	14.8	3.7	23.5	.0	19.8	100.0
		13.5	.3	.2	2.1	.8	6.0	39.2	15.6	10.4	.1	11.9	100.0
		12.0	.0	.8	10.4	1.4	4.1	25.0	21.3	7.9	.8	16.3	100.0
		1.3	.4	.4	9.0	.9	15.5	14.6	5.2	42.1	.4	10.3	100.0
		10.0	.6	.6	3.9	1.3	8.2	21.7	15.8	12.1	.6	25.4	100.0
		9.5	.0	1.2	2.4	.0	19.0	17.9	9.5	4.8	.0	35.7	100.0

19.5% of cases in the original group are correctly classified

Figure 6.10: The classification results from the multiple discriminant analysis of the PCA scores values of Run 1E (primary vasculature) of the Primary Dataset.

PCA are significant and (2) if the variance within the cross-section of each taxon is less than the variance between taxa.

6.3.1 Run 2: Results

The results of the MDA on Run 2 are shown in Figure 6.11, Figure 6.12, and Figure 6.13. For a total of 160 cases, all independent variables (Principal components) are significant except for principal component 5 (t[5]) and principal component 8 (t[8]). The ANOVA table (testing the equality of group means) in Figure 6.11, shows that PC1 has the smallest value of Wilks' Lambda and PC2 the next smallest value. Beyond these two variables, however, the interpretation of the Wilks' Lambda values with respect to the relative significance of the principal components is fairly complicated. The most evident is the lack of sequential increase in value among successive principal components. The Standardized Canonical Discriminant Function Coefficients table, also located in Figure 6.11, confirms that PC1 has the greatest influence over the first discriminant function. The rest of the principal components do not match with their appropriately numbered functions. In the canonical discriminant function plot of the micrographs in Figure 6.12, the positions of the group centroids are defined by squared Mahalanobis distances. The plot shows separation of the taxon centroids, and the arrangement of the plot is similar to that of the scores plots from the PCA of Run 2 (Figure 5.38). Indeed, the classification results shown in Figure 6.13 indicate that 75.6% of micrographs were correctly reclassified.

6.3.2 MDA Run 2: Conclusions

The results of the MDA of Run 2 are consistent with PCA results and conclusions drawn from them. The canonical discriminant function plot and the classification results based on the discriminant analysis of the PCA scores from the first 11 principal components suggest that taxa can be discriminated based on a combination of microstructural characteristics. The results of reclassification for each taxon indicate that the majority of the micrographs in one cross-section were correctly re-assigned. This result confirms that the variation within a single cross-section (i.e., between micrographs) is less than the variation between different taxa. As in the MDA results

of the Haversian canals and primary vasculature, the discrepancies between the influences of principal components 3, 4, 6, 7, 9, and 10 over the discriminant functions is suspected to be a result of the different mathematical treatment of the data in PCA versus MDA. The discrepancies are not critical to the conclusions of the test. Using the scores values from 11 principal components, 76% of known sample in the Primary Dataset can be reassigned to their respective taxon using a 95% confidence interval.

Analysis Case Processing Summary

Unweighted Cases		N	Percent
Valid		160	100.0
Excluded	Missing or out-of-range group codes	0	.0
	At least one missing discriminating variable	0	.0
	Both missing or out-of-range group codes and at least one missing discriminating variable	0	.0
	Total	0	.0
Total		160	100.0

Tests of Equality of Group Means (ANOVA)

	Wilks' Lambda	F	df1	df2	Sig.
t[1]	.185	65.535	10	149	.000
t[2]	.595	10.130	10	149	.000
t[3]	.804	3.625	10	149	.000
t[4]	.744	5.139	10	149	.000
t[5]	.915	1.385	10	149	.192
t[6]	.685	6.854	10	149	.000
t[7]	.814	3.413	10	149	.000
t[8]	.904	1.580	10	149	.118
t[9]	.764	4.610	10	149	.000
t[10]	.705	6.226	10	149	.000

Standardized Canonical Discriminant Function Coefficients

	Function						
	1	2	3	4	5	6	7
t[1]	1.153	.018	-.173	-.006	.001	.078	.023
t[2]	.722	-.119	.809	-.305	.210	-.306	.094
t[3]	-.320	.345	-.085	-.430	.582	.518	.306
t[4]	.115	-.115	.226	.743	.535	.137	-.326
t[6]	-.017	.812	-.287	.246	.177	-.490	.234
t[9]	.128	.272	.513	.495	-.388	.343	.457
t[10]	.121	.797	.350	-.210	-.152	.150	-.535

Figure 6.11: A series of tables from the multiple discriminant analysis of the PCA scores of Run 2 micrographs of the Primary Dataset. The scores values for each principal component are significant to 95% confidence level.

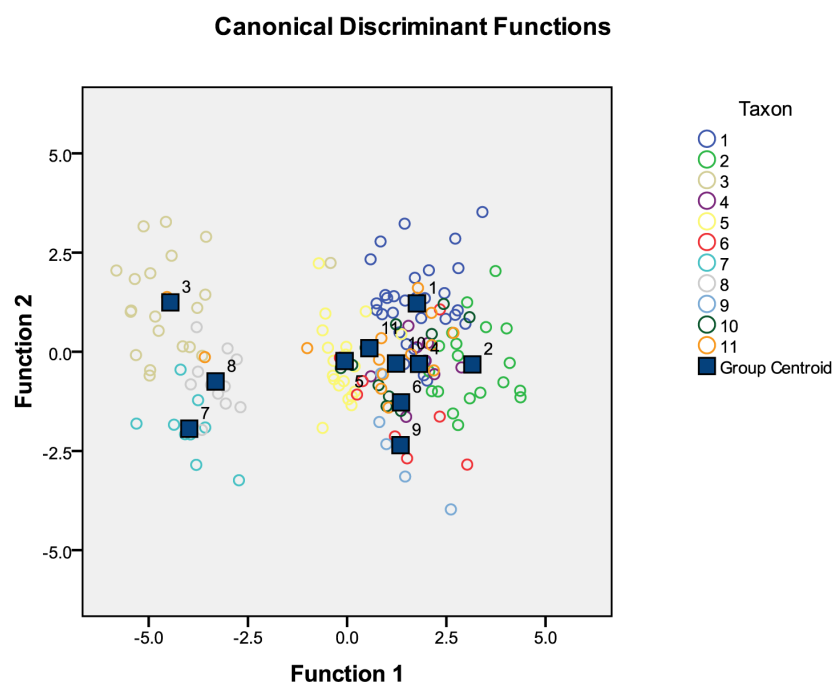


Figure 6.12: The canonical discriminant functions plot from the multiple discriminant analysis of the PCA scores of Run 2 of the Primary Dataset.

		Classification Results ^a											Total
		Predicted Group Membership											
Taxo	Count	1	2	3	4	5	6	7	8	9	10	11	
1	26	0	0	0	1	0	0	0	0	0	3	2	32
2	0	13	0	2	0	2	0	0	0	0	1	1	19
3	0	0	19	0	0	1	0	0	1	0	0	0	21
4	0	0	0	7	0	1	0	0	0	0	0	0	8
5	1	0	0	1	12	0	0	0	0	0	3	3	20
6	0	0	0	0	1	6	0	0	0	0	1	0	8
7	0	0	0	0	0	0	10	0	0	0	0	0	10
8	0	0	0	0	0	0	0	1	10	0	0	0	11
9	0	0	0	0	0	0	0	0	0	5	0	0	5
10	2	0	0	1	1	0	0	0	0	0	7	1	12
11	1	1	0	0	0	2	0	0	2	0	2	6	14
%	81.3	.0	.0	3.1	.0	.0	.0	.0	.0	.0	9.4	6.3	100.0
	.0	68.4	.0	10.5	.0	10.5	.0	.0	.0	.0	5.3	5.3	100.0
	.0	.0	90.5	.0	4.8	.0	.0	.0	4.8	.0	.0	.0	100.0
	.0	.0	.0	87.5	.0	12.5	.0	.0	.0	.0	.0	.0	100.0
	5.0	.0	.0	5.0	60.0	.0	.0	.0	.0	.0	15.0	15.0	100.0
	.0	.0	.0	.0	12.5	75.0	.0	.0	.0	.0	12.5	.0	100.0
	.0	.0	.0	.0	.0	.0	100.0	.0	.0	.0	.0	.0	100.0
	.0	.0	.0	.0	.0	.0	9.1	90.9	.0	.0	.0	.0	100.0
	.0	.0	.0	.0	.0	.0	.0	.0	100.0	.0	.0	.0	100.0
	16.7	.0	.0	8.3	8.3	.0	.0	.0	.0	.0	58.3	8.3	100.0
	7.1	7.1	.0	.0	14.3	.0	.0	.0	14.3	.0	14.3	42.9	100.0

75.6% of cases in the original group are correctly classified

Figure 6.13: The classification results from the multiple discriminant analysis of the PCA scores of Run 2 of the Primary Dataset.

Chapter 7

Microstructural Variation in *Odocoileus virginianus*: The Ribs as a Case Study

7.1 Introduction

What is the extent of microstructural variation within a single specimen? This chapter presents two case studies that begin to explore the variation within the skeleton of a single specimen of *Odocoileus virginianus* (white-tailed deer). The results presented in Chapter 5 of this dissertation suggest that tetrapods can be taxonomically distinguished by the morphology of their bone microstructure. The experimental design of the Primary Dataset simplified the variation between taxa. Each taxon was represented by a single cross-section through a specific bone. But what if each taxon were represented by two cross-sections from different bones of the same specimen or even two cross-sections taken from the same bone? Would the variance in bone microstructural morphology between different cross-sections of one specimen still be smaller than the variance between taxa? This chapter builds on the analyses and results of Chapters 5 and 6 to explore those questions.

The present case studies in single-specimen microstructural variation include exploration of (1) the intra-skeletal variation among left ribs 2 through 12 and (2) the intra-bone variation in *O. virginianus* rib 7. Information on the deer specimen and the micromorphological details of each rib can be found in Chapter 4. The datasets for both case studies will be explored using Principal Component Analysis (PCA) and,

where applicable, Multiple Discriminant Analysis (MDA). Chapters 5 and 6 provide good treatment of each statistical method, respectively, so that the details will not be repeated here. The procedure by which the microstructural units were directly measured and the derivation of the calculated metrics for both *O. virginianus* case studies were identical to the procedure used for the Primary Dataset. The hierarchy of *O. virginianus* data organization is also similar to that of the Primary Dataset. The only difference from the Primary Dataset is that, instead of comparing the microstructural differences among taxa (Tier 1), the intra-skeletal case-study is comparing the microstructural difference among ribs (Tier 1), and the intra-bone case-study compares 5 cross-sections from the same rib (Tiers 1 and 2). All other Tiers (micrograph samples, types of microstructures, and metrics of single microstructural units) are analogous to the organization of the Primary Dataset. For a detailed discussion of the tiered hierarchy, see Chapter 5.

As discussed in Chapter 4, the ribs were chosen for intra-skeletal and intra-bone case studies because (1) during formation, the ribs undergo intramembranous ossification unlike the bones of the appendicular skeleton, such as the tibiae in the Primary Dataset, which form by endochondral ossification, (2) ribs do not bear weight, (3) the ribs are serially repeated bones, and (4) ribs and rib fragments are abundant in the fossil record, yet have been deemed of little taxonomic value. Analysis of the ribs for microstructural variation acknowledges the possibility of microstructural differences between bones of different formation processes, as well as between weight-bearing and non-weight-bearing bones. As serially repeated skeletal elements, ribs offer the chance to examine “closely related” bones in order to detect any variation. For example, if there is a great amount of variation among the ribs of the white-tailed deer, it would be reasonable to hypothesize that a comparison among the other bones in the skeleton would likewise yield high microstructural variability. If this were the case, however, the variation in different bones would have to be formally tested. Ribs are of particular interest to this project because of the abundance of this skeletal element in the fossil record. The gross morphology of the rib body shows a “piscis” or pointed oval geometry in cross-section, allowing even small fragments to be identified as ribs. Unfortunately, the gross morphology of even a complete rib holds little taxonomic information, and the rib rarely can be identified taxonomically in the absence of more distinctive skeletal elements. The outcome of the current study on the variation of bone microstructure within the deer ribs will indicate the applicability

of the microstructural technique to fossil rib fragments and the likelihood of success of continued intra-skeletal analysis of microstructural variation.

7.2 Intra-skeletal variation

The microstructural features used to evaluate the intra-skeletal variation in *O. virginianus* were measured from one mid-bone cross-section of each of the 12 left ribs. Left rib 1 was not included in the final dataset because of error in micrographic documentation. In preparation for PCA of the data, 13,572 microstructural units of the five types (primary vasculature, primary lacunae, secondary lacunae, secondary osteons, and Haversian canals) were marked by hand and then measured automatically using the Welsh algorithm. The distribution and number of the microstructural units per rib can be found in Figure 7.1.

Rib #	# of Micrographs	Secondary Osteons	Haversian Canals	Primary Lacunae	Secondary Lacunae	Primary Vasculature	TOTAL
2	36	329	325	161	180	151	1146
3	40	295	298	180	202	307	1282
4	41	276	273	184	180	355	1268
5	43	206	214	211	164	790	1585
6	40	196	199	171	157	889	1612
7	42	208	209	192	202	710	1521
8	36	204	201	176	162	570	1313
9	32	224	224	164	138	544	1294
10	27	252	245	122	126	255	1000
11	20	194	187	61	97	158	697
12	25	217	210	132	84	211	854
TOTAL	382	2601	2585	1754	1692	4940	13572

Figure 7.1: A summary table showing the number of each type of microstructure measured per rib. The total number of microstructural units measured for this case study was 13,572.

7.2.1 Analysis

The organization of the intra-skeletal dataset is analogous to the data input structure of PCA Run 2 of the Primary Dataset (Chapter 5). As discussed above, the only

difference is that instead of comparing 11 taxa, this dataset compares 11 left ribs by analysis of cross-sections. For PCA of the intra-skeletal dataset, metric values for each type of microstructure are averaged per micrograph. Each row of the input corresponds to a micrograph from part of the one, mid-body cross-section made for each of the 11 left ribs of the deer. Each micrograph is considered here to be one “sample”, for a total of 382 samples (m). Because of the size difference in the cortex of the mid-body sections among the left ribs, some ribs are represented by more micrographs (samples) than others. Each column in the PCA input matrix corresponds to a microstructural metric, such as the length of the major axis of a secondary osteon. The analysis of the intra-skeletal dataset begins with 11 metric values (see Chapters 3 and 5) for the primary vasculature, 10 metrics for the Haversian canals, 10 metrics for the secondary osteons, 8 metrics for the primary lacunae, 8 metrics for the secondary lacunae, and an additional 3 metrics comparing measurements of certain microstructural features (Figure 5.16), for a total of 50 metrics (n).

7.2.2 PCA Results

Prior to PCA of the intra-skeletal dataset, micrograph 24 of left rib 05 was removed from the analysis because this micrograph had the largest number of missing metric values compared to other micrographs in the dataset. Fifteen principal components initially were calculated for the intra-skeletal dataset. The Kaiser-Guttman rule indicated the retention of 12 principal components (Figure 7.2 A), explaining 87% of the variance in the dataset. Given the large number (50) of variables (i.e., all the bone microstructure metrics), to capture this degree of variance in the first 12 components is good. However, a scree plot of the eigenvalues shows the “elbow” of the slope at principal component 6 (Figure 7.2 B). According to the Cattell’s Scree Test, five principal components (one component less than the “elbow” value) should be retained for the intra-skeletal dataset. The difference in the number of principal components per the Kaiser-Guttman rule and the Cattell Scree Test is large. However, the variance that is explained for each of the principal components beyond PC5 is small, indicated by r^2 values of less than 8% each for PC6 through PC15.

The PCA of the intra-skeletal dataset resulted in five principal components explaining 64% of variance in the dataset. The number of principal components was reduced in

Principal Component	r^2	r^2 cumulative	Eigenvalue
1	0.2227	0.2227	11.138
2	0.1449	0.3677	7.2482
3	0.1096	0.4773	5.4815
4	0.08881	0.5661	4.4406
5	0.07129	0.6374	3.5648
6	0.04451	0.6819	2.2258
7	0.04353	0.7255	2.1765
8	0.03392	0.7594	1.6962
9	0.03151	0.7909	1.5759
10	0.02845	0.8194	1.4226
11	0.02413	0.8435	1.2068
12	0.02166	0.8652	1.0831
13	0.01976	0.8849	0.9884
14	0.01854	0.9035	0.9274
15	0.01714	0.9206	0.857



A

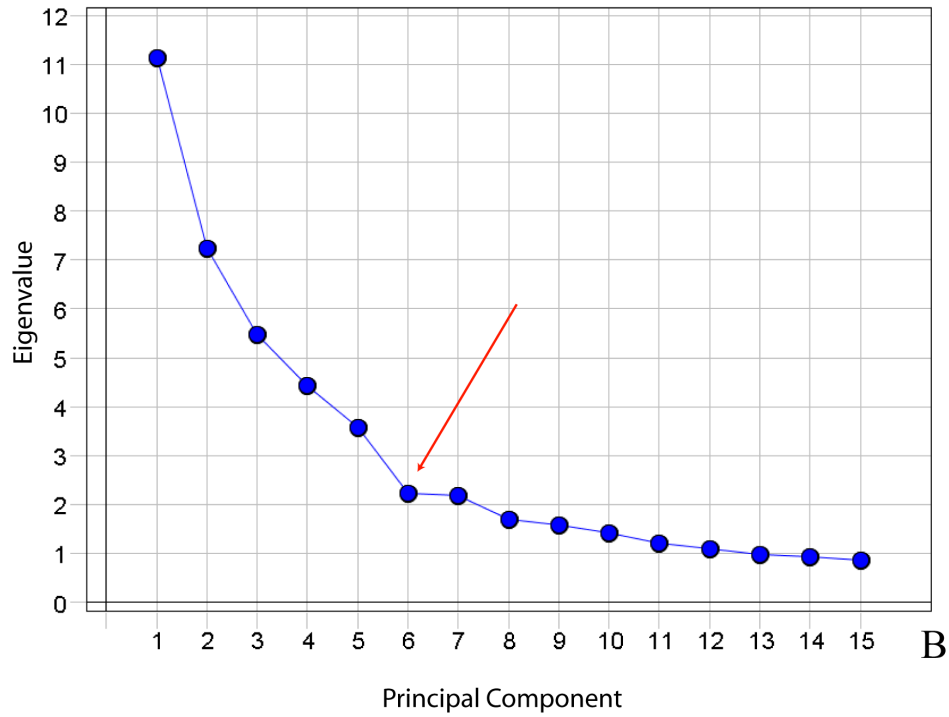


Figure 7.2: A table (A) and scree plot (B) of the eigenvalues associated with the PCA exploring the variance in mid-body cross-sections of Ribs 2 through 12. The red star represents the eigenvalue cut-off per the Kaiser-Guttman rule. The red arrow on the scree plot points to the “elbow” that indicates the number of principal components that should be retained per the Cattell scree test.

order to make sure that the data would not be overfitted. The scores plot does not show separation of the rib cross-sections based on the size, shape, and orientation of bone microstructures (Figure 7.3). Because there are no class distinctions based on rib number, the loadings are not discussed. One of the advantages of PCA over other statistical methods, especially when applied to exploratory datasets, is demonstrated here. A PCA will always generate principal components, a T matrix, and a P matrix, regardless of whether there is any pattern in the dataset. However, if there is no pattern in the scores plot, then the loadings also are uninformative in terms of distinguishing any (non-existent) pattern. If this is the case, no further statistical treatment is necessary to test for significance of the variance between samples. If the scores plot did reveal a pattern, however, such as in Run 2 of the Primary Dataset, the loadings should be evaluated. PCA shows patterns within the data and the variables that explain most of the variance, but it is not ideal for evaluating whether the pattern is statistically significant. Point clouds of data are mapped using scalar values, such that one scores plot cannot be directly compared to another. A dataset, especially if it is exploratory, should then be analyzed for statistically significant variance, as was done for the Primary Dataset in Chapter 6.

The results of the PCA of the intra-skeletal dataset support the hypothesis that bone microstructural morphology varies more between taxa than among bones of the same individual. Such information supports the validity of taxonomic discrimination on the basis of microstructural morphology. The lack of any patterning in the scores plot with respect to rib number suggests that the morphological expression of the microstructures does not vary among the mid-bodies of serially repeated bones. Therefore, regardless of which rib is evaluated, the specimen may still be classified as *O. virginianus*.

7.3 Intra-bone Variation

The microstructural features used to evaluate the intra-bone variation in *O. virginianus* were measured from five cross-sections taken from left rib 7. A discussion on where along the rib body the cross-sections were extracted can be found in Chapter 4. In preparation for PCA of the data, 7,550 microstructural units of the five types

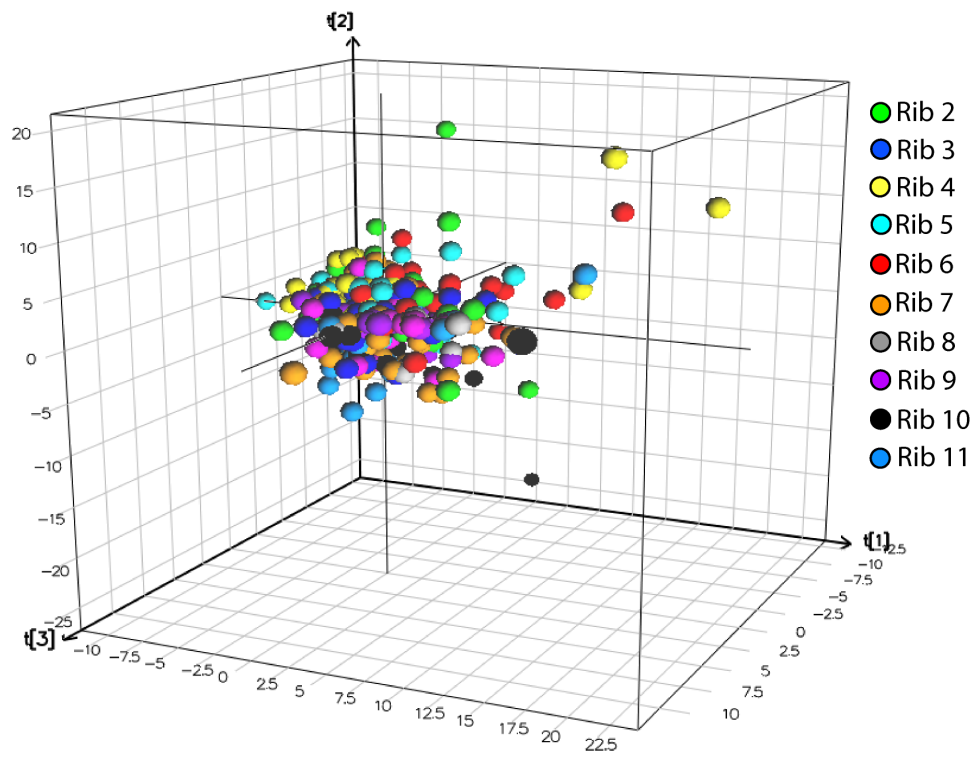


Figure 7.3: The scores of the inter-rib case study are plotted in three dimensions, corresponding to the first, second, and third principal components.

(primary vasculature, primary lacunae, secondary lacunae, secondary osteons, and Haversian canals) were marked by hand and then measured automatically using the Welsh algorithm. The distribution and number of the microstructural features per cross-section on rib 7 can be found in Figure 7.4.

Rib 7 Cut #	# of Micrographs	Secondary Osteons	Haversian Canals	Primary Lacunae	Secondary Lacunae	Primary Vasculature	TOTAL
1	52	378	377	208	201	934	2098
2	51	303	308	241	181	674	1707
3	42	208	209	196	202	715	1530
4	39	220	220	185	151	471	1247
5	51	236	237	221	208	66	968
TOTAL	235	1345	1351	1051	943	2860	7550

Figure 7.4: A summary table showing the number of each type of microstructure measured per cross-section of Rib 7. The total number of microstructural units measured for this case study was 7,550.

7.3.1 Analysis

The organization of the intra-bone dataset is identical to the data input structure of PCA Run 2 of the Primary Dataset (Chapter 5). As discussed above, the only difference is that instead of comparing 11 taxa or 11 left ribs, this dataset compares 5 cross-sections from left rib 7. For PCA of the intra-bone dataset, metric values for each type of microstructure are averaged per micrograph. Each row of the input corresponds to a micrograph from part of the one of the five cross-sections made for left rib 7 of the deer. Each micrograph is considered here to be one “sample” of data, for a total of 235 samples (m) (Figure 7.4). The width of the cortex differs along the length of the rib. Because of this size difference, some rib 7 cross-sections are represented by more micrographs (samples) than others. Each column in the PCA input matrix corresponds to a microstructural metric. The analysis of intra-bone dataset begins with 11 metric values (see Chapters 3 and 5) for the primary vasculature, 10 metrics for the Haversian canals, 10 metrics for the secondary osteons, 8 metrics for the primary lacunae, 8 metrics for the secondary lacunae, and an additional 3 metrics comparing measurements of certain microstructural features (Figure 5.16), for a total of 50 metrics (n).

7.3.2 PCA Results

Prior to PCA of the intra-bone dataset, micrograph 30 of left Rib 7, Cut 05 was removed from the analysis because this micrograph did not have any reported values except for the metrics of the primary lacunae. Fifteen principal components (PC) were calculated for the intra-skeletal dataset. The Kaiser-Guttman rule would suggest the retention of 11 principal components, explaining 89% of the variance in the dataset. A scree plot of the eigenvalues shows a smooth slope with no obvious “elbow” at which to limit the number of principal components. Even though the variance that is explained for each of the principal components after PC3 is relatively small compared to the first three components, indicated by r^2 values of less than 10% each for PC4 through PC11, all 11 are retained for this analysis.

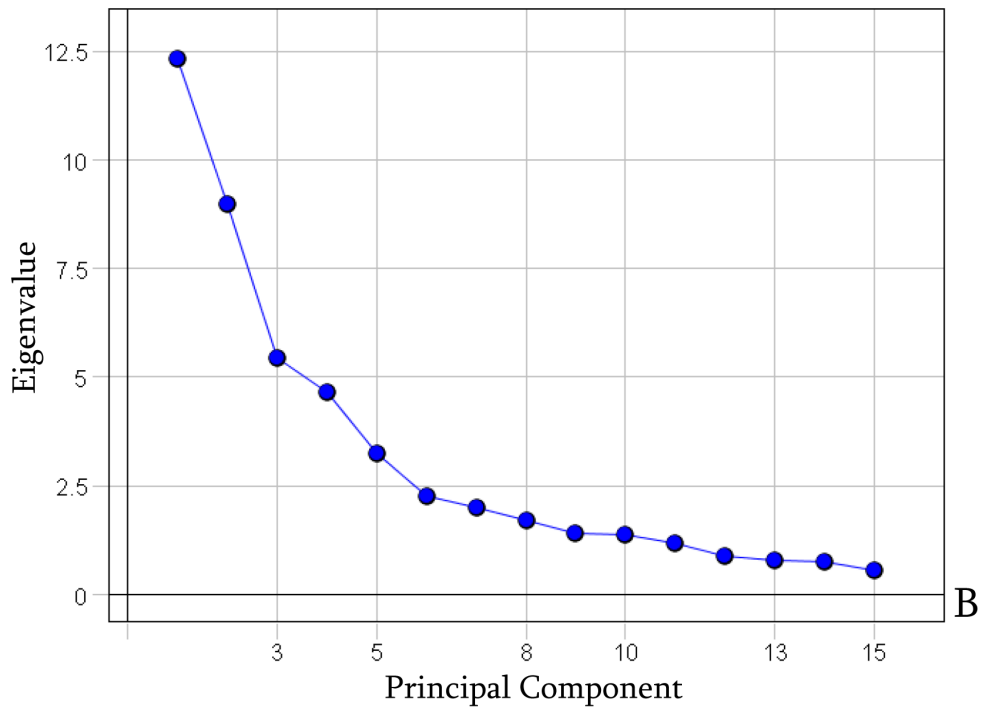
The PCA of the intra-bone dataset resulted in 11 principal components explaining 89% of variance in the dataset (Figure 7.5). The scores plot of the data does not show any clustering of the data points according to the position of the cross-section along Rib 7 (Figure 7.6). Most of the data points are clustered about the origin. There is, however, a pattern of dispersal in the PC1-PC2 (X-Y) plane that is worth noting here (Figure 7.7 A). Whereas most of the samples from Cut 1 plot at the origin of the graph, there is also a dispersal pattern of some points in the positive direction of PC 1 and the negative direction of PC2. Most samples of Cut 5 plot around the origin, but the points near the origin are situated in the quadrants of negative PC1 values compared to Cut 1, whose points about the origin are in the positive PC1 quadrants. Those Cut 2 data points displaced from the origin are dispersed mostly along positive and negative PC2. The points of Cut 3 disperse slightly into negative PC1 space.

The loadings plot shows the variables that are most likely responsible for the dispersal patterns (Figure 7.8). The Rib 7 cross-sections cannot, with any reasonable level of confidence, be distinguished from each other on the basis of the size, shape, and orientation of microstructural features. However, those points that do not sit at the graphical origin of the scores plot seem to disperse in specific directions according to cross-section placement along the rib. The variance along positive values of PC1 can be attributed mostly to variables pertaining to the size of the primary lacunae, size of the primary vasculature, and PVLlong. Anti-correlated with these variables, but still explaining a large amount of the variance along negative PC1, are variables PLA and

Principal Component	r^2	r^2 cumulative	Eigenvalue
1	0.2462	0.2462	12.31
2	0.1794	0.4256	8.974
3	0.1085	0.5342	5.4276
4	0.09286	0.6271	4.643
5	0.06481	0.6919	3.2405
6	0.04509	0.737	2.2545
7	0.03976	0.7767	1.9884
8	0.03398	0.8107	1.6994
9	0.02846	0.8392	1.4234
10	0.02737	0.8666	1.3685
11	0.02325	0.8898	1.1625
12	0.01764	0.9074	0.8823
13	0.01598	0.9234	0.7993
14	0.01533	0.9388	0.7665
15	0.01134	0.9501	0.5671



A



B

Figure 7.5: A table of the eigenvalues (A) associated with the PCA exploring the variance in microstructural morphology within Rib 7. The scree plot of the eigenvalues (B) does not show a distinct “elbow”. The red star indicates the cut-off for retained eigenvalues under the Kaiser-Guttman rule.

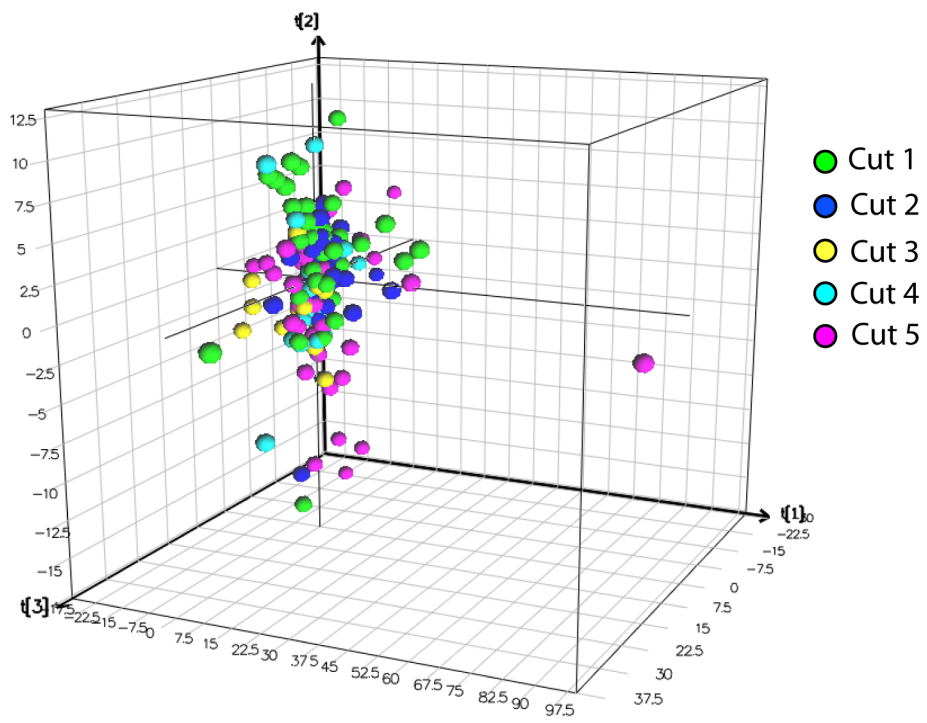


Figure 7.6: The scores of the intra-rib case study are plotted in three dimensions that correspond to the first, second, and third principal components.

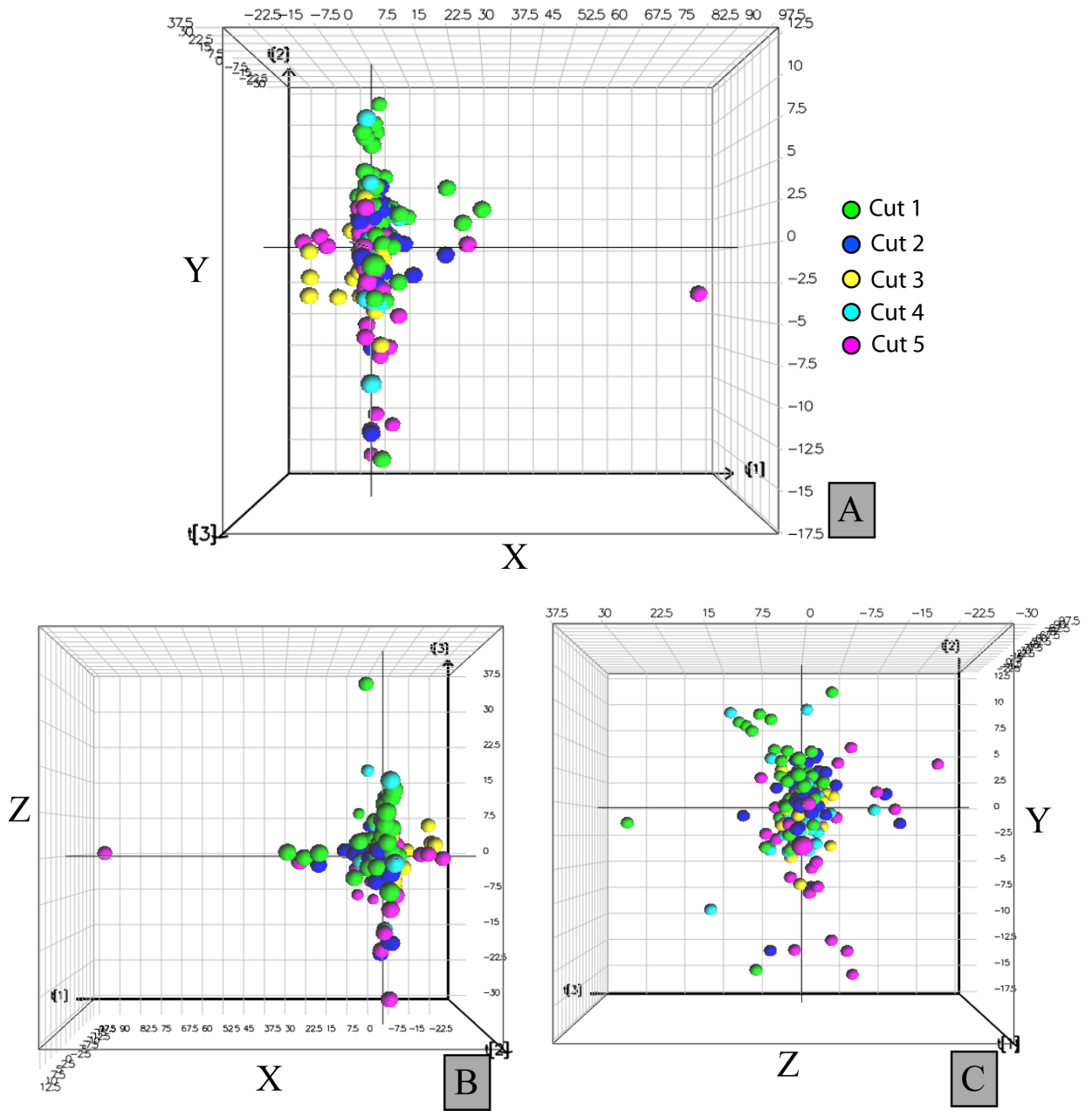


Figure 7.7: Orthogonal views of the intra-rib dataset looking onto the X-Y plane down the positive Z-axis (A), the X-Z plane viewed down the positive Y-axis (B), and the Y-Z plane viewed down the positive X-axis (C).

PVR. The variables along the positive PC1 axis are those that control the variance in some of the points from Cut 1, whereas the variance in four points from Cut 3 is explained by the variables PVR and PLR in the negative PC1 direction. Most of the variance along PC2 can be explained by the variables relating to the size of the secondary osteons and Haversian canals along the positive PC2 axis and variables relating to the size of the secondary lacunae, HCR, and SOHCR along the negative PC2 axis. Therefore, the variance in the dispersed points of Cut 5 can be attributed mostly to the variables describing the size of secondary osteons and Haversian canals. The remaining Cut 1 dispersed points lie along the negative PC2 axis, where much of the variance can be explained by the shape of the Haversian canal (HCR), SOHCR, and the size of the secondary lacunae. In summary, PC1 and PC2 of the intra-bone dataset are defined such that most of the variance along PC1 can be explained by the characteristics of primary microstructural features and PC2 can be explained by the characteristics of secondary microstructural features.

7.3.3 Multiple Discriminant Analysis of the Intra-bone Dataset

Although the scores plot of the intra-bone dataset does not show any separate clustering of the data points according to specific cross-section, the unique patterns of dispersal of points for Cuts 1 and 5 warrant a closer look with additional statistical treatment. Osteologically, Cut 1 and Cut 5 were the proximal-most and distal-most cross-sections extracted from Rib 7, respectively. It is not clear from PCA whether the variance between the cross-sections is significant. Therefore, the section-to-section variance is tested here using Multiple Discriminant Analysis.

Multiple Discriminant Analysis of the 5 cross-sections from Rib 7 used the scores values from the first 11 principal components from the PCA presented above. Although the distribution of points in the scores plot for intra-bone variation does not show the intimate intermingling displayed in the inter-rib case study, the points do not cluster according to cross-section as they did in the PCA of the Primary Dataset.

The results of the MDA analysis on the five cross-sections of Rib 7 are shown in Figure 7.9 and Figure 7.10. For a total of 234 cases (one micrograph is equal to one case), all principal components are significant to a 95% confidence interval except for

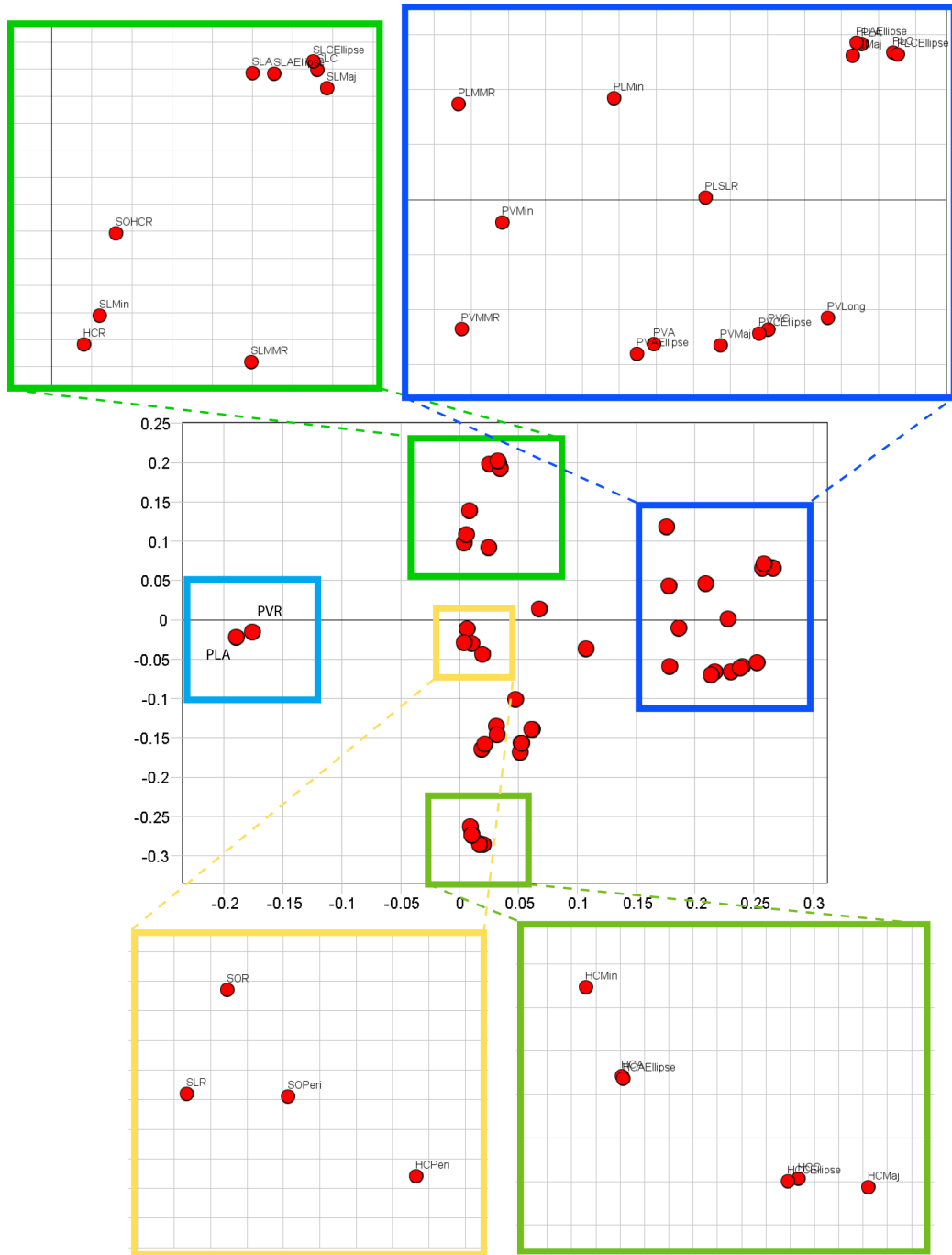


Figure 7.8: The loadings plot for the intra-bone dataset, highlighting the variables that explain the greatest amount of the variance along principal component 1 (blue boxes) and principal component 2 (green boxes). The yellow box highlights the variables in the dataset that explain very little of the variance.

t[5]. The Analysis of Variance (ANOVA) table (testing the equality of group means) shown as part of Figure 7.9, displays the Wilks' Lambda values for each independent variable (scores values of principal components 1 through 11). The smaller its Wilks' Lambda value, the more important is the variable in the discriminant function. In this analysis, the scores values of principal component 4 (t[4]) have the smallest Wilks' Lambda. The second test of the relative importance of the independent variables in predicting the dependent variables (Taxa) is shown in the Standardized Canonical Discriminant Function Coefficients table, also found in Figure 7.9. The values in this table serve the same function as beta weights in a multiple regression analysis and can be used to evaluate each independent variable's unique contribution to each discriminant function. Here, the highest values indicate greatest importance. The MDA produced 4 discriminant functions. There is no particular pattern in the function coefficients that pertained to the principal components, mostly likely a result of the different mathematical approaches of PCA and MDA. Although the scores values are the result of data compression in the PCA, MDA transforms the scores again in order to determine the resulting canonical discriminant functions. The table in Figure 7.9 showing the Wilks' Lambda values for the canonical discriminant functions indicates that all four discriminant functions are significant in explaining the data.

In the canonical discriminant function plot of the secondary osteons in Figure 7.10, the group centroids are defined by squared Mahalanobis distances. The plot shows that the centroids of Rib 7 cross-sections 2, 3, and 4 are in close proximity to one other, whereas the centroids from cross-sections 1 and 5 are the farthest apart on the plot. The classification results shown in Figure 7.10 indicate that 59.8% of cases were correctly classified. Because the reclassification of samples is based on a 95% confidence interval, it is most likely that the samples from Cut 1 and Cut 5 would have the most samples correctly reclassified based on the visual display of the centroid positions in Figure 7.10. A closer look at the classification results reveals that Cuts 1 and 5 of Rib 7, indeed, had the largest percentage of correctly reclassified samples, with 71% and 68% of the samples reclassified, respectively. Based on the results of MDA alone, it is not possible to distinguish which microstructural metrics may be causing these distinctions. However, on the orthogonal views of the 3D scores plot (Figure 7.7), Cut 1 and Cut 5 of Rib 7 show some distinct patterning in the X-Y plane (PC1-PC2). Whereas neither group of the rib cut samples is tightly clustered, the samples from Cut 1 are situated about the origin, and along positive PC1 and positive

PC2. A review of the PCA loadings (Figure 7.8) indicates that most of the variance along the positive PC1-PC2 axes is explained by the size, shape, and orientation of the primary vascular canals and the size and shape of the primary lacunae. The sample points of Cut 5 are mainly situated about the origin (intermingled with samples from Cut 1) and along negative PC1 and PC2. Variables PVR and PLA account for the greatest amount of variance along negative PC1. The variables describing the size and shape of the Haversian canals are significant along negative PC2.

7.4 Conclusion

The two case studies on a single specimen of a white-tailed deer were used to explore to what extent the bone microstructural types would vary within the skeleton. The case studies also addressed the significance of this variation and how the variation would affect future taxonomic datasets. The statistical analyses of the inter-rib case study supported the notion that mid-bone (or mid-diaphysis in the case of long bones) cross-sections of multiple bones in the skeleton could be properly identified taxonomically by reference to a database containing only information on the mid-diaphysis of a specific type of bone or bones (in this case study, serially repeated ribs). Analogous case studies applied to additional bones would further test this hypothesis. Future case studies must also include analysis of mid-diaphyseal (mid-bone) cross-sections from different bones in the same skeleton. A dataset of this type may include a comparison of the microstructural variation in the mid-diaphyseal cross-sections of the deer femur, tibia, and humerus.

The question of whether one likewise could make a successful taxonomic identification based on any random cross-section along the length of the long bone diaphysis or the rib body has a much less clear answer. The results of the intra-rib analyses indicate that perhaps only the extreme proximal and distal ends of bones should be avoided in this type of analysis, as evidenced by the distinct microstructural variation between Rib 7 Cut 1 and Cut 5 and the lower resolution among Cuts 2, 3, and 4. Although the total number of properly reclassified samples was still less than those for the Primary dataset, the relatively large amount of reclassified samples (i.e., indicating that different cross-sections of the same bone were not statistically indistinguishable) in

Analysis Case Processing Summary

Unweighted Cases		N	Percent
Valid		234	100.0
Excluded	Missing or out-of-range group codes	0	.0
	At least one missing discriminating variable	0	.0
	Both missing or out-of-range group codes and at least one missing discriminating variable	0	.0
	Total	0	.0
Total		234	100.0

Tests of Equality of Group Means (ANOVA)

	Wilks' Lambda	F	df1	df2	Sig.
t[1]	.941	3.567	4	229	.008
t[2]	.851	10.000	4	229	.000
t[3]	.931	4.260	4	229	.002
t[4]	.822	12.377	4	229	.000
t[5]	.978	1.288	4	229	.275
t[6]	.940	3.682	4	229	.006
t[7]	.878	7.979	4	229	.000
t[8]	.839	11.010	4	229	.000
t[9]	.942	3.555	4	229	.008
t[10]	.940	3.645	4	229	.007
t[11]	.939	3.726	4	229	.006

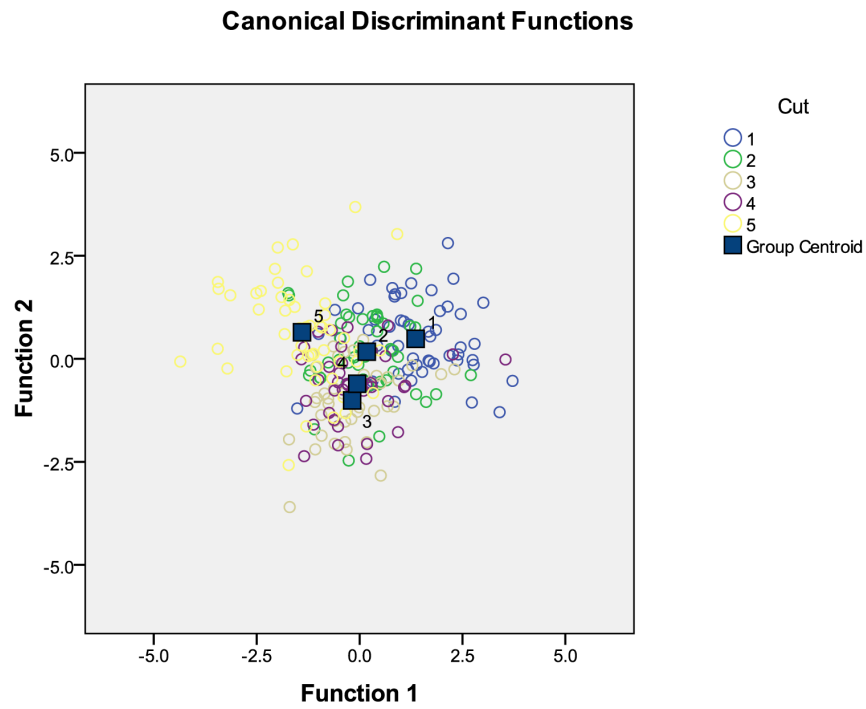
Standardized Canonical Discriminant Function Coefficients

	Function			
	1	2	3	4
t[1]	.256	.448	.142	.057
t[2]	.704	.179	.129	-.049
t[3]	.388	-.025	-.283	.389
t[4]	.303	.773	.014	-.046
t[6]	.079	-.285	.316	.597
t[7]	.576	-.327	.276	.086
t[8]	.637	-.255	-.436	-.023
t[9]	-.133	.196	.399	.556
t[10]	.272	-.288	.371	-.381
t[11]	-.122	.065	-.590	.335

Wilks' Lambda of Canonical Discriminant Functions

Test of Function(s)	Wilks' Lambda	Chi-square	df	Sig.
1 through 4	.294	275.972	40	.000
2 through 4	.548	135.733	27	.000
3 through 4	.766	60.013	16	.000
4	.904	22.854	7	.002

Figure 7.9: A series of tables from the multiple discriminant analysis of the PCA scores of the intra-bone dataset. The scores values for each principal component are significant to 95% confidence level.



Classification Results^a

		Cut	Predicted Group Membership					Total
			1	2	3	4	5	
Original	Count	1	37	8	2	2	3	52
		2	8	24	3	12	4	51
		3	4	3	23	8	4	42
		4	4	5	4	22	4	39
		5	1	5	6	4	34	50
%		1	71.2	15.4	3.8	3.8	5.8	100.0
		2	15.7	47.1	5.9	23.5	7.8	100.0
		3	9.5	7.1	54.8	19.0	9.5	100.0
		4	10.3	12.8	10.3	56.4	10.3	100.0
		5	2.0	10.0	12.0	8.0	68.0	100.0

59.8% of cases in the original groups are correctly classified

Figure 7.10: The classification results from the multiple discriminant analysis of the PCA scores values of the intra-bone dataset.

the intra-bone dataset warrants additional testing of the variation along the length of a bone. Additional analogous studies should be done using a variety of long bones and ribs. In the interim, it can be stated that the location of the cross-section within the bone may be more important in the analysis than which bone is used in attempting to extract taxonomic information from bone microstructure.

Chapter 8

Conclusions and Perspectives

The inspiration for this dissertation and course of research was the Platonic view that, behind the apparent and fuzzy complexity of the world, one may find simple and pure structures. The pure notion of a “taxon” is still not fully understood. Over time, scientists have created a series of rules to follow in order to guide a language of taxonomy and to facilitate scholarly communication. However, Nature’s ability to construct a continuum can never be underestimated. For centuries, we have been trying to define where one taxon ends and another taxon begins. One hundred years from now, taxonomists may still be debating the species concept and searching for ways to make taxonomy a quantitative venture.

The work presented in this dissertation is the beginning of one such quantitative taxonomic procedure. It was not developed in isolation from the established, qualitative taxonomic methods at this time, but instead serves to augment those processes, making taxonomic designation more reliable. Scientists have been trying to create a method by which vertebrates can be taxonomically identified by their bone microstructure since the 1800’s, but without success. Thus, the results and conclusions presented in this dissertation serve as a benchmark in osteohistology.

8.1 Purpose

The main purpose of this research was to extract useful taxonomic information from an untapped source—bone microstructure. For the first time, fragmentary skeletal remains can be analyzed in a useful, quantitative way. This is a transformative

development, in that previously unidentifiable skeletons now become useful to anyone in the field. An increase in identifiable specimens allows for a greater number of testable paleo-hypotheses. Moreover, this new quantitative taxonomic method can serve a larger purpose than simply filling the fossil record with identified skeletons. The world in which we live is ever changing, and scientists seek evidence of the timing and natures of those changes, in part through the fossil record. They particularly struggle to make sense of the basic driving forces behind the shifts in climate through time and the perpetuation/viability of species. It is an advantage to be able to closely evaluate environmental and climate shifts in the past to gain insight into what may happen in the future.

Paleoecological reconstruction allows us to peer into the environments of the geological past through the interpretation of the geology and the paleontology of ancient rock formations. Based on an “inversed” Uniformitarian notion, we can apply this information to a “using the past to predict the future” approach. The latter comes from close examination of the effects of climate change on the environment and on biomass distribution in the past, as well as the acquisition of insight into the courses of species decline during mass extinction. Restrictions on the number of identifiable species place significant limits on paleoecological reconstruction and on determination of the rate of species decline during a mass extinction. Not uncommonly, a species is defined on the basis of one specimen—a clear problem when testing certain hypotheses. Are we currently undergoing a mass extinction? That debate continues, but perhaps we can come closer to a conclusion through enhanced ability to access the change in species number and type during the courses of the past five large mass extinctions. The desired increase in the number of taxonomic data points could come through application of the new method presented here. The results of this dissertation suggest that this approach to paleoecological research will be realized in the near future.

8.2 Conclusions

The chapters of this dissertation culminate in three exciting and promising conclusions. From this exploration stage in taxonomic osteohistology, it was found that

(1) tetrapods can be distinguished taxonomically by a combination of quantitative measurements characterizing the size, shape, and orientation of five types of cortical bone microstructures, (2) the measureable microstructural variation within one thin-section is less than the variation between taxa, and (3) the variation among the ribs of one specimen is small, suggesting that the morphology of the microstructural types will not vary significantly throughout the skeleton. The three conclusions support the continuation of this research, as well as its application to the study of bone microstructural systems in extinct tetrapods.

This project began by examining only secondary bone structures (secondary osteons, Haversian canals) as a means to taxonomically distinguish taxa. The microstructural metrics evolved to include primary bone microstructures and lacunae (both primary and secondary) after visually comparing thin-sections of several different taxa. Even prior to quantitative measurement, the variation of the size and shape of primary structures between different taxa was very clear. The size of primary lacunae compared to the size of the secondary lacunae seemed to be different within a taxon as well as between taxa. New metrics were added to quantitatively reflect the foreseen variation. The Primary Dataset had the advantage of being very broad in taxonomic scope (i.e., taxa were not very “close” on the mammalian phylogenetic tree). Whereas some amount of taxonomic separation was expected with the method, the results of Run 2 of the Primary Dataset were quite surprising. Not only was there taxonomic separation, but most of the micrographs from each taxon were clustered together, suggesting that the variation in bone microstructural morphology was small within one cross-section. It was expected that the metrics values for the primary vascular canals would provide most of the distinguishing power in the Primary Dataset; initial visual examination of the primary canals showed quite obvious size, shape, and orientation differences between taxa. However, most of variance in the Primary Dataset was attributed to the size and shape of the Haversian canals, size and shape of the primary and secondary lacunae, and the size ratios of the actual circumference of the microstructural units to their best-fit ellipse circumferences. The primary and secondary lacunae, although the smallest microstructural type in the method, have the largest overall influence on the taxonomic separation of mammalian specimens.

The microstructural metrics that addressed the orientation of microstructural units with respect to the periosteal bone surface and the longitudinal axis of the diaphysis

did not have as much diagnostic power as expected. These metrics were included after careful consideration of research in bone biomechanics. The effect of locomotion on bone strength and structure hinted at a possible correlation between microstructural orientation and locomotive type, and the mammals in the Primary Dataset represent many locomotive lifestyles. Taking into account these mammals' habitat, stance, and bone structure, the stresses on their bones throughout life would clearly not be the same. For example, the snowshoe hare is a saltator (hopper), whereas the Primates have an arboreal lifestyle. The hare and the primates will have different types and directions of stresses placed on their bone through time. During the remodeling process, bones adapt to external stresses. Hypothetically, the features of the remodelled bone should reflect the type and direction of stress in order to strengthen the bone from future damage. The directional aspect of this hypothesis was not supported by the metrics of microstructural orientation applied in this study.

Despite the hope for an ultimately simple means to distinguish tetrapods by the morphology of their bone microstructures, there is some complexity that will have to be addressed by future research. Not all taxa in the Primary Dataset were separated taxonomically with equal spread. Whereas some taxa were easily distinguished from others in the dataset, some mammals, such as the Rhesus monkey did not exhibit a recognizable pattern of clustering or separation from other taxa. In the absence of a clear phylogenetic or locomotive "reason" for these results, what does this mean? Such questions call for systematic examination of a larger number of samples from each taxon and a study spanning a greater diversity of taxa.

8.3 Future Work

The scope of possible future work on this subject is vast. Increasing the number of specimens of each taxon, as well as the number of taxa in the dataset, in a systematic survey of bone microstructure is the obvious route to expand the significance of this research in taxonomic identification. However, increasing our knowledge of the variation within a single specimen is the immediate next step in quantitative osteohistological taxonomy. Analysis of the deer ribs showed promising results, but similar analysis of the remainder of the post cranial skeleton of *O. virginianus* will

reveal the variation within and between different bones. It is unclear at this point whether the values and variation in the size, shape, and orientation of the five types of microstructures will remain sufficiently consistent throughout the skeleton to allow all bones in the specimen to be properly re-classified as “white-tailed deer.”

There is much to learn about the variation in bone microstructure with respect to taxon at various hierarchical levels. Based on the results presented in this dissertation, additional metrics will be added to future analyses that may result in additional taxonomic resolution. Maintaining the goal of finding the simplest solution to the challenge, the thin-sections used in this dissertation were not stained. The lack of staining prevented bone microstructures, such as canaliculi and circumferential lamellae, from being clearly visible under the microscope. Staining of future thin-sections will allow the morphology of these microstructures to be measured and included in analyses. The metrics used in the quantitative method do not account for the spatial arrangement of the microstructures with respect to each other in the cortex. The arrangement of the microstructures could hold additional taxonomic information. Although difficult to quantify, microstructural arrangement will also be included in future analyses.

During the course of this work, additional unforeseen situations arose that also must be addressed in future analyses. It was known before any analyses that the population distribution of microstructural types was not the same across mammalian taxa. There were several instances where one micrograph did not show the full suite of five microstructural types. For instance, in the bear, the bone in the thin-section is almost entirely remodeled, resulting in many missing values for primary vasculature and primary lacunae. Given that the amount of secondary bone increases with age, the absence of primary structures in the cross-section does not mean that it was never present. In another example, several mammal micrographs did not show any primary vascular canals, although they did show other primary features and the bones were not heavily remodeled. Again, this resulted in missing values. However, the missing values in the remodeled bear and in the avascular mammals are different types of missing values. How could this information be encoded in the dataset? If the primary cortex is avascular, this information may contribute to distinguishing that taxon, but it was not taken into account during the analyses in this dissertation. Extracting

a maximum of useful information content from these “missing value” situations is a primary aim of future work.

To what level will this method allow taxonomic resolution? The answer to this question is not clear from the results of the Primary Dataset. In order to explore this question, future datasets must be populated with multiple specimens from the same “Family”, genus, and/or species. The limitations on the acquisition of samples for the Primary Dataset prevented such tests in this dissertation. Based on the current level of success of the new method, it is hoped that future requests for specific specimens will be granted with less reservation and that the additional samples will aid the exploration of taxonomic resolution.

There is so much untapped information in the microstructure of bones that not all of the courses of future research are not mentioned here. The major planned extension of this work is its application to the fossil record. A totally different extension by myself and/or others is to the analysis of locomotion in vertebrates, both from biophysical and evolutionary points of view.

8.4 Perspectives

As we move our respective disciplines forward, we can only hope to honor and respect those scientists who have come before us, in some situations suggesting that their conclusions can be amended to reflect new data. The basic hypothesis tested here is simple. Many others have attempted previously to infer how bone microstructure and taxonomy are related, but the most likely solution could not have been uncovered until now. The advantage of testing this hypothesis in the 21st century is the availability of technology to enable reproducible measurement on a large scale and rapid statistical testing of a huge database. Developing the fundamental biological and methodological groundwork and testing hypotheses certainly required a large investment of effort and dogged perseverance! But without such basic tools as a petrographic microscope with a digital camera, a high-precision computer algorithm that measured the hand-marked images in an instant, and the Evince software that made PCA a true joy (if there can be such a thing) to work with, it is quite possible that the results of this dissertation

would have been as inconclusive as the results of those who previously attempted to fathom the relationship between bone microstructure and taxonomy.

Whereas the analysis of microstructures in other studies addressed tens of microstructures, over 37,000 microstructures were analyzed in this study. In these first-case studies, sample size did matter. Only quantitative analysis of large numbers of microstructures enabled the statistical separation of characteristic distributions of diagnostic features. This large dataset—the first of its kind—serves as a base for all future research in osteohistological taxonomy.

In recognition of the complexity of the relations uncovered here, the signal identified is the result of a combination of principal components defined by different bone microstructural features. Results in previous chapters clearly show that no single bone microstructure or principal component is sufficient to identify taxa. Just as modern measurement and analysis technology enabled the measurement and documentation of huge numbers of features, modern statistical tools allowed the data to be interrogated and understood in terms of principal components and multi-dimensional models. The results suggest that those who made previous attempts to identify taxa on the basis of bone microstructure may have failed because they did not (or could not) consider combinations of components.

Beyond the details of statistics and multi-dimensional models, this work represents a new perspective on and direction in taxonomic research. The implications of the research will not only serve the paleo-community, but also the broader, international scientific community that seeks to advance our knowledge of the delicate balance between the Earth's environment and her inhabitants. There is much more exploratory research on the taxonomic variation of bone microstructure to be done, but each new study will add to a growing database of information that can be used to give us a clearer view of the ecological past.

Appendix A

Terms and Definitions

Basic Multicellular Unit (BMU) - The collection of cells involved in creating secondary osteons during bone remodeling (Martin and Burr, 1989).

Cement Line - The boundary of uncertain composition that separates the secondary osteon from the surrounding bone. Also referred to as the cement sheath (Locke, 2004) or the reversal line.

Circumferential Lamellae-The layers of bone that underlie the periosteum and endosteum, often in concentric form.

Eigenvalue-The change in length that occurs when the corresponding eigenvector is multiplied by its matrix.

Eigenvector-A unit length vector that retains its direction when multiplied to the matrix that it corresponds to. An ($m \times n$) matrix can have as many as n unique eigenvectors, each of which will have its own eigenvalue.

Endosteum- The layer of cells, connective tissue, and blood vessels lining the inner face (medullary cavity) of hollow bones (Locke, 2004).

Interstitial lamellae - Derived from laminar bone, filling some of the space between osteons after the loss of capillary network sheets (Locke, 2004).

Lamellae - Bone layers in both laminar and osteonic bone, each consisting of a 20-50m thick layer of collagen fibers on which mineral salts may be deposited. The

fiber orientation varies and often defines several types of bone such as woven, parallel fibered, lamellar, and fibrolamellar (modified from Locke 2004).

Laminae - Primary bone made from 4-20 lamellae laid down between capillary network sheets and surviving as interstitial lamellae between osteons and in endosteal and periosteal layers. Laminar bone is always primary (Locke, 2004). Laminar bone texture has historically been called “primary lamellar” or “mature plexiform bone” (Martin and Burr, 1989).

Osteoblast - Bone cells concerned with bone deposition.

Osteoclast - Bone cells concerned with bone resorption.

Osteocyte - A bone cell formed by the incorporation of an osteoblast into the bone matrix.

Osteoid - Pre-osseous tissue, lamellae before ossification ((Locke, 2004).

Periosteum - The layers of cells, connective tissue, and blood vessels that protects the outer surface of bones (Locke, 2004)

Primary Lacunae - a small space containing an osteocyte in bone or chondrocyte in cartilage. In this dissertation the lacunae is designated “primary” if it is housed within primary bone.

Primary Osteon - A cylinder of concentric lamellae around a tubular space, the primary vascular canal, containing blood vessels. Primary osteons form along the periosteal surface of bones nearing maturity and lack a cement sheath (Locke, 2004).

Secondary Lacunae - a small space containing an osteocyte in bone or chondrocyte in cartilage. In this dissertation the lacunae is designated “secondary” if it is housed within secondary bone.

Secondary Osteon - A replacement of laminar bone derived from capillary networks and having a cement sheath defining the outer border (Currey, 1962). The basic multicellular unit of bone remodeling (Parfitt, 1979). Also referred to as Haversian systems.

Tetrapod - Vertebrate animals having four feet, legs or leglike appendages. Amphibians, reptiles, dinosaurs/birds, and mammals are tetrapods. Snakes are also tetrapods by decent and secondary loss of the limbs. The earliest tetrapods radiated from the Sarcopterygii (lobe-finned fishes)

Volkman's canals - The radially oriented spaces with blood vessels connecting capillary sheets and to a lesser extent, osteons. They are often diagonal to the long axis of the bone (Locke, 2004).

Appendix B

Diagnostic Characters in Dinosaurian Species

Details of the dinosaurian species differences are given below. The most recently designated species of each genus was used as the reference taxon. The number of differences was calculated by the diagnostic features present in the most recently named species that differed from all other species with that genus, unless otherwise specified. The genera are listed in alphabetical order.

Amtosaurus

Species: *A. magnus* (Kurzanov and Tumanova, 1978); *A. archibaldi* (Averianov, 2002)

1. Three rather than two exits for N. hypoglossus (XII) in *A. archibaldi*.
2. Smaller angle between the ventral surfaces of the basioccipital and basisphenoid (90 rather than 120) in *A. archibaldi*.
3. The basipterygoid processes more posteriorly placed in *A. archibaldi*

Apatosaurus

Species: *A. ajax* (Marsh, 1877); *A. excelsus* (Marsh, 1879); *A. louisae* (Holland, 1915); *A. parvus* (Upchurch et al., 2004)

1. Posterior dorsal centra are wider than high in *A. parvus*

2. Acromial ridge at 90 degrees to the long-axis of the scapular blade in *A. parvus*
3. Medial proximal process of the ulna exceeds the length of the anterior proximal process by at least 20% in *A. parvus*
4. There is constriction in the distal half of the shaft of McIII in *A. parvus*
5. Transverse and dorsoventral diameters of the distal end of Mc V are sub-equal in *A. parvus*.

Camarasaurus

Species: *C. supremus* (Cope, 1876); *C. grandis* (Marsh, 1877); *C. lentus* (Marsh, 1889); *C. lewisi* (Jensen, 1988) see McIntosh et al. (1996)

1. very deep, narrow bifurcation of spines of presacral vertebrae persist back from cervical 3 to dorsal 11 with a trace showing in dorsal 12 in *C. lewisi*
2. increased angle between axis of sacrum and ilium in *C. lewisi*
3. much more strongly developed ossified ligaments in the posterior dorsal and particularly in the sacral regions linking the spine of one vertebra with the diapophysis of the succeeding vertebra in *C. lewisi*
4. articular processes of the pre- and post-zygapophyses large and rectangular in *C. lewisi*
5. heads of chevrons strongly bridged over with bone in *C. lewisi*
6. each chevron has two distinct articular surfaces of equal dimension in *C. lewisi*
7. the anterior chevron articular surface articulated with the preceding vertebra being horizontal in *C. lewisi*
8. the posterior chevron articular surface articulating with the succeeding vertebra being oriented downward at an angle of 60 degrees in *C. lewisi*

***Camptosaurus* Species:** *C. dispar* (Marsh, 1879); *C. prestwichii* (Marsh, 1879); *C. aphanoecetes* (Carpenter and Wilson, 2008)

1. mandibular symphysis short and more vertically oriented in *C. aphanoecetes*
2. coronoid process relatively taller in *C. aphanoecetes*
3. postzygapophyses of axis extend well beyond posterior face of centrum in *C. aphanoecetes*
4. axis neural spine above postzygapophyses laterally compressed, not expanded laterally to form deep pocket in *C. aphanoecetes*
5. cervical centra shorter compared to height, especially in mid-cervicals in *C. aphanoecetes*
6. mid- and posterior cervical amphiplatyon to weakly plani-concave, not opisto-coelus in *C. aphanoecetes*
7. cervical centrum 7 wedge-shaped in lateral view in *C. aphanoecetes*
8. neural arches of posterior cervical very tall in *C. aphanoecetes*
9. anterior dorsal centra shorter compared to height in *C. aphanoecetes*
10. anterior caudal centra not angled poasteroventrally in *C. aphanoecetes*
11. mid-caudal centrum with small chevron facet in *C. aphanoecetes*
12. mid-caudal neural spine long and slender in *C. aphanoecetes*
13. postzygapophyse located high on neural spine in *C. aphanoecetes*
14. scapular blade arched in profile, not straight, and distal end steeply sloped in *C. aphanoecetes*
15. deltopectoral crest low triangle, not prominent in *C. aphanoecetes*
16. ilium with more vertical pubic penduncle in *C. aphanoecetes*
17. dorsal rim of ilium arched in *C. aphanoecetes*
18. prepubic process proportionally larger in *C. aphanoecetes*
19. postpubic process lower with rounded distal end in *C. aphanoecetes*

20. pubis with posterior projecting iliac peduncle forming a large, acetabular notch in *C. aphanoecetes*
21. ischium with small distal foot in *C. aphanoecetes*

Caudipteryx

Species: *C. zoui* (Ji et al., 1998); *C. dongi* (Zhou and Wang, 2000)

1. longer ilium in *C. dongi*
2. smaller sternal plates in *C. dongi*
3. different McI:McII ratio in *C. dongi*
4. ischium short in *C. dongi*

Centrosaurus

Species: *C. apertus* (Lambe, 1904); *C. brinkmani* (Ryan and Russell, 2005)

1. supraorbital horncores are inflated in *C. brinkmani*
2. horncores project laterally over the orbit in *C. brinkmani*
3. posterior parietal bar has a number of small accessory dermal ossifications that fuse along the caudal and dorsal surfaces and contribute to the substance of P1 and P2 in *C. brinkmani*
4. accessory dermal ossifications can be variably developed as short spines that may or may not be fused along their adjacent margins in *C. brinkmani*
5. P3 is variably developed as a short, tongue-like hook or tapered spike that is dorsolaterally oriented in *C. brinkmani*

Chasmosaurus

Species: *C. canadensis* (Lambe, 1902); *C. belli* (Lambe, 1914); *C. russelli* (Sternberg, 1940); *C. mariscalensis* (Lehman, 1989); *C. irvinensis* (Holmes et al., 2001)

1. transversely broad snout in *C. irvinensis*
2. nasal horn core short and transversely broad in *C. irvinensis*
3. brow horn absent in *C. irvinensis*
4. jugal notch on anterior squamosal broadly rounded and open in *C. irvinensis*
5. squamosal tapers little posteriorly, subrectangular in outline in *C. irvinensis*
6. squamosal projects almost directly laterally in *C. irvinensis*
7. Posterior parietal bar straight in dorsal and anterior aspects in *C. irvinensis*
8. posterior parietal bar projects only slightly posterior to the squamosal in *C. irvinensis*
9. maximum diameter of the parietal fenestra less than the length of the preorbital area of the skull in *C. irvinensis*
10. ten epoccipitals on the posterior parietal bar in *C. irvinensis*
11. lateral epoccipital low and shield-shaped in *C. irvinensis*
12. remaining eight epoccipitals nearly indistinguishably coossified together in *C. irvinensis*
13. epoccipitals composed of flattened posterioventral laminae that wrap around the back of the bar and larger laminae that curve strongly dorsally and anteriorly over the bar in *C. irvinensis*

Chirostenotes

Species: *C. elegans* (Parks, 1933); *C. pergracilis* (Sues, 1997)

1. overall larger size in *C. pergracilis*
2. possession of a more elongate and shallower dentary in *C. pergracilis*
3. a proportionally longer mandibular symphysis in *C. pergracilis*

4. the presence of a median ridge on the dorsal (lingual) aspect of the mandibular symphysis in *C. pergracilis*

Diplodocus

Species: *D. longus* (Marsh, 1878); *D. lacustris* (Marsh, 1884); *D. carnegii* (Hatcher, 1901); *D. hayi* (Holland, 1924)

1. deeply excavated lower edge of the exoccipital in *D. hayi*
2. no frontanel on the upper surface of the skull in the parietal region in *D. hayi*

Dryosaurus

Species: *D. altus* (Marsh, 1878); *D. lettowvorbecki* (Virchow, 1919) see Galton (1983)

1. weak first haemal arch in *D. lettowvorbecki*
2. larger humerus/scapula ratio in *D. lettowvorbecki*
3. strong distal intercondylar grooves in humerus in *D. lettowvorbecki*
4. strong olecranon process in *D. lettowvorbecki*
5. angular outline of distal end of ulna in *D. lettowvorbecki*
6. angular outline of distal end of radius in *D. lettowvorbecki*
7. larger length ratio of metatarsals I:III in *D. lettowvorbecki*
8. wide premaxilla/prefrontal suture in *D. lettowvorbecki*
9. the maxilla is rounded with a few large ridges at the palatine suture in *D. lettowvorbecki*
10. different maxillary tooth count in *D. lettowvorbecki*
11. different dentary tooth count in *D. lettowvorbecki*

12. small jugal margin of the antorbital fossa in *D. lettowvorbecki*
13. small palpebral in *D. lettowvorbecki*
14. straight anterior edge of postorbital in lateral view in *D. lettowvorbecki*
15. short anterior process of squamosal in *D. lettowvorbecki*
16. shorter median length of parietal in *D. lettowvorbecki*
17. deep excavation of the anterior edge of the paraoccipital process in *D. lettowvorbecki*
18. large foramen for the internal carotid artery in *D. lettowvorbecki*
19. gentle rounded edge of trigeminal foramen in *D. lettowvorbecki*
20. prominent rugosity below the trigeminal foramen on the prootic and basisphenoid in *D.lettowvorbecki*
21. large ratio of max length of skull to max width of skull in *D. lettowvorbecki*

Edmontonia

Species: *E. longiceps* (Sternberg, 1928); *E. rugosidens* (Gilmore, 1930)

1. wider palate in *E. rugosidens*
2. more prominent supraorbital boss in *E. rugosidens*

Haplocanthosaurus

Species: *H. priscus* (Hatcher, 1903); *H. delfi* (McIntosh and Williams, 1988)

1. overall larger in size in *H. delfi*
2. girdle bones more robust in *H. delfi*
3. femur more robust in *H. delfi*

4. pubis heavier distally in *H. delfi*
5. distal end of ischium broader in *H. delfi*
6. ischium not rotated inward and not fused to its mate in *H. delfi*
7. v-shaped, anteriolaterally projecting laminae present on neural spines of middle dorsals in *H. delfi*
8. greater development of the medial laminae on the posterior dorsal neural spines in *H. delfi*

Gryposaurus

Species: *G. notabilis* (Lambe, 1914); *G. incurvimanus* (Parks, 1920); *G. latidens* (Horner, 1992)

1. extremely wide dentary teeth in *G. latidens*
2. short dentary teeth in *G. latidens*
3. excavations on the ventral surface of the premaxillae for union of the anteroventral maxillary processes of the maxillae in *G. latidens*

Iguanodon

Species: *I. anglicus* (Holl, 1829); *I. bernissartensis* (Boulenger, 1881); *I. dawsoni* (Lydekker, 1888); *I. fittoni* (Lydekker, 1889); *I. atherfieldensis* (Hooley, 1925); *I. lakotaensis* (Weishampel and Bjork, 1989)

1. supraoccipital incised beneath the parietal and squamosals in *I. lakotaensis*
2. loss of median ridge on supraoccipital in *I. lakotaensis*
3. single aperture for both branches of the facial nerve in *I. lakotaensis*
4. relatively large antorbital fenestra in *I. lakotaensis*

5. loss of contact between the maxilla and lacrimal at the jugal-maxilla articulation in *I. lakotaensis*
6. relatively small maxillary teeth in *I. lakotaensis*
7. relatively small dentary teeth in *I. lakotaensis*
8. few maxillary tooth families in *I. lakotaensis*
9. low tooth density in *I. lakotaensis*
10. reduced z-spacing and longer wave of alternating teeth from the back of the jaws in the mandibular dentition. In *I. lakotaensis*

Lambaeosaurus

Species: *L. lambei* (Parks, 1923); *L. magnicristatus* (Sternberg, 1935)

1. skull moderately massive in *L. magnicristatus*
2. hood very long, high and thin superiorly in *L. magnicristatus*
3. facial slope gentle anteriorly, then very sharply upturned and thrown strongly forward in *L. magnicristatus*
4. upper part of premaxilla expanded to cover narial slit far forward in *L. magnicristatus*
5. upper limb of premaxilla developed into very high, thin crest above narial passage in *L. magnicristatus*
6. up-turned lower lip of premaxilla very large, strongly swollen and thrown sharply forward in *L. magnicristatus*
7. diagonal groove across lower limb not well-defined in *L. magnicristatus*
8. nasal extending backward as narrow process to flank the premaxilla posteriorly in *L. magnicristatus*
9. orbit broadly rounded superiorly in *L. magnicristatus*

10. prefrontal well-developed and flanking over lower limb of premaxilla and tip of nasal in *L. magnicristatus*
11. 1 ilium of light construction, moderately down-curved and thin interno-externally in *L. magnicristatus*

Leptoceratops

Species: *L. gracilis* (Brown, 1914); *L. cerorhynchus* (Brown and Schlaikjer, 1942)

1. Nasal proportionally large in *L. cerorhynchus*
2. nasal deep and heavy in *L. cerorhynchus*
3. very well-developed horn core in *L. cerorhynchus*
4. dentary long in *L. cerorhynchus*
5. dentary with a straight ventral margin in *L. cerorhynchus*

Microraptor

Species: *M. zhaoianus* (Xu et al., 2000); *M. gui* (Xu et al., 2003)

1. prominent biceps tuberosity on radius in *M. gui*
2. much shorter manual digit I in *M. gui*
3. strongly curved pubis in *M. gui*
4. bowed tibia in *M. gui*

Melanorosaurus

Species: *M. readi* (Haughten, 1924); *M. thabanensis* (Gauffre, 1993)

1. fourth trochanter on femur oblique in *M. thabanensis*

2. fourth trochanter far from the medial edge in *M. thabanensis*
3. lesser trochanter far from medial edge in *M. thabanensis*

Ornithomimus

Species: *O. velox* (Marsh, 1890a); *O. edmontonicus* (Sternberg, 1933)

1. *O. edmontonicus* is a larger specimen
2. *O. edmontonicus* is more gracile
3. ascending astragalus process is longer and narrower in *O. edmontonicus*
4. metatarsals relatively longer in *O. edmontonicus*

Parasaurolophus

Species: *P. walkeri* (Parks, 1922); *P. tubicen* (Wiman, 1931); *P. cyrtocristatus* (Ostrom, 1961)

1. cranial crest of *P. cyrtocristatus* is approximately 1/3 the length
2. cranial crest curves strongly downward behind the occiput in *P. cyrtocristatus*

Pinacosaurus

Species: *P. grangeri* (Gilmore, 1933); *P. mephistocephalus* (Godefroit et al., 1999)

1. Two pairs of premaxillary foramina leading to premaxillary sinuses in *P. mephistocephalus*
2. “gland” opening facing rostrally in *P. mephistocephalus*
3. both lower and upper premaxillary foramina much smaller than “gland” opening in *P. mephistocephalus*

4. external nares only visible in dorsal view in *P. mephistocephalus*

Plateosaurus

Species: *P. engelhardti* (Meyer, 1837); *P. gracilis* (Huene, 1908) see also Yates (2003)

1. proximodistally narrow neural spines on the proximal caudal vertebrae in *P. gracilis*
2. retaining a larger and sharply defined brevis shelf on the ilium in *P. gracilis*

Polacanthus

Species: *P. foxii* (Hulke, 1881); *P. rudgwickensis* (Blows, 1996)

1. *P. rudgwickensis* is significantly larger (30%) than *P. foxii*
2. large, robust dorsal vertebrae with wide, round centrum faces (smaller with slightly heart-shaped faces in *P. foxii*)
3. anterior caudal vertebrae with tall, round articular faces (slightly heart-shaped in *P. foxii*)
4. lateral processes with two inferior ridges merging into the centrum margins forming a depression between them (absent in *P. foxii*)
5. one superior ridge occupying almost the entire centrum length and forming a tall neural arch (less well developed in *P. foxii*)
6. scapular spine close to dorsal border in *P. rudgwickensis*
7. large, deep posterior ribs (smaller in *P. foxii*)
8. long tibia (shorter in *P. foxii*)
9. massive, presacral dermal spines with rounded bases that are solid over the posterior end in *P. rudgwickensis*

10. ventrally hollowed and very thin rounded roof-shaped scutes with tall dorsal keel (unknown in *P. foxii*)

Prosaurolophus

Species: *P. maximus* (Brown, 1916); *P. blackfeetensis* (Horner, 1992)

1. nasal excavation which is formed entirely by the nasal in *P. blackfeetensis*
2. nasal excluding the prefrontal and premaxilla in *P. blackfeetensis*

Protoceratops

Species: *P. andrewsi* (Granger and Gregory, 1923); *P. hellenikorhinus* (Lambert et al., 2001)

1. ventral edge of the dentary straight in *P. hellenikorhinus*
2. caudal edge of the angular formed by a caudally facing triangular surface in *P. hellenikorhinus*
3. long projection of the squamosal contacting the quadratojugal in *P. hellenikorhinus*
4. straight and strongly reduced longitudinal ridge on maxilla in *P. hellenikorhinus*

Psittacosaurus

Species: *P. mongoliensis* (Osborn, 1923); *P. osborni* (Young, 1930); *P. sinensis* (Young, 1958); *P. youngi* (Chao, 1962); *P. guyangensis* (Cheng, 1983); *P. xinjiangensis* (Serenó and Chao, 1988); *P. meileyingensis* (Serenó and Chao, 1988); *P. neimongoliensis* (Russell, 1996); *P. ordosensis* (Russell, 1996); *P. mazongshanensis* (Xu, 1997); *P. sibiricus* (Voronkevich et al., 2000)

1. skull width exceeds skull length in *P. sibiricus*

2. premaxillary maximum length to height ratio less than 60% in *P. sibiricus*
3. postorbital with short medial process in *P. sibiricus*
4. postorbital has no contribution to the orbital margin in *P. sibiricus*
5. jugal with deep cleft for quadratojugal extending to posterior face of jugal horn in *P. sibiricus*
6. angular with prominent angular tuber in *P. sibiricus*
7. 23 presacral vertebrae in *P. sibiricus*

Rhabdodon

Species: *R. priscus* (Matheron, 1869); *R. septimanicus* (Buffetaut and Le Loeuff, 1991)

1. stronger lateral concave curvature of the dentary in *R. septimanicus*
2. no shelf located lateral to the tooth row in *R. septimanicus*
3. coronoid process not displaced laterally in *R. septimanicus*

Ricardoestesia

Species: *R. gilmorei* (Currie et al., 1990); *R. isosceles* (Sankey, 2001)

1. teeth shaped like isosceles triangles in lateral view in *R. isosceles*
2. in basal cross-section, tooth is a labio-lingually compressed oval *R. isosceles*
3. denticles minute, square, uniformly sized from base to tip in *R. isosceles*
4. Anterior denticles often considerably smaller than posterior denticles in *R. isosceles*
5. Interdenticle spaces minute and barely visible, denticles closely spaced in *R. isosceles*

6. Denticle tips straight or faintly rounded, but not pointed in *R. isosceles*
7. 7-11 denticles/mm in *R. isosceles*

Saurolophus

Species: *S. osborni* (Brown, 1912); *S. angustirostris* (Hu, 1973); see Maryanska and Osmolska (1981)

1. Narrower skull in *S. angustirostris*
2. longer crest in *S. angustirostris*
3. relatively smaller length of the maxillary dental battery in *S. angustirostris*
4. longitudinal bony septum present in *S. angustirostris*
5. irregular chambers on the anterior surface of the crest in *S. angustirostris*
6. size of external nares in *S. angustirostris*
7. position of external nares in *S. angustirostris*
8. shorter lacrimal in *S. angustirostris*
9. elongated anterior jugal in *S. angustirostris*
10. more bowed quadrate in *S. angustirostris*
11. straight scapula in *S. angustirostris*
12. radius almost equals humerus in *S. angustirostris*
13. 8 sacrals in *S. angustirostris*
14. long, curved preacetabular process in *S. angustirostris*
15. postacetabular process tapering backwards in *S. angustirostris*
16. gently bowed lower and upper edges of the prepubis in *S. angustirostris*
17. pes approximately 1/3 femur length in *S. angustirostris*

18. MtIII/femur ratio larger in *S. angustirostris*
19. Ph III-2/ Ph III-1 ratio larger in *S. angustirostris*

Saurornithoides

Species: *S. mongoliensis* (Osborn, 1924a); *S. junior* (Barsbold, 1974)

1. *S. junior* is 3 times larger than *S. mongoliensis*
2. *S. junior* and *S. mongoliensis* have difference dental formulas

Sphaerotholus

Species: *S. buchholzae* (Williamson and Carr, 2002); *S. goodwini* (Williamson and Carr, 2002)

1. caudal view of skull in *S. goodwini* possesses a parietosquamosal bar that reduces in depth laterally to a lesser extent than *S. buchholzae*
2. the parietal is reduced to a thin slip between the squamosals in *S. goodwini*

Spinosaurus

Species: *S. aegyptiacus* (Stromer, 1915); *S. maroccanus* (Russell, 1996)

1. difference length/height ratio in the mid-cervical vertebrae of *S. maroccanus*

Struthiosaurus

Species: *S. austriacus* (Bunzel, 1871); *S. transylvanicus* (Nopsca, 1915); *S. languedocensis* (Garcia and Pereda Suberbiola, 2003)

1. *S. languedocensis* is a small-sized nodosaurid

2. ischium directed immediately caudal to the acetabulum in *S. languedocensis*
3. distal dorsal centra very compressed laterally and hour-glass shaped in *S. languedocensis*

Syntarsus

Species: *S. rhodesensis* (Raath, 1969); *S. kayentakatae* (Rowe, 1989)

1. paired cranial crest formed by lacrimal and possibly nasal in *S. kayentakatae*
2. fusion of fibula to the calcaneum in *S. kayentakatae*

Titanosaurus

Species: *T. indicus* (Lydekker, 1877); *T. blanfordi* (Lydekker, 1879)

1. caudal centra cylindrical with no signs of lateral compression in *T. blanfordi*
2. transverse diameter of articular surfaces wider than the vertical diameter in *T. blanfordi*
3. facets for articulation of chevron bones not placed on distinct ridges of bone in *T. blanfordi*

Valdosaurus

Species: *V. canaliculatus* (Galton, 1975); *V. nigeriensis* (Galton and Taquet, 1982)

1. proximal end of lesser trochanter of femur below that of the greater trochanter in *V. nigeriensis*
2. deep medial pit on shaft is separated from the base of the fourth trochanter by a raised area in *V. nigeriensis*

Velociraptor

Species: *V. mongoliensis* (Osborn, 1924a); *V. osmolskae* (Godefroit et al., 2008)

1. Long, rostral plate of maxilla with elongation index = 38 in *V. osmolskae*
2. Promaxillary fenestra subequal in size to the maxillary fenestra in *V. osmolskae*
3. Promaxillary fenestra tear-drop shaped in *V. osmolskae*
4. long axis of the promaxillary fenestra perpendicular to the dorsal border of the maxilla in *V. osmolskae*
5. long axis of maxillary fenestra parallel to the dorsal border in *V. osmolskae*
6. Ten maxillary teeth with short, unserrated carina on the apical side of mesial edge in *V. osmolskae*
7. incipient serrations on distal carina of maxillary teeth in *V. osmolskae*

Zalmoxes

Species: *Z. robustus* (Nopsca, 1900); *Z. shqiperorum* (Weishampel et al., 2003)

1. dentary has a wide, angular buccal emargination that forms a horizontal platform extending for the full length of the dentition behind and medial to the coronoid process in *Z. shqiperorum*
2. a scapular blade that is narrow and strap-like proximally and expands sharply posterodistally in *Z. shqiperorum*
3. expansion of the region adjacent to the coracoid suture and acromial process in *Z. shqiperorum*
4. the acromial process forms a prominent flange in *Z. shqiperorum*
5. an ischium with a boot-like distal expansion in *Z. shqiperorum*

Appendix C

Determination of Longitudinal Orientation

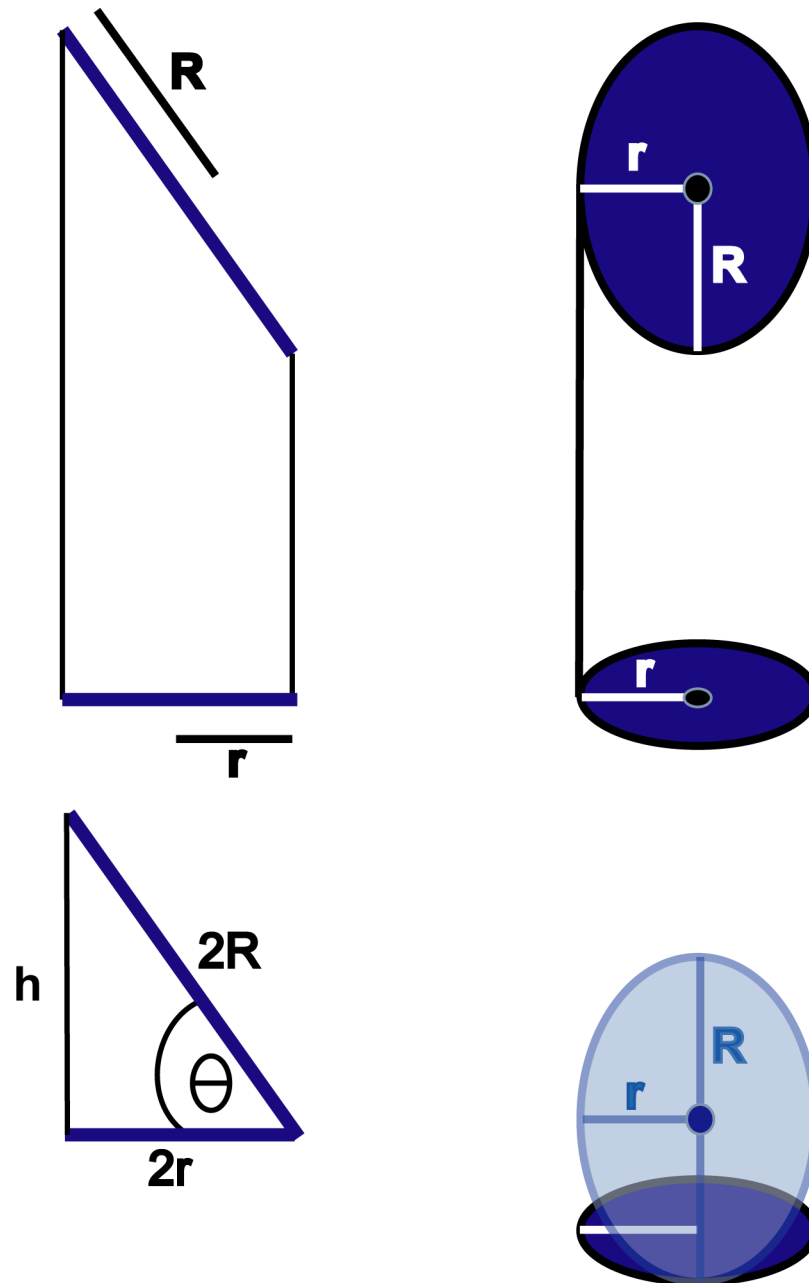
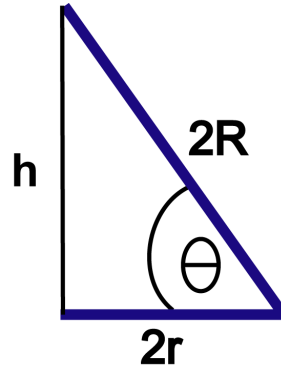
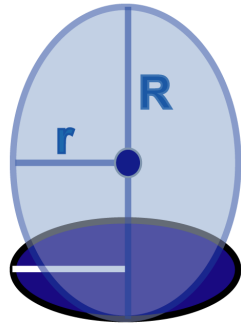


Figure C.1: A series of schematics representing cylindrical microstructural bodies (secondary osteons, Haversian canals, primary vasculature). The angle Θ is the angle that the cylindrical microstructural body deviates from parallel with the longitudinal axis of the diaphysis. The variable r is equal to the radius of the minor axis of the microstructure and R is equal to the radius of the major axis of the microstructure.



$$h^2 + (2r)^2 = (2R)^2$$

$$\sin \Theta = \frac{h}{2R}$$

$$(2R(\sin \Theta))^2 + (2r)^2 = (2R)^2$$

$$h = 2R(\sin \Theta)$$

$$(\sin \Theta)^2 = \frac{(2R)^2 - (2r)^2}{(2R)^2}$$

$$(\sin \Theta)^2 = 1 - \frac{(2r)^2}{(2R)^2}$$

$$(\sin \Theta)^2 = 1 - \frac{(r)^2}{(R)^2}$$

$$\Theta = \sin^{-1} \left(\sqrt{1 - \frac{(r)^2}{(R)^2}} \right)$$

$$(\sin \Theta) = \sqrt{1 - \frac{(r)^2}{(R)^2}}$$

Figure C.2: Θ is determined using a derivation of the Pythagorean Theorem

References

- L. Agassiz. *Recherches sur les poissons fossiles*, volume 3. Neuchatel, Switzerland, 1843.
- R. Amprino. La structure du tissu osseux envisage comme expression de differences dans la vitesse dw l'acrosissement. *Archives de Biologie*, 58:315–330, 1947.
- R. Amprino. A contribution to the functional meaning of the substitution of primary by secondary bone tissue. *Acta Anatomica*, 5(3):291–300, 1948.
- R. Amprino. On the growth of cortical bone and the mechanism of osteon formation. *Acta Anatomica*, 52:177–187, 1963.
- R. Amprino and G. Marotti. A topographic quantitative study of bone formation and reconstruction. In H.J.J. Blackwood, editor, *Bone and Tooth, Proc. 1st European Symposium*, pages Chap.2, 6. Pergamon Press, London, 1964.
- A. Ardizzoni. Osteocyte lacunar size-lamellar thickness relationships in human secondary osteons. *Bone*, 28(2):215–219, 2001.
- J.M. Asara, M.H. Schweitzer, L.M. Freimark, M. Phillips, and L.C. Cantley. Protein sequences from mastodon and tyrannosaurus rex revealed by mass spectrometry. *Science*, 316:280–285, 2007.
- A. Ascenzi and E. Bonucci. A quantitative investigation of the birefringence of the osteon. *Acta Anatomica*, 44:236–262, 1961.
- A. Ascenzi and E. Bonucci. The ultimate tensile strength of single osteons. *Acta Anatomica*, 58:160–183, 1964.
- A. Ascenzi and E. Bonucci. The tensile properties of single osteons. *The Anatomical Record*, 158:375–386, 1967.
- A. Ascenzi and E. Bonucci. The compressive properties of single osteons. *The Anatomical Record*, 161:377–392, 1968.
- A. Ascenzi and E. Bonucci. The shearing properties of single osteons. *The Anatomical Record*, 172:499–510, 1972.
- A. Ascenzi, E. Bonucci, and D.S. Bocciarelli. An electron miroscope study of osteon calcification. *Journal of Ultrastructure Research*, 12:287–303, 1965.

- M.-G. Ascenzi, A. Ascenzi, A. Benvenuti, M. Burghammer, S. Panzavolta, and A. Bigi. Structural differences between "dark" and "bright" isolated human osteonic lamellae. *Journal of Structural Biology*, 141:22–33, 2003.
- M.-G. Ascenzi, M. Andreuzzi, and J.M. Kabo. Mathematical modeling of human secondary osteons. *Scanning*, 26:25–35, 2004.
- J.E. Aubin, K. Turksen, and J.N.M. Heersche. Osteoblastic cell lineage. In M. Noda, editor, *Cellular and Molecular Biology of Bone*, pages 1–45. 1993.
- A.O. Averianov. An ankylosaurid (ornithischia:ankylosauria) braincase from the upper cretaceous bissekty formation of uzbekistan. *Bulletin Institut Royal des Sciences Naterelles*, 72:97–110, 2002.
- G Baltadchiev. Morphology of the haversian canal. an electron microscopic study. *Folia Medica*, 36(1):21–28, 1994.
- R. Baron. General principles of bone biology. In *Primer on the Metabolic Bone Diseases of Mineral Metabolism*, pages 1–8. Fifth edition edition, 2003.
- R. Baron, J-H. Ravesloot, L. Neff, D. Chakraborty, D. Chatterjee, A. Lomri, and W. Horne. Cellular and molecular biology of the osteoclast. In M. Noda, editor, *Cellular and Molecular Biology of Bone*, pages 445–494. 1993.
- P.M. Barrett, P. Hailu, P. Upchurch, and A.C. Burton. A new ankylosaurian dinosaur (ornithischia: Ankylosauria) from the upper cretaceous of shanxi province, people's republic of china. *Journal of Vertebrate Paleontology*, 18(2):376–384, 1998.
- R. Barsbold. Sauronithoididae, a new family of small theropod dinosaurs from central asia and north america. *Palaeontologica Polonica*, 30:5–22, 1974.
- A. Basilevsky. *Statistical Factor Analysis and Related Methods. Theory and Applications*. John Wiley and Sons, New York, 1994.
- M.J. Benton. Fossil quality and naming dinosaurs. *Biology Letters*, Published Online (doi:10.1098/rsbl.2008.0402):1–4, 2008.
- M.J. Benton and P.N. Pearson. Speciation in the fossil record. *Trends in Ecology and Evolution*, 16(7):405–411, 2001.
- W.T. Blows. A new species of polacanthus (ornithischia; ankylosauria) from the lower cretaceous of sussex, england. *Geological Magazine*, 133(6):671–682, 1996.
- M. de Boef and H.C.E. Larsson. Bone microstructure: quantifying vascular orientation. *Canadian Journal of Zoology*, 85:63–70, 2007.

- J.F. Bonaparte. Cretaceous tetrapods of argentina. In G. Arrata, editor, *Munchner Geowissenschaftliche Abhandlungen, Reihe A, Geologie und Palaontologie: Contributions of Southern South American to Vertebrate Paleontology*, volume 30, pages 73–130. Munchen, 1996.
- B. Borah, G.J. Gross, T.E. Dufresne, T.S. Smith, M.D. Cockman, P.A. Chmielewski, M.W. Lundy, J.R. Hartke, and E.W. Sod. Three-dimensional microimaging, finite element modeling, and rapid prototyping provide unique insights into bone architecture in osteoporosis. *The Anatomical Record (New Anat.)*, 265:101–110, 2001.
- A.L. Boskey. Mineral analysis provides insights into the mechanism of biomineralization. *Calcified Tissue International*, 72:533–536, 2003.
- J. Botha and A. Chinsamy. Growth patterns deduced from the bone histology of the cynodonts diademodon and cynognathus. *Journal of Vertebrate Paleontology*, 20 (4):705–711, 2000.
- G.A. Boulenger. Rappaport de p.j. van beneden ”sur l’are pelvien chez les dinosauriens de bernissart par m.g.a. boulenger”. *Bulletin de l’ Academie royale des Sciences, des Lettres et des Beaux-Arts de Belgique, 3e Serie*, 1:600–608, 1881.
- A.E. Broadus. Mineral balance and homeostasis. In *Primer on the Metabolic Bone Diseases and Disorders of Mineral Metabolism*, pages 105–111. Fifth edition edition, 2003.
- C.A. Brochu. Osteology of *Tyrannosaurus Rex*:insights from a nearly complete skeleton and high-resolution computed tomographic analysis of the skull. *Journal of Vertebrate Paleontology*, 22:1–138, 2003.
- T.G. Bromage, H.M. Goldman, S.C. McFarlin, J. Warshaw, A. Boyde, and C.M. Riggs. Circularly polarized light standards for investigations of collagen fiber orientation in bone. *The Anatomical Record (Part B: New Anatomist)*, 274B:157–168, 2003.
- B. Brown. A crested hadrosaur from the edmonton cretaceous. *Bulletin of the American Museum of Natural History*, 31:131–136, 1912.
- B. Brown. A new trachodont dinosaur, hypacrosaurus, from the edmonton cretaceous of alberta. *Bulletin of the American Museum of Natural History*, 32:395–406, 1913.
- B. Brown. Anchiceratops, a new genus of horned dinosaurs from the edmonton cretaceous of alberta, with discussion of the origin of the ceratopsian crest and the braincasts of anchiceratops and tracodon. *Ibid*, 33:539–548, 1914.
- B. Brown. A new crested dinosaur, prosaurolophus maximus. *Ibid*, 35:709–716, 1916.

- B. Brown and E.M. Schlaikjer. The skeleton of leptoceratops with the description of a new species. *American Museum Novitates*, 1169:1–15, 1942.
- M.W. Browne. A comparison of factor analytic techniques. *Psychometrika*, 33(3): 267–334, 1968.
- V.v. Bruns. *Lehrbuch der Allegemeinen. Anatomie des Menschen*. Vieweg und sohn, Braunschweig, 1841.
- E. Buffetaut. Remarques anatomiques et paleohistologiques sur dyrosaurus phosphaticus, crocodilian mesosuchien des phosphates ypresiens die tunisie. *Annales de paleontology*, 68(4):327–341, 1982.
- E. Buffetaut and J. Le Loeuff. Une nouvelle espce de rhabdodon (dinosauria, ornithischia) de cretace de l'herault (sud de la france). *Comptes Rendus de l'Academie des Sciences, Serie II. Mecanique, physique, chimie, sciences de l'univers, sciences de la terre*, 312:943–948, 1991.
- V. de Buffrenil, A. de Ricqles, C.E. Ray, and D.P. Domning. Bone histology of the ribs of the archaeocetes (mammalia: Cetacea). *Journal of Vertebrate Paleontology*, 10(4):455–466, 1990.
- S. Bumrerraj and J.L. Katz. Scanning acoustic microscopy study of human cortical and trabecular bone. *Annals of Biomedical Engineering*, 29:1034–1042, 2001.
- E. Bunzel. Die reptilfauna der gosauformation in der neuen welt bei wiener-neustadt. *Abhanglungen der Kaiserlich-Koniglichen Geologischen Reichsanstalt*, 5:1–18, 1871.
- D.B. Burr, M.B. Schaffler, and R.G. Frederickson. Composition of the cement line and its possible mechanical role as a local interface in human compact bone. *Journal of Biomechanics*, 21(11):939–945, 1988.
- J.O. Calvo and L. Salgado. Rebbachisaurus tessonei sp. nov. a new sauropoda from the albian-cenomanian of argentina; new evidence on the origin of the diplodocidae. *Gaia*, 11:13–33, 1995.
- K. Carpenter and Y. Wilson. A new species of camptosaurus (ornithopoda: Dinosauria) from the morrison formation (upper jurassic) of dinosaur national monument, utah, and a biomechanical analysis of its forelimb. *Annals of the Carnegie Museum*, 76(4):227–263, 2008.
- M.A. Carrasco. Variation and its implication in a population of cupidinimus (heteromyidae) from hepburn's mesa, montana. *Journal of Vertebrate Paleontology*, 18(2):391–402, 1998.
- D.R. Carter and D.M. Spengler. Mechanical properties and composition of cortical bone. *Clinical Orthopedics and Related Research*, 135:192–217, 1978.

- R.B. Cattell. The scree test for the number of factors. *Multivariate Behavioral Research*, 1:629–637, 1966.
- R.B. Cattell. *The scientific use of factor analysis in behavioral and life sciences*. Plenum Press, New York, 1978.
- S.T. Chao. A new species of psittacosaur from laiyang, shantung. *Vertebrata Pal-Asiatica*, 6:349–360, 1962.
- Z. Cheng. [reptilia]. In *Mesozoic Stratigraphy and Paleontology of the Guyang Coal-Bearing Basin, Nei Mongoll Autonomous Region, China*, pages 349–360. Geology Press, Beijing, 1983.
- A. Chinsamy. Physiological implications of the bone histology of syntarsus rhodesiensis (saurischia, theropoda). *Palaeontologia Africana*, 27:77–82, 1990.
- A. Chinsamy. Preparation of fossil bone for histological examination. *Palaeontologia Africana*, 29:39–44, 1992.
- A. Chinsamy. Histological perspectives on growth in the birds struthio camelius and sagittarius serpentarius. *Courier Forschungsinstitut Senckenberg*, 181:317–323, 1995a.
- A. Chinsamy. Ontogenetic changes in the bone histology of the late jurassic ornithopod dryosaurus lettowvorbecki. *Journal of Vertebrate Paleontology*, 15(1):96–104, 1995b.
- A. Chinsamy. Assessing the biology of fossil vertebrate through bone histology. *Palaeontologia Africana*, 33(29-35), 1997.
- A. Chinsamy and P.M. Barrett. Sex and old bones? *Journal of Vertebrate Paleontology*, 17(2):450, 1997.
- A. Chinsamy and B. Rubidge. Dicynodont (therapsida) bone histology: phylogenetic and physiological implication. *New Mexico Museum of Natural History and Science Bulletin* 3, page 116, 1993.
- A. Chinsamy, L.M. Chiappe, and P. Dodson. Growth rings in mesozoic birds. *Nature*, 368:196–197, 1994.
- A. Chinsamy, L.D. Martin, and P. Dodson. Bone microstructure of the diving hesperornis and the volant ichthyornis from the niobrara chalk of western kansas. *Cretaceous Research*, 19(2):225–235, 1998a.
- A. Chinsamy, T. Rich, and P. Vickers-Rich. Polar dinosaur bone histology. *Journal of Vertebrate Paleontology*, 18(2):385–390, 1998b.

- J. Cohen and W.H. Harris. The three-dimensional anatomy of haversian systems. *The Journal of Bone and Joint Surgery*, 40A:419–434, 1958.
- D.M. Cooper, A.L. Turinsky, C.W. Sensen, and B. Hallgrímsson. Quantitative, 3d analysis of the canal network in cortical bone by micro-computed tomography. *The Anatomical Record (Part B: New Anatomist)*, 274B:169–179, 2003.
- R.R. Cooper, J.W. Milgram, and R.A. Robinson. Morphology of the osteon. *The Journal of Bone and Joint Surgery*, 48A(7):1239–1271, 1966.
- E.D. Cope. Description of some vertebrate remains from the fort union beds of montana. *Ibid*, 28:248–261, 1876.
- J. Cruveilhier. *The Anatomy of the Human Body*. Harper and Brothers, New York, 1844.
- J. Cubo, F. Ponton, M. Laurin, E. de Margerie, and J. Castanet. Phylogenetic signal in bone microstructure of sauropsids. *Systematic Biology*, 54(4):562–574, 2005.
- M. Cuppone, B.B. Seedhom, E. Berry, and A.E. Ostell. The longitudinal young’s modulus of cortical bone in the midshaft of human femur and its correlation with ct scanning data. *Calcified Tissue International*, 74:302–309, 2004.
- J.D. Currey. Differences in the blood supply of bone and different histological types. *Quarterly Journal of Microscopic Science*, 101:351, 1960.
- J.D. Currey. The histology of the bone of a prosauropod dinosaur. *Palaeontology*, 5(2):238–246, 1962.
- J.D. Currey. Some effects of aging in human haversian systems. *Journal of Anatomy*, 98:69–75, 1964.
- J.D. Currey. *Bones: Structure and Mechanics*. Princeton University Press, Princeton, New Jersey, 2002.
- J.P. Currie and X.J. Zhao. A new carnosaur (dinosauria, theropoda) from the jurassic of xinjiang, people’s republic of china. *Canadian Journal of Earth Sciences*, 30: 2037–2081, 1993.
- P.J. Currie, J.K. Rigby Jr., and R.E. Sloan. Theropod teeth from the judith river formation of southern alberta, canada. In K. Carpenter and P.J. Currie, editors, *Dinosaur Systematics, Approaches and Perspectives*, pages 107–125. Cambridge University Press, Cambridge, 1990.
- K.A. Curry. Ontogenetic histology of apatosaurus (dinosauria: Sauropoda); new insights on growth rates and longevity. *Journal of Vertebrate Paleontology*, 19(4): 654–665, 1999.

- C. Davenport and M. Ruddell. Identification of equus species, based on bone histology. *Journal of Vertebrate Paleontology*, 15(Supplement to 3):25A, 1995.
- C.M.C. Diaz and V. Rajtova. Comparative study of lamellar bone in some carnivora. *Folia Morphologica*, 23(3):221–229, 1975.
- I. Eckardt and H.-J. Hein. Quantitative measurements of the mechanical properties of human bone tissues by scanning acoustic microscopy. *Annals of Biomedical Engineering*, 29:1043–1047, 2001.
- A.T.M. Elewa. Morphometric studies on three ostracod species of the genus *Digmocthere mandelstam* from the middle eocene of egypt. *Palaeotologica Electronica*, 6(2):1–11, 2003.
- D.H. Enlow. Functions of the haversian system. *American Journal of Anatomy*, 110:269–305, 1962.
- D.H. Enlow. *Principles of Bone Remodeling*. Thomas, Springfield, Illinois, 1963.
- D.H. Enlow. An evaluation of the use of bone histology in forensic medicine and anthropology. In G. Evans, editor, *International Congress on Anatomy Symposium on Joints and Bones*, pages 92–111. Berlin Heidelberg, New York, 1966.
- D.H. Enlow. The remodeling of bone. *Yearbook of Physical Anthropology*, 20:19–34, 1977.
- D.H. Enlow and S.O. Brown. A comparative histological study of fossil and recent bone tissues, part 1. *Texas Journal of Science*, 8:403–443, 1956.
- D.H. Enlow and S.O. Brown. A comparative histological study of fossil and recent bone tissues, part 2. *Texas Journal of Science*, 9:185–214, 1957.
- D.H. Enlow and S.O. Brown. A comparative histological study of fossil and recent bone tissues, part 3. *Texas Journal of Science*, 10:187–230, 1958.
- B.S. Everitt and G. Dunn. *Applied Multivariate Data Analysis*. Oxford University Press, New York, 1992.
- J.S. Foote. The comparative histology of femoral bones. *Transactions of the American Microscopic Society*, 30:87–140, 1911.
- J.S. Foote. The comparative histology of the femur. *Smithsonian Miscellaneous Collections, Publication 2232*, 61(8):1–9, 1913.
- J.S. Foote. A contribution to the comparative histology of the femur. *Smithsonian Contributions to Knowledge*, 33(3):280p., 1916.

- A Forster and H-J. Goldbach. Die histologische differenzierung von femurdiaphysen neugeborener, kleinkinder und kleiner haustiere. *Deutsch Z Gerichtsmed*, 43:273–289, 1954.
- P. Frasca, R.A. Harper, and J.L. Katz. Isolation of single osteons and osteon lamellae. *Acta Anatomica*, 95:122–129, 1976.
- H.M. Frost. Human haversian system measurements. *Henry Ford Hospital Medical Bulletin*, 9:45–47, 1961.
- H.M. Frost. *Bone Remodeling Dynamics*. Charles C. Thomas, Springfield, Illinois, 1963.
- H.M. Frost. Dynamics of bone remodeling. In *Bone Biodynamics*, page 315. Little and Brown, Boston, 1964.
- H.M. Frost. *Bone Dynamics in Osteoporosis and Osteomalacia*. Thomas, Springfield, Illinois, 1966.
- P.M. Galton. English hysilophodontid dinosaurs (reptilia: Ornithischia). *Palaeontology*, 18(4):741–752, 1975.
- P.M. Galton. The cranial anatomy of dryosaurus, a hypsilophodontid dinosaur from the upper jurassic of north america and east africa, with a review of hypsilophodontids from the upper jurassic of north america. *Geologica et Palaeontologica*, 17: 207–243, 1983.
- P.M. Galton. The poposaurid thecodontian teratosaurus suevicus v. meyer, plus referred specimens mostly based on prosauropod dinosaurs, from the middle stubensandstein (upper triassic) of nordwurttemberg. *Stuttgarter Beitrage zur Naturkunde, Series B*, 116:1–29, 1985.
- P.M. Galton and H. P. Powell. The ornithischian dinosaur camptosaurus prestwichii from the upper jurassic of england. *Palaeontology*, 23(2):411–443, 1980.
- P.M. Galton and P. Taquet. Valdosaurus, a hypsilophodontid dinosaur from the lower cretaceous of europe and africa. *Geobios*, 15(2):147–157, 1982.
- G. Garcia and X. Pereda Suberbiola. A new species of struthiosaurus (dinosauria: Ankylosauria) from the upper cretaceous of villevyrac (southern france). *Journal of Vertebrate Paleontology*, 23(1):156–165, 2003.
- F. Gauffre. The most recent melanorosauridae (saurischia, prosauropoda), lower jurassic of lesotho, with remarks on the prosauropod phylogeny. *Neues Jahrbuch fur Geologie und Palaontologie. Monatshefte*, 11:648–654, 1993.

- R. Georgia and I. Albu. The haversian canal network in the femoral compact bone in some vertebrates. *Morphology and Embryology*, 34(3):155–159, 1988.
- J. Gielis. A generic geometric transformation that unifies a wide range of natural and abstract shapes. *American Journal of Botany*, 90(3):333–338, 2003.
- C.W. Gilmore. A new coelurid dinosaur from the belly river cretaceous of alberta. *Bulletin of the Canadian Department of Mining and Geological Survey*, 38:1–12, 1924.
- C.W. Gilmore. On dinosaurian reptiles from the two medicine formation of montana. *Proceedings of the United States National Museum*, 77:1–39, 1930.
- C.W. Gilmore. Two new dinosaurian reptiles from mongolia with notes on some fragmentary specimens. *American Museum Novitates*, 679:1–20, 1933.
- P. Godefroit, X. Pereda Suberbiola, H. Li, and Z. Dong. A new species of the ankylosaurid dinosaur pinacosaurus from the late cretaceous of inner mongolia (p.r. china). *Bulletin de l'Institut Royal des Sciences Naturelles de Belgique, Sciences de la Terre*, 69(B):17–36, 1999.
- P. Godefroit, J.P. Currie, L. Hong, S.C. Yong, and D. Zhi-Ming. A new species of velociraptor (dinosauria: Dromaeosauridae) from the upper cretaceous of northern china. *Journal of Vertebrate Paleontology*, 28(2):432–438, 2008.
- H-J. Goldbach and H. Hinuber. Versuch einer systematic der formelemente des sug-etierknochens. *Deutsch Z Gerichtsmed*, 44:578–588, 1955.
- W. Granger and W.K. Gregory. Protoceratops andrewsi, a pre-ceratopsian dinosaur from mongolia. *American Museum Novitates*, 72:1–9, 1923.
- T.R. Gregory. The bigger the c-value, the larger the cell: Genome size and red blood cell size in vertebrates. *Blood Cells, Molecules, and Diseases*, 27:830–843, 2001.
- W. Gross. Die typen des mikroskopischen knochenbaues bei fossilen stegocephalen und reptilien. *Z. Anat.*, 103:731–764, 1934.
- L. Guttman. Some necessary conditions for common factor analysis. *Psychometrika*, 19:149–162, 1954.
- J. Haines and J.S. Crampton. Improvements to the method of fourier shape analysis as applied in morphometric studies. *Palaeontology*, 43(4):765–783, 2000.
- R.W. Haines. The evolution of epiphyses and of endochondral bone. *Biological Views of the Cambridge Philosophical Society*, 17:267–292, 1942.
- A.R. Hakistan, W.T. Rogers, and R.B. Cattell. The behavior of number-of-factors rules with simulated data. *Multivariate Behavioral Research*, 17(193-219), 1982.

- T. Hara, E. Tanck, J. Homminga, and R. Huiskes. The influence of microcomputed tomography threshold variation on the assessment of structural and mechanical trabecular bone properties. *Bone*, 31(1):107–109, 2002.
- L. Harsanyi. Differential diagnosis of human and animal bone. In G. Grupe and A.N. Garland, editors, *Histology of Ancient Human Bone*, volume 79-94. 1990.
- J.B. Hatcher. Diplodocus (marsh): its osteology, taxonomy, and probable habits, with a restoration of the skeleton. *Memoirs of the Carnegie Museum*, 1(1):1–61, 1901.
- J.B. Hatcher. Osteology of haplocanthosaurus, with description of new species and remarks on probable habits of the sauropoda, and the age and origin of atlantosaurus beds. *Memoirs of the Carnegie Museum*, 2:1–75, 1903.
- S.H. Haughten. Fauna and stratigraphy of the stormberg series. *Annals of the South African Museum*, 12:21–437, 1924.
- C. Havers. Osteologia nova, or some new observations of the bones, and the parts belonging to them, with the manner of their accretion and nutrition. 1691.
- L.M. Havill. Osteon remodeling dynamics in macaca mulatta: normal variation with regard to age, sex, and skeletal maturity. *Calcified Tissue International*, 74:95–102, 2004.
- X.-L. He, K. Li, K.-J. Cai, and Y.-H. Gao. [omeisaurus tianfuensis - a new species of omeisaurus from dashanpu, zigong, suchuan.]. *J. Chengdu College Geology*, Supplement 2:185–205, 1984.
- X.-L. He, S.-H. Yang, K.-J. Cai, K. Li, and Z.-W. Liu. [a new species of sauro-pod, mamenchisaurus tianfuensis sp. nov.] (in chinese). *Proceedings of the 30th International Geological Congress*, 12:83–86, 1996.
- J. Hert, P. Fiala, and M. Petrtyl. Osteon orientation of the diaphysis of the long bones in man. *Bone*, 15(3):269–277, 1994.
- J. Hey. The mind of the species problem. *Trends in Ecology and Evolution*, 16(7): 326–329, 2001.
- H. Hinuber. *Die Unterschiede in Feinbau von Menschen- und Tierknochen als gericht-srathliches Differentialdiagnostikum*. Ph. d., University of Marburg, 1951.
- W. Hogler, C.J.R. Blimkie, C.T. Cowell, A.F. Kemp, J. Briody, P. Wiebe, N. Farpour-Lambert, C.S. Duncan, and H.J. Woodhead. A comparison of bone geometry and cortical density at the mid-femur between prepuberty and young adulthood using magnetic resonance imaging. *Bone*, 33:771–778, 2003.

- F. Holl. *Handbuch der Petrefactenkunde, Pt. 1*. Quedlinburg, 1829.
- W.J. Holland. The osteology of *Diplodocus Marsh*, with special reference to the restoration of the skeleton of *Diplodocus Carnegiei* Hatcher, presented by Mr. Andrew Carnegie to the British Museum, May 12, 1905. *Memoirs of the Carnegie Museum*, 6(6):225–278, 1906.
- W.J. Holland. Heads and tails, a few notes relating to the structure of the sauropod dinosaurs. *Annals of the Carnegie Museum*, 9(3-4):273–278, 1915.
- W.J. Holland. The skull of *Diplodocus*. *Memoirs of the Carnegie Museum*, 9:397–403, 1924.
- R.B. Holmes, C. Forster, M. Ryan, and K.M. Shepherd. A new species of *Chasmosaurus* (Dinosauria: Ceratopsia) from the dinosaur park formation of southern Alberta. *Canadian Journal of Earth Sciences*, 38:1423–1438, 2001.
- T.R. Jr. Holtz. A new phylogeny of the carnivorous dinosaurs. In B.P. Prez-Moreno, T. Holtz, J. L. Sanz, and J. J. Moratalla, editors, *Gaia 15: Aspects of Theropod Paleobiology*. Museu Nacional de Historia Natural, Lisbon, Portugal, 1998.
- T.R. Jr. Holtz, R.E. Molnar, and J.P. Currie. Basal tetanurae. In D.B. Weishampel, P. Dodson, and H. Osmolska, editors, *The Dinosauria*, pages 71–110. University of California Press, 2 edition, 2004.
- R.W. Hooley. On the skeleton of *Iguanodon atherfieldensis* sp. nov. from the Wealden shales of Atherfield (Isle of Wight). *Quarterly Journal of the Geological Society of London*, 81:1–61, 1925.
- J.D. Horel. A rotated principal component analysis of the interannual variability of the northern hemisphere 500mb height field. *Monthly Weather Review*, 109:2080–2092, 1981.
- J.R. Horner. Cranial morphology of *Prosaurolophus* (Ornithischia: Hadrosaurinae) with description of two new hadrosaurid species and an evaluation of hadrosaurid phylogenetic relationships. *Museum of the Rockies Occasional Paper*, 2:120, 1992.
- J.R. Horner and J.D. Currey. Embryonic and neonatal morphology and ontogeny of a new species of *Hypacrosaurus* (Ornithischia, Lambeosauridae) from Montana and Alberta. In K. Carpenter, B.E. Hirsch, and J.R. Horner, editors, *Dinosaur Eggs and Babies*, pages 312–336. Cambridge University Press, 1994.
- J.R. Horner, A. de Ricqlès, and K. Padian. Variation in dinosaurian skeletochronology indicators: implications for age assessment and physiology. *Paleobiology*, 25(3):285–304, 1999.

- J.R. Horner, A. de Ricqles, and K. Padian. Long bone histology of the hadrosaurid dinosaur *maiasaura peeblesorum*: growth dynamics and physiology based on an ontogenetic series of skeletal elements. *Journal of Vertebrate Paleontology*, 20(1): 115–129, 2000.
- J.R. Horner, K. Padian, and A. de Ricqles. Comparative osteohistology of some embryonic and perinatal archosaurs: developmental and behavioral implications for dinosaurs. *Paleobiology*, 27(1):39–58, 2001.
- L. Hou, S.W. Chao, and S.C. Chu. [new discovery of sauropod dinosaurs from sichuan] (in chinese). *Vertebrata Pal-Asiatica*, 14(160-165), 1976.
- C. Hu. [a new hadrosaur from the cretaceous of chuncheng, shantung] (in chinese). *Acta Geologica Sinica*, 2:179–202, 1973.
- C.J. Huberty. *Applied Discriminant Analysis*. Wiley Interscience, 1994.
- F. von Huene. On the age of the reptile faunas contained in the magnesian conglomerate at bristol and in the elgin sandstone. *Geological Magazine, New Series*, 5(3): 99–100, 1908.
- J.W. Hulke. *Polacanthus foxii*, a large undescribed dinosaur from the wealden formation in the isle of wight. *Philosophical Transactions of the Royal Society of London*, 172:653–662, 1881.
- A.P. Hunt, M.G. Lucas, A.B. Heckert, R.M. Sullivan, and M.G. Lockley. Late triassic dinosaurs from the western united states. *Geobios*, 31:551–531, 1998.
- C.R. Jacobs and F. Echstein. Computer simulation of subchondral bone adaptation to mechanical loading in an incongruous joint. *The Anatomical Record*, 249:317–326, 1997.
- Z.F.G. Jaworski, B. Duck, and G. Sekaly. Kinetics and osteoclasts and their nuclei in evolving secondary haversian systems. *Journal of Anatomy*, 133(3):397–405, 1981.
- J. Jensen. A fourth new sauropod dinosaur from the upper jurassic of the colorado plateau and sauropod bipedalism. *The Great Basin Naturalist*, 48(2):121–145, 1988.
- Q. Ji, J.P. Currie, M.A. Norell, and S-A. Ji. Two feathered dinosaurs from north-eastern china. *Nature*, 393:753–761, 1998.
- L.C. Johnson. Morphologic analysis in pathology: The kinetics of disease and general biology in bone. In H.M. Frost, editor, *Bone Biodynamics*. Little and Brown, Boston, 1964.
- L.C. Johnson. The kinetics of skeletal remodeling. *Birth Defects Original Article Series 2*, pages 66–142, 1966.

- I.T. Jolliffe. *Principal Component Analysis*. Springer, New York, 1986.
- J. Jowsey. Studies of haversian systems in man and some animals. *Journal of Anatomy*, 100:857–864, 1966.
- J. Jowsey. Age and species differences in bone. *Cornell Veterinarian*, 58:74–94, 1968.
- H.F. Kaiser. The application of electronic computers to factor analysis. *Educational and Psychological Measurements*, 20:141–151, 1960.
- H. Kamioka, T. Honjo, and T. Takano-Yamamoto. A three-dimensional distribution of osteocyte processes revealed by the combination of confocal laser scanning microscopy and differential interference contrast microscopy. *Bone*, 28(2):145–149, 2001.
- B. Kenyeres and M. Hegyi. Unterscheidung des menschlichen und tierischen knochengewebes. *Vierteljahresschr Gerichtsmed*, 26:225–232, 1903.
- K.I. Kim, K. Jung, and H.J. Kim. Face recognition using kernel principal components analysis. *IEEE Signal Processing Letters*, 9(2):40–42, 2002.
- A. Kiprijanoff. Studien uber die fossilen reptilian russlands. *Memoire de l'Academie Imp. Sci. de St. Petersbourg*, 18:97–103, 1881.
- J. Kragstrup. Osteons in trabecular bone. morphometric studies of bone formed by remodeling. *Danish Medical Bulletin*, 32(6):287–295, 1985.
- J. Kragstrup and F. Melsen. Three-dimensional morphology of trabecular bone osteons reconstructed from serial sections. *Metabolic Bone Disease and Related Research*, 5(3):127–130, 1983.
- S.M. Kurzanov and T.A. Tumanova. [on the structure of the endocranium in some ankylosaurs from mongolia]. *Paleontologicheskii Zhurnal*, pages 90–96, 1978.
- S.A. Kuznetsov, M. Riminucci, N. Ziran, T.W. Tsutsui, A. Corsi, L. Calvi, H.M. Kronenberg, E. Schipani, P.G. Robey, and P. Bianco. The interplay of osteogenesis and hematopoiesis: expression of a constitutively active pth/pthrp receptor osteogenic cells perturbs the establishment of hematopoiesis in bone and of skeletal stem cells in the bone marrow. *The Journal of Cell Biology*, 167(6):1113–1122, 2004.
- L.M. Lambe. On the vertebrata of the mid-cretaceous of the northwest territory 2. new genera and species from the belly river series (mid-cretaceous). *Geological Survey of Canada, Contributions to Canadian Paleontology*, 3(2):23–81, 1902.
- L.M. Lambe. On the squamosal-parietal crest of the horned dinosaurs centrosaurus apertus and monoclonius canadensis from the cretaceous of alberta. *Transactions of the Royal Society of Canada*, 1(10):3–12, 1904.

- L.M. Lambe. A new genus and species of ceratopsia from the belly river formation of alberta. *Ibid*, 27:109–116, 1913.
- L.M. Lambe. On the forelimb of a carnivorous dinosaur from the belly river formation of alberta, and a new genus of ceratopsian from the same horizon, with remarks on the integument of some cretaceous herbivorous dinosaurs. *Ibid*, 27(10):129–135, 1914.
- L.M. Lambe. On eoceratops canadensis, gen. nov., with remarks on other genera of cretaceous horned dinosaurs. *Canada, Department of Mines, Geological Survey, Museum Bulletin*, 12:1–49, 1915.
- O. Lambert, P. Godefroit, H. Li, C.Y. Shang, and Z. Dong. A new species of protoceratops (dinosauria, neoceratopsia) from the late cretaceous of inner mongolia (p.r. china). *Bulletin de l'Institut Royal des Sciences Naturelles de Belgique Sciences de la Terre*, 71 (suppl.):5–28, 2001.
- L.E. Lanyon and S. Bourn. The influence of mechanical function on the development and remodeling of the tibia. *Journal of Bone and Joint Surgery*, 61A:263–273, 1979.
- J. Le Loeuff and E. Buffetaut. Tarascosaurus salluvicus, new genus, new species, a theropod dinosaur from the upper cretaceous of southern france. *Geobios*, 25: 585–594, 1991.
- T.M. Lehman. Chasmosaurus mariscalensis, sp. nov., a new ceratopsian dinosaur from texas. *Journal of Vertebrate Paleontology*, 9(2):137–162, 1989.
- J. Leidy. Notice of remains of extinct reptiles and fishes, discovered by dr. f.v. hayden in the badlands of the judith river, nebraska territory. *Proceedings of the Academy of Natural Science Philadelphia*, 8:72–73, 1856.
- R. Lewin. Recognizing ancestors is a species problem. *Science*, 234(4783):1500, 1986.
- J.B. Lian, G.S. Stein, and J.E. Aubin. Bone formation: Maturation and functional activities of osteoblast lineage cells. In *Primer on the Metabolic Bone Diseases and Disorders of Mineral Metabolism*, pages 13–28. 2003.
- R.L. Linn. A monte carlo approach to the number of factors problem. *Psychometrika*, 33:37–72, 1968.
- M. Locke. Structure of long bone in mammals. *Journal of Morphology*, 262:546–565, 2004.
- R. Lydekker. Notices of new and other vertebrata from indian tertiary and secondary rocks. *Records of the Geological Survey of India*, 10:30–43, 1877.

- R. Lydekker. Indian pre-tertiary vertebrata, part 3. *Palaeontologia Indica. Series 1-16*, 1(3):1–36, 1879.
- R. Lydekker. Note on a new wealden iguanodont and other dinosaurs. *Quarterly Journal of the Geological Society of London*, 44:46–61, 1888.
- R. Lydekker. On the remains and affinities of five genera of mesozoic reptiles. *Ibid*, 45:41–59, 1889.
- G.A. Mantell. Notice on the iguanodon, a newly discovered fossil reptile, from the sandstone of tilgate forest, in sussex. *Philosophical Transactions of the Royal Society of London*, 115:179–186, 1825.
- G. Marotti and A.Z. Zallone. Changes in the vascular network during the formation of haversian systems. *Acta Anatomica*, 106:84–100, 1980.
- O.C. Marsh. A new order of extinct reptilia (stegosauria) from the jurassic of the rocky mountains. *The American Journal of Science*, 14(84):513–514, 1877.
- O.C. Marsh. Notice of new dinosaurian reptiles. *Ibid*, 15(241-244), 1878.
- O.C. Marsh. A notice of new jurassic reptiles. *American Journal of Science (Third Series)*, 18:510–515, 1879.
- O.C. Marsh. Principal characters of american jurassic dinosaurs. part vii. on the diplodocidae, a new family of the sauropoda. *American Journal of Science*, 27 (158), 1884.
- O.C. Marsh. Notice of gigantic horned dinosauria from the cretaceous. *Ibid*, 38: 173–175, 1889.
- O.C. Marsh. Additional characters of the ceratopsidae, with notice of new cretaceous dinosaurs. *Ibid*, 39:418–426, 1890a.
- O.C. Marsh. Description of new dinosaurian reptiles. *Ibid*, 39(81-83), 1890b.
- O.C. Marsh. The typical ornithopoda of the american jurassic. *American Journal of Science, Series 3*, 48:85–90, 1894.
- R.B. Martin and D.B. Burr. A hypothetical mechanism for the stimulation of osteonal remodeling by fatigue damage. *Journal of Biomechanics*, 15:137–139, 1982.
- R.B. Martin and D.B. Burr. *Structure, Function, and Adaptation of Compact Bone*. Raven Press, New York, 1989.
- T. Maryanska and H. Osmolska. Cranial anatomy of saurolophus angustirostis with comments on the asian hadrosauridae (dinosauria). *Palaeontologia Polonica*, 42: 5–24, 1981.

- P. Matheron. Notes sur les reptiles fossiles des depots fluvio-lacustres cretaces du bassin a lignite de fuveau. *Bulletin de la Socit Gologique de France, series 2*, 26: 781–795, 1869.
- A.L. McAlester. Some comments of the species problem. *Journal of Paleontology*, 36 (6):1377–1381, 1962.
- J.H. McElhaney. The charge distribution of the human femur due to load. *Journal of Bone and Joint Surgery*, 49A:1561–1571, 1967.
- J.S. McIntosh and M.E. Williams. A new species of sauropod dinosaur, haplocanthosaurus delfsi sp. nov., from the upper jurassic morrison formation of colorado. *Kirtlandia*, 43(2-26), 1988.
- J.S. McIntosh, W.E. Miller, K.L. Stadtman, and D.D. Gillette. The oseology of camarasaurus lewisi (jensen, 1988). *Geology Studies*, 41:73–115, 1996.
- L.N. Metz, R.B. Martin, and A.S. Turner. Histomorphometric analysis of the effects of osteocyte density on osteonal morphology and remodeling. *Bone*, 33:753–759, 2003.
- H. von Meyer. Briefliche mitteilung an prof. bronn uber plateosaurus engelhardti. *Neues Jahrbuch fur Mineralogie, Geognoise, Geologie und Petrefakten-Kunde*, page 316, 1837.
- H. von Meyer. Reptilian aus dem stubensandstein des obern keupers. *Palaeontographica*, A 61:253–276, 1861.
- W. Miller. The structure of species, outcomes of speciation and the 'species problem': ideas for paleobiology. *Palaeogeography, Palaeoclimatology, Palaeoecology*, 176:1–10, 2001.
- B.M. Mishof, P. Roschger, W. Tecsh, P.A. Baldock, A. Valenta, P. Messmer, J.A. Eisman, A.L. Boskey, E.M. Gardiner, P. Fratzl, and K. Klaushofer. Targeted over-expression of vitamin d receptor in osteoblasts increases calcium concentration without affecting structural properties of bone mineral crystals. *Calcified Tissue International*, 73:251–257, 2003.
- S. Mishra and M.L. Knothe Tate. Effect of lacunocanalicular architecture on hydraulic conductance in bone tissue: implication for bone health and evolution. *The Anatomical Record Part A*, 273A:752–762, 2003.
- S. Mohsin, D. Taylor, and T.C. Lee. Three-dimensional reconstruction of haversian systems in ovine compact bone. *European Journal of Morphology*, 40(5):309–315, 2002.

- R. Mori, T. Kodaka, and Y. Naito. Delayed osteon formation in long-bone diaphysis of an 11-year-old giant cow with dermal dysplasia. *The Journal of Veterinary Medical Science*, 61(2):101–106, 1999.
- R. Mori, T. Kodaka, T. Sano, N. Yamagishi, M. Asari, and Y. Naito. Comparative histology of the laminar bone between young calves and foals. *Cells Tissues Organs*, 175:43–50, 2003.
- D.M. Mulhern and D.H. Ubelaker. Differences in osteon banding between human and nonhuman bone. *Journal of Forensic Science*, 46(2):220–222, 2001.
- D.M. Mulhern and D.H. Ubelaker. Histologic examination of bone development in juvenile chimpanzees. *American Journal of Physical Anthropology*, 122:127–133, 2003.
- G.R. Mundy, D. Chen, and B.O. Oyajobi. Bone remodeling. In *Primer on the Metabolic Bone Diseases and Disorders of Mineral Metabolism, Fifth Edition*, pages 46–57. 2003.
- J. Nemeskeri and L. Harsanyi. Problems of the investigation of cremated bones. *Anthropol Kozl*, 12:99–116, 1968.
- F. Nopsca. Dinosaurierreste aus sibenburgen. i. schadel von limnosaurus transsylvanicus nov. gen. et spec. *Denkschriften der Kaiserlichen Akademie der Wissenschaften. Mathematisch-naturwissenschaftliche Klasse*, 68:555–591, 1900.
- F. Nopsca. Die dinosaurier der siebenbrgischen landesteile ungarms. *Mitteilung des Jahrbuches der Knigliche Ungarische Geologische Reichsanstalt*, 23:1–26, 1915.
- C. Nyssen-Behets, P-Y. Duchesne, and A. Dhem. Structural changes with aging in cortical bone of the human tibia. *Gerontology*, 43:316–325, 1997.
- C. L. Organ, A.M. Shedlock, A. Meade, M. Pagel, and S.V. Edwards. Origin of avian genome size and structure in non-avian dinosaurs. *Nature*, 446:180–184, 2007.
- H.F. Osborn. Two lower cretaceous dinosaurs from mongolia. *Ibid*, 95:10, 1923.
- H.F. Osborn. Sauropoda and theropoda of the lower cretaceous of mongolia. *American Museum Novitates*, 128:1–8, 1924a.
- H.F. Osborn. Three new theropoda, protoceratops zone, central mongolia. *Ibid*, 144 (1-12), 1924b.
- J.H. Ostrom. A new species of hadrosaurian dinosaur from the cretaceous of new mexico. *Journal of Paleontology*, 35(3):575–577, 1961.

- K. Padian, A. de Ricqlès, and J.R. Horner. Bone histology determines identification of a new fossil taxon of pterosaur (reptilia: Archosauria). *Comptes Rendus de l'Academie des Sciences, Serie II. Sciences de la Terre et des Planetes*, 320(1): 77–84, 1995.
- K. Padian, A. de Ricqlès, and J.R. Horner. Dinosauria growth rates and bird origins. *Nature*, 412:405–408, 2001.
- K. Padian, J.R. Horner, and A. de Ricqlès. Growth in small dinosaurs and pterosaurs: the evolution of archosaurian growth strategies. *Journal of Vertebrate Paleontology*, 24(3):555–571, 2004.
- A.M. Parfitt. Quantum concept of bone remodeling and turnover: Implications from the pathogenesis of osteoporosis. *Calcified Tissue International*, 28:1–5, 1979.
- A.M. Parfitt. The physiologic and clinical significance of bone histomorphometric data. In R.R. Recker, editor, *Bone Histomorphometry: Techniques and Interpretation*. CRC Press, Boca Raton, 1983.
- S. Park, Y.K. Ku, M.J. Seo, D.Y. Kim, J.E. Yeon, K.M. Lee, S-C. Jeong, W.K. Yoon, C.H. Harn, and H.M. Kim. Principal components analysis and discriminant analysis (pca-da) for discriminating profiles of terminal restriction fragment length polymorphism (t-rflp) in soil bacteria communities. *Soil Biology and Biochemistry*, 38:2344–2349, 2006.
- W.A. Parks. The osteology of the trachodont dinosaur kritosaurus incurvimanus. *University of Toronto Studies, Geological Series*, 11:1–75, 1920.
- W.A. Parks. Parasaurolophus walkeri, a new genus and species of crested trachodont dinosaur. *Ibid*, 13(1-32), 1922.
- W.A. Parks. Corynthosaurus intermedius, a new species of trachodont dinosaur. *University of Toronto Studies, Geological Series*, 15:1–57, 1923.
- W.A. Parks. New species of dinosaurs and turtles from the belly river formation of alberta. *University of Toronto Studies, Geological Series*, 34:1–33, 1933.
- R. Pawlicki. Metabolic pathways of the fossil dinosaur bones. part v: Morphological differentiation a osteocyte lacunae and bone canaliculi and their significance in the system of extracellular communication. *Folia histochemica et cytobiologica*, 23(3): 165–174, 1985.
- S. Pfeiffer. Variability in osteon size in recent human populations. *American Journal of Physical Anthropology*, 106:219–227, 1998.

- L.H. Pi, H. Ouyang, and Y. Ye. [a new species of sauropod from zigong, sichuan: Mamenchisaurus youngi] (in chinese). In *Department of Spatial Planning and Regional Economy. [Papers on Geoscience Contributed to the 30th International Geological Congress]*, pages 87–91. China Economic Publishing House, 1996.
- R.M.V. Pidaparti and D.B. Burr. Collagen fiber orientation and geometry effects on the mechanical properties of secondary osteons. *Journal of Biomechanics*, 25(8): 869–880, 1992.
- M. Portigliatti-Barbos, P. Bianco, and A. Ascenzi. Distribution of osteonic and interstitial components in the human femoral shaft with reference to structure, calcification, and mechanical properties. *Acta Anatomica*, 115:178–186, 1983.
- M. Portigliatti-Barbos, P. Bianco, A. Ascenzi, and A. Boyde. Collagen orientation in compact bone: Ii. distribution of lamellae in the whole of the human femoral shaft with reference to its mechanical properties. *Metabolic Bone Disease and Related Research*, 5:309–315, 1984.
- S. Qiu, D.P. Fyhrie, S. Palnitkar, and D.S. Rao. Histomorphometric assessment of haversian canal and osteocyte lacunae in different-sized osteons in human rib. *The Anatomical Record Part A*, 272A:520–525, 2003.
- J.T. Queckett. Additional observation on the intimate structure of bone. *Transaction of the Micros Society of London*, 2:40–42, 1849a.
- J.T. Queckett. On the intimate structure of bone as composing the skeleton in the four great classes of animals. *Transaction of the Micros Society of London*, 2:46–48, 1849b.
- J.T. Queckett. *Descriptive and illustrated catalogue of the histological series contained in the Museum of the Royal College of Surgeons of England*, volume 2. London, 1855.
- M.A. Raath. A new coelurosaurian dinosaur from the forest sandstone of rhodesia. *Arnoldia (Rhodesia)*, 4(28):1–25, 1969.
- W.S. Rasband. Imagej, 1997-2008.
- S. Ray, J. Botha, and A. Chinsamy. Bone histology and growth patterns of some non-mammalian therapsids. *Journal of Vertebrate Paleontology*, 24(3):634–648, 2004.
- O.A. Reig. La presencia de dinosaurios saurisquios en los "estratos de ischigualasto" (mesotriasico superior) de las provincias de san juan y la rioja (republica argentina). *Ameghiniana*, 3(3-20), 1963.
- J.M. Rensberger and M. Watabe. Fine structure of bone in dinosaurs, birds, and mammals. *Nature*, 406:619–622, 2000.

- A. de Ricqlès. Quelques observations paleohistologiques sur le dinosaurian sauropode bothriospondylus. *Annales de Paleontologie Vertebrates*, 6:157–209, 1968.
- A. de Ricqlès. Vers une histoire de la physiologie thermique; les données histologiques et leur interprétation fonctionnelle. *Comptes Rendus Hebdomadaires des séances de l'Académie des sciences. D, Sciences naturelles*, 275:1745–1749, 1972.
- A. de Ricqlès. Evolution of endothermy: histological evidence. *Evolutionary Theory*, 1:51–80, 1974.
- A. de Ricqlès. Tissue structures of dinosaur bone: functional significance and possible relation to dinosaur physiology. *A Cold Look at the Warm-blooded Dinosaurs, AAAS Selected Symposia Series*, 28:103–139, 1980.
- A. de Ricqlès. On the usefulness and prospects of bone histology for vertebrate paleontology. *Paleopathology Association News*, 5:16, 1986.
- A. de Ricqlès. Some remarks on palaeohistology from a comparative evolutionary point of view. In G. Grupe and A.N. Garland, editors, *Histology of Ancient Human Bone*, pages 37–78. 1990.
- A. de Ricqlès, K. Padian, and J.R. Horner. Comparative biology and the bone histology of extinct tetrapods: what does it tell us? *ICVM Abstracta*, page 246, 1997.
- A. de Ricqlès, K. Padian, and J.R. Horner. The bone histology of basal birds in phylogenetic and ontogenetic perspectives. In J. Gauthier and L.F. Gall, editors, *New Perspectives on the Origin and Early Evolution of Birds: Proceedings of the International Symposium in Honor of John H. Ostrom*, pages 411–426. Peabody Museum of Natural History, New Haven, 2001.
- A. de Ricqlès, K. Padian, J.R. Horner, E.-T. Lamm, and N. Myhrvold. Osteohistology of *Confuciusornis sanctus* (theropoda: Aves). *Journal of Vertebrate Paleontology*, 23(2):373–386, 2003.
- A.J. Ricqlès, F.J. Meunier, J. Castanet, and H. Francillon-Vieillot. Comparative microstructure of bone. In B.K. Hall, editor, *Bone, Volume 3: Bone Matrix and Bone-Specific Products*, pages 1–78. 1991.
- A.G. Robling and S.D. Stout. Morphology of the drifting osteon. *Cells Tissues Organs*, 164:192–204, 1999.
- A.G. Robling and S.D. Stout. Histomorphometry of human cortical bone: application to age estimation. In M.A. Katzenberg and S.R. Saunders, editors, *Biological Anthropology of the Human Skeleton*. Wiley-Liss, Inc., New York, 2000.

- G.A. Rodan and T.J. Martin. Role of osteoblasts is hormonal control of bone resorbtion-a hypothesis. *Calcified Tissue International*, 33:349–351, 1981.
- C. Rouiller, L. Huber, E. Kellenberger, and E. Rutishauser. La structure lamellaire de l'osteone. *Acta Anatomica*, 14(1-2):9–22, 1952.
- T. Rowe. A new species of theropod dinosaur syntarsus from the early jurassic kayenta formation of arizona. *Journal of Vertebrate Paleontology*, 9(2):125–136, 1989.
- U. Ruangwit. The split-line phenomenon and the microscopic structure of bone. *American Journal of Physical Anthropology*, 26:319–330, 1967.
- D.A. Russell. Isolated dinosaur bones from the middle cretaceous of the tafilalt, morocco. *Bulletin du Museum national d-histoire naturelle. Section C de la terre, paleontologie, geologie, minerologie*, 18(2-3):349–402, 1996.
- M.J. Ryan and A.P. Russell. A new centrosaurine ceratopsid from the oldman formation of alberta and its implications for centrosaurine taxonomy and systematics. *Canadian Journal of Earth Sciences*, 42:1369–1387, 2005.
- Julia T. Sankey. Late campanian southern dinosaurs, aguja formation, big bend, texas. *Journal of Paleontology*, 75(1):208–215, 2001.
- J. Schaffer. Uber den feineren bau fossiler knochen. *Sitzungsber Kaiserl Akad Wiss Math Naturwiss KI*, 3-7:319–382, 1889.
- M.H. Schweitzer, J.L. Wittmeyer, and J.R. Horner. Gender-specific reproductive tissue in ratites and tyrannosaurus rex. *Science*, 308:1456–1460, 2005a.
- M.H. Schweitzer, J.L. Wittmeyer, J.R. Horner, and J.K. Toporski. Soft-tissue vessels and cellular preservation in tyrannosaurus rex. *Science*, 307:1952–1955, 2005b.
- M.H. Schweitzer, Z. Suo, R. Avci, J.M. Asara, M.A. Allen, F.T. Arce, and J.R. Horner. Analyses of solt tissue from tyrannosaurus rex suggest the presence of protein. *Science*, 316:277–280, 2007.
- E.D. Sedlin and H.M. Frost. Variations in rate of human osteon formation. *Canadian Journal of Biochemistry and Physiology*, 41:19–22, 1963.
- A.L. Seitz. Vergleichende studien uber den milroskopischen knochenbau fossiler und rezenter reptilian. *Nova Acta Akad Leop Carol Naturfoersch*, 87:230–370, 1907.
- P.C. Sereno and S.T. Chao. Psittacosaurus xinjiangensis (ornithischia: Ceratopia), a new species of psittacosaur from the lower cretaceous of northwestern china. *Journal of Vertebrate Paleontology*, 8(4):353–356, 1988.

- W. Siedlicki, K. Siedlicki, and J. Schlansky. Mapping techniques in pattern analysis. In E.S. Galsema and L.N. Kanal, editors, *Pattern Recognition and Artificial Intelligence*. Elsevier Science, Amsterdam, 1988.
- G.G. Simpson. The species concept. *Evolution*, 5(4):285–298, 1951.
- I.J. Singh, E.A. Tonna, and C.P. Gandel. A comparative histological study of mammalian bone. *Journal of Morphology*, 144(4):421–437, 1974.
- A. Sirieix and G. Downey. Commercial wheatflour authentication by discriminant analysis of near infrared reflectance spectra. *Journal of Near Infrared Spectroscopy*, 1:187–197, 1993.
- J.G. Skedros, S.C. Su, and R.D. Bloebaum. Biomechanical implications of mineral content and microstructural variation in cortical bone of horse, elk, and sheep calcanei. *The Anatomical Record*, 249:297–316, 1997.
- J.G. Skedros, M.W. Mason, and R.D. Bloebaum. Modeling and remodeling in a developing artiodactyl calcaneus: a model for evaluating frost’s mechanostat hypothesis and its corollaries. *The Anatomical Record*, 263:167–185, 2001.
- J.G. Skedros, K.J. Hunt, P.E. Hughes, and H. Winet. Ontogenetic and regional morphologic variations in the turkey ulna diaphysis: implications for functional adaptation of cortical bone. *The Anatomical Record Part A*, 273A:609–629, 2003a.
- J.G. Skedros, C.L. Sybrowsky, T.R. Parry, and R.D. Bloebaum. Regional differences in cortical bone organization and microdamage prevalence in rocky mountain mule deer. *The Anatomical Record Part A*, 274A:837–850, 2003b.
- J.G. Skedros, K.J. Hunt, and R.D. Bloebaum. Relationship of loading history and structural and material characteristics of bone: Development of the mule deer calcaneus. *Journal of Morphology*, 259:281–307, 2004.
- R.R. Sokal. The species problem reconsidered. *Contemporary Systematic Philosophies, Systematic Zoology*, 22(4):360–374, 1973.
- D.G. Steele and C.A. Bramblett. *The Anatomy and Biology of the Human Skeleton*. Texas A&M University Press, College Station, Texas, 1988.
- C.M. Sternberg. A new armored dinosaur from the edmonton formation of alberta. *Transactions of the Royal Society of Canada, Series 3*, 22:93–106, 1928.
- C.M. Sternberg. A new ornithomimus with complete abdominal cuirass. *Canadian Field Naturalist*, 47(5):79–83, 1933.
- C.M. Sternberg. Hooded hardrosaurs of the belly river series of the upper cretaceous, a comparison, with description of new species. *Canada, Department of Mines, Nateral History Museum Bulletin 77, Geological Series*, 77:1–37, 1935.

- C.M. Sternberg. Certatopsidae from alberta. *Journal of Paleontology*, 14:468–480, 1940.
- J.S. Steyer, M. Laurin, J. Castanet, and A. de Ricqlès. First histological and skeletochronological data on temnospondyl growth: palaeoecological and palaeoclimatological implications. *Palaeogeography, Palaeoclimatology, Palaeoecology*, 206:193–201, 2004.
- S.D. Stout, B.S. Brunnsden, C.F. Hildebolt, P.K. Commean, K.E. Smith, and N.C. Tappen. Computer-assisted 3d reconstruction of serial sections of cortical bone to determine 3d structure of osteons. *Calcified Tissue International*, 65(280-284), 1999.
- E. Stromer. Ergebnisse der forschungsreisen prof. e. stromers in den wsten gyptens. ii. wirbeltier-reste der baharije-stufe (unterstes cenoman). 3. das original des theropoden spinosaurus aegyptiacus nov. gen., nov. spec. *Abhandlungen der Kniglich Bayerischen Akademie der Wissenschaften, Mathematisch-physikalische Classe.*, 28(3): 1–32, 1915.
- H-D. Sues. On chirostenotes, a late cretaceous oviraptorosaur (dinosauria: Theropoda) from western north america. *Journal of Vertebrate Paleontology*, 17 (4):698–716, 1997.
- R.M. Sullivan. Revision of the dinosaur stegoceras lambe (ornithischia, pachycephalosauria). *Journal of Vertebrate Paleontology*, 23(1):181–207, 2003.
- N.C. Tappen. Three-dimensional studies of resorption space and developing osteons. *American Journal of Anatomy*, 149:301–332, 1977.
- S.L. Teitelbaum. Ranking c-jun in osteoclast development. *The Journal of Clinical Investigation*, 114(4):463–465, 2004.
- D.D. Thompson and M. Gunness-Hey. Bone mineral-osteon analysis of yupik-inupiaq skeletons. *American Journal of Physical Anthropology*, 55:1–7, 1981.
- R.B. Todd and W. Bowman. *The Physiological and Physiology of Man*. Blanchard and Lea, Philidelphia, 1845.
- J. Tolar, S.L. Teitelbaum, and P.J. Orchard. Osteoporosis. *The New England Journal of Medicine*, 351(27):2839–2849, 2004.
- J. Tomes and C. De Morgan. Observations on the structure and development of bone. *Philosophical Transactions of the Royal Society of London*, 143:109–139, 1853.
- Umbio. Evince, 2009.

- P. Upchurch, Y. Tomida, and P.M. Barrett. A new specimen of apatosaurus ajax (sauropoda: Diplodpcidae) from the morrison formation (upper jurassic) of wyoming, usa. *National Science Museum Monographs*, 26, 2004.
- J. Vinther, D.E.G. Briggs, R.O. Prum, and V. Saranathan. The colour of fossil feathers. *Biology Letters*, 4(5):522–525, 2008.
- H. Virchow. Atlas and epistopheus bei den schildkroten. *Sitzungs-berichte der Gesellschaft naturforschender Freunde ze Berlin*, 8:303–332, 1919.
- N.J. Wachter, G.D. Krischak, M. Mentzel, M.R. Sarkar, T. Ebinger, L. Kinzl, L. Claes, and P. Augat. Correlation of bone mineral density with strength and microstructural parameters of cortical bone in vitro. *Bone*, 31(1):90–95, 2002.
- D.B. Weishampel and P.R. Bjork. The first indisputable remains of iguanodon (ornithischia: Ornithopoda) from north america: Iguanodon lakotaensis, sp. nov. *Journal of Vertebrate Paleontology*, 9(1):56–66, 1989.
- D.B. Weishampel, C-M. Jianu, Z. Csiki, and D.B. Norman. Osteology and phylogeny of zalmoxes (n.g.), an unusual euornithopod dinosaur from the latest cretaceous of romania. *Journal of Systematic Palaeontology*, 1(2):65–123, 2003.
- D.B. Weishampel, P.M. Barrett, R.A. Coria, J. Le Loeuff, X. Xing, Z. Xijin, A. Sahni, E.M.P. Gomani, and C.R. Noto. Dinosaur distribution. In D.B. Weishampel, P. Dodson, and H. Osmlska, editors, *The Dinosauria*, pages 517–606. 2nd edition edition, 2004.
- J.M. Weller. The species problem. *Journal of Paleontology*, 35(6):1181–1192, 1961.
- S.W. Whitson. Tight junction formation in the osteon. *Clinical Orthopaedics and Related Research*, 86:206–213, 1972.
- B. Williams, D. Waddington, D.H. Murray, and C. Farquharson. Bone strength during growth: influence of growth rate on cortical porosity and mineralization. *Calcified Tissue International*, 74:236–245, 2004.
- T.E. Williamson and T.D. Carr. A new genus of derived pachycephalosaurian from western north america. *Journal of Vertebrate Paleontology*, 22(4):779–801, 2002.
- C. Wiman. Parasaurolophus tubican, nov. sp., aus der kreide in new mexico. *Ibid*, 7(5):1–11, 1931.
- X. Xu. A new psittacosaur (psittacosaurus mazongshanensis sp. nov.) from mazongshan area, gansu province, china. *Sino-Japanese Silk Road dinosaur expedition*, pages 48–67, 1997.

- X. Xu, Z. Zhou, and X Wang. The smallest known non-avian theropod dinosaur. *Nature*, 408:705–708, 2000.
- X. Xu, Z. Zhou, X Wang, X. Kuang, F. Zhang, and X. Du. Four-winged dinosaurs from china. *Nature*, 421:335–340, 2003.
- A.M. Yates. A new species of the primitive dinosaur thecodontosaurus (saurischia: Sauropodomorpha) and its implications for the systematics of early dinosaurs. *Journal of Systematic Palaeontology*, 1:1–42, 2003.
- V.L. Yeager, S. Chiemchanya, and P. Chaiseri. Changes in size of lacunae during the life of osteocytes in osteon of compact bone. *Journal of Gerontology*, 30(1):9–14, 1975.
- C.C. Young. On some new dinosaurs from western suiyan, inner mongolia. *Bulletin of the Geological Society of China*, 2:159–166, 1930.
- C.C. Young. On a new sauropod, with notes on other fragmentary reptiles from szechuan. *Bulletin of the Geological Society of China*, 19(3):279–315, 1939.
- C.C. Young. On a new sauropod from yiping, szechuan, china. *Acta palaeontologica Sinica*, 2(4):355–369, 1954.
- C.C. Young. New sauropods from china. *Vertebrata Pal-Asiatica*, 2:1–28, 1958.
- C.C. Young and H.-C. Chao. [mamechisaurus hochuanensis sp. nov.] (in chinese). *Institute of Vertebrate Paleontology and Paleoanthropology, Monograph Series A*, 8 (1-30), 1972.
- K.Y. Yueng and W.L. Ruzzo. Principal components analysis for clustering gene expression data. *Bioinformatics*, 19(9):763–774, 2001.
- Y. Zhang, K. Li, and Q.-H. Zeng. [a new species of sauropod from the late jurassic of the sichuan basin (mamenchisaurus jingyanensis sp. nov.)] (in chinese). *Journal of Chengdu University of Technology*, 25:61–68, 1998.
- Z. Zhou and X Wang. A new species of caudipteryx from the xixian foration of liaoning, northeast china. *Vertebrata Pal-Asiatica*, 38:111–127, 2000.

Curriculum Vitae

Stephanie Novak Kuster

- Born** January 22, 1979
Baltimore, Maryland USA
- Degrees** B.S. Geological Sciences, May 2001
University of North Carolina, Chapel Hill, NC USA
- M.S. Geological Sciences, May 2004
University of North Carolina, Chapel Hill, NC USA
- M.A. Earth and Planetary Sciences, May 2005
Washington University, Saint Louis, MO USA
- Ph.D. Earth and Planetary, August 2009
Washington University, Saint Louis, MO USA
- Professional Societies** Society of Vertebrate Paleontology
Geological Society of America
Society for Integrative and Comparative Biology
Paleontological Society
- Select Honors and Awards** Tolman Prize, Outstanding Grad. Teaching Assistant, 2007
Letter of Recognition, Outstanding performance as a teaching assistant, 2004-2005 academic year, 2005
Wheeler Fellowship, Washington University, 2003-2008
Best Graduate Student Poster Presentation Award, Anadarko-ExxonMobil Student Symposium, 2003
R. Jerry Britt Award in Coastal Plain Geology, Department of Geological Sciences, UNC-Chapel Hill, 2003

**Peer-reviewed
publications**

Peyer, K., Carter, J.G., Sues, H-D., **Novak, S.E.**, Olsen, P.E. 2008. "A new suchian archosaur from the Upper Triassic of North Carolina." *Journal of Vertebrate Paleontology* 28(2): 363-381.

Kuster, S.E. (in revision). "Microstratigraphic context and position of fossil vertebrates from the Late Cretaceous of the Nile Valley, Egypt." *South African Journal of Geology*.

Kuster, S.E. (in review). "A new specimen of Postosuchus from the Late Triassic Coelophysus Quarry, Ghost Ranch, New Mexico." *Journal of Vertebrate Paleontology*.

Kuster, S.E. (in revision). "Using pasta to demonstrate description and classification of fossil invertebrates." *Journal of Geoscience Education*.

August 2009

Tetrapod Microstructure Identification, Kuster, Ph.D. 2009